



MONASH University

CHARACTERISATION OF ROCK  
DYNAMIC BEHAVIOUR BY FULL-  
FIELD MEASUREMENTS

HAOZHE XING

(Doctor of Philosophy)



A thesis submitted for the degree of *Doctor of Philosophy* at  
Monash University in 2019  
(Department of Civil Engineering)





## **Copyright notice**

© Haozhe Xing (2019).



## Declaration

This thesis contains no material which has been accepted for the award of any other degree or diploma at any university or equivalent institution and that, to the best of my knowledge and belief, this thesis contains no material previously published or written by another person, except where due reference is made in the text of the thesis.

Signature:

Print Name: Haozhe Xing

Date: 2019.06.12



# **ABSTRACT**

## **CHARACTERISATION OF ROCK DYNAMIC BEHAVIOUR BY FULL-FIELD MEASUREMENTS**

A thesis submitted for the degree of Doctor of Philosophy

Haozhe Xing

Department of Civil Engineering

Monash University

2019

A picture is a key to understanding. Scientific breakthroughs are often built upon the successful visualisation of objects beyond human eyes. Regarding the deformation characteristics and fracture patterns of rock in dynamic-loading experiments, the investigation has long been filled with blank spaces due to the difficulties existing technology had with generating images fast enough to capture. High-speed photography changes all of this. Researchers can now freeze the deformation and visualise processes they have never seen previously. A sequence of images provides a basic understanding of the rock deformation. With the aid of digital optical measurements, the stress, strain and stress intensity factors of rock during dynamic loading can to be determined in a direct and non-destructive way. As one of the digital optical measurements, digital image correlation (DIC) is long believed to be one of the most promising and ideal means to measure the dynamic deformation of brittle materials because of its accuracy, applicability and operability. By integrating the stereovision principle into DIC algorithm, a 3D-DIC is capable of detecting the complex and out-of-plane displacement.

The main contribution of this thesis is using the coupled high-speed imaging and 3D-DIC measurement to study the 3D full-field dynamic behaviour of rock at high strain rates from  $10^1$  to  $10^5 \text{ s}^{-1}$ . The setup and experiment procedures for implementing high-speed 3D-DIC in

rock dynamic test were described in detail. The minimum inter-frame time for rock deformation analysis reaches 5 microseconds and the accuracy of measured strain is as precise as tens of micro-strain. The scale of the research object ranges from 1 cm<sup>3</sup> to 1000 cm<sup>3</sup>. The difference of rock deformation obtained by DIC method and traditional strain-gauge methods in Split Hopkinson pressure bar (SHPB) test was discussed. The error between 2D-DIC and 3D-DIC in rock dynamic deformation was evaluated.

Based on the high-speed 3D-DIC technique, the full-field deformation of rock under high strain-rate loading was studied with the identification of dynamic Poisson's ratio and Young's modulus as well as their relationship with strain rates. The stress thresholds for crack initiation and development under dynamic loading were determined. The full-field fracture evolution of rock under high strain-rate loading such as initiation, branching and coalescence were identified. The environmental effects from internal (grain size and rock type) and external (CO<sub>2</sub>, water, brine and heat) aspects on rock dynamic properties and fracturing patterns were discussed. The macro dynamic behaviour was studied with microscopic investigation in terms of mineral composition and distribution. The real-time structural response and damage evaluation of rock slab subjected to intermediate-velocity projectile impact are also investigated with the high-speed photography and 3D-DIC technique.

## **Publications during enrolment**

**Xing, H. Z.**, Zhang, Q. B., Braithwaite, C. H., Pan, B., & Zhao, J. (2017). High-speed photography and digital optical measurement techniques for geomaterials: fundamentals and applications. *Rock Mechanics and Rock Engineering*, 50(6), 1611-1659.

**Xing, H. Z.**, Zhang, Q. B., Ruan, D., Dehkhoda, S., Lu, G. X., & Zhao, J. (2018). Full-field measurement and fracture characterisations of rocks under dynamic loads using high-speed three-dimensional digital image correlation. *International Journal of Impact Engineering*, 113, 61-72.

**Xing, H. Z.**, Zhang, Q. B., & Zhao, J. (2018). Stress Thresholds of Crack Development and Poisson's Ratio of Rock Material at High Strain Rate. *Rock Mechanics and Rock Engineering*, 51(3), 945-951.

**Xing, H. Z.**, Wu, G. L. N., Dehkhoda, S., Ranjith, G. & Zhang, Q. B. (2019). Fracture and mechanical characteristics of CO<sub>2</sub>-saturated sandstone at extreme loading conditions. *International Journal of Rock Mechanics and Mining Sciences*.50, 1611-1659.

**Xing, H. Z.**, Wu, G. L. N., Zhang, Q.B., Dehkhoda, S., & Zhao, J. Perforation model of thin rock slab subjected to rigid projectile impact at an intermediate velocity. To be submitted.

**Xing, H. Z.**, Hu, W.R., Zhang, Q.B., Dehkhoda, S., & Zhao, J. Characterization of dynamic constitutive constants of rock using coupled DIC-DEM inverse method. To be submitted.

**Xing, H. Z.**, Wu, G. L. N., Dehkhoda, S., Zhang, Q. B., & Zhao, J. (2018). A preliminary study of using high-speed Digital Image Correlation (DIC) to characterize the penetration on geomaterial. In *Rock Dynamics and Applications 3* (pp. 175-178). CRC Press.

**Xing, H. Z.**, Wu, G. L. N., Zhang, Q.B., Dehkhoda, S., & Zhao, J. (2018). Characterization of thermal/strain rate effect on the rock fracture using high-speed 3D-DIC. 10th Asian Rock Mechanics Symposium.

**Xing, H. Z.**, Dehkhoda, S., Zhang, Q. B., & Zhao, J. (2018). The dynamic fracturing patterns of multiple types of rock with Brazilian tests investigated by high-speed 3D-DIC. 11<sup>th</sup> International Conference on Structural Integrity and Failure.





## ACKNOWLEDGEMENTS

The deepest admiration and gratitude are to my main supervisor, Professor Jian Zhao. I appreciate your trust, your guidance and your encouragement not only in the academic research but also in the philosophy of life. Special acknowledgement is to my co-supervisors, Dr. Qianbing Zhang and Dr. Sevda Dehkhoda from whom I learnt invaluable experience of research skills.

Thanks to chairs and panels attended in all milestones throughout my PhD study, they are Prof. Mohan Yellishetty, Dr. Ha Bui, Dr. Yihai Fang; Professor Abdelmalek Bouazza, Dr. Stephan Arndt, Dr. Chunshun Zhang; Prof. P.G. Ranjith, Prof. Hai Vu, Dr. Phu Nguyen.

Thanks to administrative staff at the Department of Civil Engineering, Mrs. Jenny Manson, Mrs. Irene Sgouras, Ms. Tara Fry and Ms. Noi Souvandy. Technical support from Mr. Long Goh, Mr. Mike Leach, Mr. Jeffery Doddrell from Civil Engineering, Mr. Junnel Alegado from Earth Science, Ms Xiya Fang from Monash Center for Electron Microscopy.

I would like to thank Prof. Guoxin Lu and Prof. Dong Ruan of Swinburne University of Technology for supporting the experimental resource. Thanks to Mr. Jianjun Zhang, Mr. Nanthan Edwards and Mr. Collin Dingfelder for technical support there.

Through these years I have had a great deal of help and suggestions from the current and former members at Monash University. Special thanks go to Gonglinan Wu, Lei He, Yang Zou, Yanlong Zheng, Xing Li, Kai Liu, Wei Xiong, Minghe Ju, Jing Li, Tingwen Sun, Wanrui Hu, Huachuan Wang and Xiaofeng Li.

I would like to thank my master supervisor Prof. Mingyang Wang who encouraged me to pursue my PhD overseas.

I acknowledge the financial support provided by the China Scholarship Council (201503170221) and CSIRO top-up scholarship

I wish to thank Ms. Meixin Zhou with whose company the PhD life becomes colourful.

Finally, I would like to express my love to my father, Mr. Guoquan Xing and my mother, Ms. Zhen Luo. Thanks for your unconditional and endless love.



# CONTENTS

ABSTRACT .....	i
ACKNOWLEDGEMENTS .....	iv
LIST OF FIGURES .....	ix
CHAPTER 1 INTRODUCTION .....	1
1.1 Background .....	1
1.2 Objectives and scopes .....	3
1.3 Structures of thesis .....	5
CHAPTER 2 REVIEW OF HIGH-SPEED IMAGING AND DIGITAL OPTICAL FULL-FIELD MEASUREMENT TECHNIQUES FOR GEOMATERIALS .....	7
2.1 Introduction .....	7
2.2 High-speed photography .....	10
2.3 Recent applications of high-speed photography to geomaterials .....	12
2.3.1 Sand Movement .....	12
2.3.2 Penetration .....	16
2.3.3 Fracturing .....	21
2.3.4 Spalling .....	30
2.3.5 Fragmentation .....	33
2.4 High-speed digital optical measurement techniques and their applications to geomaterials ..	39
2.4.1 Photoelasticity Coating .....	40
2.4.2 Moiré .....	44
2.4.3 Caustics .....	46
2.4.4 Holographic Interferometry .....	49
2.4.5 Particle Image Velocimetry (PIV) .....	51
2.4.6 Digital Image Correlation (DIC) .....	57
2.4.7 Infrared Thermography .....	59
2.5 Concluding remarks .....	61
References .....	64
CHAPTER 3 EXPERIMENTAL SET-UP .....	83
3.1 Material preparation .....	83
3.2 Material specification .....	84
3.3 Loading device .....	88

3.3.1 Quasi-static system.....	88
3.3.2 SHPB system.....	90
3.4 Acquisition system .....	92
3.5 Full-field measurement.....	94
3.5.1 High-speed photography .....	94
3.5.2 High-speed 3D-DIC .....	105
3.6 Summary .....	114
References .....	115
CHAPTER 4 DYNAMIC PROPERTIES AND FRACTURE PATTERNS OF ROCK BY FULL-FIELD MEASUREMENT .....	118
4.1 Introduction .....	118
4.2 Experimental set-up.....	123
4.3 Full-field deformation measurement .....	123
4.3.1 Strain and strain rate pattern.....	123
4.3.2 Comparison between 3D-DIC and strain-gauge method.....	126
4.3.3 Comparison between 3D-DIC and 2D-DIC .....	130
4.4 Identification of dynamic properties .....	132
4.5 Stress threshold for fracture .....	135
4.5.1 Identification of dynamic stress thresholds .....	135
4.5.2 Strain rate effect .....	137
4.6 Strain localisation and fracture characteristics .....	138
4.6.1 Strain localisation and fracture evolution.....	138
4.6.2 Post-failure characteristics.....	143
4.7 Recommendations for further work.....	144
4.8 Summary .....	145
References .....	146
CHAPTER 5 INTRINSIC AND EXTERNAL EFFECTS ON DYNAMIC BEHAVIOUR OF ROCK .....	152
5.1 Introduction .....	152
5.2 Background .....	153
5.2.1 Grain size effect.....	153
5.2.2 Rock type effect.....	154
5.2.3 Thermal effect .....	156
5.2.4 Fluid effect .....	157
5.3 Grain size effect.....	159

5.4 Rock type effect .....	164
5.5 Thermal effect .....	171
5.6 Carbon dioxide effect .....	179
5.6.1 Experimental set-up .....	179
5.6.2 Results .....	181
5.6.3 Discussion .....	190
5.7 Summary .....	195
References .....	196
CHAPTER 6 DYNAMIC BEHAVIOUR OF ROCK SLAB UNDER INTERMEDIATE-VELOCITY PROJECTILE IMPACT .....	202
6.1 Introduction .....	203
6.2 Experimental set-up .....	205
6.2.1 Material specification .....	205
6.2.2 Loading equipment and projectile .....	206
6.2.3 High-speed imaging and 3D-DIC measurement .....	207
6.3 Results .....	208
6.3.1 Damage mode and parameters .....	208
6.3.2 Projectile kinematic measurement .....	212
6.4 Perforation model .....	213
6.4.1 Perforation limit and ballistic limit .....	213
6.4.2 Residual velocity .....	220
6.5 Discussion .....	226
6.6 Summary .....	230
References .....	231
CHAPTER 7 CONCLUSIONS AND FUTURE WORKS .....	234
7.1 Conclusions .....	234
7.2 Limitation and future work .....	236



# LIST OF FIGURES

## Chapter 1

<b>Fig. 1.1</b> Scopes, activities and roadmap of research presented in this thesis.....	4
------------------------------------------------------------------------------------------	---

## Chapter 2

<b>Fig. 2.1</b> Sallie Gardner at a Gallop (Muybridge 1878) (The photographs were taken at a distance of around 70 cm corresponding to a time interval of approximately 0.04 s.).....	11
<b>Fig. 2.2</b> Layout of the wind tunnel during the experiment (Jiang, Dong et al. 2015).....	12
<b>Fig. 2.3</b> A sequence of sand saltation (A to E) and the composite trajectory image (F) (Wang, Wang et al. 2008).....	15
<b>Fig. 2.4</b> Sequence images of grains ejected from grain ridge following drop impact. The high-speed images showed that grains ejected from the top of the ridge have the highest initial velocity and launch angles, whereas grains from the middle and bottom parts of ridge have lower ejected velocities and launch angles following grain-to-grain collisions. (Furbish, Hamner et al. 2007). ....	15
<b>Fig. 2.5(a)</b> Schematic of test configuration for directly observing a two-dimensional view of the impact and penetration event. The dimension of the tank is 35 cm×25 cm×182 cm (width×depth×height) <b>(b)</b> Images of sphere traveling at 141 m/s (Borg, Morrissey et al. 2013). ....	17
<b>Fig. 2.6</b> A sequence of high-speed images, showing a flat-ended projectile exiting the back of the sample, along with a volume of sand (Collins, Addiss et al. 2011). ....	18
<b>Fig. 2.7(a)</b> High-speed visualization of a cone projectile penetrating into the transparent soil and at projectile velocity of 13.6 m/s. (Chen, Omidvar et al. 2014) <b>(b)</b> Progressive snapshots of penetration into transparent sucrose saturated granular fused quartz shot at the centre of the target. (Guzman, Iskander et al. 2015).....	19
<b>Fig. 2.8</b> Experimental set-up for the granite targets during the tests, the dimension is 0.6m×0.6m×0.1m (length×width×thickness) (Seah, Børvik et al. 2011). ....	20
<b>Fig. 2.9</b> High-speed images at various time intervals showing the responses at the front and rear sides of a granite target plate when impacted by an ogive-nose projectile at $V_s = 279\text{m/s}$ (Seah, Børvik et al. 2011). ....	20
<b>Fig. 2.10</b> The cracking and coalescence processes in a gypsum specimen at a frame rate of 24,096 fps. <b>(a)</b> Tensile wing cracks initiated from the two pre-existing flaws. <b>(b)</b> Additional cracks initiated from the flaw tips. <b>(c)</b> A coalescent shear crack developed to link up the two inner flaw tips <b>(d)</b> Geometry of a flaw pair defined by bridging angle ( $\alpha$ ), flaw inclination angle ( $\beta$ ) and ligament length (L). (Wong and Einstein 2009). ....	22
<b>Fig. 2.11</b> Sequence of impact fracture of plain concrete by the drop-weight machine at a frame rate of 500 fps (Mindess and Bentur 1985).....	23
<b>Fig. 2.12</b> Initiation of fracture of Haute-Marne argillite specimens under compression test (Cai, Kaiser et al. 2007). ....	24
<b>Fig. 2.13</b> Influence of confinement on the failure process in aluminium nitride(reproduced from (Ramesh, Hogan et al. 2015) and original source (Hu, Ramesh et al. 2011)). Photographs taken every 2 $\mu\text{s}$ with exposure times of 500 ns and white regions in the specimen indicate damaged regions. Left: Unconfined uniaxial dynamic compressive loading in the horizontal direction, red arrows show the WC platens and blue arrows show damage regions and crack propagation. Right: Failure during planar confinement (in the vertical direction) and dynamic compressive loading (in the horizontal direction), blue arrows show damage regions and red arrows indicate crack propagation.....	25

<b>Fig. 2.14</b> High-speed images of dynamic BD test of marble at 60,000 fps with the resolution of 448×192 pixels (ZOC: zone of camera, ZOI: zone of interest) (Zhang and Zhao 2013). .....	26
<b>Fig. 2.15</b> Photographs of dynamic gabbro fracture process of SR specimen by SHPB test. The time intervals between the neighboring images were all 2.857ms (Zhang, Kou et al. 2000).....	27
<b>Fig. 2.16</b> Crack propagating process of an NSCB marble, the observable moving crack-tip is indicated by an arrow in the images (Zhang and Zhao 2013). .....	27
<b>Fig. 2.17</b> Selected images of rock fracture propagation induced by charge explosion and obtained by an ultra-high-speed camera at 1.5 Mfps (modified after (Bieniawski 1968)). .....	28
<b>Fig. 2.18</b> The final fracture structure in a sealed-charge experiment depicted in two directions (Left image: parallel to the borehole axis. Right image: perpendicular to this axis. ‘E’ marks the position of the explosive charge and ‘D’ is the detonation wire.) (Rossmanith, Knasmillner et al. 1996). ....	29
<b>Fig. 2.19</b> Four examples of high-speed images showing fracture in diamond, with propagating cracks denoted by arrows. The white arrows show the edge of the dark, vertical shock front in the PMMA matrix. Each frame is labelled with the time in microseconds after shock wave arrival. Cracks can be seen growing in each sequence (Willmott and Field 2006).....	30
<b>Fig. 2.20(a)</b> Schematic of typical spalling test by SHPB with a high-speed photography system (Klepaczko and Brara 2001), <b>(b)</b> Captured fracture process with two spalls under loading from the left side of concrete specimen (Brara, Camborde et al. 2001), <b>(c)</b> the spalling test on Kimachi sandstone (a is the initiation of the explosion and b is 240ms after the explosion.) (Kubota, Ogata et al. 2008).....	32
<b>Fig. 2.21</b> Selected frames of a high-speed photographic sequence of impact fracture of a plaster sphere with the diameter 50 mm by double impact tests, at the frame rate of 2,000 fps, the contact force P (in kN) as well as the contact velocity v (in m/s) (Wu, Chau et al. 2004).....	34
<b>Fig. 2.22</b> Ultra-high-speed camera observations for two fragmentation tests: (a) Crinoidal limestone with thickness of 8mm, at striking velocity of 200 m/s (b) Beaucaire limestone with thickness of 12mm, striker velocity at 101 m/s (Grange, Forquin et al. 2008). .....	35
<b>Fig. 2.23</b> Evolution of the debris cloud of gabbro for 21J impact at (a) 3.75 ms, (b) 10 ms, and (c) 20 ms after impact. Frame rate at 8,000 fps. Various fragmentation mechanisms are labelled in the figure, including plate-like fragments spalled from the rear surface and those crushed ahead of the projectile (Hogan, Spray et al. 2013).....	36
<b>Fig. 2.24 (a)</b> The front of the gas-particle mixture after fragmentation, samples were drilled from volcanic rocks in cylinder (l=6 cm, d= 2.5 cm), frame rate at 14,000 fps. (Alatorre-Ibargüengoitia, Scheu et al. 2011). <b>(b)</b> Individual frames from a sequence of a typical rock fragmentation experiment, frame rate at 10,000 fps. (Fowler, Scheu et al. 2009): a. Before depressurization of the autoclave (0ms). b. 0.3ms after decompression, the upper part of the sample has fractured. c. After 1.1ms, fractures have occurred throughout the sample. d. By 2.4ms, the rock has disintegrated (Fowler, Scheu et al. 2009).....	37
<b>Fig. 2.25</b> Image sequence for wet sand dynamic compression experiment. Large cracks can be observed in Frame 2. The cracked particle breaks into large sub-particles in Frame 3. White arrows indicate large cracks in the sand particle. The resolution was 640×48 pixels at the frame rate of 54,321 fps (Parab, Claus et al. 2014). .....	38
<b>Fig. 2.26</b> Sequence of expanding ring fragmentation of Lake Quarry Granite driven by impact plate. The ring sample was seen to stretch, fracture radially and move off outwards as fragments at 1 Mfps with the resolution of 1,082×974 pixels (Kirk 2014). .....	39
<b>Fig. 2.27</b> Loaded photoelasticity coating in a plane polari-scope (Younis 2012). .....	42
<b>Fig. 2.28(a)</b> Isochromatic-fringe patterns around a crack propagating in a marble plate dynamically loaded by a steel wedge in notch technique; inter-frame interval of 4 μs, and crack propagation	



velocity of 965 m/s. Reproduced from (Daniel and Rowlands 1975); <b>(b)</b> Dynamic isochromatic-fringe pattern for strain-wave propagation in Salem limestone (Fourney, Dally et al. 1976); <b>(c)</b> Cracks in Solenhofen limestone. Extension rate of crack between frames 4 and 5 is in excess of 10.8 mm/ $\mu$ s (Glenn and Jaun 1978).....	44
<b>Fig. 2.29</b> Schematic of <b>(a)</b> four-beam Moiré interferometry to record the $N_x$ and $N_y$ fringe patterns, which depicts the U and V displacement fields, and <b>(b)</b> shadow Moiré, which depicts the W displacement fields (Post, Han et al. 2012), <b>(c)</b> Moiré-fringe patterns corresponding to vertical displacements in a marble specimen dynamically loaded on the edge, at 1,004,500 fps and ruling of 400 lines/cm. (Daniel and Rowlands 1975). ....	46
<b>Fig. 2.30</b> The principle of the caustics image refractive caustics for <b>(a)</b> a transparent specimen, and <b>(b)</b> an opaque specimen by reflective caustics (Kiser, Eigensatz et al. 2013). ....	47
<b>Fig. 2.31</b> Reflective caustic images of a three-point bending rock specimen impacted by a drop-weight machine (YANG, YUE et al. 2009).....	48
<b>Fig. 2.32(a)</b> Caustics surrounding the tip of flaw after blasting (Yang, Yue et al. 2008, Yang, Yue et al. 2008, Yang, Yang et al. 2009) <b>(b)</b> The caustics image of propagation of main cracks and secondary cracks in PMMA with flaws under explosion loads of PMMA model (Yang, Wang et al. 2016), and <b>(c)</b> Off-focused caustic patterns of dynamic crack propagation in a PMMA specimen subjected to tensile loading with two collinear cracks (Yao, Xu et al. 2005). ....	49
<b>Fig. 2.33(a)</b> Optical arrangement for the high-speed digital holographic interferometry (Pedrini, Osten et al. 2006), <b>(b)</b> Typical fringe patterns at 11 $\mu$ s and 16 $\mu$ s after detonation resulting from an explosive point load in a half space of pink Westerly granite (Holloway, Patacca et al. 1978) and <b>(c)</b> A holographic interferometric fringe pattern taken at 46 $\mu$ s after explosion of a charge of 51 mg DDNP above the surface of a marble sample (Li et al. 1999).....	51
<b>Fig. 2.34</b> Typical setup of the PIV (Raffel, Willert et al. 2013).....	52
<b>Fig. 2.35 (a)</b> Raw and processed images illustrating the penetration event and velocity vectors 1 ms after impact. The field of view is approximately 8 cm $\times$ 10 cm and the impact velocity is 35 m/s (Borg, Morrissey et al. 2013), <b>(b)</b> Eulerian trajectories from t=1 ms to t=5 ms, 4000 fps and a spatial resolution of 1280 $\times$ 6960 pixels, where white rectangular is the exploded view of Eulerian trajectories below the cone tip and black rectangular is the exploded view of Eulerian trajectories along the cone shaft (Chen, Omidvar et al. 2014), <b>(c)</b> High-speed image of the target rear with interrogation area for 30 mm thick target and impact energy of 735 J. Vector field (blue arrows in the online version) contour from PIV measurements with projected ejecta vectors (red colour in the online version) (Hogan, Spray et al. 2014) and <b>(d)</b> PIV images of the first fragments ejection showing the displacement field during the rockburst process (Wang, Liu et al. 2015).....	55
<b>Fig. 2.36(a)</b> Data for 45° impact: (A) Single raw image from set, (B) Top view of vector plot with each vector colour representing the vertical velocity component, and (C) Side view of same data set with vectors coloured similarly (Heineck, Schultz et al. 2002), <b>(b)</b> Schematic of the 3D PIV setup within the NASA Ames Vertical Gun Range facility and <b>(c)</b> Vector plots showing the velocities of particles within the laser plane as measured using 3D PIV (90° impacts in a, 30° impacts in b). The colour bars represent the measured velocities within the laser plane for each time step in (m/s) (Anderson, Schultz et al. 2003). ....	56
<b>Fig. 2.37</b> Dynamic vertical strain fields of a NSCB specimen of Fangshan marble by DIC (Zhang and Zhao 2013).....	58
<b>Fig. 2.38</b> Contour plots of the longitudinal displacements (parallel to the projectile) for penetration of sand by flat-ended rod at 200 m/s. Colour bar denotes lateral displacement in mm. Time after impact: <b>(a)</b> 150 ms, <b>(b)</b> 250 ms, <b>(c)</b> 350 ms, <b>(d)</b> 450 ms, <b>(e)</b> 550 ms, and <b>(f)</b> 750 ms (Collins, Addiss et al. 2011).....	59

<b>Fig. 2.39</b> Transient target thermographs of marble plates impacted by SHPB at different impacting velocities (modified after (Shi, Wu et al. 2007)).....	61
----------------------------------------------------------------------------------------------------------------------------------------------------------------	----

## Chapter 3

<b>Fig. 3.1</b> Specimen manufacturing machine: <b>(a)</b> Coring machine <b>(b)</b> Diamond cutter and <b>(c)</b> Surface grinder .....	83
<b>Fig. 3.2</b> Photograph of marble, sandstone and gabbro .....	84
<b>Fig. 3.3</b> Microscopic images of thin sections of medium-grained sandstones.....	85
<b>Fig. 3.4(a)</b> A medium-grained Hawkesbury sandstone specimen <b>(b)</b> Ultrasonic wave method to determine the wave velocity.....	85
<b>Fig. 3.5</b> Photographs of sandstones of three grain sizes (left to right: CG, MG and FG sandstone) .....	85
<b>Fig. 3.6</b> Microscopic images of thin sections of (a)CG and (b)FG (right) sandstone .....	86
<b>Fig. 3.7</b> JEOL JSM-7001F scanning electron microscopy (SEM) at Monash Centre for Electron Microscopy.....	86
<b>Fig. 3.8</b> SEM images of CG, MG and FG sandstone.....	87
<b>Fig. 3.9</b> Microscopic images of the thin sections of (a)gabbro and (b)marble.....	88
<b>Fig. 3.10</b> Shimadzu 100 KN compression machine .....	89
<b>Fig. 3.11(a)</b> photograph of the quasi-static compression and <b>(b)</b> BD test .....	90
<b>Fig. 3.12(a)</b> photograph of the dynamic compression and <b>(b)</b> BD test.....	91
<b>Fig. 3.13</b> Geometry of the SHPB .....	92
<b>Fig. 3.14</b> Data acquisition and signal generator system.....	93
<b>Fig. 3.15</b> Laser beams to measure striker velocity.....	93
<b>Fig. 3.16</b> Illustration of interframe time, exposure time and illumination time. A: a long illumination and short exposures controlled by the camera, and B: a long camera exposure illuminated by short bursts of illumination (after Versluis 2013). .....	95
<b>Fig. 3.17</b> An oblique impact of a steel ball into fine very loose sand creates a splash followed by a jet in the backward direction (Lohse, Bergmann et al. 2004).....	96
<b>Fig. 3.18</b> GS Vitec Multi LED Light .....	99
<b>Fig. 3.19</b> Schematic of TTL triggering signals integrated in SHPB .....	100
<b>Fig. 3.20</b> Schematic of <b>(a)</b> CCD sensor and <b>(b)</b> CMOS sensor .....	101
<b>Fig. 3.21</b> Survey of current HS cameras based on CMOS and CCD technologies (the maximum resolution is proportional to the area of the representative rectangle of each camera), courtesy of Dr. Reu. (Reu and Miller 2008).....	103
<b>Fig. 3.22</b> Phantom V2511 ultra-high-speed camera.....	104
<b>Fig. 3.23</b> Schematic of a reference subset before deformation and a target subset after deformation. The center position of the target subset is obtained through searching the peak position of the distribution of the correlation coefficient (Pan, Xie et al. 2010).....	106
<b>Fig. 3.24</b> Binocular stereovision illustration. (O1, O2 are origins of left and right cameras; M1 and M2 are reference and deformed points in the 3D space, respectively).....	107
<b>Fig. 3.25</b> Schematic of 3D-DIC and deformation field determination.....	107
<b>Fig. 3.26</b> Photo of the SHPB and high-speed imaging system .....	111
<b>Fig. 3.27</b> A typical well-speckled sandstone specimen.....	112
<b>Fig. 3.28</b> A typical calibration process by capturing standard grid target.....	113
<b>Fig. 3.29</b> Synchronized views of specimens in two cameras .....	113

## Chapter 4

<b>Fig. 4.1</b> Stress-strain diagrams showing the stages of crack development (Martin 1993). ( $\Delta V$ , change in volume; $V$ , initial volume). .....	122
<b>Fig. 4.2(a)</b> Setup of the SHPB system <b>(b)</b> static compression machine and high-resolution cameras system .....	123
<b>Fig. 4.3</b> Compressive wave propagating within the sandstone at a strain rate of $120 \text{ s}^{-1}$ ('E' is the virtual extensometer along the centre axis, and 'P' is the centre point of the AOI). .....	124
<b>Fig. 4.4</b> Strain distribution along middle line of AOI in x direction from 10 to $25 \mu\text{s}$ at a strain rate of $120 \text{ s}^{-1}$ .....	125
<b>Fig. 4.5</b> Strain rate field distribution through sandstone specimen at the strain rate of $120 \text{ s}^{-1}$ . ....	126
<b>Fig. 4.6</b> Typical experimental data at the strain rate of $120 \text{ s}^{-1}$ : <b>(a)</b> raw voltage data from oscilloscope, <b>(b)</b> stress and strain history derived by strain gauge signals and the 3D-DIC, and <b>(c)</b> Dynamic equilibrium check.....	127
<b>Fig. 4.7</b> Stress-strain curves: the strain histories obtained by <b>(a)</b> strain gauges and <b>(b)</b> a virtual extensometer. ....	129
<b>Fig. 4.8</b> Average strain rates along the middle line within AOI by 3D-DIC and strain rates by strain gauge (compressive strain rate is positive in this chart).....	130
<b>Fig. 4.9</b> Strain history from extensometer by high-speed 2D-DIC and 3D-DIC at a strain rate of $70 \text{ s}^{-1}$ . .....	131
<b>Fig. 4.10</b> Strain distribution at $50 \mu\text{s}$ along the centre line of AOI by 2D- and 3D-DIC at a strain rate of $70 \text{ s}^{-1}$ .....	132
<b>Fig. 4.11</b> Poisson's ratio evolution of sandstone with different strain rates (star indicates peak strain position) .....	133
<b>Fig. 4.12(a)</b> Cross section from front view by X-ray tomography <b>(b)</b> Grain rotation model .....	133
<b>Fig. 4.13(a)</b> Reconstructed 3D shape and strain field of a specimen at $30 \mu\text{s}$ at the strain rate of $120 \text{ s}^{-1}$ , <b>(b)</b> Illustration of averaging the strain value in a field, (pixel size was enlarged for illustration) .....	136
<b>Fig. 4.14</b> Volumetric strain corresponding to stress thresholds of sandstone under strain rate of $120 \text{ s}^{-1}$ .....	137
<b>Fig. 4.15</b> Critical <b>(a)</b> strains, <b>(b)</b> stresses and <b>(c)</b> normalised stresses in dynamic loading tests ....	138
<b>Fig. 4.16(a)</b> Strain field evolution and <b>(b)</b> images of the evolution of visible cracks at a strain rate of $120 \text{ s}^{-1}$ .....	139
<b>Fig. 4.17</b> Strain fields at different stages in different directions at strain rate of <b>(a)</b> $93 \text{ s}^{-1}$ and <b>(b)</b> $70 \text{ s}^{-1}$ .....	140
<b>Fig. 4.18</b> Stress thresholds and corresponding strain fields of sandstone under strain rate of $120 \text{ s}^{-1}$ .....	141
<b>Fig. 4.19(a)</b> Strain fields at $220 \mu\text{s}$ by high-speed 2D- and 3D-DIC at the strain rate of $70 \text{ s}^{-1}$ <b>(b)</b> 3D shape and out-of-plane displacement field at $220 \mu\text{s}$ with the strain rate of $70 \text{ s}^{-1}$ .....	142
<b>Fig. 4.20</b> Dynamic increase factor (DIF) as a function of strain rate.....	143
<b>Fig. 4.21</b> Main part of residual pieces after tests of <b>(a)</b> dynamic loading <b>(b)</b> quasi-static loading. ....	144

## Chapter 5

<b>Fig. 5.1</b> Strength of CG, MG and FG under different strain rates.....	160
<b>Fig. 5.2(a)</b> Young's modulus and <b>(b)</b> Poisson's ratio verses different grain size and strain rates..	161
<b>Fig. 5.3 (a)</b> Normalised stress threshold of crack initiation and <b>(b)</b> unstable development verses different grain size and strain rates.....	162
<b>Fig. 5.4</b> Strain localisation development in <b>(a)</b> CG 02 <b>(b)</b> MG 02 and <b>(c)</b> FG 03. ....	163
<b>Fig. 5.5</b> Horizontal displacement (mm) in gabbro, marble and sandstone (up to down) .....	166
<b>Fig. 5.6</b> Vertical displacement (mm) in gabbro, marble and sandstone (up to down) .....	166
<b>Fig. 5.7</b> Out-of-plane displacement (mm) in gabbro, marble and sandstone (up to down).....	167
<b>Fig. 5.8</b> 3D view of the surface of <b>(a)</b> gabbro <b>(b)</b> marble and <b>(c)</b> sandstone at 60 $\mu$ s.....	168
<b>Fig. 5.9</b> vertical strain field ( $e_{yy}$ ) in gabbro, marble and sandstone (up to down).....	169
<b>Fig. 5.10</b> Topography of the fracture surface of <b>(a)</b> gabbro, <b>(b)</b> marble and <b>(c)</b> sandstone after dynamic loading by SEM.....	170
<b>Fig. 5.11</b> Flow chart estimating the strength of the rock.....	170
<b>Fig. 5.12</b> Post-failure fragments of gabbro, marble and sandstone in <b>(a)</b> quasi-static test and <b>(b)</b> dynamic test.....	171
<b>Fig. 5.13(a)</b> Muffle furnace to heat the sandstone <b>(b)</b> Colour change of Hawkesbury sandstone with increasing temperature (specimens from left to right were at 20 °C, 200 °C, 400 °C, 800 °C, 1200 °C) .....	172
<b>Fig. 5.14(a)</b> variation in density and wave velocity of rocks with treatment temperature; <b>(b)</b> variation in dynamic tensile strength with treatment temperature; <b>(c)</b> dynamic compressive strength versus strain rate at different temperatures; <b>(d)</b> strain rate sensitivity coefficient of dynamic compressive strength at different temperatures.....	174
<b>Fig. 5.15(a)</b> Elastic modulus versus strain rate at different temperatures, <b>(b)</b> Poisson's ratio versus strain rate at different temperatures.....	175
<b>Fig. 5.16</b> Variation in normalized stable ( $\sigma_{ci}$ ) and unstable stress ( $\sigma_{cs}$ ) of rocks with treatment temperatures .....	177
<b>Fig. 5.17(a)</b> Vertical strain fields ( $e_{yy}$ ) of the initiation of strain localisation at different temperature treatments, left to right temperature: 20 °C to 1200 °C, strain rate: 114, 116, 110, 110 and 118 $s^{-1}$ <b>(b)</b> Vertical strain fields ( $e_{yy}$ ) of fractured rock at post-peak stages with different temperature treatments, left to right temperature: 20 °C to 1200 °C, strain rate: 114, 116, 110, 110 and 118 $s^{-1}$ .....	178
<b>Fig. 5.18</b> Horizontal strain fields ( $e_{xx}$ ) of fractured rock with different temperature treatments, left to right temperature: 20 °C, 400 °C and 1200 °C, strain rate: 114, 110 and 118 $s^{-1}$ .....	178
<b>Fig. 5.19</b> SEM images of the grain in <b>(a)</b> 400°C and <b>(b)</b> 1200 °C treated sandstone specimen .....	179
<b>Fig. 5.20(a)</b> Desiccators for water saturation <b>(b)</b> Chamber for high-pressure CO <sub>2</sub> injection .....	180
<b>Fig. 5.21</b> Photograph of the setup for <b>(a)</b> dynamic compression and <b>(b)</b> dynamic tension test.....	181
<b>Fig. 5.22</b> Typical stress-strain curves of <b>(a)</b> dry vs dry +CO <sub>2</sub> , <b>(b)</b> water vs water +CO <sub>2</sub> , <b>(c)</b> NaCl vs NaCl +CO <sub>2</sub> , <b>(d)</b> Poisson's ratio evolution in dry, dry+CO <sub>2</sub> and water + CO <sub>2</sub> , <b>(e)</b> Compressive strength variation against strain rate in all treatments, <b>(f)</b> Tensile strength in all treatments at loading rate of 100 $\pm$ 3 GPa/s .....	182
<b>Fig. 5.23</b> Crack and volumetric strain evolutions and identification of the stress thresholds in D2 and DC2 .....	187
<b>Fig. 5.24</b> Vertical strain fields ( $e_{yy}$ ) of the <b>(a)</b> initiation of strain localisation at 60 $\mu$ s since wave propagating into the specimen (circles indicate where strain localisations initiate) <b>(b)</b> the post-failure at 250 $\mu$ s since wave propagating into the specimen corresponding to different treatments .....	190

<b>Fig. 5.25</b> Vertical strain fields ( $e_{yy}$ ) of BD test <b>(a)</b> at 50 $\mu\text{s}$ and <b>(b)</b> the maximum strain of BD test on each sample at 100 $\mu\text{s}$ . (circles indicate the maximum strain localisation) .....	190
<b>Fig. 5.26</b> Typical SEM images of <b>(a)</b> dry specimen without treatment, <b>(b)</b> Quartz corrosion in the set of dry+CO <sub>2</sub> saturation, <b>(c)</b> Quartz corrosion and clay mineral precipitation in the set of pure water saturation with CO <sub>2</sub> , <b>(d)</b> Calcite dissolution in the set of pure water saturation with CO <sub>2</sub> , <b>(e)</b> Secondary precipitation of Kaolinite clay in the set of water saturation with CO <sub>2</sub> , and <b>(f)</b> NaCl re-crystallisation in the set of 20% NaCl saturation .....	192

## Chapter 6

<b>Fig. 6.1(a)</b> Microscopic image of the thin section of sandstone <b>(b)</b> Speckled sandstone slab .....	206
<b>Fig. 6.2</b> Schematic of the experiment setup .....	206
<b>Fig. 6.3(a)</b> Geometry and <b>(b)</b> Photo of the projectile and split sabot .....	207
<b>Fig. 6.4</b> Setup of three high-speed cameras in projectile impact .....	208
<b>Fig. 6.5</b> Failure modes: A. Penetration, B. Bending deflection C. Scabbing; D Non-tunnelling perforation; E Tunnelling perforation; .....	209
<b>Fig. 6.6</b> Damage zones and concerned parameters in <b>(a)</b> high-velocity perforation <b>(b)</b> intermediate-velocity perforation .....	212
<b>Fig. 6.7</b> Process of test F1 penetrating into the slab, projectile end (cross) is used to track velocity .....	212
<b>Fig. 6.8</b> Illustration of mean resistance (Fang and Wu 2017) .....	214
<b>Fig. 6.9</b> Calibration of S and $\mu$ in Eq. 4 for projectiles of three types of noses .....	215
<b>Fig. 6.10</b> Cone plugging zone formation .....	217
<b>Fig. 6.11</b> Angle of the plugging zone versus velocity for all projectiles .....	217
<b>Fig. 6.12</b> Height of scabbing in all impacts .....	219
<b>Fig. 6.13</b> A critical perforation in F9, flat projectile at 178 m/s. ....	220
<b>Fig. 6.14</b> Three typical ejection modes: <b>(a)</b> HS-5; <b>(b)</b> HS-1; <b>(c)</b> F-7, left: out-of-displacement boundary by 3D-DIC, right: scabbing fragmentation; .....	222
<b>Fig. 6.15</b> Fragments ejection velocity (a) Mode A: same with projectile (b) Mode B: correlated to projectile.....	222
<b>Fig. 6.16</b> Schematic of <b>(a)</b> actual rear crater compared to ejection volume (dash line) by Eq. 20 <b>(b)</b> Equivalent ejection volume (coarse solid line) representing ejection volume under different impact velocities. ....	223
<b>Fig. 6.17(a)</b> Out-of-plane displacement field in F-1 by 3D-DIC, <b>(b)</b> Ejection fragment diameter determined by Eq.20 and high-speed 3D-DIC .....	224
<b>Fig. 6.18</b> Predictions of residual velocity versus initial velocity and test data of (a) HS (b) flat (c) conical projectile (I: unperforated, II: Mode A ejection, III: Mode B ejection) .....	225
<b>Fig. 6.19</b> Key stages in the perforation of <b>(a)</b> HS-5 and <b>(b)</b> HS-1 (A, Penetrating; B, Peak compressive wave reaches bottom, scabbing starts, (tunnel starts for HS-1); C, Shear plugging starts; D, Extrusion from rear face; E, Projectile and debris eject out).....	226
<b>Fig. 6.20</b> Illustration of perforation on thin slab at high velocity (over 500 m/s).....	228

## LIST OF TABLES

### Chapter 2

<b>Table 2.1</b> Summary of digital optical techniques for dynamic stress and deformation analysis (Field, Walley et al. 2004) .....	40
--------------------------------------------------------------------------------------------------------------------------------------	----

### Chapter 3

<b>Table 3.1</b> Some common high strain-rate tests of geomaterials and their required frame rates. ....	95
<b>Table 3.2</b> Types of lighting available for high-speed photography (Fuller 2009) .....	99
<b>Table 3.3</b> Brief summary of high-speed 3D-DIC in dynamic tests .....	108
<b>Table 3.4</b> Summary of the main results on high-speed DIC application to rock materials with SHPB test .....	110

### Chapter 4

<b>Table 4.1</b> Errors in 2D to 3D-DIC (positive time means postpone and vice versa) .....	131
<b>Table 4.2</b> Poisson's ratio and Young's modulus vs strain rates .....	134
<b>Table 4.3</b> Thresholds of stresses (MPa) and corresponding strains ( $\epsilon$ ) under different strain rates	137
<b>Table 4.4</b> Critical normalised stress, strain difference and time ( $\mu$ s) for strain localisation or visible crack .....	140

### Chapter 5

<b>Table 5.1</b> Mechanical properties for sandstones of different grain sizes.....	159
<b>Table 5.2</b> Strength of CG, MG and FG under different strain rates .....	160
<b>Table 5.3</b> Young's modulus and Poisson's ratio of CG, MG and FG at different strain rates .....	161
<b>Table 5.4</b> Stress thresholds of CG, MG and FG under different strain rates.....	162
<b>Table 5.5</b> Specimen ID, loading condition and the tensile strength .....	164
<b>Table 5.6</b> Compression and tensile strength corresponding to different strain rates and temperatures .....	173
<b>Table 5.7</b> Normalized stable and unstable crack stress thresholds corresponding to different temperatures .....	176
<b>Table 5.8</b> Summary of treatment conditions and specimen number.....	180
<b>Table 5.9</b> Mechanical properties of different treated samples under different strain rates.....	183
<b>Table 5.10</b> Tensile strength of different treated samples.....	186
<b>Table 5.11</b> Normalised stable and unstable crack stress thresholds corresponding to different treatments .....	188

### Chapter 6

<b>Table 6.1</b> Specifications of the projectiles.....	207
<b>Table 6.2</b> Ballistic damage mode and parameters for each test, unit (mm).....	209
<b>Table 6.3</b> Typical damaged slabs and projectile after impact tests.....	210
<b>Table 6.4</b> Velocity and duration during penetration.....	213
<b>Table 6.5</b> Calibrated empirical constant S and mean deceleration coefficient $\mu$ .....	216
<b>Table 6.6</b> Initial velocity and residual velocity of projectile .....	225

## CHAPTER 1 INTRODUCTION

### 1.1 BACKGROUND

The comprehensive understanding of dynamic behaviour of rock under different dynamic loadings is always significant in dealing with various rock engineering problems, for example underground excavation projects, earthquake research, blasting events and mining. Sources of dynamic loads in rock engineering are in the form of time histories of particle acceleration, velocity and displacement, where an increased rate of loading induces a change in mechanical properties and fracture behaviour. By identifying the mechanical properties and fracturing patterns of rock under dynamic loading, the risk in engineering construction can be reduced through predicting the dynamic failure mode and degree; on the other hand, the efficiency and productivity in rock excavation can be boosted by guiding the rock fragmentation as designed such as hard-rock cutting for sustainable access to minerals.

To investigate the dynamic behaviour of rock in laboratory, the SHPB test and ballistic impact test are widely used. SHPB has been recognised as the most successful loading technique for testing the dynamic property at the strain rate from  $10^1$  to  $10^4 \text{ s}^{-1}$ . By analysing the strain signals in incident and transmitted bar, the stress-strain curve of rock under high strain rates is determined. In addition to the mechanical properties, dynamic deformation and fracturing features of rock are no less important and more challenging to measure in the dynamic behaviour of rock. In terms of ballistic impact on rock, the main concern is the breakage and fragmentation characteristics caused by high-velocity projectile. At the beginning, the failure can only be assessed by the naked eyes for the ultimate failure status. With the application of high-speed photography on rock dynamics, the deformation and fracturing development were qualitatively investigated. When the combination of digital optical measurement technique with high-speed photography was carried out, the full-field quantitative deformation information of rock at a high-strain rate is available. The use of microscopic measurement such as X-Ray computer tomography scanning and scanning electron microscopy (SEM) brought the investigation of rock dynamics mechanism into microscopic age. The progress of the measurement means extended the rock dynamics research to different external conditions such as at high temperature and fluid saturation.

## CHAPTER 1 INTRODUCTION

The studies on the dynamic behaviour of rock basically include dynamic properties and dynamic fracture patterns and their relationship with the intrinsic, external environmental effect as well as loading condition. The post analysis of the fragmentation is also of interest to investigate the damage level, the microscopic measurement on the fragments such as the micro-crack or topography of rock grain.

Although the dynamic behaviour of rock materials has been investigated using a variety of experimental techniques, the work is neither complete nor systematic. The following issues remain to be addressed:

- The dynamic mechanical properties of rock such as Young's modulus and Poisson's ratio were only calculated indirectly.
- It is required to critically assess the inertial effect (wave dispersion, lateral and axial inertial effect) and accuracy of dynamic behavior of rock derived from strain gauge signals in SHPB
- The stress threshold for crack initiation and development under high strain-rate loading is unclear. The real-time and full-field fracturing of rock under dynamic uniaxial compression have not been revealed.
- The effect from intrinsic properties, such as rock type and grain size, the external effect, such as thermal and CO<sub>2</sub> treatment, on the rock dynamic behaviour have not been discovered.
- The assessment of projectile perforation on thin slab especially at intermediate velocity is seldom studied. The intermediate-velocity perforation model to predict the terminal ballistic parameters as well as the real-time perforation process are filled with blank spaces.



## 1.2 OBJECTIVES AND SCOPES

The aim of this thesis is to perform quantitatively experimental methods gaining further knowledge to fulfill the aforementioned research gaps in dynamic behaviour of rocks. It is important to design reliable experimental methods, to determine mechanical properties, to measure full-field deformation field, and to investigate fracturing mechanisms of rock materials at laboratory scale. More specifically, the main objectives are classified into the following categories:

- **Aim 1. Deformation & mechanical properties.**

Direct identification of mechanical properties such as Young's modulus and Poisson's ratio of rock under high strain-rate loading. Understanding the full-field deformation pattern through direct optical measurement and its advantages over traditional strain gauge method.

- **Aim 2. Fracturing patterns.**

Quantification of the stress threshold for each crack stage of rock under high strain-rate loading, characterization of the full-field fracture evolution of rock with the considerations of strain rate effect.

- **Aim 3. Intrinsic and external effect on rock dynamic behavior.**

Investigation of grain size, rock type, thermal and fluid treatment (water, brine and CO<sub>2</sub>) effects on the dynamic behavior of rock. Comprehensive understanding of the mechanism of intrinsic and external effects from the microscopic perspective (mineral distribution and composition alternation).

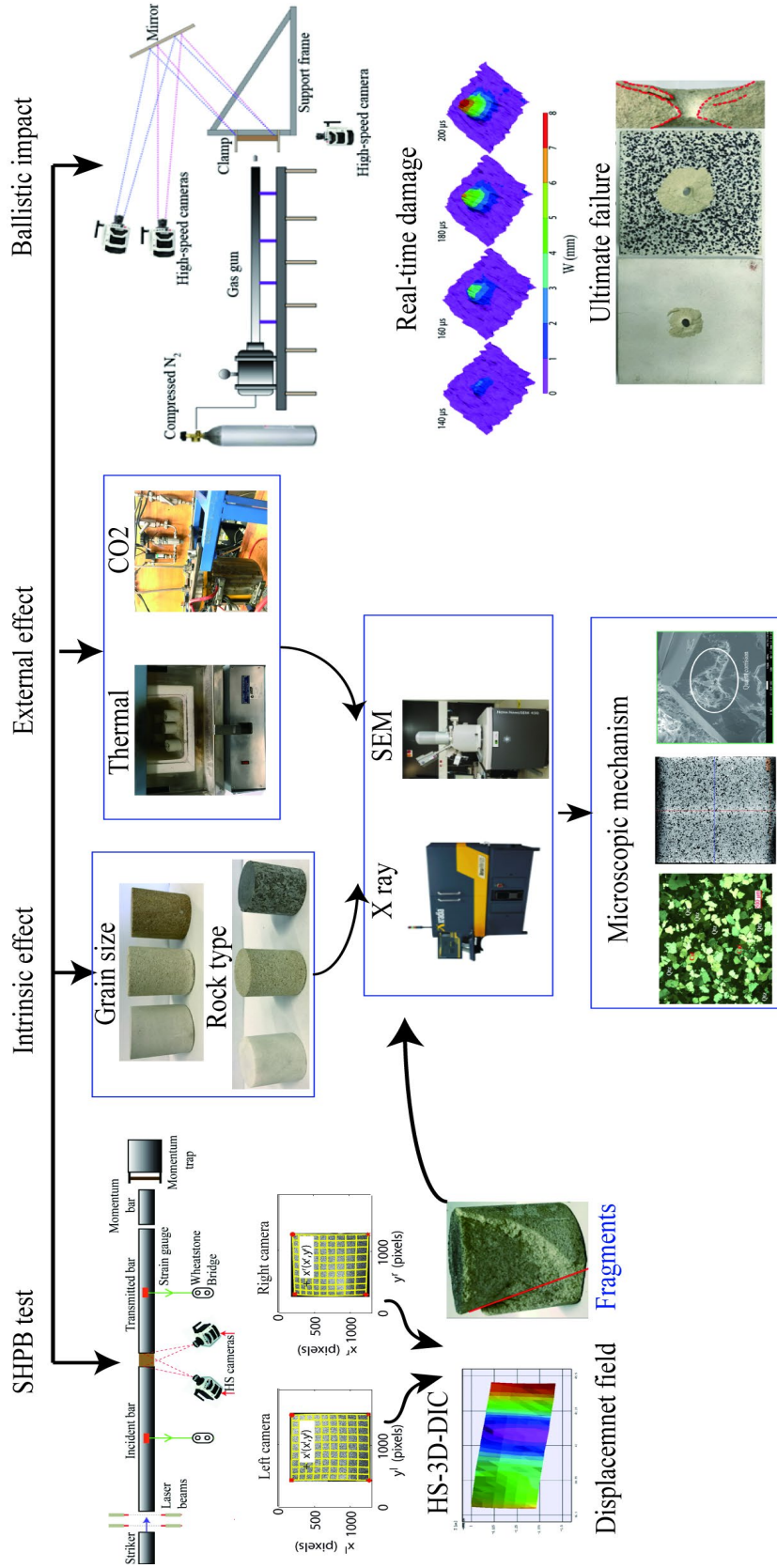
- **Aim 4. Intermediate-velocity perforation model for thin rock slab.**

Characterization of the damage mode, parameters and establishment of the model to predict the perforation limit, ballistic limit and residual velocity. Identification of the real-time damage process during the intermediate-velocity perforation.

The research scope of the thesis is shown in Fig. 1.1. In terms of the loading method, two dynamic loading apparatus are included which are SHPB and gas gun. In SHPB test, the dynamic compression and tension are conducted with the strain rate between  $10^1$  and  $10^4$  s<sup>-1</sup>. The gas gun launches the projectile with the velocity ranging from 120 m/s to 403 m/s to impact the rock slab. The object to study in the thesis mainly includes three types of rocks

## CHAPTER 1 INTRODUCTION

which are sandstone, marble and gabbro representing sedimentary, metamorphic and igneous rock. The measurements contain strain gauge and high-speed photography coupled with 3D-DIC. The post failure measurement is implemented by microscopic ways such as thin section of mineral composition, X-ray tomography for grain distribution and SEM for grain topography. The investigated variables in the experiment include the strain rate, intrinsic (grain size and rock type) and external (thermal and CO<sub>2</sub>) factors.



**Fig. 1.1** Scopes, activities and roadmap of research presented in this thesis

### **1.3 STRUCTURES OF THESIS**

This thesis has seven chapters.

#### **Chapter 1-Introduction**

An overview of rock dynamic behaviour and associated experimental techniques, the research gaps in previous studies, the objectives, scopes and structure of this thesis.

#### **Chapter 2-Review of high-speed imaging and digital optical full-field measurement techniques for geomaterials**

This chapter presents the state-of-the-art techniques in high-speed photography for geomaterial. First, the high-speed imaging history and basic knowledge of high-speed photography are reviewed. Second is a critical assessment of the application of the high-speed photography in geomaterial. At last, high-speed digital optical measurements in geomaterial and their advantages and limits are reviewed in detail.

#### **Chapter 3-Experimental set-up**

In this chapter, the preparation and specification of the specimens tested in this study are provided in detail. The principle and configuration of loading device for the dynamic and quasi-static test are described with the testing procedure. The data acquisition system and its integration into SHPB are introduced from both hardware and software aspects. The full-field measurement is afterwards introduced from high-speed photography and 3D-DIC perspectives. The main factors in high-speed photography such as parameter setting, triggering illumination principle and high-speed camera selection are introduced. The recommended setup for aforementioned factors in rock dynamic test is given as well. The principle and the procedure of high-speed 3D-DIC integration into SHPB testing system are provided.

#### **Chapter 4-Dynamic properties and fracture of rock by full-field measurement**

This chapter aims at identifying the full-field strain and strain rate fields directly on the rock specimen in SHPB tests by high-speed 3D-DIC method. The strain and strain rate results determined by DIC method and one-dimensional wave theory were discussed. The error between 2D- and 3D-DIC was investigated. The dynamic Poisson's ratio and Young's modulus were directly identified with their strain-rate sensitivity. Stress and strain thresholds

of crack development in rock under different high strain rates were investigated. The full-field fracturing evolution such as initiation, branching, and coalescence are revealed.

### **Chapter 5-Intrinsic and external effects on dynamic behaviour of rock**

Based on the knowledge in Chapter 4, in which the dynamic mechanical properties and fracturing patterns of rock under normal environmental conditions are studied. This chapter presents the dynamic behaviour of rock under coupled intrinsic/external environment and strain-rate conditions. Intrinsic effects are investigated from the aspects of grain sizes and rock types. External effects focus on the thermal and fluid (water, brine and CO<sub>2</sub>) treatment. Microscopic studies on rock specimens before and after the treatment are carried out to explain the environmental effect on the dynamic behaviour.

### **Chapter 6-Dynamic behaviour of rock slab under intermediate-velocity projectile impact**

This chapter studies the rock dynamic behaviour at a higher strain-rate loading, penetration. In this chapter, 24 shots are conducted on sandstone thin slabs with three nose-shape projectiles at velocities ranging from 120 m/s to 403 m/s. Three ultra-high-speed cameras are applied to capture the perforation process at frame rates up to 380,000 frames per second (fps). The volume and velocity of ejected fragments are obtained by high-speed 3D digital image correlation (DIC). A perforation model of thin slab at intermediate impact velocity is established. Equations of perforation limit, ballistic limit and residual velocity are proposed, respectively. The perforation mechanism and the critical velocity defining intermediate and high-velocity impact are identified.

### **Chapter 7-Conclusions, future works and engineering applications**

This chapter is to give a brief overview of the findings of the main research topics, the advance in the state-of-the-art, and recommendations for future work.



## **CHPATER 2 REVIEW OF HIGH-SPEED IMAGING AND DIGITAL OPTICAL FULL-FIELD MEASUREMENT TECHNIQUES FOR GEOMATERIALS**

Much of the materials in this chapter has been included in the publication by Xing et al. (2017) in *Rock Mechanics and Rock Engineering* (Vol.50, pp.1611-1659), titled ‘high-speed photography and digital optical measurement techniques for geomaterials: fundamentals and applications’.

### **2.1 INTRODUCTION**

Geomaterials can be defined as ‘Processed or unprocessed soils, rocks or minerals used in the construction of buildings or structures, including man-made construction materials manufactured from soils, rocks or minerals (Fookes 1991)’. Therefore, in addition to rock and soil, some man-made materials including concrete and bricks can also be considered as geomaterials. A complete review of the behaviour and testing methods of geomaterials under quasi-static loading is given by (Mayne, Coop et al. 2009). The behaviour of geomaterials under dynamic loading is a topic of extensive research interest owing to the importance to industry, various environmental concerns and society as a whole (Braithwaite 2009, Zhou and Zhao 2011, Zhang 2014, Zhang and Zhao 2014, Zhang, Braithwaite et al. 2017). Dynamic loading events can be natural in origin, for example earthquakes, meteorite impact and volcanic eruptions. Alternatively, the loading can be man-made such as mining, tunnelling, and hydraulic fracturing. Therefore, a deep insight into the behaviour of geomaterials subjected to dynamic loading is essential to prevent or alleviate the threat of natural disaster to human life, and on the other hand, to improve the development of natural resources and inform best practice in civil engineering and construction (Forquin 2017). However, due to the difficulties associated with measuring and recording events within short duration unable to be observed adequately by the naked eyes, dynamic properties of geomaterials have not been well understood for a long period of time.

High-speed photography is particularly useful in geomechanical tests under dynamic loading owing to the scales and frame rates involved. The definition of high-speed photography varies in different sources. One classical definition divides the historic implementations of high-speed photography into four categories, which vary according to framing rate and the

## CHAPTER 2 REVIEW OF HIGH-SPEED IMAGING AND DIGITAL OPTICAL FULL-FIELD MEASUREMENT TECHNIQUES FOR GEOMATERIALS

used technologies (Peres 2013). From low to high frame rate, these categories are: (a) high-speed, 50 to 500 frames per second (fps), using intermittent film motion and mechanical shuttering; (b) very high-speed, 500 to 100,000 fps, using continuously moving film, image compensation, and digital video systems; (c) ultra-high-speed, 100,000 to 10 million fps (Mfps), using stationary film with moving image systems and electronically with image converter cameras; and (d) super high-speed, in excess of 10 Mfps, where film has been largely superseded by electronic imaging and recording. Modern high-speed systems are invariably electronic in nature. However, as well as temporal resolution, to gain a full appreciation of the capabilities of an imaging system it is necessary to consider the spatial resolution. As (Fuller 1994) states, a more comprehensive description of high-speed imaging can be proposed as: recording optical or electro-optical information with adequately short exposures and fast enough framing rates for an event to be evaluated with a temporal and dimensional resolution which satisfies the experimenter. Therefore, the definition of high-speed photography covers all of the imaging systems discussed in this review.

The following conferences provides a good platform for dissemination of the state of the art in high-speed imaging:

- The British Association for High-speed Photography (AHSP) founded in 1954 organizes activities and annual conferences to discuss the latest development.
- DYMAT Technical Meeting in 2013 was on the topic of ‘High speed imaging for dynamic testing of materials and structures’.
- The Society for Experimental Mechanics (SEM) organized a panel on Imaging at High Strain Rates in 2013 annual conference. In 2014, a “High Rate Image” panel was organized for the fourth year in a row.
- The Society of Photo Instrumentation Engineers (SPIE) has hold many conferences on photonics subjects and published the Proceedings of the International Congresses on High-speed Photography and Photonics since 1954. The latest one is the 31st International Congress in 2016.

In general, with high-speed photography, the scene is captured using a high framing rate to record motion, which can later be played back at a reduced rate for analysis. However, in



## CHAPTER 2 REVIEW OF HIGH-SPEED IMAGING AND DIGITAL OPTICAL FULL-FIELD MEASUREMENT TECHNIQUES FOR GEOMATERIALS

some cases, the analysis may still be observation based, but digitizing the images either by scanning or electronic capturing allow for quantitative measurements. Nowadays, the utility of high-speed photography has been greatly improved in combination with optical measurement techniques and computer calculation. A detailed background and description of some representative optical measurement techniques can be found in Refs. (Sharpe 2008, Rastogi 2015). Using digital image processing techniques such as particle image velocimetry (PIV) and digital image correlation (DIC), it is possible to examine material deformation, through the visualization of displacement, strain or stress field at the microsecond ( $\mu\text{s}$ ) timescale. This can be achieved with a wide range of measurement sensitivities and resolutions as well as being a non-contact diagnostic with the relatively simple setup. In terms of high-speed photographic technology, *High-speed Photography and Photonics* (Ray 2006) presents a comprehensive examination of the principles and applications as well as a review of the historical development (Honour 2009). Reviews of optical techniques combined with high-speed photography are given in Refs. (Field, Walley et al. 2004, Field, Proud et al. 2009). A systematic description of a full-field optical method for solid mechanics is available (Rastogi and Hack 2012). The applications of high-speed photography and digital optical measurement have been recently reviewed in the areas including fluid mechanics (Dear and Field 1988, Versluis 2013), bubbles and drops (Lauterborn and Hentschel 1985, Thoroddsen, Etoh et al. 2008), glass and ceramics (Walley 2014), ballistics (Settles 2006), and phoniatrics (Hertegård, Larsson et al. 2003). However, it would be of considerable benefit to the geo-mechanical community to have a summary of the conducted research in this field, as current efforts to implement high-speed imaging are complicated by material related issues which have been solved by other researchers.

This chapter concentrates on the application and performance evaluation of high-speed photography and combined digital optical measurement techniques in geomaterial experiments. The current introduction is followed by a discussion of some fundamentals of high-speed photography. In Section 2.3, applications of high-speed photography to granular flow, penetration, crack fracturing, spalling and fragmentation are reviewed. In each subsection, the definition and the significance of the topic are presented before a description of typical experimental setups (particularly the camera setup), as well as sequences of

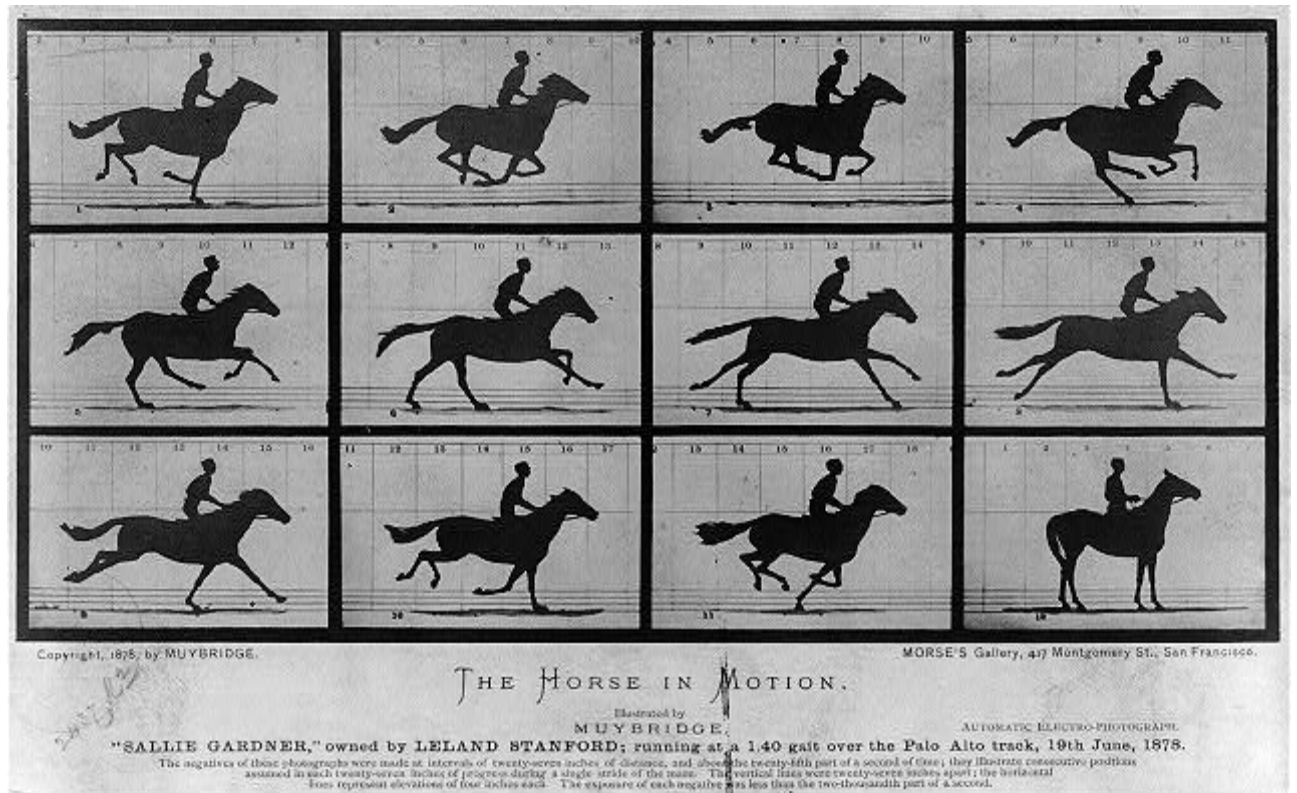
example images and testing results. Section 2.4 reviews seven combined digital optical measurement techniques in geomaterials, including photoelasticity, Moiré, caustic, holographic interferometry (HI), infrared thermography (IRT), PIV and DIC. The fundamental principle of each optical method is given, and the development and the original use of these methods are described. By showing sequences of typical images, an evaluation of the efficacy of each method as related to geomaterials is provided. Finally, a brief summary and future directions are presented.

## **2.2 HIGH-SPEED PHOTOGRAPHY**

High-speed imaging technology relied initially on having highly light sensitive emulsions, but it was unavailable in the early years of photography. The goal of high-speed photography in the early days was sufficient speed to record a street scene without the people being blurred. It is often stated that the first instance of what we would now call high-speed photography was to settle a hotly debated issue ‘is there a moment in a horse’s gait when all four hooves are off the ground at once?’ in 1872 (NMAH 2001). The photographer, Eadweard Muybridge, was a pioneer of scientific research in motion analysis. He devised a camera system consisting of 12 (later 24) individual cameras capturing images on photographic glass plates and triggered by the horse's legs via tripwires in 1878. The photographs were taken in succession one twenty-fifth of a second apart, with the shutter speeds calculated to be less than 1/2000 s. This famous sequence was named Sallie Gardner at a Gallop (Muybridge 1878), as shown in Fig. 2.1. In 1888, George Eastman invented photographic film and the Kodak cameras that housed it making photography a process much more widely available (Eastman 1888). In 1892 the British Scientist Boys suggested an original design of rotating mirrors (Boys 1892), which could be used for a high-speed imaging system, and this principle is still in use today. One of the early drivers for faster framing with cameras came from the desire to reproduce motion smoothly, and thus it requires a number of frames per second to be taken. A 16 mm cine high-speed camera was developed by the Kodak in the 1930s, which eventually reached up to 5000 fps (Bourne 2013). Another great pioneer, Edgerton, invented the electronic flash stroboscope, which allowed illumination to provide the “high-speed”

## CHAPTER 2 REVIEW OF HIGH-SPEED IMAGING AND DIGITAL OPTICAL FULL-FIELD MEASUREMENT TECHNIQUES FOR GEOMATERIALS

nature rather than the imaging system, and took many iconic photographs, e.g. the corona formed by the water impacting into the milk (Edgerton and Killian 1954).



**Fig. 2.1** Sallie Gardner at a Gallop (Muybridge 1878) (The photographs were taken at a distance of around 70 cm corresponding to a time interval of approximately 0.04 s.)

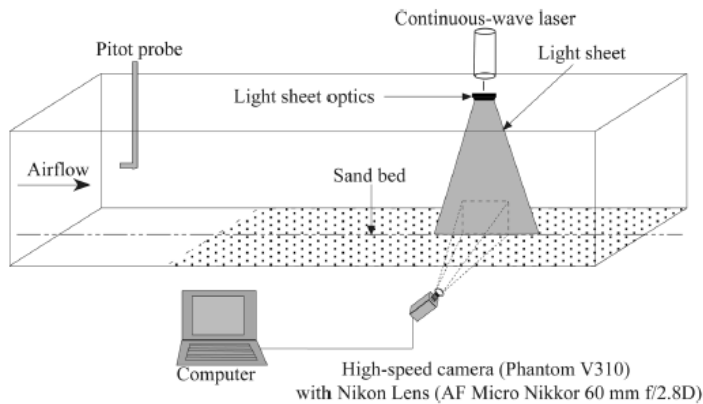
The main development motivation for high-speed imaging came, as with much high-rate scientific research, in the wake of the Manhattan project. Coupled with a desire to study ballistics in greater depth (Fuller 2005), it gave birth to the modern understanding of high-speed photography. In the 1950s, rotating mirror technology was capable of recording at 1 Mfps (Coleman 1959, Bowden and McOnie 1967). Afterwards, a series of rotating mirror, streak cameras and rotating prism cameras sprang up (Courtney-Pratt 1973, Courtney-Pratt 1986). For applications where fewer images were required at a higher rate, the image converter camera was developed by Courtney-Pratt in 1949 (Courtney-Pratt 1949) using the technology converting light to charged particles and then back again, which allowed for the “image” to be steered using charged plates to fall on spatially separated areas of the recording medium. In the 1980s, no marked advances in high-speed cameras showed up, since the film-based high-speed camera approached the theoretical maximum performance possible due to

physical limitations (Huston 1978). In contrast, the digital high-speed photography underwent its fast development due to a great breakthrough in photosensitive media, resulting in the photosensitive emulsions replaced gradually by electronic semiconductor devices (CCD or CMOS) in the high-speed camera.

## 2.3 RECENT APPLICATIONS OF HIGH-SPEED PHOTOGRAPHY TO GEOMATERIALS

### 2.3.1 Sand Movement

In nature, sand movements are mostly driven by wind or water. The motion of wind-blown grains occurs via three major modes: saltation, suspension, and creep (Bagnold 1941, Bagnold 2012). Saltation refers to the sand propelled by the wind in short hops above the surface of the sand bed. It has received much attention because saltating grains account for 50–75 % of the total aeolian transport, and saltation acts as the key link in transferring momentum between the moving air and the underlying bed (Bagnold 1941). The parameters of saltating sand, including the velocity, angle (direction), length and height of the trajectory are the basic physical characteristics. The most common application of high-speed imaging in such experiments is to record the movement of sand and then image processing or statistical methods are used to determine the trajectory parameters and to reconstruct the trajectory process. A typical experimental setup involves a wind tunnel and is shown schematically in Fig. 2.2.

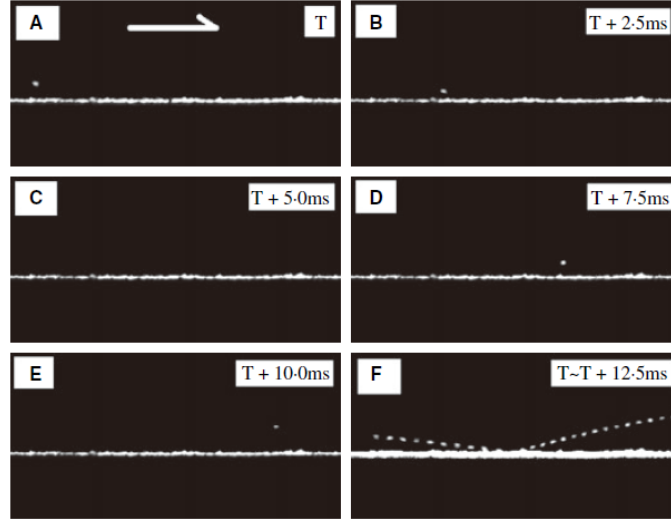


**Fig. 2.2** Layout of the wind tunnel during the experiment (Jiang, Dong et al. 2015).

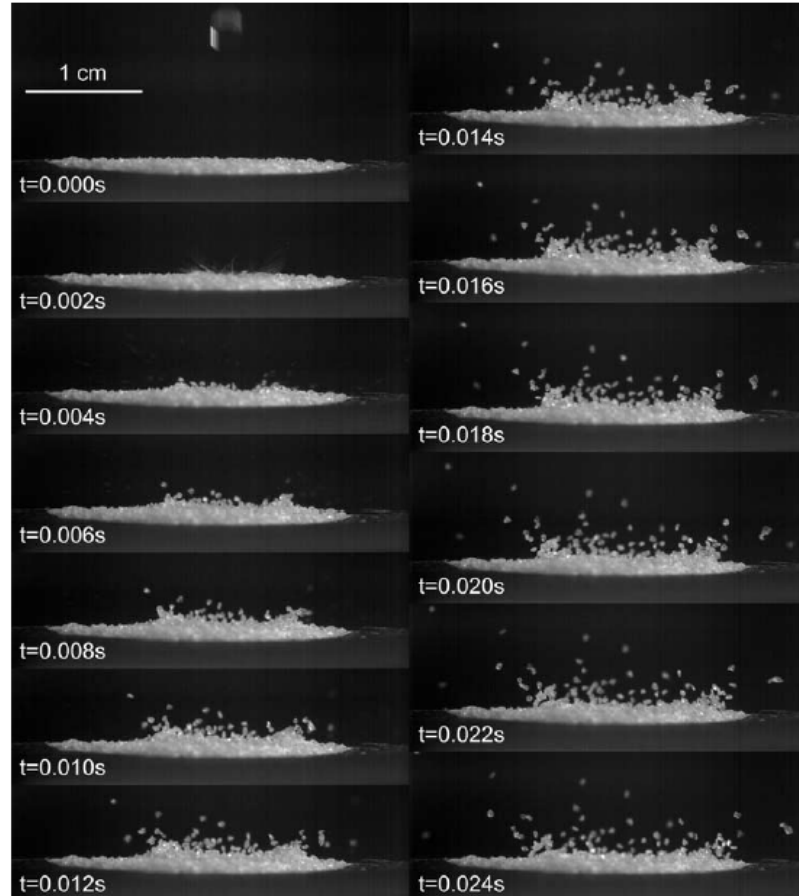
## CHAPTER 2 REVIEW OF HIGH-SPEED IMAGING AND DIGITAL OPTICAL FULL-FIELD MEASUREMENT TECHNIQUES FOR GEOMATERIALS

A continuous laser beam was transformed into a thin light plane by using light-sheet optics to illuminate a narrow vertical-center plane aligned with the flow direction to visualize the moving particles. The sand was moved by the free-stream wind whose velocity was measured by a Pitot-static probe. Afterwards, the consecutive images containing velocity information of particles are processed with a particle tracking velocimetry (PTV) method (Maas, Gruen et al. 1993). (Wang, Wang et al. 2008) used an Ultima-APX high-speed digital camera (Photron) to record the sand grain/bed collision process. The resolution was  $1024 \times 512$  frame rate at 2000 fps. The light source is a PICL-NEX twin cold lighting system. After modulation, the light was transported by a fibre to generate a thin sheet. The results showed that the kinetic energy restitution coefficient and the collision angle are the relevant parameters for understanding the process of a grain impacting and rebounding, as shown in Fig. 2.3. (Wang, Wang et al. 2009) employed a PCO-1200hs high-speed digital camera (PCO AG) which was set at a resolution of  $1280 \times 1024$  at 500 fps to record the sand creep movement in horizontal plane. Unlike the view from the side, which can record particle images with a black background, the camera imaged from above the sand bed on a section in the middle and towards the rear (with respect to the flow direction) making it possible to record the creep of sand grains and their maintained positions. A light sheet is not applicable but a volume illumination mode was employed, which is usually used for three-dimensional (3D) velocity measurements (Willert and Gharib 1992) and a micro-PIV measurement (Meinhart, Wereley et al. 2000). Since the images contain fixed grains, the traditional PTV algorithm is hard to be used. Therefore, an unsigned image subtraction was adopted to form a new image queue from original images, in which each subsequent image was subtracted from the one before, leaving an image of creeping grains. In another experiment, (Zhang, Wang et al. 2014) used an Ultima-APX camera (Photron) to record the movement of the illuminated saltating sand on a sand bed. The resolution was set at  $1024 \times 512$  pixels at 2,000 fps. The imaging zone was arranged at the rear of the sand bed parallel to the flow direction, 0.7 m from the leading edge and centrally aligned in the spanwise direction. The saltating trajectory was reconstructed by an overlapping particle tracking algorithm and the kinetic parameters of saltating grains were abstracted by differential schemes. Moreover, the acceleration of saltating sand grains was obtained directly from the reconstructed trajectory, and the climbing stage of the saltating trajectory represents a critical process of energy transfer while

the sand grains travel through air. (Zhang, Wang et al. 2007) used a high-speed CMOS camera (Fastcam-APX) to capture consecutive particle images with a resolution of  $1024 \times 512$  pixels at 2000 fps. The instantaneous velocity fields of saltating particles were determined by high-speed photography in combination with the PTV method. Ensemble-averaged data were estimated, including the resultant velocity, mass concentration and streamwise mass flux distribution. Their results demonstrate that the resultant particle velocity has an approximate log-linear profile with vertical height. Both the particle concentration and streamwise mass flux decay dramatically in the near surface region, then decline mildly beyond this region. (Jiang, Dong et al. 2015) captured the movement of the saltating sand in a wind tunnel by using a Phantom V310 camera at 5,000 fps with the resolution of  $600 \times 800$  pixel. The imaging zone was at the middle of the sand bed, towards the downwind end. Movement parameters were derived from a digital recording of the trajectory. However, it is still difficult to reconstruct an accurate and quick particle trajectory from images. More detailed sand saltating experiments are referred to (Zou, Wang et al. 2001, Ilstad, Elverhøi et al. 2004, Yang, Wang et al. 2009). Water moves sand in two ways: one is by water flow and the other is by raindrop impact. (Ilstad, Elverhøi et al. 2004) the subaqueous debris flows (Locat and Lee 2005) through a set of laboratory experiments examining the behaviour within the flow and its dependence on the sand/clay ratio at a fixed water content. In another experiment, the pore-fluid pressure and total stress were measured (Ilstad, Marr et al. 2004). In both experiments, the high-speed camera was employed to record data of the velocity field for different positions inside the debris flow. Through particle tracking, the mobility of subaqueous debris flows is obtained. When sand is impacted by a rain drop, part of its momentum is transferred to the sediment grains, which leads to so called “rain splash” (i.e., large grains are ejected into arched trajectories away from impact sites). It is generally accepted that rain splash transport increases with a land surface slope (Moeyersons and De Ploey 1976) and grains on an inclined surface commonly go through a downslope drift. This drift motion has received considerable attention in hillslope geomorphology and erosional processes on agricultural lands (Ellison 1944, De Ploey and Savat 1968, Van Dijk, Meesters et al. 2002). Furbish investigated the details of the momentum transfer from drops to grains which leads to downslope drift at 500 fps of drops impacting sand targets under controlled conditions in the laboratory (Furbish, Hamner et al. 2007), as shown in Fig 2.4.



**Fig. 2.3** A sequence of sand saltation (A to E) and the composite trajectory image (F) (Wang, Wang et al. 2008).



**Fig. 2.4** Sequence images of grains ejected from grain ridge following drop impact. The high-speed images showed that grains ejected from the top of the ridge have the highest initial velocity and launch angles, whereas grains from the middle and bottom parts of ridge have lower ejected velocities and launch angles following grain-to-grain collisions. (Furbish, Hamner et al. 2007).

### 2.3.2 Penetration

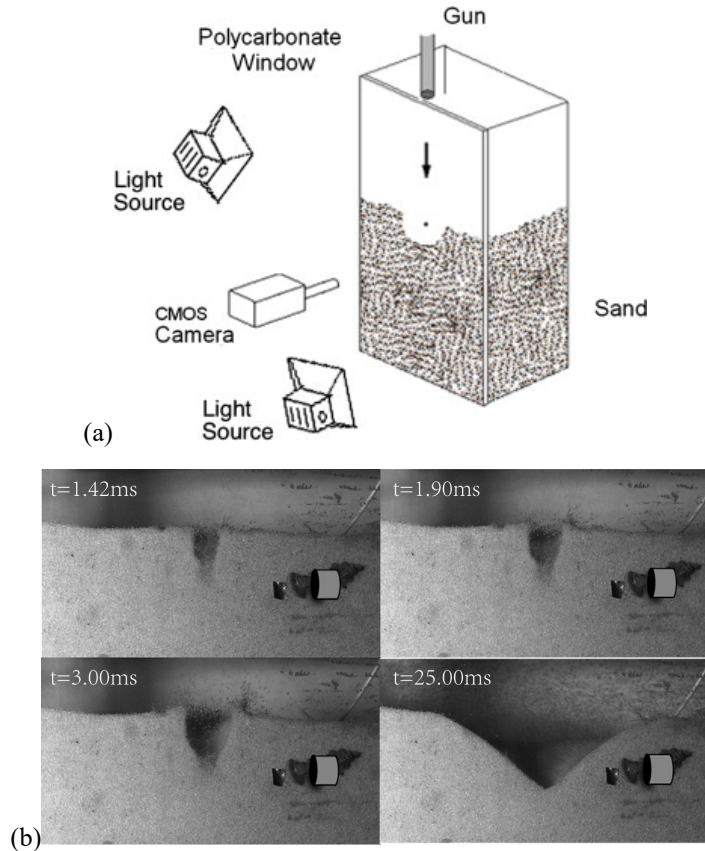
Penetration takes place when a projectile enters a target without passing through it, however perforation occurs when the projectile completely passes through the target. The degree of penetration resistance is a significant parameter to understand in protective engineering. On the one hand, it is hard to simulate penetration accurately by simulation software. On the other hand, computational codes require sensible levels of experimental validation. This complication also extends to theoretical analysis, though many empirical theories of penetration have been established over the years, usually with the assistance of high-speed photography. The applications of high-speed photography to these experiments are generally to measure the penetrator prior to impacting, and to examine the interaction between a projectile and geomaterial during penetration.

(True 1975) used a high-speed camera to investigate the penetration of projectiles into seafloor soils at rates up to 5000 fps. Qualitative information on soil deformation patterns was obtained, and the penetrator velocity determined by scaling distances and calculating the film speed. The camera was also used to observe projectile instability at 1000 fps and to provide data (e.g., flight stability and penetration depth) on the projectile impact velocity at 48 fps. Penetration experiments in various sizes of sand have been performed to evaluate the penetrating processes or determine the penetration resistance (Allen, Mayfield et al. 1957, Culp and Hooper 1961, Braslau 1970, Cole 2010). (Cintala, Berthoud et al. 1999) used a high-speed photography method that was illuminated by a stroboscopic laser to measure ejecta velocities during the impacts of aluminium projectiles into the coarse-grained sand. Their studies show that the impact velocity had slight effect on the functional relationship between the scaled, radial launch position and either the speed or the angle of ejection. (Borg, Morrissey et al. 2013) designed a vertically mounted compressed air gun with a 4.5 mm diameter launch tube, which then was used to launch a projectile at the velocity ranging of 30~200 m/s into a tank (35 cm × 25 cm × 18 cm) filled with Ottawa sand. Images were collected with a Photron RS camera at a minimum frame rate of 3000 fps, and illuminated by two halogens lamps. Owing to the long record time (around 2 seconds) and the large field of view (30 cm × 61 cm) with a resolution of 512 × 1,024 pixels (approximately 3 pixels per grain of sand), the entire penetration event was recorded, setup and typical images are shown

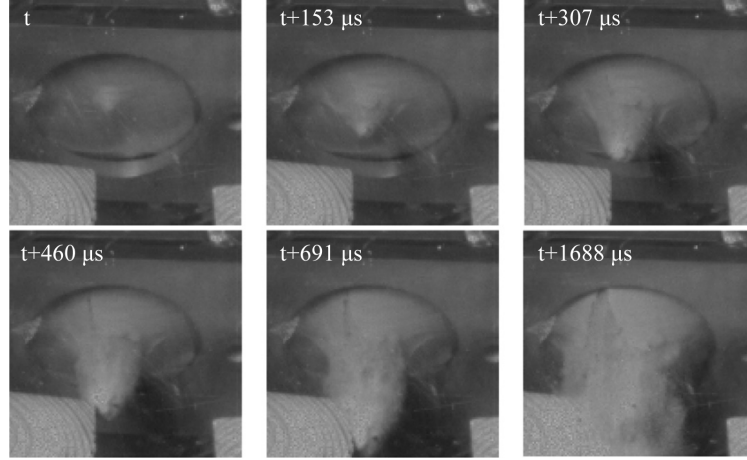


## CHAPTER 2 REVIEW OF HIGH-SPEED IMAGING AND DIGITAL OPTICAL FULL-FIELD MEASUREMENT TECHNIQUES FOR GEOMATERIALS

in Fig. 2.5. It can be seen that a cavity was formed around the contact between the nose of the projectile and sand, but there was little interaction between the sides of the projectile and the sand. (Collins, Addiss et al. 2011) changed the point of view to record the projectile exiting through the end of the specimen, as shown in Fig. 2.6. The main diagnostic of this study was flash x-rays. High-speed photography suggested that the displacement ahead of the rod formed at early impacting stages, but kept a steady-state in the rest of the event.

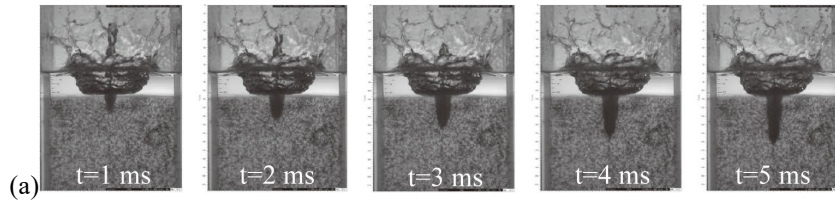


**Fig. 2.5(a)** Schematic of test configuration for directly observing a two-dimensional view of the impact and penetration event. The dimension of the tank is 35 cm×25 cm×182 cm (width×depth×height) **(b)** Images of sphere traveling at 141 m/s (Borg, Morrissey et al. 2013).

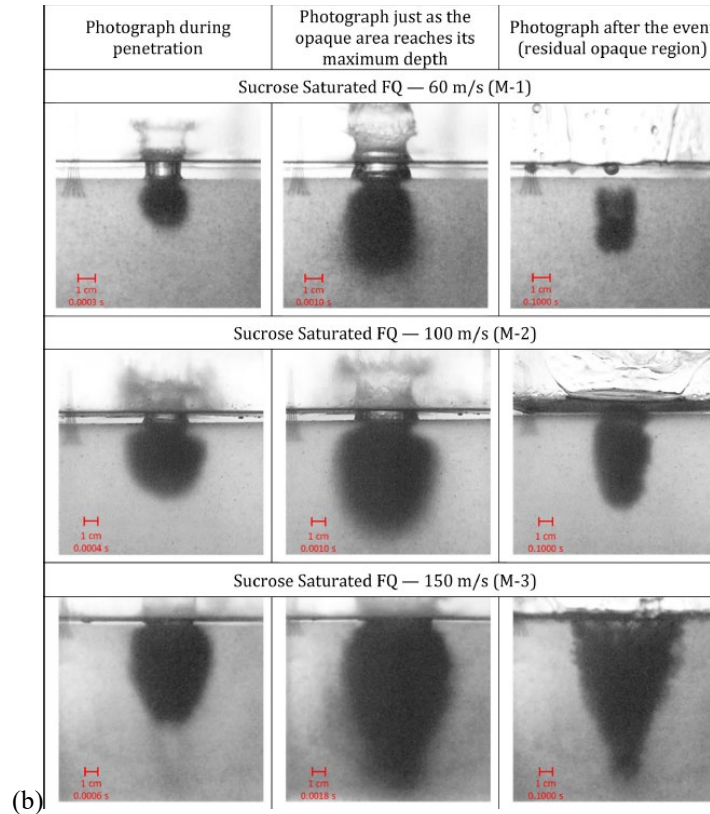


**Fig. 2.6** A sequence of high-speed images, showing a flat-ended projectile exiting the back of the sample, along with a volume of sand (Collins, Addiss et al. 2011).

The development of transparent materials provides alternative to visualize the internal deformation under penetration. (Chen, Omidvar et al. 2014) employed a conical nose projectile accelerating into a transparent soil (fused quartz saturated in a matched refractive index pore fluid made of mineral oil) target at an impact velocity of 13.6 m/s, shown in Fig. 2.7(a). The whole penetration event was recorded with the NAC HX5 camera at 4000 fps and a spatial resolution of  $1280 \times 960$  pixels was corresponded to a field view of  $217 \times 163$  mm. It was found that the splash created by the air accompanying the projectile displaced oil on the top of the target (approximately 25 mm), and that the projectile impacted the surface of the saturated soil. A cone-like cavity was created in the target material during the penetration event. (Guzman, Iskander et al. 2015) visualized the penetration of a spherical projectile into the centre of a saturated granular target made of fused quartz waste at speeds of 60, 100 and 150 m/s, as shown in Fig. 2.7(b). The transparent sand was made of fused quartz waste product with pore fluid made of sucrose. The penetration process was recorded by a NAC HX-5 camera at 10,000 fps. The opaque zone appeared circular during initial penetration and transitioned into the shape of an elongated cone in shots with higher initial velocities.



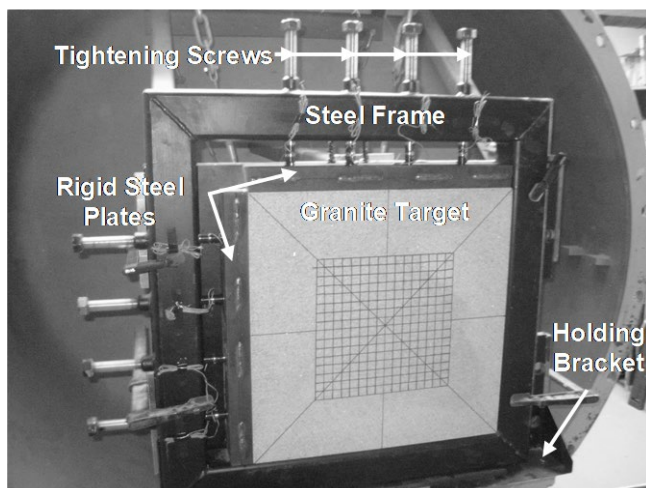
## CHAPTER 2 REVIEW OF HIGH-SPEED IMAGING AND DIGITAL OPTICAL FULL-FIELD MEASUREMENT TECHNIQUES FOR GEOMATERIALS



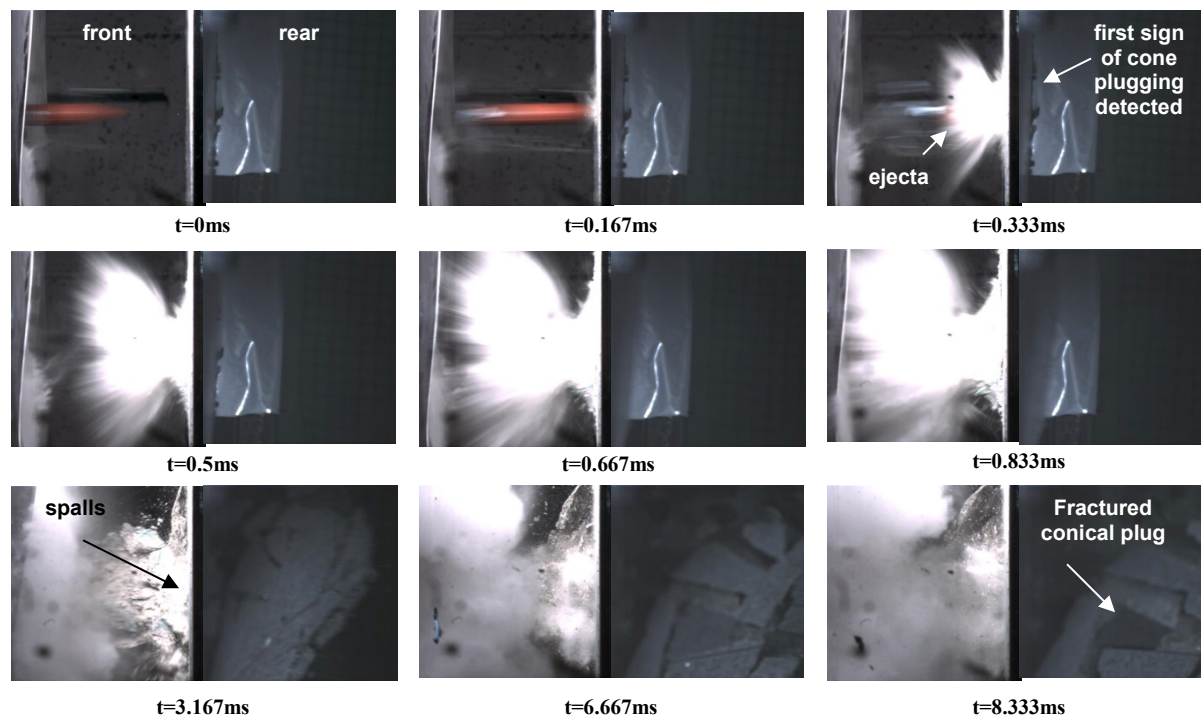
**Fig. 2.7(a)** High-speed visualization of a cone projectile penetrating into the transparent soil and at projectile velocity of 13.6 m/s. (Chen, Omidvar et al. 2014) **(b)** Progressive snapshots of penetration into transparent sucrose saturated granular fused quartz shot at the centre of the target. (Guzman, Iskander et al. 2015)

Børvik applied high-speed imaging to examine the ballistic perforation resistance of high-strength concrete slabs (Borvik, Gjorv et al. 2007). The projectiles were not visibly damaged or deformed as a result of the penetration process as ascertained by the series of high-speed camera images taken during the experiments. The measured initial versus residual projectile velocity curve for C75 concrete is given, but the accuracy of these measurements is uncertain. Because anisotropic fracture of concrete often resulted in the change of projectile direction during penetration, and the concrete debris tended to trigger the optical devices during penetration, it was possible to determine the residual velocity in only some of the tests. In 2011, Seah and Børvik conducted the penetration tests. Iddefjord granite by using ogive-nose projectiles made of Arne tool steel (Seah, Børvik et al. 2011), as shown in Fig. 2.8. From the high-speed digital images, it was possible to determine the impact velocity, the first sign of cone plugging and the fractured conical plug, as shown in Fig. 2.9.

## CHAPTER 2 REVIEW OF HIGH-SPEED IMAGING AND DIGITAL OPTICAL FULL-FIELD MEASUREMENT TECHNIQUES FOR GEOMATERIALS



**Fig. 2.8** Experimental set-up for the granite targets during the tests, the dimension is  $0.6\text{m} \times 0.6\text{m} \times 0.1\text{m}$  (length  $\times$  width  $\times$  thickness) (Seah, Børvik et al. 2011).



**Fig. 2.9** High-speed images at various time intervals showing the responses at the front and rear sides of a granite target plate when impacted by an ogive-nose projectile at  $V_s = 279\text{m/s}$  (Seah, Børvik et al. 2011).

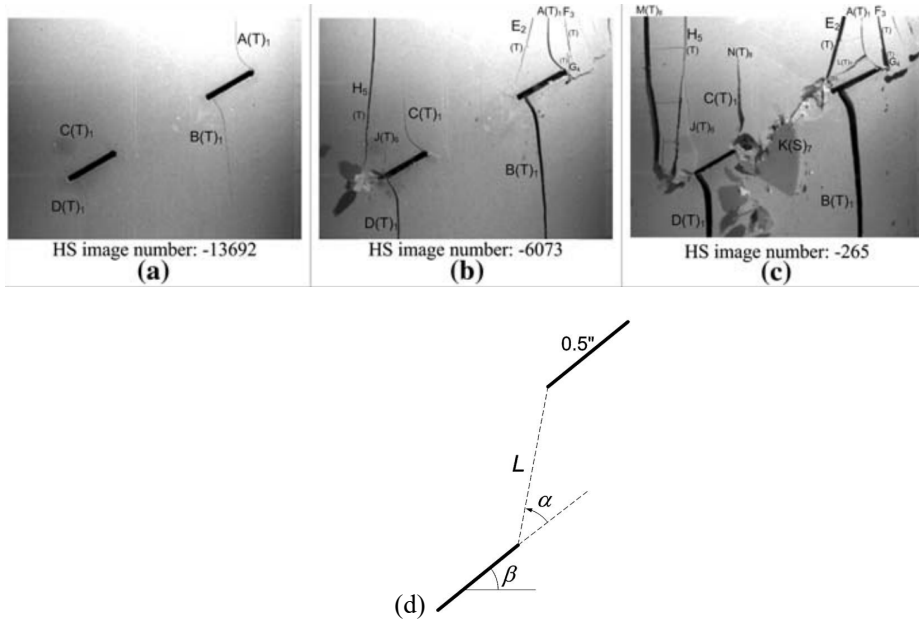
### 2.3.3 Fracturing

Fracturing includes the process of crack initiation, propagation, interaction, and eventual coalescence. Fracturing in rock is one of the most popular research focuses in geomechanics as a large number of engineering designs and implementations such as rock slope stability assessments, tunnel support design, and fluid flow prediction can benefit from a greater understanding of fracture. However, the crack velocity in the geomaterials easily exceed 1000 m/s not only in dynamic experiments but also in quasi-static experiments. If the nature of a crack is determined solely by the examination of fractographic features, the signs of shearing obfuscate the pre-existing tensile cracking (Einstein and Meyer 1999) and the true identity of tensile cracks cannot be identified, which can be obtained in the sequence of images captured by high-speed cameras. Perhaps the most important technique for crack speed measurements is high-speed imaging (Ravi-Chandar 2004).

#### (a) Static tests

(Wong and Einstein 2006) used a high-speed camera to observe the fracturing behaviour of prismatic specimens containing single flaws and found that tensile wing cracks (TWCs) were in most cases the first cracks to appear in fracture propagation from the existing flaws independent of aperture and material. (Wong and Einstein 2009) summarized the fundamentals of their experimental techniques using a high-speed camera, video capturing operation for examining crack behaviour. (Wong and Einstein 2009) studied the cracking and coalescence behaviour in prismatic laboratory-moulded gypsum and Carrara marble specimens containing two parallel pre-existing open flaws by using the uniaxial compression tests. A Phantom V5.0 camera was used to monitor specimen from the front face, and the camera was triggered manually to capture images when the crack(s) coalesced or specimen failure occurred. The frame rate and image resolution settings varied among specimens ranging from 1000 fps to 24000 fps. The typical fracturing process is shown in Fig. 2.10. The influence of flaw inclination angle, the ligament length, the bridging angle (Fig. 2.10d) and the influence of material type on coalescence patterns were studied in detail, and the differences of crack fracturing characteristics between marble and gypsum in response to the applied compression loading were elucidated. (Song, Li et al. 2014, Song, Li et al. 2015) conducted uniaxial and biaxial loading and unloading tests on marble with single and double

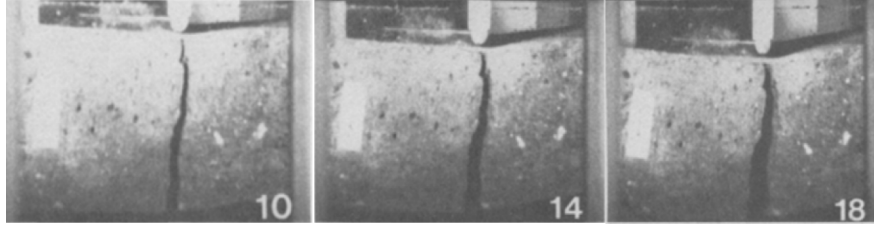
pre-existing cracks inclined at  $45^\circ$ . A Photron Fastcam SA5 was employed to record the process of the crack initiation, propagation, coalescence and final failure. It was found that the crack propagation and coalescence mode of specimens under biaxial loading was different from that under uniaxial loading or unloading, and the type and quantity of cracks in specimens subjected to unloading were much more complicated than the uniaxial specimen.



**Fig. 2.10** The cracking and coalescence processes in a gypsum specimen at a frame rate of 24,096 fps. **(a)** Tensile wing cracks initiated from the two pre-existing flaws. **(b)** Additional cracks initiated from the flaw tips. **(c)** A coalescent shear crack developed to link up the two inner flaw tips **(d)** Geometry of a flaw pair defined by bridging angle ( $\alpha$ ), flaw inclination angle ( $\beta$ ) and ligament length ( $L$ ). (Wong and Einstein 2009).

### (b) Dynamic tests

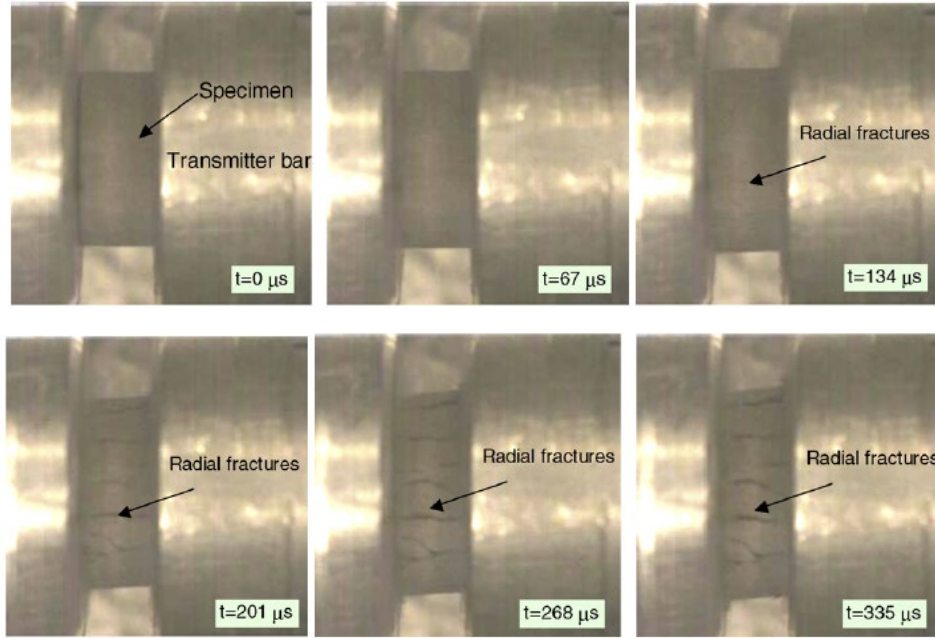
The testing principle of drop-weight machines is use of gravitational potential energy, through controlling a hammer with known height and weight. Due to some limitations of the testing machines (refer to *section 2.1* in (Zhang and Zhao 2014) for details), only a few studies have been conducted using drop-weight machines to investigate the characteristics of fragmentation (Whittles, Kingman et al. 2006) and fracture (Islam and Bindiganavile 2012). The fracture behaviours of plain concrete, fibre reinforced concrete, and plain concrete with conventional reinforcement, were studied with a three-point bending specimen impacted by a drop-weight machine by (Mindess and Bentur 1985). High-speed photographs were taken at 500 fps, which facilitated monitoring of crack opening during the fracture event, as shown in Fig 2.11.



**Fig. 2.11** Sequence of impact fracture of plain concrete by the drop-weight machine at a frame rate of 500 fps (Mindess and Bentur 1985).

The SHPB is regarded as the most successful loading technique corresponding to strain rates of  $10^1$ - $10^4$  s<sup>-1</sup> (Lindholm 1964, Zhang and Zhao 2014). The crack initiation, propagation, and coalescence processes of geomaterials under dynamic loading have been well investigated by various types of SHPB tests. The first application of high-speed photography technology in the SHPB tests on geomaterials was made (Perkins and Green 1968) on Solenhofen limestone with dynamic compression at strain rate 10 s<sup>-1</sup>. A Calumet View Camera was used with high-speed Polaroid, the IOX12.7 cm sheet film, to obtain a conveniently large format without enlargement. The lens shutter was operated in the bulb condition. A General Radio Strobe served as a short duration (0.8  $\mu$ s) and high-intensity light source. (Cai, Kaiser et al. 2007) used a high-speed camera to visualize the initiation of failure and subsequent deformation of the Meuse/Haute-Marne argillite specimens at frame rates from 15,000 to 20,000 fps. The direct compression specimens were found to deform and fail uniformly around the circumference of the specimen, by a radial cracking process, as shown in Fig. 2.12. (Kimberley and Ramesh 2011) performed compression SHPB experiments on ordinary chondrite and a Hadland DRS Ultra-8 camera was used to record the dynamic failure process. Two high-intensity flash sources were used to illuminate the specimen and diagnostics were triggered by a strain gauge. The interframe time was 1  $\mu$ s with 200 ns exposure time, but only eight frames in total were captured. A shared triggering signal was used to synchronize the high-speed camera with the loading pulse, and thus the stresses of the specimen corresponding to the specific times was known. The crack growth speeds experiments were estimated from images by comparing with the scale ruler. (Luo, Du et al. 2015) used a Cordin 550-62 camera to record the dynamic compressive behaviour of dry Mason sand under confinement using SHPB and observed sand deformation and failure processes such as rotation, slippage, fracture, and compaction.

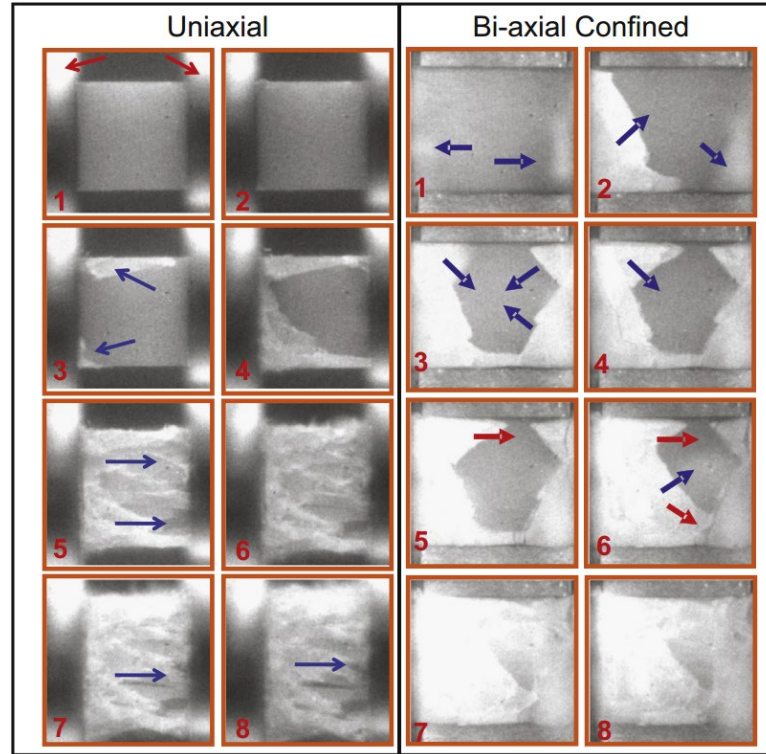




**Fig. 2.12** Initiation of fracture of Haute-Marne argillite specimens under compression test (Cai, Kaiser et al. 2007).

The failure processes are varied when a confining pressure is applied. (Hu, Ramesh et al. 2011) used a DRS Hadland Ultra 8 camera to perform real-time visualization of the failure processes in the aluminium nitride during loading under a modified Hopkinson bar with and without confining stresses. Direct visualization of the confined failure process was obtained through the use of a one-dimensional confinement technique. The camera was capable of capturing up to 8 frames with an exposure time as low as 10 ns and a framing rate up to 100 Mfps. Two Photogenic Powerlight 2500DR flashes were used to provide illumination, and were triggered by an independent strain gauge on the incident bar. Fig. 2.13 shows that the axial cracks propagated at speeds of several hundred meters per second under uniaxial dynamic compression, but no axial cracking was observed in the bi-axial confined specimens. It was demonstrated that the application of a biaxial confining stress could re-orient the principal direction of crack growth during compression, producing diffuse shear-dominated cracks.

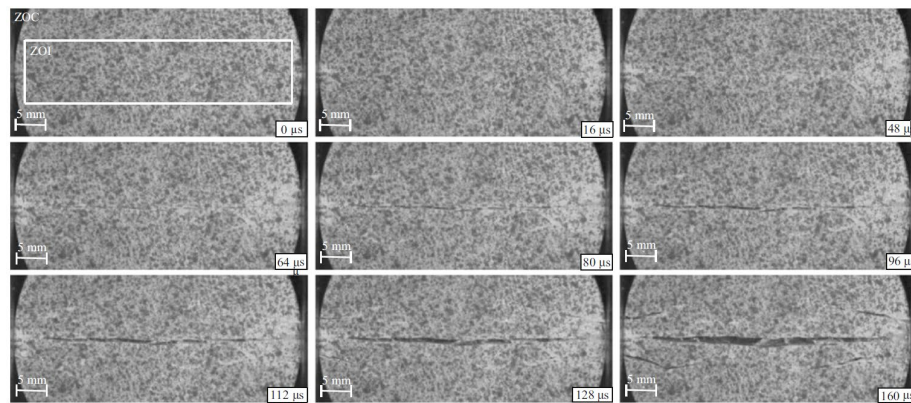




**Fig. 2.13** Influence of confinement on the failure process in aluminium nitride(reproduced from (Ramesh, Hogan et al. 2015) and original source (Hu, Ramesh et al. 2011)). Photographs taken every  $2\mu\text{s}$  with exposure times of 500 ns and white regions in the specimen indicate damaged regions. Left: Unconfined uniaxial dynamic compressive loading in the horizontal direction, red arrows show the WC platens and blue arrows show damage regions and crack propagation. Right: Failure during planar confinement (in the vertical direction) and dynamic compressive loading (in the horizontal direction), blue arrows show damage regions and red arrows indicate crack propagation.

The Brazilian disc (BD) test is an ISRM suggested method to obtain the tensile strength of rocks (ISRM 1978, Li and Wong 2013). (Zhang and Zhao 2013) conducted SHPB BD tests on Fangshan marble using Photron Fastcam SA1.1, a macro-lens (Kenko PRO 300 2.0 $\times$  objective lens), a set of extension tube (Kenko 12, 20 and 36 mm), and a ring-shaped flash light (Pallite VIII 120 V). As shown in Fig. 2.14, the resolution of the zone of camera (ZOC) was 448 $\times$ 192 pixels at 60,000 fps, and the zone of camera (ZOI) was selected as 420 $\times$ 150 pixels for further DIC calculation. The main crack orientation was parallel to the impact direction and axial crack divided the specimen into at least two pieces. There were two kinds of obviously observed failure, i.e., shear failure and tensile failure, and the extent of two shear failure zones at contact points of the disk depended on loading rate. (Wong, Zou et al. 2014) observed the dynamic cracking processes of Carrara marble aided by a Phantom V310 camera at 100,000 fps with the resolution of 72 $\times$ 288 pixels. There were some distinct

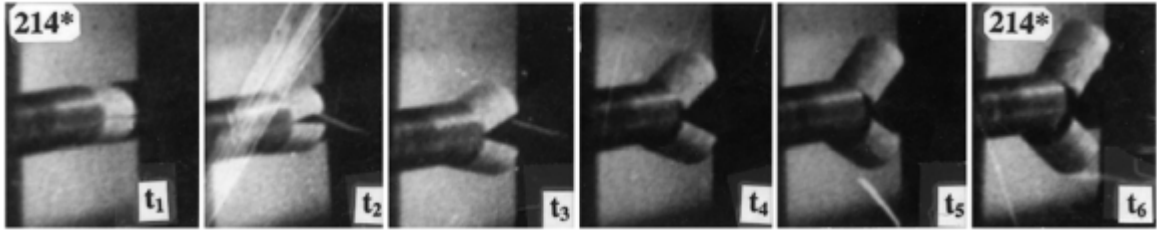
differences in the white patch geometry and initiation load under quasi-static and dynamic loading. (Zhou, Li et al. 2014) conducted BD tests under a compressive pre-stress which was in the same direction as the loading direction. By analysing the photographs of specimen failure taken by a high-speed camera, they revealed that the type II failure pattern (central cracking with crushed wedges) should actually be classified as type I (diametrical split). High-speed photography also showed that the damage zones were formed at the bar/specimen contact areas first when the impact stress increased quickly. As a result, the type III failure patterns appeared. Without the help of the high-speed camera, the original fracture patterns could only be found by checking the fragments of failed specimens and were not able to reveal the real phenomena such as cracks initiating from the damage zone rather than the specimen centre. Reducing this failure at the bar/specimen interface is a good argument for using curved anvils.



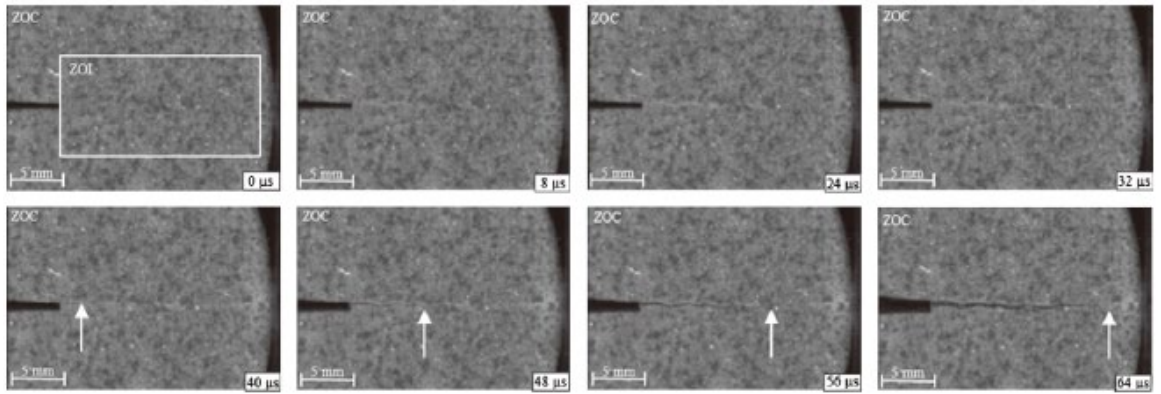
**Fig. 2.14** High-speed images of dynamic BD test of marble at 60,000 fps with the resolution of 448×192 pixels (ZOC: zone of camera, ZOI: zone of interest) (Zhang and Zhao 2013).

Two of ISRM suggested fracture toughness measurement methods, the short rod (SR) and notched semi-circular bending (NSCB) methods, were further used to determine the dynamic fracturing behaviour of rocks (Zhang, Kou et al. 2000, Chen, Xia et al. 2009, Dai, Chen et al. 2010, Zhang and Zhao 2013). A high-speed framing camera was employed to show the motion of the SR specimen and the fragments of Fangshan gabbro and Fangshan marble (Zhang, Kou et al. 2000). The frame rate was set at 350 fps, and thus the interval of two neighbouring images was around 2.857 ms, as shown in Fig. 2.15. One of the most classic direct uses of high-speed imaging in quantitative analysis of geomaterials is to determine crack propagation velocity. As shown in Fig. 2.16, crack initiation time and propagation

velocity can easily be determined by a sequence of images and the crack velocity of Fangshan marble was approximately 680 m/s (Zhang and Zhao 2013). (Zhang and Zhao 2014) took high-speed photographs of the gabbro until the NSCB specimen was split into two almost equal fragments, and each flying fragment had both rotational and translational motion. The translational velocity was calculated by the subsequent translational movement of the centre of mass and the time from the corresponding photographs, and the angular velocity was estimated by the change in rotational angle with respect to time.



**Fig. 2.15** Photographs of dynamic gabbro fracture process of SR specimen by SHPB test. The time intervals between the neighboring images were all 2.857ms (Zhang, Kou et al. 2000).

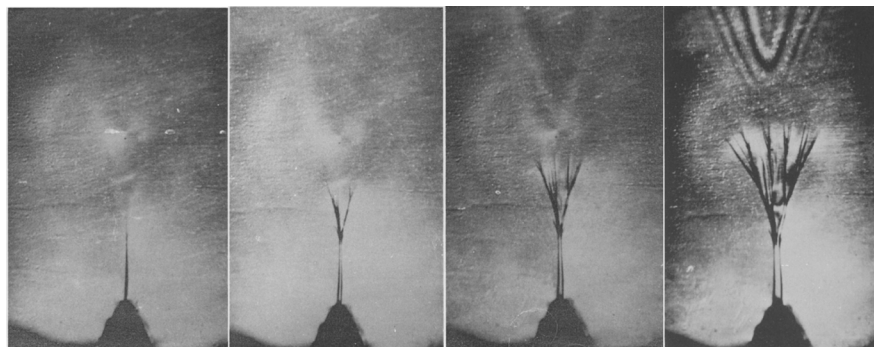


**Fig. 2.16** Crack propagating process of an NSCB marble, the observable moving crack-tip is indicated by an arrow in the images (Zhang and Zhao 2013).

### (c) Blasting and impacts

As early as the 1960s, (Bieniawski 1967, Bieniawski 1967, Bieniawski 1968) used a high-speed camera at 1.6 Mfps to study crack propagation in rocks, as shown in Fig. 2.17. The fracture velocity of Norite rock was plotted in two parts: stable fracture propagation and unstable fracture propagation. It was observed that fracture propagation started with a lower crack velocity and then until the limit of stable fracture propagation (beyond which unstable propagation and bifurcation occurs) the elastic energy released by crack extension was not

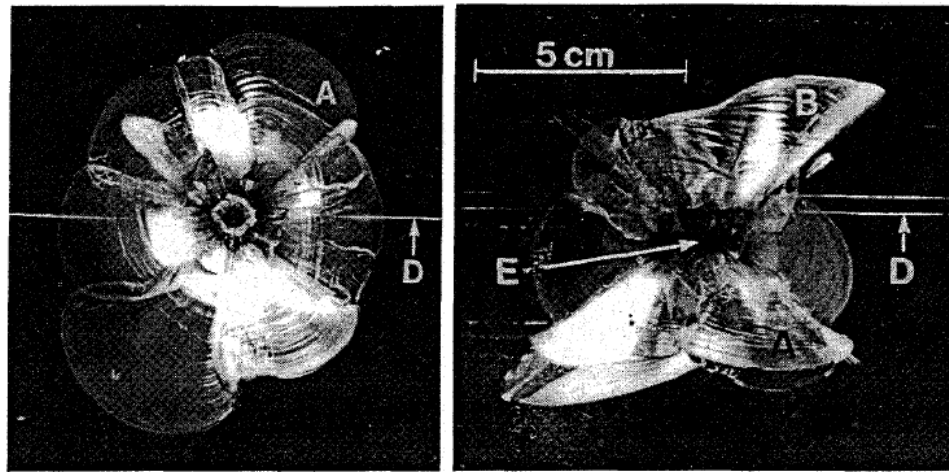
sufficient to maintain fracture. At a later stage, when the elastic energy released was able to maintain fracture, the crack velocity increased rapidly to a limit where it maintained a constant value, namely, the terminal fracture velocity. The experiment confirmed that the terminal velocity was a phenomenon characteristic of brittle fracture. Once the terminal fracture velocity was reached, the phenomenon of crack forking (bifurcation or branching) took place, that is, additional cracks were formed at an angle to the original crack



**Fig. 2.17** Selected images of rock fracture propagation induced by charge explosion and obtained by an ultra-high-speed camera at 1.5 Mfps (modified after (Bieniawski 1968)).

When underground caverns and tunnels are excavated by drilling and blasting, the formation of a flat excavation surface and damage to the walls have to be controlled to reduce the overbreak. As a result, the technique of smooth blasting has been developed (Persson, Holmberg et al. 1993). However, it is hard to investigate the fracture mechanism of rock in smooth blasting because the blast wave from one hole generates a closed crack in an adjacent hole which is subsequently developed by the blast in the next hole, thus creating a fracture surface. One use of high-speed photography in sealed charge experiments is that numerical models can be verified by comparing with experimental results. However, the rock is opaque, so sealed charge experiments were normally conducted with Poly (methyl methacrylate) to simulate the fracturing behaviour, also known as PMMA. In laboratory experiments, the fracture patterns in PMMA are practically identical to the fracture patterns in rock but different in scale which is believed to be useful in investigating the fracturing mechanism (Kutter and Fairhurst 1971). (Rossmanith, Knasmillner et al. 1996) used a 3D cube-type laboratory models fabricated from PMMA, transparent enough to be observed, to undertake dynamic loading from explosives (Rossmanith, Knasmillner et al. 1996). Fig. 2.18 shows the fracture structures, which were captured by a Craz-Schardin-type multiple-spark gap

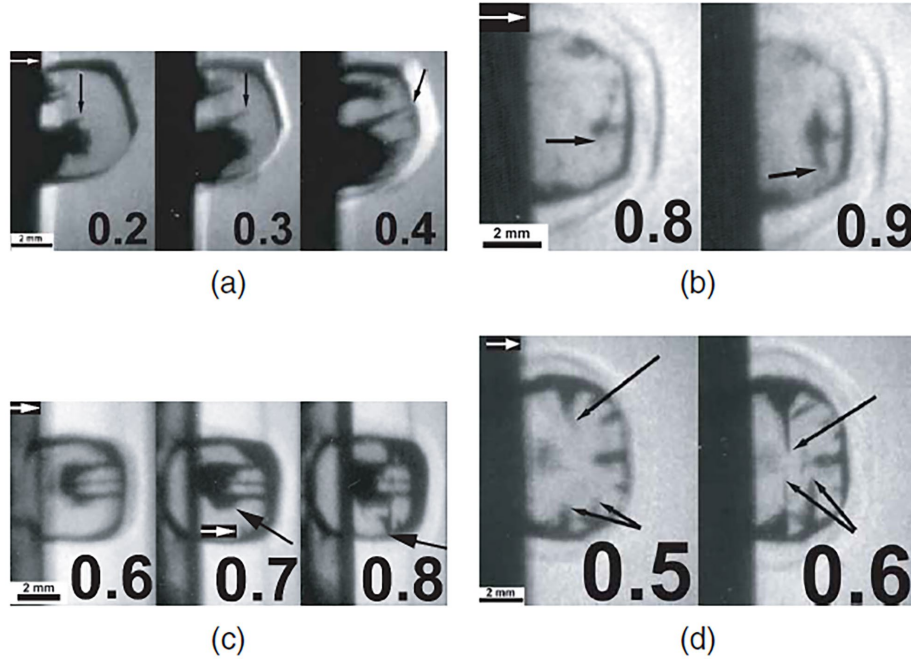
camera at 5000 fps. By recording the dynamic evolution of blast-induced fractures, a qualitative description of 3D fracture propagation caused by the detonation of explosives for three model geometries was obtained. The descriptions of blast-induced fractures under controlled conditions in the laboratory could be used to validate numerical codes. To clarify the effect of rock pressure on crack generation during tunnel blasting, Jung et al. conducted the blasting tests not only on PMMA plates but also on marble plates and sandstone blocks under the assumption that the borehole on the expected fracture line in the tunnel was under initial rock pressure (Jung, Utagawa et al. 2001). A colour 35-mm film Model 124 Framing Camera by Cordin, was used to check the crack initiation and propagation processes in three different materials due to blasting, at a frame rate of  $2 \times 10^5$  fps.



**Fig. 2.18** The final fracture structure in a sealed-charge experiment depicted in two directions (Left image: parallel to the borehole axis. Right image: perpendicular to this axis. 'E' marks the position of the explosive charge and 'D' is the detonation wire.) (Rossmannith, Knasmillner et al. 1996).

At higher strain rates, experiments are normally carried out in gas guns. In this series of experiments by (Willmott and Field 2006), samples of natural diamond were set into PMMA and then subjected to shock loading from a flyer plate. A DRS 501 image converter camera was used at 10 Mfps to observe crack growth and measure velocities. Typical images in Fig. 2.19 show that the fracture of diamond is strongly related to the presence of initial flaws in the specimens. Velocities in excess of  $10 \text{ km s}^{-1}$  were recorded for the cracks and it was speculated that this was due to multiple initiation sites and crack coalescence.





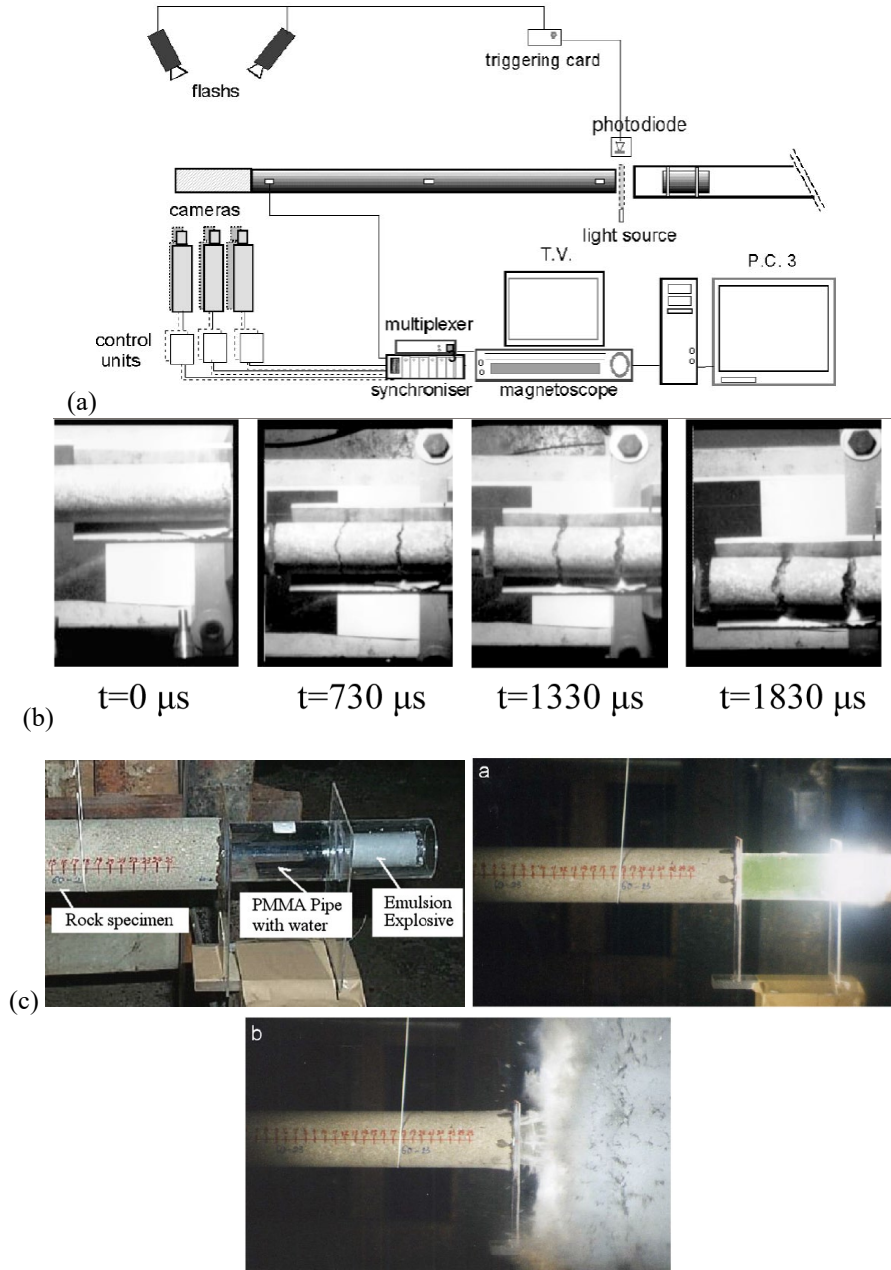
**Fig. 2.19** Four examples of high-speed images showing fracture in diamond, with propagating cracks denoted by arrows. The white arrows show the edge of the dark, vertical shock front in the PMMA matrix. Each frame is labelled with the time in microseconds after shock wave arrival. Cracks can be seen growing in each sequence (Willmott and Field 2006).

### 2.3.4 Spalling

For some protective structures, like shelters, plates protecting against explosions and collisions and many others, it is important that pieces are not ejected from the rear of the material through tensile failure or spalling. Spalling is a process that can be carried out in controlled laboratory conditions (Klepaczko and Brara 2001). Spalling refers to a specific form of fracture, which occurs when a compressive wave reaches a free surface and is reflected as a rarefaction wave. In particular though interactions with other waves, the rarefaction passing back through the material can “pull” the material to the extent where the tensile strength is exceeded causing a failure surface to develop. (Klepaczko and Brara 2001) observed the spalling process of wet and dry concrete by using a coupled fast video system consisting of six CCD fast cameras in Fig. 2.20(a). Each camera produced a high-resolution image (800×590 pixels) at frame rate up to 1 Mfps, and the sequence of spalling images allowed independent determination of the ejection velocity of the fragments. It was found that at such loading rate (up to 5000 GPa/s), dynamic strength exceeds the quasi-static value up to 10 times. It is demonstrated that the high rate sensitivity of the fracture stress should be taken into consideration by the cumulative fracture criterion based on the rate dependent

process of material separation. (Brara, Camborde et al. 2001, Brara and Klepaczko 2006) conducted a series of spalling experiments and numerical simulations on concrete specimens to determine dynamic strength and fragmentation processes, as shown in Fig. 2.20(b). (Cho, Ogata et al. 2003) also measured the fractured planes in dynamic tension tests on Inada granite and Tage tuff to investigate the strain-rate dependency of the tensile strength. (Schuler, Mayrhofer et al. 2006) studied the behaviour of cylindrical concrete specimens positioned at the end of the incident bar to initiate spalling. It was designed to measure the tensile strength and the specific fracture energy. The velocities of the fragments were related to the fracture energy and were measured using a high-speed camera. (Kubota, Ogata et al. 2008) conducted tests on Kimachi sandstone with dimensions of 60mm diameter and 300mm length. The tensile wave was generated by an explosive charge coupled to the sample via a water buffer section, which was able to be varied in length to alter the amplitude of the loading pulse in different experiments, as shown in Fig. 2.20(c). The position of the crack was determined by a model 124 framing-type Cordin camera. The experimental results showed that the distance from the free end to the fracture position varied even when the loading condition was same. It was suggested that this was because the shock wave reduced the strength in the whole damage zone (containing the fracture cross section) rather than just in the fracture cross section. An alternative explanation would simply be that the tensile strength of the inhomogeneous rock specimen is not constant along the length, or from sample to sample. (Pierron and Forquin 2012) used an ISIS CCD camera (Shimadzu HPV-1) with a spatial resolution of  $312 \times 260$  pixels to record images of a grid bonded onto a concrete specimen to allow for a virtual field method to identify the mechanical properties of concrete during spalling. Because the fill factors of ISIS-CCD sensor which are very low compared to standard CCD or CMOS sensors, as mentioned previously. In the direction of the 312 pixels (or x-direction), the fill factor is only 13%, whereas in the other direction, it is closer to more standard sensors with a value of 76%. The camera was rotated so that the specimen movement occurred along the vertical direction of the camera along which the fill factor was higher.

## CHAPTER 2 REVIEW OF HIGH-SPEED IMAGING AND DIGITAL OPTICAL FULL-FIELD MEASUREMENT TECHNIQUES FOR GEOMATERIALS



**Fig. 2.20(a)** Schematic of typical spalling test by SHPB with a high-speed photography system (Klepaczko and Brara 2001), **(b)** Captured fracture process with two spalls under loading from the left side of concrete specimen (Brara, Camborde et al. 2001), **(c)** the spalling test on Kimachi sandstone (a is the initiation of the explosion and b is 240ms after the explosion.) (Kubota, Ogata et al. 2008).

Due to the architecture of the ISIS sensor, only a small portion of each pixel is allocated to the photogate. This results in fill factors (the proportion of the sensor which is photosensitive) that are very low compared to standard CCD or CMOS sensors, as mentioned in Section 2.2.2. In the direction of the 312 pixels (or x-direction), the fill factor is only 13%, whereas in the other direction, it is closer to more standard sensors with a value of 76%. The authors

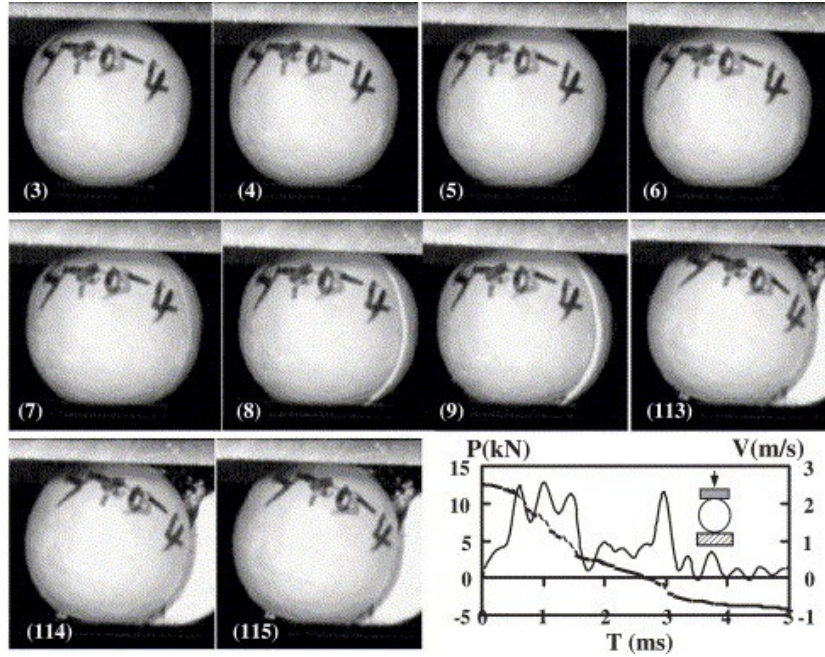


had to rotate the camera so that the specimen movement occurred along the vertical direction of the camera along which the fill factor was higher.

### **2.3.5 Fragmentation**

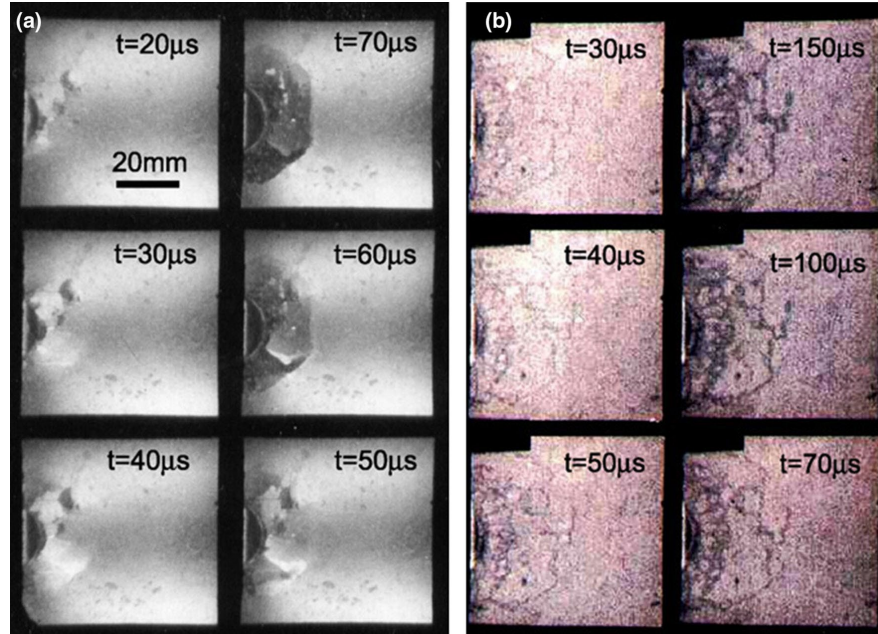
Fragmentation is a spatially and temporally discrete process governed by flaws (inherent and random), material properties (e.g., toughness, hardness) and structure (e.g., grain orientation and size) (Grady and Benson 1983). The dynamic fracture and fragmentation of geomaterials are of interest in particular for mining engineers (Shockey, Curran et al. 1974, Grady and Kipp 1979, Levy and Molinari 2010). The reasons for fragmentation can be easily understood both from the viewpoint of mechanics that the tensile stress exceeds the tensile strength, and in the viewpoint of energy that dynamic loading provides the body with kinetic energy, allowing for the creation of fracture surfaces (Meyers 1994).

Research into fragmentation of geomaterials with the aid of high-speed imaging can date back to the 1950s. (Hino 1956) proposed the fundamental principle of rock failure in blasting using shock wave theory, and introduced a theory to determine the dynamic tensile strength of rock materials from the velocities of fragments produced by the detonation of an explosive charge. A high-speed photographic and a chronotron meter method were devised to measure the fragment velocities. The dynamic tensile strength of rock evaluated from the velocity measurements was found to be more than twice the static strength. High-speed camera records were obtained for the rock fragments ejected by impact craters at three nominal framing rates ( $10^4$ ,  $10^5$ , and  $10^6$  fps) (Gault, Moore et al. 1963). (Arbiter, Harris et al. 1969) conducted drop-shatter impact tests on various sand-cements particles and glass spheres with diameters ranging from 150 to 250 mm, and high-speed photography was used to observe the failure patterns of spherical particles. (Wu, Chau et al. 2004) compressed 141 spheres dynamically with a double impact test and examined various parameters including material strength, sphere size, and impact energy. A MotionScope® PCI system was used to capture the process of breakage at the frame rate up to 8,000 fps. As shown in Fig. 2.21, the impact occurred between frames 3 and 4, and a planar crack was initiated in frame 7, which corresponded to 1.5–2 ms after impact. Frames 113 to 115, corresponding to 53ms later, showed some crushed material falling from the contact zone. Since the spheres were not transparent, it was impossible to observe the fractured development inside the sphere.



**Fig. 2.21** Selected frames of a high-speed photographic sequence of impact fracture of a plaster sphere with the diameter 50 mm by double impact tests, at the frame rate of 2,000 fps, the contact force  $P$  (in kN) as well as the contact velocity  $v$  (in m/s) (Wu, Chau et al. 2004)

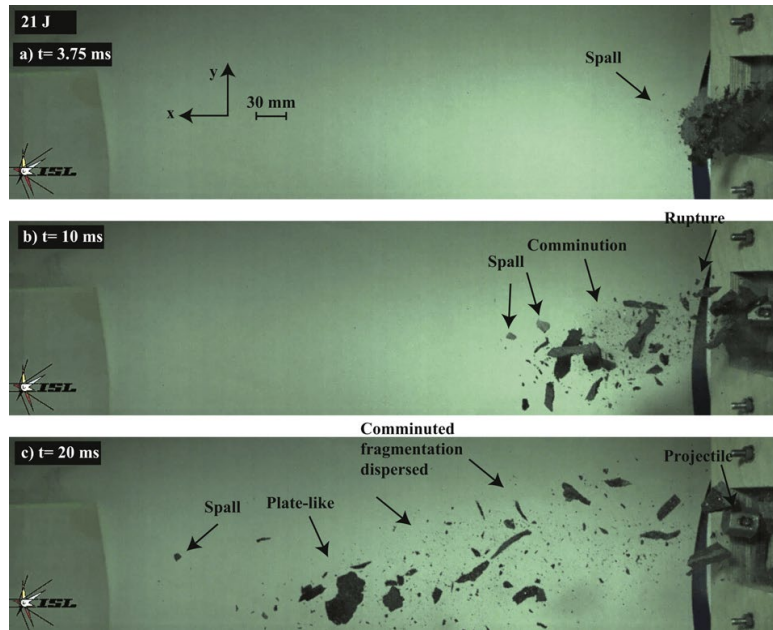
Ballistic edge-on impact (EOI) is commonly used to investigate, either in real-time or post-mortem, crack patterns under dynamic loading conditions (Hornemann, Rothenhausler et al. 1984, Strassburger, Senf et al. 1994). The inter-frame time needed for the high-speed photography in EOI is a few microseconds with ceramics (Denoual and Cottenot 1998) or glass (Brajer, Forquin et al. 2003), and few tens of microseconds for rock and concrete slabs. Edge-on impact tests were conducted on Crinoidal limestone and Beaucaire limestone to compare the fragmentation pattern differences (Grange, Forquin et al. 2008). High-speed photography was used to observe the details of fragmentation. Since some openings were too small, the images did not show all of the cracks that were visible post-experiment in Crinoidal limestone. As seen in Fig. 2.22(a), a few radial cracks were visible when  $t > 40 \mu\text{s}$  and a few circular-front cracks centred on the impact point were seen to emerge  $30 \mu\text{s}$  after impact in Crinoidal limestone. In Beaucaire limestone, radial cracks development stopped  $10 \mu\text{s}$  after impact and a second large emerging crack was observed  $30 \mu\text{s}$  after impact, as can be seen in Fig. 2.22(b). The fragmentation distribution could be well described using Weibull statistics.



**Fig. 2.22** Ultra-high-speed camera observations for two fragmentation tests: (a) Crinoidal limestone with thickness of 8mm, at striking velocity of 200 m/s (b) Beucaire limestone with thickness of 12mm, striker velocity at 101 m/s (Grange, Forquin et al. 2008).

The kinetic energy of moving fragments is usually investigated by tracking them using high-speed photography (Blair 1960). Hogan used a Photron APX Ultima camera filming at 8000 fps to capture fragment trajectories of 10 mm thick gabbro tiles at the rear of targets impacted by railgun-launched projectiles (Hogan, Spray et al. 2013). The sequence of captured images was shown in Fig. 2.23. A tracking algorithm written in Matlab was used to track ejecta larger than 0.8 mm which corresponded to the length of two pixels according to the resolution of the camera. As a result, the ejecta size, velocity, mass, and kinetic energy were measured. It was shown that approximately 11~16% of the kinetic energy (21J) of the projectile was converted to that of fragments before the perforation occurred. It would increase to around 50% when the kinetic energy was 305 J. (Hogan, Spray et al. 2013) continued to conduct tests on four kinds of materials, i.e., a fine-grained tonalitic granitoid, gabbro, a fine-grained syenitic granitoid, and a coarse grained monzonitic granitoid. In that study, the images were contrast enhanced by Matlab to aid the tracking algorithm. Percentiles of the distribution of mass, momentum and kinetic energy were examined with respect to ejecta lengths. Percentile lengths of ejecta decreased with increasing normalized impact energy. Fittings of the non-dimensional ejecta lengths provided reasonable collapse for the percentile values. However, it should be noted in the distributions that fragments smaller than 0.8 mm were not visible to

the camera. The two-dimensional field was not able to give any reliable information about the rotational kinetic energy or out-of-plane displacement/velocity of the fragments. A consecutive investigation was conducted, in which the dynamic fragmentation of a fine-grained granitoid material was examined (Hogan, Spray et al. 2014). Target thicknesses and impact energies ranged from 7 to 40 mm and 12 to 2,500 J respectively. This time the high-speed camera was aiming at the rear of the target instead of from side view to better understand lateral ejecta field behaviour. After the impact, PIV and image enhancement techniques were used to measure the size and velocity of material ejected laterally which was meaningful for predicting mechanisms of ejecta cloud formation.

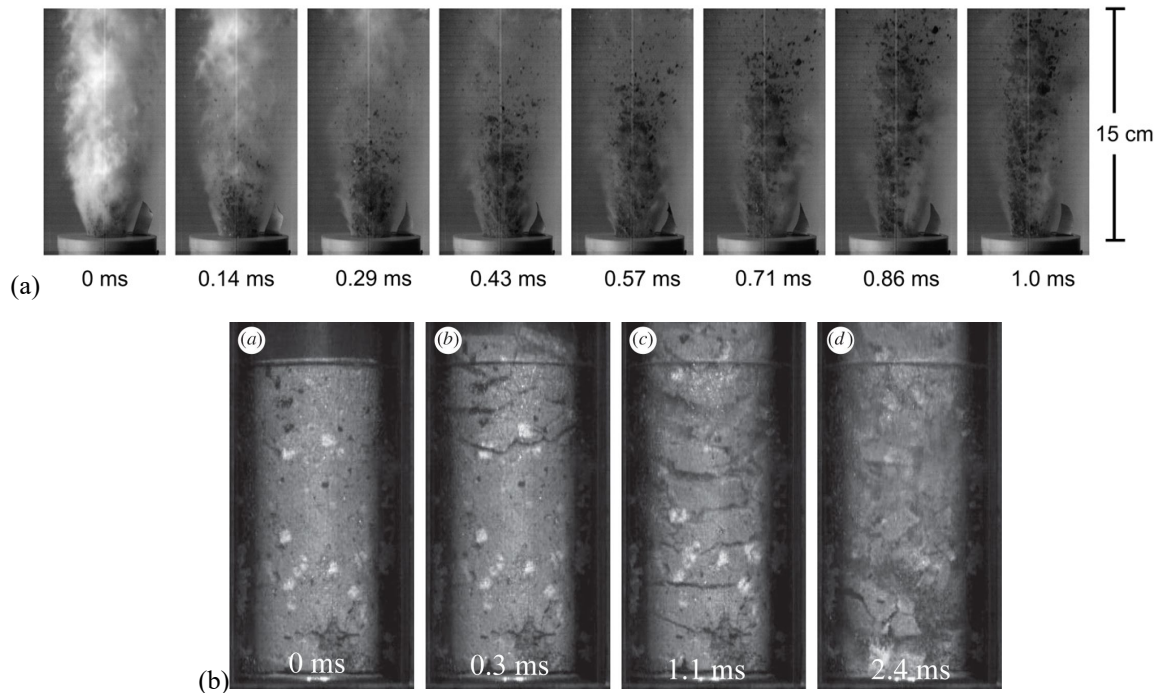


**Fig. 2.23** Evolution of the debris cloud of gabbro for 21J impact at (a) 3.75 ms, (b) 10 ms, and (c) 20 ms after impact. Frame rate at 8,000 fps. Various fragmentation mechanisms are labelled in the figure, including plate-like fragments spalled from the rear surface and those crushed ahead of the projectile (Hogan, Spray et al. 2013).

(Alatorre-Ibargüengoitia, Scheu et al. 2011) used a Phantom V710 and Photron SA-5 high-speed cameras at 14,000 fps to observe the ejection of a gas-particle mixture in a shock tube apparatus. The samples were drilled volcanic rocks, with the aim of investigating the influence of the fragmentation process on eruption dynamics. Variations in sample porosity and applied pressures (4-20 MPa), were investigated. The high-speed photography recorded the full ejection for 300-400 ms. Typical images at 20 MPa are shown in Fig. 2.24(a). A systematic change in the particle size with time was not observed, but a diverse range of



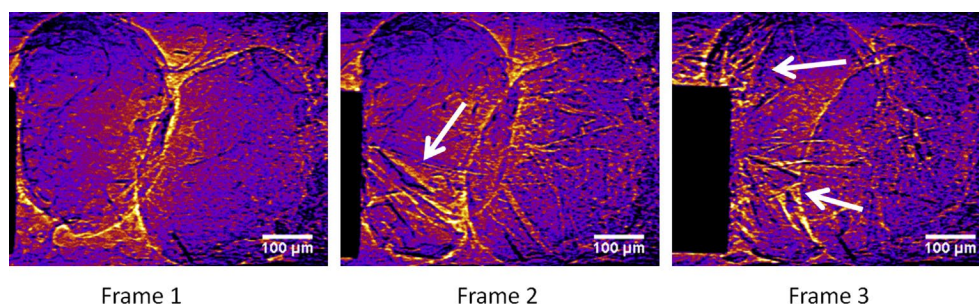
particle sizes was captured throughout. It can be seen that the higher the initial driving pressure, the fewer large particles ( $>8$  mm) were generated. No measurable acceleration of the gas-particle mixture was recorded by the high-speed camera. Detailed analyses of the videos at the initial stage revealed that the size of the particles had no relationship to ejection velocities, and it was common that relatively large particles moved at approximately the same velocity as smaller particles. Another study of volcanic eruptions with high-speed photography was conducted by (Fowler, Scheu et al. 2009). It was hypothesised that fragmentation of magma was the reason why explosive volcanic eruptions differed from quiet volcanic activity. Photron Fastcam camera was used to capture the sequential fracturing of the rock at 10,000 fps, as shown in Fig. 2.24(b). The rock cylinder was placed in a transparent tube with high gas pressure. Fragmentation of porous magma was induced by rapid decompression. The photographs indicated that the fragmentation started at the top of the sample and continued downwards. Two types of fractures were observed: the fractures were parallel to the sample surface and dissected the entire sample into discs (layers); and the internal fracturing of an expelled fragment.



**Fig. 2.24 (a)** The front of the gas-particle mixture after fragmentation, samples were drilled from volcanic rocks in cylinder ( $l=6$  cm,  $d=2.5$  cm), frame rate at 14,000 fps. (Alatorre-Ibargüengoitia, Scheu et al. 2011). **(b)** Individual frames from a sequence of a typical rock fragmentation experiment, frame rate at 10,000 fps. (Fowler, Scheu et al. 2009): a. Before depressurization of the autoclave (0ms). b. 0.3ms after decompression, the upper

part of the sample has fractured. c. After 1.1ms, fractures have occurred throughout the sample. d. By 2.4ms, the rock has disintegrated (Fowler, Scheu et al. 2009).

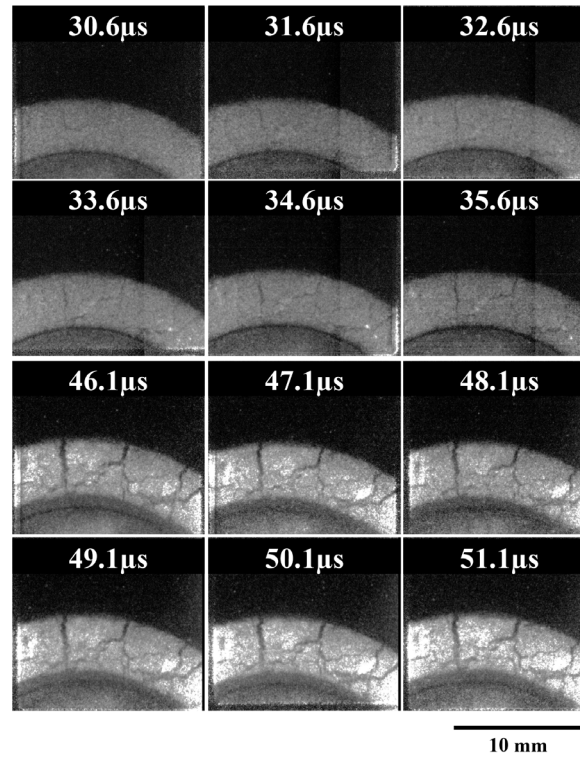
High-speed pulverization of sand (i.e., sand breaking into many sub-particles) usually occurs in the process of penetration in front of the projectile. With the help of high-speed X-Ray imaging, the actual failure process for individual sand particles under dynamic loading was first observed in-situ by (Parab, Claus et al. 2014). A modified Hopkinson bar apparatus synchronised with an X-ray phase contrast imaging (PCI) setup was developed to study the damage mechanisms in dry and wet sand particles under dynamic compressive loading. In the tests, a Photron Fastcam SA1.1 camera was used to capture images at 54,321 fps with the resolution of 640×480 pixels. The captured images are shown in Fig. 2.25. It can be seen that in the dry sand, one sand particle was observed pulverized as well as an extensive interfacial cracking. Wet sand was broken into big sub-particles followed by pulverization.



**Fig. 2.25** Image sequence for wet sand dynamic compression experiment. Large cracks can be observed in Frame 2. The cracked particle breaks into large sub-particles in Frame 3. White arrows indicate large cracks in the sand particle. The resolution was 640×48 pixels at the frame rate of 54,321 fps (Parab, Claus et al. 2014).

In Kirk's study (Kirk 2014), an Invisible Vision UHSi 12-24 Camera and an Opteka mirror lens with a 500 mm focal length was used to take high-speed photographs during the fragmentation process of the Lake Quarry Granite rings driven by a small explosive charge in a copper driver tube (i.e., the method is similar to that detailed in (Marquez, Braithwaite et al. 2016)). The camera took 12 images in quick succession and then another 12 images after a 10 μs delay, as shown in Fig. 2.26. The delay was due to downloading of the first set of images from the camera into the memory before taking the second set of images. Images were taken every 1 μs with a 0.5 μs exposure time and the resolution was 1,082×974 pixels. The experiments were illuminated by flash lamps. The high-speed photography allowed the crack growth and fracture patterns in the rings to be observed. Although it was useful for interpreting the results from the other diagnostics, it did not give any qualitative results for

comparison with fragmentation. It was indeed possible to make broad estimates of the time and length scale of the fragmentation, as well as to make comparisons with more idealised theoretical fracture models.



**Fig. 2.26** Sequence of expanding ring fragmentation of Lake Quarry Granite driven by impact plate. The ring sample was seen to stretch, fracture radially and move off outwards as fragments at 1 Mfps with the resolution of 1,082×974 pixels (Kirk 2014).

## 2.4 HIGH-SPEED DIGITAL OPTICAL MEASUREMENT TECHNIQUES AND THEIR APPLICATIONS TO GEOMATERIALS

Digital optical measurement techniques are varied in their scope and application, and include such diverse techniques as profilometry (Wyant, Koliopoulos et al. 1984), optical fibre sensors (Grattan and Meggitt 1995) and optical coherence tomography (Fercher, Drexler et al. 2003). In this section, we outline some of the most frequently used non-contact full-field optical measurement techniques for dynamic stress, strain or temperature field and their applications in geomaterial experiments combined with high-speed photography. Table 2.1 gives a summary of these techniques.

## CHAPTER 2 REVIEW OF HIGH-SPEED IMAGING AND DIGITAL OPTICAL FULL-FIELD MEASUREMENT TECHNIQUES FOR GEOMATERIALS

**Table 2.1** Summary of digital optical techniques for dynamic stress and deformation analysis (Field, Walley et al. 2004)

Method	Measured parameter	Sensitivity	Accuracy	Light source
<b>Photoelasticity</b>	$\sigma_1 - \sigma_2$	Variable	Variable	Incoherent
<b>Geometric Moiré</b>	$u_x$ or $u_y$	Grating pitch $p \approx 5-1000 \mu\text{m}$	$\sim p/10$	Incoherent
<b>Moiré interferometry</b>	$u_x$ or $u_y$	Grating pitch $p \approx \lambda$	$\sim p/10$	Coherent
<b>Caustics</b>	$\partial u_z / \partial x, \partial u_z / \partial y$	Variable	Variable	Incoherent
<b>Holographic interferometry</b>	$u_x, u_y$ and $u_z$	$\lambda/2$	$\sim \lambda/50$	Coherent
<b>Particle image velocimetry</b>	$u_x, u_y$ and $u_z$	$\sim 1$ pixel of digital image	$\sim 1/10$ pixel of digital image	Incoherent
<b>Digital image correlation</b>	$u_x, u_y$ and $u_z$	$\sim 1/100,000$ of the field of view	$\sim 1/100$ pixel of digital image	Incoherent

These techniques can be classified into interferometric and non- interferometric categories according to a criterion based on the nature of the physical phenomenon involved (Surrel 2003). Among them, interferometric methods include photoelasticity, Moiré interferometry (MI), caustic and holographic interferometry. DIC, PIV and geometric Moiré are non-interferometric techniques. Interferometry requires a coherent light source, and the measurements can be very susceptible to environment disturbances like vibrations (Jacquot 2008). Thus, they are often conducted on a vibration-damped optical table in the laboratory. Moreover, the raw data from the interferometric techniques are often in the form of fringes which require further fringe processing and phase analysis techniques to obtain kinematic information like displacement. On the contrary, the non-interferometric techniques do not require coherent lighting. These techniques generally have less strict experimental requirements and determine the deformation through comparing light intensity changes from the specimen surface before and after deformation (Zhu 2015).

### 2.4.1 Photoelasticity Coating

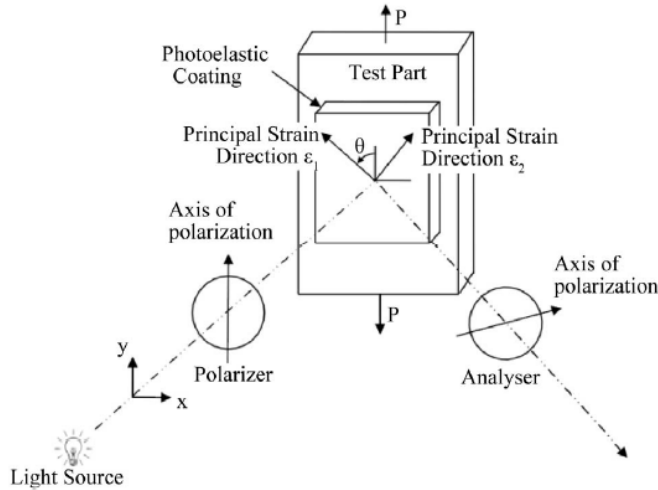
Photoelasticity is an experimental method to study the stress distribution in certain transparent materials based on the property of stress-induced temporary birefringence. It is one of the oldest and most widely used photomechanics methods, developed by Sir David Brewster (Brewster 1816), one of the founding fathers of experimental mechanics who used such techniques to understand materials and structures 200 years ago. In January 1815, he published his work on ‘load induced bi-refringence’ at the Royal Society (Brewster 1815).



In 1928, Tuzi expanded the methods to dynamic photoelasticity, to study a beam subjected to impact loading (TUZI 1928). This research also promoted the development of new high-speed photography system (Daehnke 1999) and one year later the multiple spark gap camera was developed by Cranz and Scharding (Cranz and Schardin 1929). (Riley and Dally 1969). The principle of photoelasticity utilizes the nature of birefringence in which a ray of light passing through a birefringent material “sees” two refractive indices. The relative magnitude of the refractive indices in the material directly relates to the state of stresses at that point, which is given by the stress-optic law as following,

$$\Delta = \frac{2\pi t}{\lambda} C(\sigma_1 - \sigma_2) \quad (2.1)$$

where  $\Delta$  refers to the induced retardation,  $C$  is the stress-optic coefficient,  $t$  is the specimen thickness,  $\lambda$  is the vacuum wavelength of the ray of light, and  $\sigma_1$  and  $\sigma_2$  are the first and second principal stresses, respectively. Photoelasticity is mostly applied to determine stresses or check the quality of transparent objects (e.g. glass, plastics and single crystals) with symmetrical form made of (Lagarde 2014). For opaque geomaterials, photoelastic coatings that deform with the material are used. The simplest setup consists of coating, polarizer and analyser as shown in Fig. 2.27. Stress field visualization is a widely used feature of photoelastic coating technique. Owing to the need for a suitable coating sheet, darkness, well defined optical paths and a highly skilled operator applications of this technique in geomaterials are rare, and very few recent examples exist.

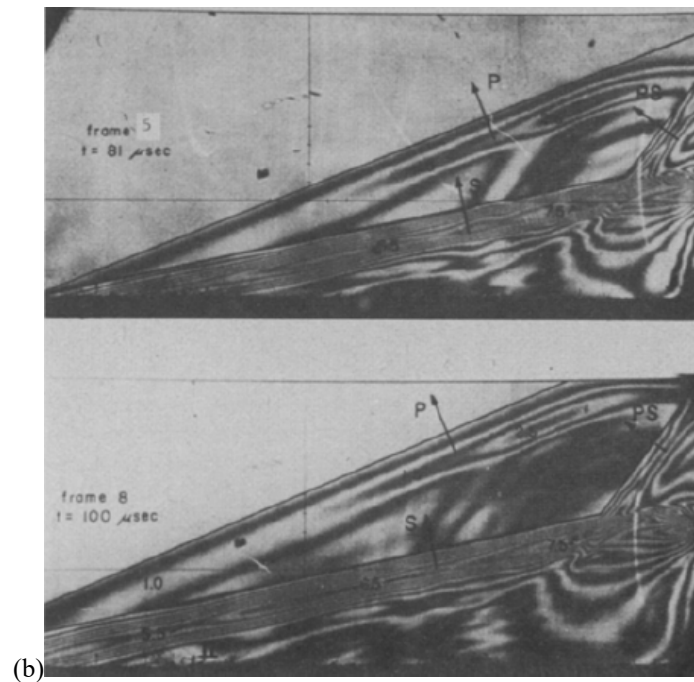
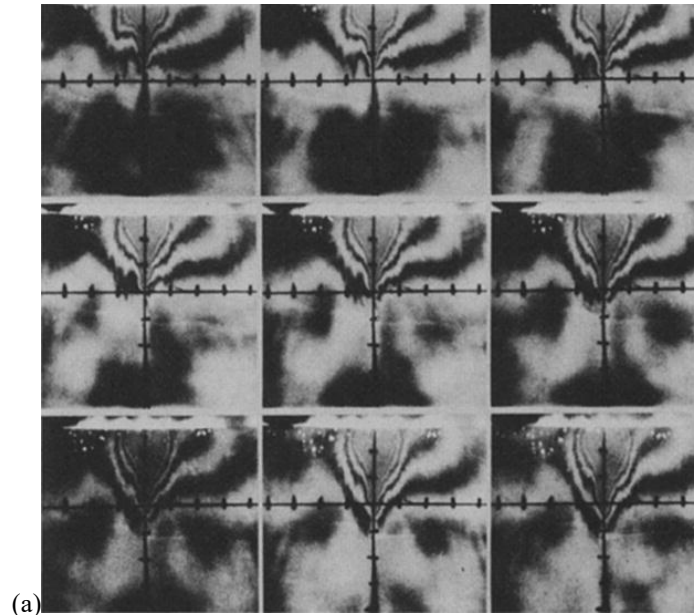


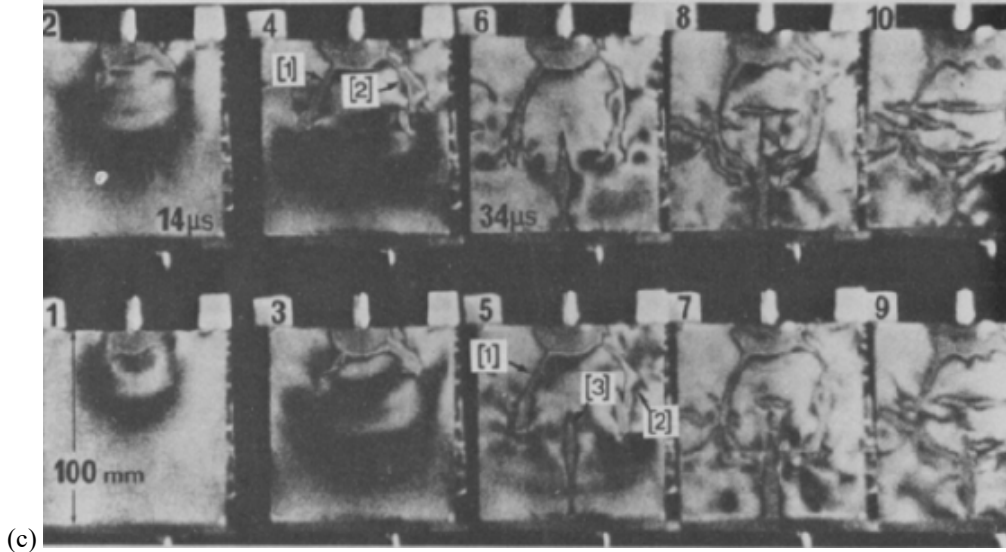
**Fig. 2.27** Loaded photoelasticity coating in a plane polari-scope (Younis 2012).

Studies on wave and fracture propagation were performed by several researchers with photoelastic coatings previously, where the results obtained were qualitative. Fig. 2.28(a) shows the isochromatic-fringe patterns around a crack propagating in a marble specimen dynamically loaded by a steel wedge using a notch technique (Daniel and Rowlands 1975). Fig. 2.28(b) illustrates cracks in Solenhofen limestone covered by a continuous coating struck on edge with a steel projectile. In this research an Imacon 700 and an Imacon 790 were employed to examine area at different levels of magnification (Glenn and Jaun 1978). The use of a continuous coating may introduce uncertainty as the coating responded to fracture not only in the specimen, but also the coating itself (Daniel and Rowlands 1975). This problem may be alleviated by using separated birefringent coatings bonded to either side of the expected path of the crack (Zhang and Zhao 2014). Fourney investigated the velocity of longitudinal stress waves, attenuation coefficients and dynamic elastic modulus in rock cores with dynamic photoelasticity (Fourney, Dally et al. 1976). The samples were 25 mm in diameter, 0.46 m long and made of Salem limestone, charcoal granite and Berea sandstone. The rods were loaded by a lead azide charge from one end, as seen in Fig. 2.28(c). A high-speed camera was operated at framing rates which could be varied in discrete steps from 30,000 to 800,000 fps. The dynamic resolution of the camera was a function of the fringe gradient and fringe velocity and its upper limit corresponded to gradients of 0.8 fringes/mm with fringe velocities of 3,000 m/s. Brittle polyester materials have high photoelasticity sensitivity, elastic modulus and low creep, time edge effect and can be easily manufactured.

## CHAPTER 2 REVIEW OF HIGH-SPEED IMAGING AND DIGITAL OPTICAL FULL-FIELD MEASUREMENT TECHNIQUES FOR GEOMATERIALS

More references can be found on simulation of the wave propagation or the crack initiation in rock by polyester with photoelasticity coating and high-speed imaging rather than directly on the rock. Some of the references are (Thomson, Ahrens et al. 1969, Fournery, Holloway et al. 1975, Rossmannith and Fournery 1982, Shukla and Damania 1987, Shukla 1991).





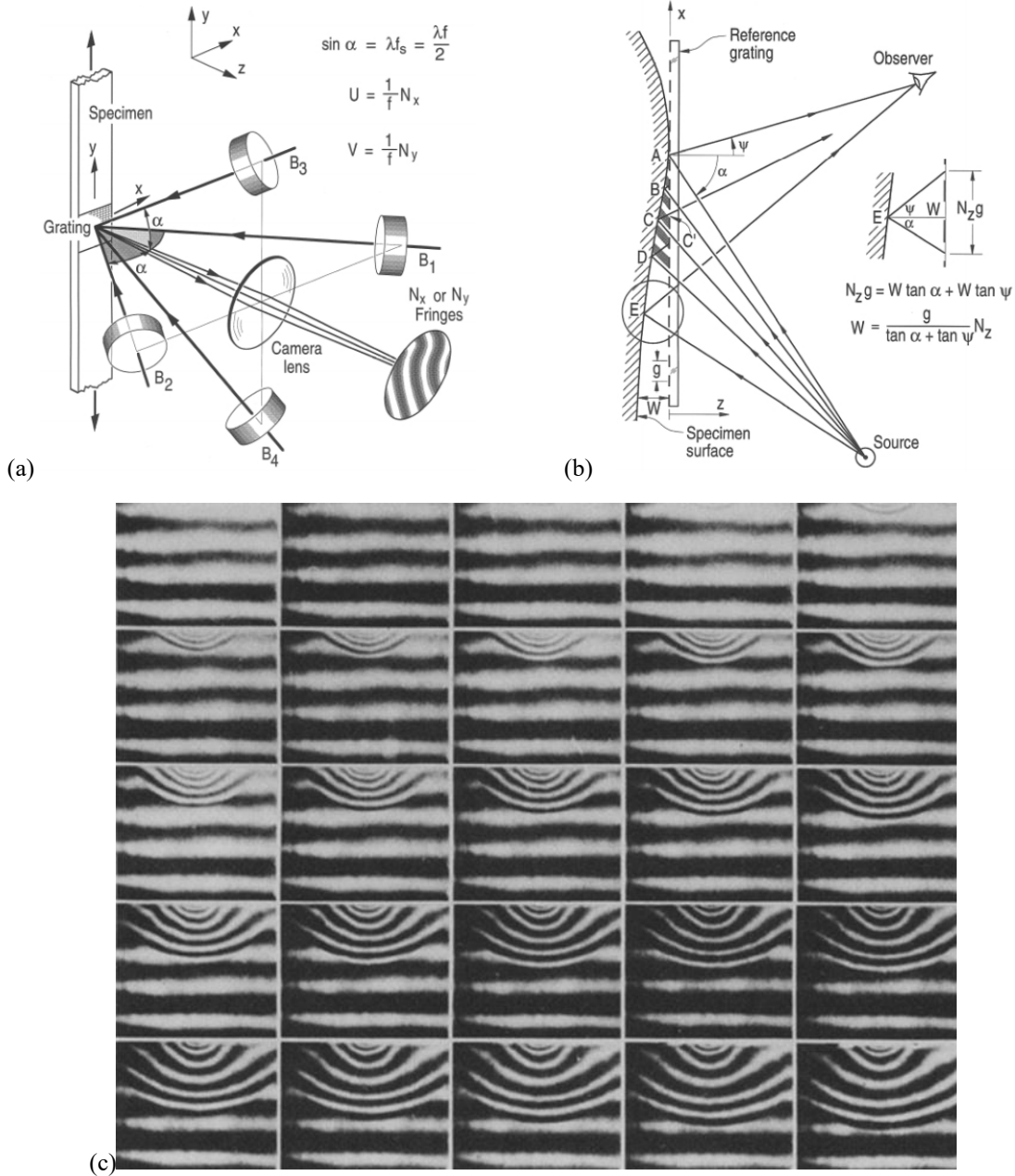
**Fig. 2.28(a)** Isochromatic-fringe patterns around a crack propagating in a marble plate dynamically loaded by a steel wedge in notch technique; inter-frame interval of  $4 \mu\text{s}$ , and crack propagation velocity of  $965 \text{ m/s}$ . Reproduced from (Daniel and Rowlands 1975); **(b)** Dynamic isochromatic-fringe pattern for strain-wave propagation in Salem limestone (Fourney, Dally et al. 1976); **(c)** Cracks in Solenhofen limestone. Extension rate of crack between frames 4 and 5 is in excess of  $10.8 \text{ mm}/\mu\text{s}$  (Glenn and Jaun 1978)

### 2.4.2 Moiré

Moiré fringes are formed by the superposition of two gratings, i.e. two arrays of uniformly spaced lines. Its application and modern scientific research into the Moiré phenomenon was not started until the 1850s with pioneering works such as (Rayleigh 1874, Righi 1887). Since then theoretical analysis of the Moiré phenomena has proceeded based on geometric or algebraic approaches (Amidror, Amidror et al. 2000). A detailed review of the Moiré phenomenon can be referred to (Patorski 1993). The Moiré fringes are contour maps of the path difference between the gratings, and as such, they have been attractive in experimental solid mechanics for the determination of surface deformation (Post, Han et al. 2000). There are two distinct Moiré techniques: geometric Moiré and Moiré interferometry. The former can be divided into in-plane Moiré and shadow Moiré for out-of-plane displacement. Moiré interferometry only looks at the in-plane displacement. The basic difference between geometric and interferometric Moiré is the frequency of the gratings used (Anastasi 1992), but Moiré interferometry is much more sensitive than geometric Moiré. In-plane geometric Moiré has been rarely applied, but shadow Moiré is still used for out-of-plane displacement which exceeds  $0.25 \text{ mm}$  across the field of view (Post, Han et al. 2012). The schematic of Moiré interferometry and shadow Moiré is shown in Figs. 2.29(a) and (b). A detailed

description of the method can be found in reference (Post, Han et al. 2012). Applications of Moiré interferometry include the fracture behaviour or failure mechanism of materials (Nicoletto, Post et al. 1982, Arakawa, Drinnon Jr et al. 1991, Epstein and Dadkhah 1993), mechanical properties of composite structures and alloy materials (Knauss, Babcock et al. 1980, Ifju, Masters et al. 1995, Mollenhauer, Iarve et al. 2006), and residual stress detection (Nicoletto 1991, Wu, Lu et al. 1998, Min, Hong et al. 2006). However, Moiré interferometry needs a special high-frequency grating on the specimen surface on which the lasers impinge from a particular direction. If higher sensitivity is required, the pattern needs to be so fine that it becomes almost impossible to obtain adequate resolution and at the same time adequate depth of focus to cover a wide and possibly deep target (Huntley and Field 1989). As a result, it has limited application for measurements of geomaterials. Fig. 2.29(c) shows the process of wave propagation observed through isochromatic-fringe patterns on bonded Moiré-fringe patterns. Moiré-fringe patterns corresponding to vertical displacements in a marble specimen dynamically loaded on the edge were recorded at a frame rate of 1,004,500 fps with a 400 lines/cm grating (Daniel and Rowlands 1975). (Meng 1994) studied stress wave propagation and dynamic crack extension in a rock plate under explosive loading using a dynamic Moiré method, recorded by a GSJ rotating mirror framing camera, at frame rates ranging from 62.5 to 2,500 kfps. The high-speed camera and flash light were triggered by the explosive charge. Based on the dynamic Moiré records, the strain fields in the specimens were analysed, and the variation of the velocity of crack propagation with time and the phenomena of crack branching and crack arresting were investigated.

## CHAPTER 2 REVIEW OF HIGH-SPEED IMAGING AND DIGITAL OPTICAL FULL-FIELD MEASUREMENT TECHNIQUES FOR GEOMATERIALS

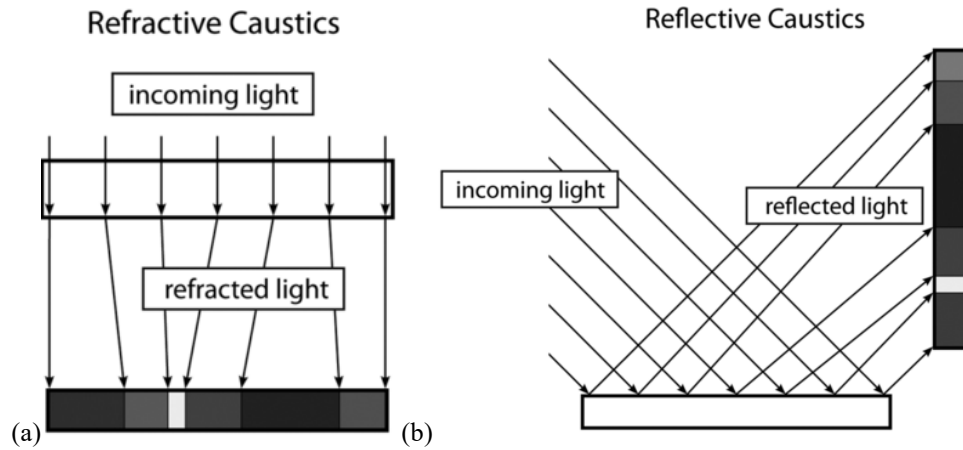


**Fig. 2.29** Schematic of (a) four-beam Moiré interferometry to record the  $N_x$  and  $N_y$  fringe patterns, which depicts the  $U$  and  $V$  displacement fields, and (b) shadow Moiré, which depicts the  $W$  displacement fields (Post, Han et al. 2012), (c) Moiré-fringe patterns corresponding to vertical displacements in a marble specimen dynamically loaded on the edge, at 1,004,500 fps and ruling of 400 lines/cm. (Daniel and Rowlands 1975).

### 2.4.3 Caustics

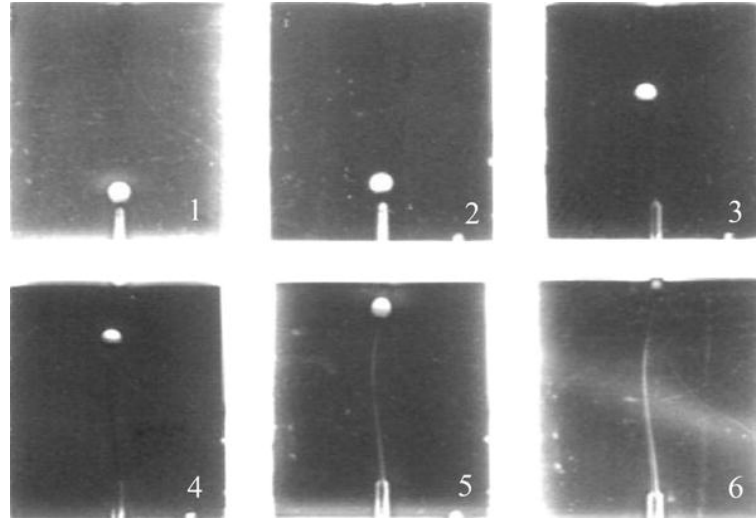
A caustic is the envelope of light rays reflected or refracted by a curved surface or object, or the projection of that envelope of rays impinging on another surface (Weinstein 1969). Making measurements by caustics was proposed by (Manogg 1964) and used extensively by

(Theocaris and Gdoutos 1972, Zehnder and Rosakis 1990, Yao and Xu 2011). It is mainly used for studies of dynamic fracture of transparent materials, as shown in Fig. 2.30(a) (Field, Walley et al. 2004, Ravi-Chandar 2004). It can equally well apply to an opaque specimen when light rays are reflected from its surface, as shown in Fig. 2.30(b), and the optical path changes with the deformation of the object surface. The caustics method avoids one of main drawbacks of the photoelastic method is that can measure in areas of plastic deformation as well as elastic. This makes it a powerful tool in the study of local stress fields and dynamic stress intensity factor (SIF) (YANG, XU et al. 2014). However, the main problems of caustics are the low resolution, the difficult analytical processing and the narrow research scope (GONG, JIA et al. 2005).



**Fig. 2.30** The principle of the caustics image refractive caustics for (a) a transparent specimen, and (b) an opaque specimen by reflective caustics (Kiser, Eigensatz et al. 2013).

(YANG, YUE et al. 2009) conducted dynamic caustic tests on a three-point bending rock specimen using a drop-weight machine. The dimension of a rock specimen was 220×50×8 mm (length×height×thickness). The pre-made crack was 10 mm in length and 0.25 mm in width. The specimen was polished to a mirror finish after cutting which gives the specimen the ability to operate reflective caustic, as shown in Fig. 2.31. The specimen was mounted in a drop hammer with a 250 mm height and a 30 kN free-falling weight, which was able to provide impacts at different loading speeds. The dynamic SIF was determined by measurements of the transverse diameter of the caustic curve. A photo-electric system consisting of a DDGS-II multi-spark high-speed camera were employed.

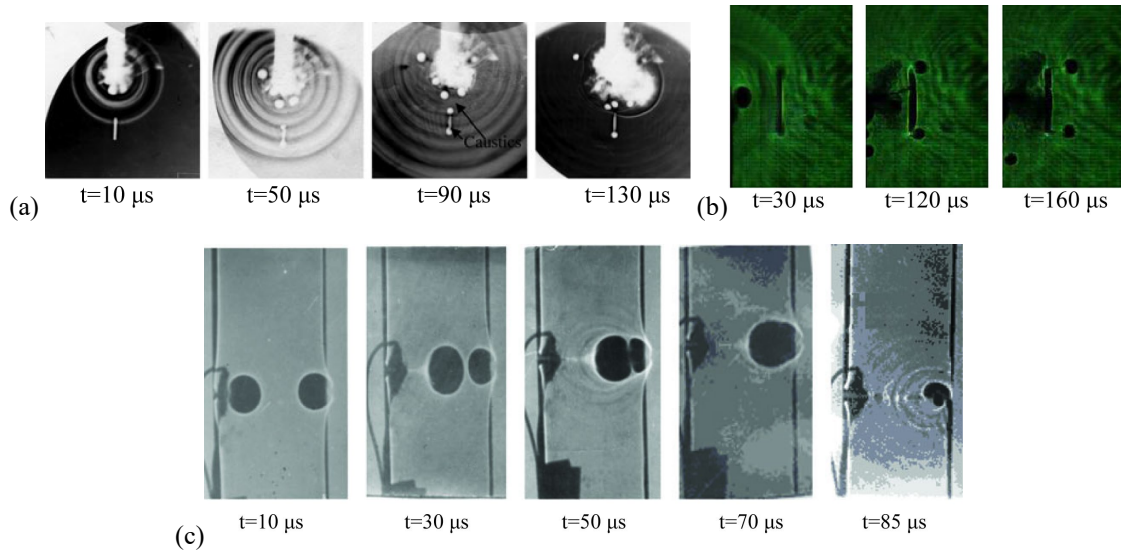


**Fig. 2.31** Reflective caustic images of a three-point bending rock specimen impacted by a drop-weight machine (YANG, YUE et al. 2009)

PMMA is often chosen for the study of crack-defect interaction mechanisms instead of actual geological materials because of its homogeneity, high mechanical strength, high transparency, low density, and easy casting. The wave speed and dynamic fracture behaviour of PMMA are very similar to certain relevant brittle solids at room temperature, and so allows for some read-across to the study of fracturing problems in geological materials under both static and dynamic loading conditions (Xu, Yao et al. 2005, Huang, Luo et al. 2009, Zhang, Guo et al. 2014, Zhang, Sun et al. 2014, Ayatollahi, Torabi et al. 2015). (LI, YANG et al. 2005) established a dynamic-caustics testing system to study the fracture of PMMA under blast loading, as PMMA was assumed to some extent have similarities with rock. Through a controlled blasting method, the initial crack was close to a mode-I crack. Yang and his co-authors studied the crack propagation mechanism and the influence of closed and open joints in rock blasting by making inferences from PMMA experiments diagnosed by dynamic caustics (Yang, Yue et al. 2008, Yang, Yang et al. 2009), as shown in Fig. 2.32(a). Recently, (Yang, Wang et al. 2016) studied the dynamic characteristics of propagation of main and secondary cracks by using a digital laser dynamic caustics method in PMMA with pore-existing flaws under explosive loading. A high-speed camera was set up to capture images with an interframe time of  $10\mu\text{s}$ , as shown in Fig. 2.32(b). Thus, crack length propagation at each time was measured to calculate the crack velocity. In another experiment, (Yang, Xu et al. 2016) studied the crack-defect interaction for mode-I running crack using digital dynamic



caustics method a with Fastcam-SA5 at 100,000 fps and exposure time of 1  $\mu$ s. Three-point-bend loading type was performed on a pre-cracked PMMA by a hammer with 1.5 kg weight dropping from a height of 550 mm. The crack velocity and dynamic SIF were obtained by the measurement. Yao and his co-authors studied various dynamic fracture phenomena of multi-cracks in PMMA by means of the caustic method with high-speed photography, such as thin plates with three or four-parallel edge cracks (Yao, Jin et al. 2002), 44 sheets with two overlapping offset-parallel cracks under tensile loading (Yao, Xu et al. 2003), and dynamic interactions between the static and propagating cracks where initially material containing two collinear-edge-cracks was subjected to tensile loading (Yao, Xu et al. 2005), as shown in Fig. 2.32(c).

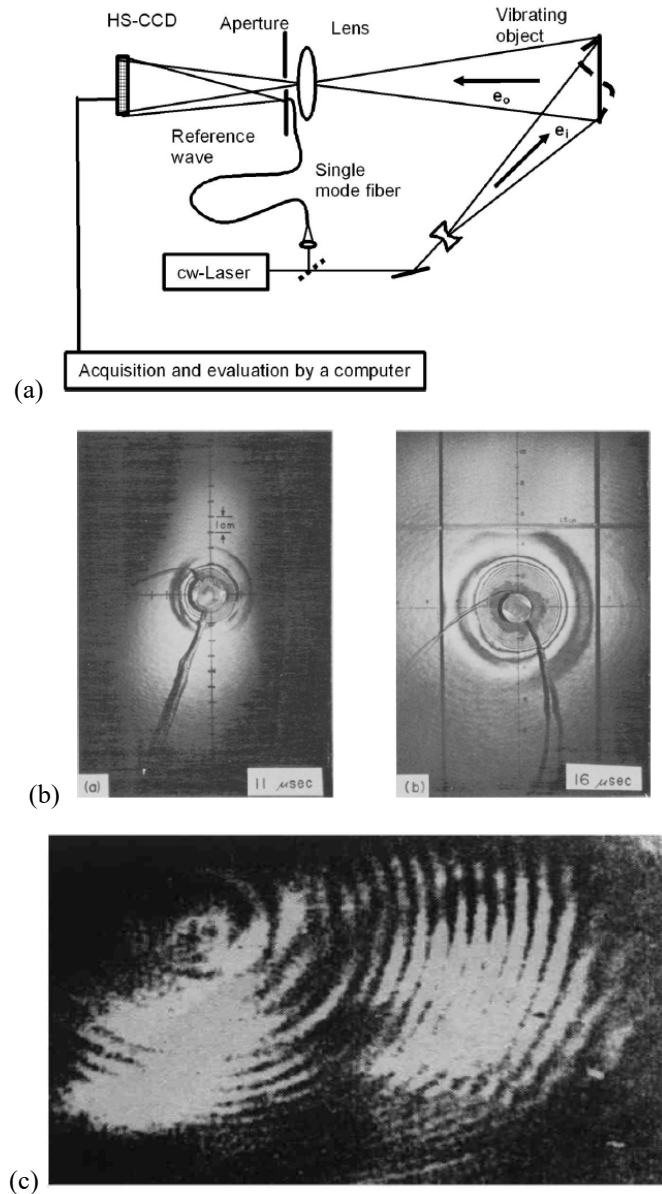


**Fig. 2.32(a)** Caustics surrounding the tip of flaw after blasting (Yang, Yue et al. 2008, Yang, Yue et al. 2008, Yang, Yang et al. 2009) **(b)** The caustics image of propagation of main cracks and secondary cracks in PMMA with flaws under explosion loads of PMMA model (Yang, Wang et al. 2016), and **(c)** Off-focused caustic patterns of dynamic crack propagation in a PMMA specimen subjected to tensile loading with two collinear cracks (Yao, Xu et al. 2005).

#### 2.4.4 Holographic Interferometry

Dynamic holographic interferometry (HI) enables dynamic displacements of optically rough surfaces to be measured with interferometric precision. The associated phenomena were first observed by (Leith and Upatnieks 1963). The early applications of HI were associated with deformation measurements of a lathe, vibration modes of turbine blades or propellers, non-destructive testing of rubber tires, the SIF of cracks, holographic photoelasticity, and mechanical behaviour of materials (Stetson and Powell 1965, Yu-wen 1979, Qin 1981, Chia,

Tong et al. 1984, Hariharan and Oreb 1986). Later some pioneering work in HI improvement and applications in mechanical engineering and biomechanics were also published (Parker and Jones 1988, Tieng and Lai 1992, Sharma, Ruffin et al. 1993, Trolinger and Hsu 1993). The principle of HI is to obtain an interference pattern between two holograms of the same object, where the first is a reference state and the second is made on the same photographic film after the movement was occurred. During reconstruction, two waves are formed and interfere beyond the hologram. Traditional HI needs wet film chemical processing, which has been gradually replaced by digital speckle techniques. Digital HI was developed later (Li, Xie et al. 2010). A simple schematic of high-speed digital HI is shown in Fig. 2.33(a). The sensitivity of the displacement measurement by HI is as high as half of the wavelength of the applied laser. Therefore, the advantage is mainly controlled by the pixel size in the CCD arrays (Rastogi 2000). In terms of disadvantages, the method requires a darkened room with complex vibration isolation, only one or two dynamic states can be recorded, and its measurement range is limited due to the fixed sensitivity, which leads to limited applications of HI in the dynamic experiments on geomaterials. (Holloway, Patacca et al. 1978) introduced the application of HI to visualize wave propagation in Westerly granite. To enhance the coherence properties, a pulsed ruby laser was applied as the light source. Detailed Procedures were presented for the formation and reconstruction of the hologram, fringe interpretation, and data reduction and presentation. The elastic-wave velocities and material constants for Westerly granite were obtained from two images with a length scale, as shown in Fig. 2.33(b). The first holographic interferometric system was set up in China to simulate explosive loading (Li, Yang et al. 1999), and the principles of the quantitative analysis of dynamic displacement fields in three dimensional were developed. The full-field surface displacement of marble samples was recorded by HI as shown in Fig. 2.33(c). It was found that when the explosive was detonated on the surface of samples, the Rayleigh wave predominated, and the main components of surface displacement were in the vertical and radial directions. Accumulation of stress was seen at crack tips.



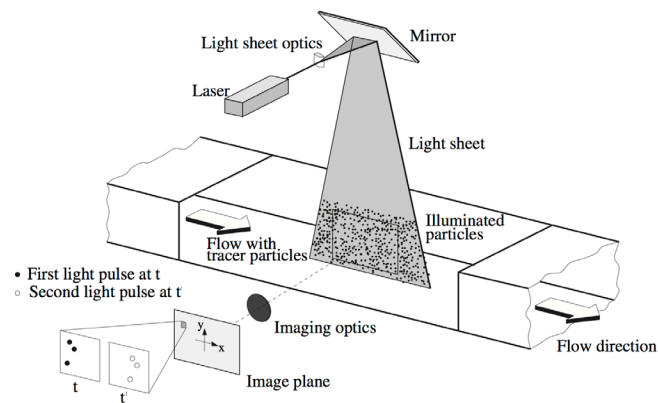
**Fig. 2.33(a)** Optical arrangement for the high-speed digital holographic interferometry (Pedrini, Osten et al. 2006), **(b)** Typical fringe patterns at 11  $\mu$ s and 16  $\mu$ s after detonation resulting from an explosive point load in a half space of pink Westerly granite (Holloway, Patacca et al. 1978) and **(c)** A holographic interferometric fringe pattern taken at 46  $\mu$ s after explosion of a charge of 51 mg DDNP above the surface of a marble sample (Li et al. 1999).

#### 2.4.5 Particle Image Velocimetry (PIV)

PIV is an optical method of flow visualization to obtain instantaneous velocity measurements and related properties in fluids. PIV has its roots in flow-visualization techniques such as particle-streak photography and stroboscopic photography (Adrian 1991). Applications of PIV include aerodynamics (Koschitzky, Moore et al. 2011), hydrodynamics (Hall, Barigou

et al. 2005), environmental research (Greated, Skyner et al. 1992), biomedical research (Lima, Wada et al. 2008) and turbulence research (Zhang, Tao et al. 1997). PIV has been widely used and achieved remarkable results in measuring flow fields and in static soil deformation tests. Through calculating the distance of individual particles travelling in two images taken with a known time difference, the whole velocity field is obtained.

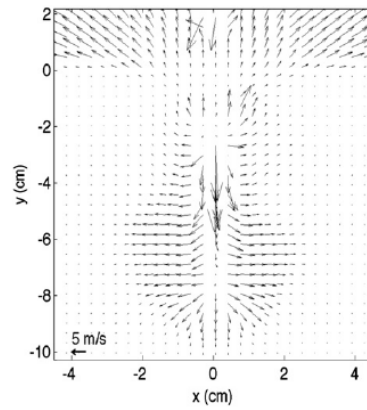
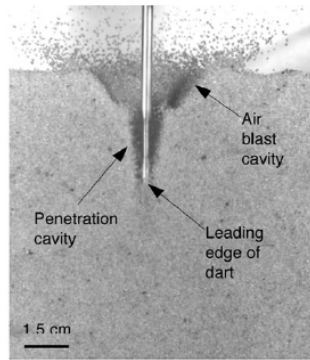
Due to the ability to track particles, high-speed PIV is employed to measure sand movement, fragmentation and penetration in geomaterials. A laser pulse is mostly used as the illumination in terms of two reasons: (1) particles in the flow can be very small that requires short exposure times to avoid blurred images, and (2) only laser light is able to be focussed on a sheet thin enough to image the particles in a plane. Tracer particles for PIV are required to satisfy two conditions: (1) they should be able to follow the flow streamlines without excessive slip, and (2) they should efficiently scatter the illuminating laser light (Prasad 2000). One of the distinguishing features of PIV is that it does not rely on the presence of targets such as grid or speckle (either naturally occurring or artificial). Deformation or movement of the particles themselves is able to provide reference points which are tracked as the experiment proceeds. This feature can alleviate the drawback of having to rely on separate tracers. An assessment of PIV performance in soil was conducted by (White, Take et al. 2003). A very high measurement precision was achieved with a random ‘soil’ image. A typical setup of the PIV is shown in Fig. 2.34. The post-processing of recorded images in PIV is analogous to DIC, a powerful optical technique widely used for deformation measurement of solids.



**Fig. 2.34** Typical setup of the PIV (Raffel, Willert et al. 2013)

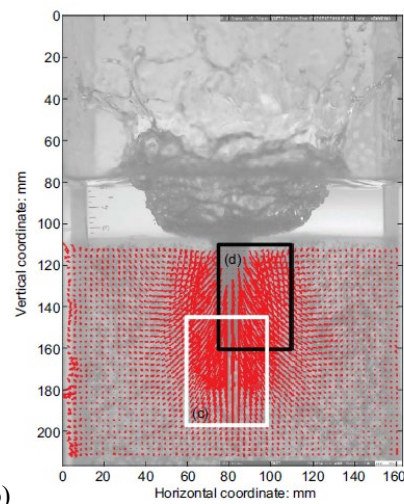
(Borg, Morrissey et al. 2013) collected light images with a Photron RS CMOS camera for general visual assessment and PIV measurements, as shown in Fig. 2.35(a). The PIV results revealed that the velocity of the sand near the projectile was quite low as compared to that of the projectile. This resulted in a thin layer of high shear near the interface between leading edge of the projectile and the sand. (Chen, Omidvar et al. 2014) also conducted penetration experiments in transparent soil, as shown in Fig. 2.35(b). The velocity field of the soil target was determined by the PIV method. A NAC HX5 camera was utilised to capture a field view of  $217 \times 163 \text{ mm}^2$  at 4000 fps with the resolution of  $1280 \times 960$  pixels. (Wang, Liu et al. 2015) used high-speed PIV to quantitatively analyse a laboratory rockburst simulation. The displacement and strain fields were obtained (Fig. 2.35(c)), and the debris trajectory was described. The high-speed solid particles were equivalent to the tracer particles in the flow field, and the PIV method was able to track the tracer particles in the flow field produced during rockburst. Hence, applications of fluid mechanics type flow field analysis could potentially be used to simulate rockburst. As mentioned previously, (Hogan, Spray et al. 2014) conducted PIV on the high-speed photographs of tonalitic granitoid fragments induced by the impact of an aluminium projectile to track the fragments velocity, as shown in Fig. 2.35(d). Since the illumination source was not a laser, the individual particles could not be defined separately. Consequently, a cell may contain multiple ejected fragments.

## CHAPTER 2 REVIEW OF HIGH-SPEED IMAGING AND DIGITAL OPTICAL FULL-FIELD MEASUREMENT TECHNIQUES FOR GEOMATERIALS

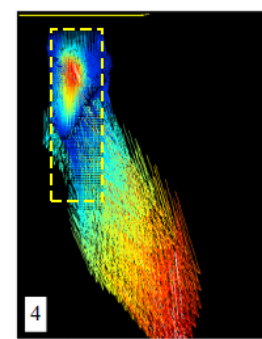
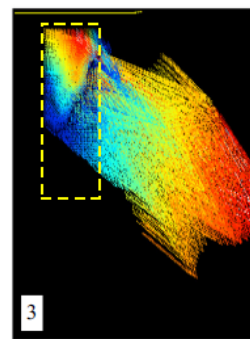
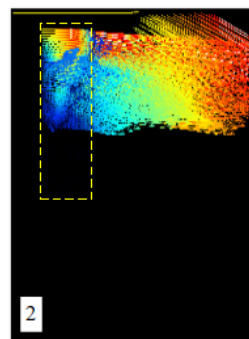
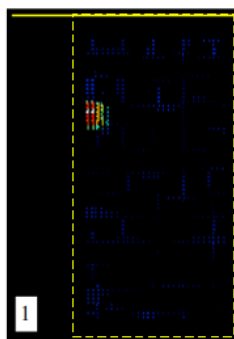


(a) Camera image

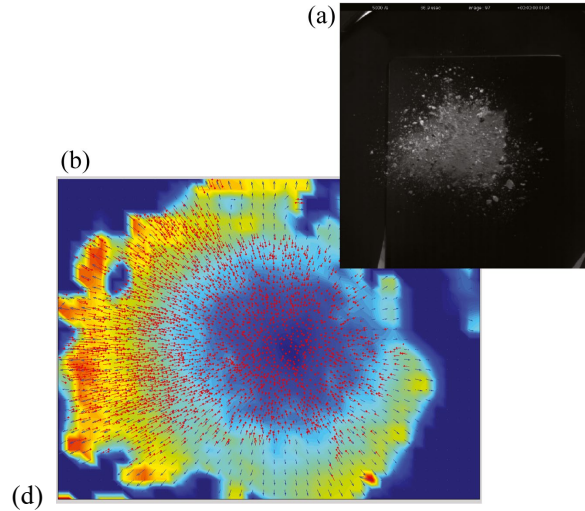
Processed image illustrating velocity vectors



(b)



(c)

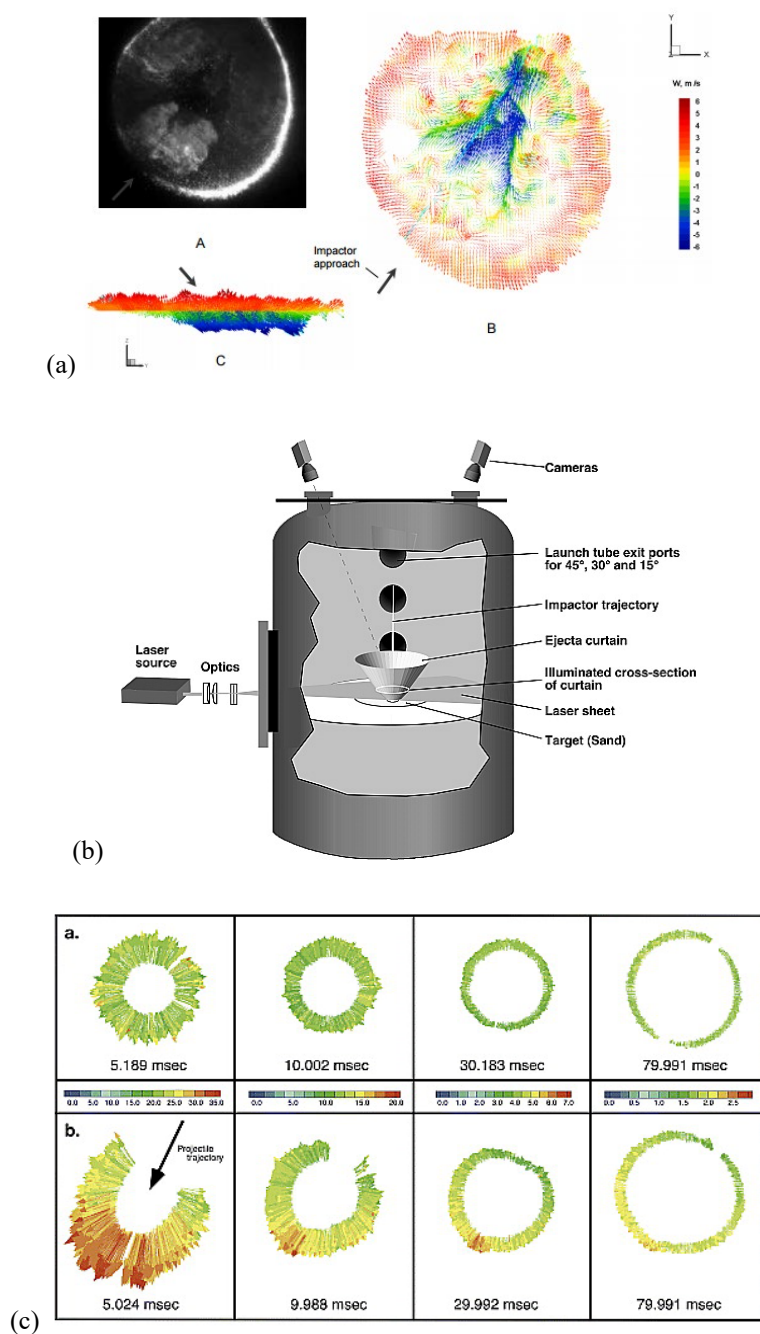


**Fig. 2.35** (a) Raw and processed images illustrating the penetration event and velocity vectors 1 ms after impact. The field of view is approximately 8 cm×10 cm and the impact velocity is 35 m/s (Borg, Morrissey et al. 2013), (b) Eulerian trajectories from t=1 ms to t=5 ms, 4000 fps and a spatial resolution of 1280×6960 pixels, where white rectangular is the exploded view of Eulerian trajectories below the cone tip and black rectangular is the exploded view of Eulerian trajectories along the cone shaft (Chen, Omidvar et al. 2014), (c) High-speed image of the target rear with interrogation area for 30 mm thick target and impact energy of 735 J. Vector field (blue arrows in the online version) contour from PIV measurements with projected ejecta vectors (red colour in the online version) (Hogan, Spray et al. 2014) and (d) PIV images of the first fragments ejection showing the displacement field during the rockburst process (Wang, Liu et al. 2015)

The NASA Ames Vertical Gun Range (AVGR) developed 3D-PIV to measure 3D ejecta particle positions and velocities. Several tests were conducted on sand in order to gain the understanding of gravity-controlled crater excavation (Anderson, Schultz et al. 2000, Schultz, Heineck et al. 2000). In 2002, 3D-PIV was successfully applied to the measurement of hypervelocity impact ejecta (Heineck et al. 2002), as shown in Fig. 2.36(a). In 2003, (Anderson, Schultz et al. 2003) presented a specific experiment in which ejection velocities, angles, and position were defined. The target was located on a platform within the large vacuum chamber. Fig. 2.36(a) shows the configuration of the 3D PIV setup. The projectile entered through one of several ports in the chamber (30° above horizontal in this sketch). The impact created an ejecta curtain that moves across the target surface as the crater grows. A horizontal laser sheet was projected into the vacuum chamber at a given height above the target surface. Two high-speed CCD cameras were located above the chamber to record the ring of illuminated ejecta particles. Some results are shown in Fig. 2.36(b), the vectors are three-dimensional and their lengths indicate magnitude of the velocity as projected onto the laser plane, the vector lengths are directly comparable between all eight images.



## CHAPTER 2 REVIEW OF HIGH-SPEED IMAGING AND DIGITAL OPTICAL FULL-FIELD MEASUREMENT TECHNIQUES FOR GEOMATERIALS



**Fig. 2.36(a)** Data for 45° impact: (A) Single raw image from set, (B) Top view of vector plot with each vector colour representing the vertical velocity component, and (C) Side view of same data set with vectors coloured similarly (Heineck, Schultz et al. 2002), **(b)** Schematic of the 3D PIV setup within the NASA Ames Vertical Gun Range facility and **(c)** Vector plots showing the velocities of particles within the laser plane as measured using 3D PIV (90° impacts in a, 30° impacts in b). The colour bars represent the measured velocities within the laser plane for each time step in (m/s) (Anderson, Schultz et al. 2003).

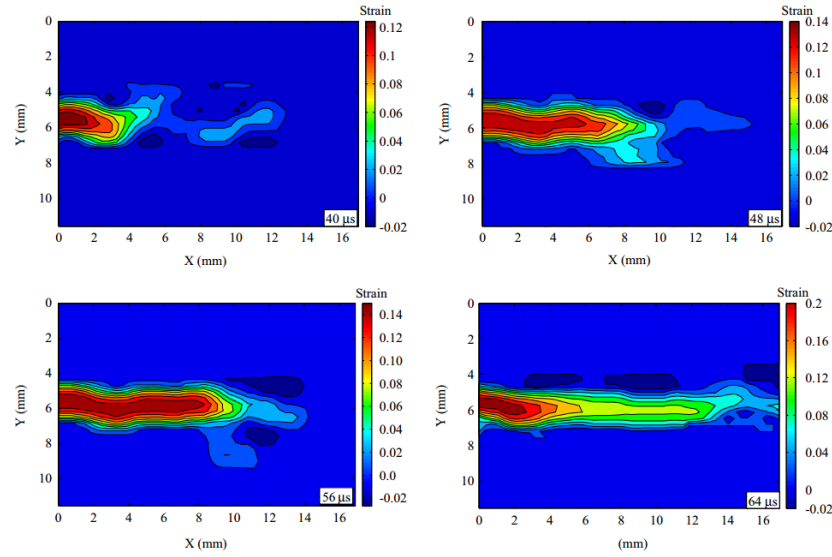


#### **2.4.6 Digital Image Correlation (DIC)**

DIC refers to the class of non-contacting methods that acquire images of an object, store images in digital form and perform image analysis to extract full-field shape, deformation and/or motion measurements (Sutton, Orteu et al. 2009). The early research was conducted in the 1980s by (Peters and Ranson 1982, Chu, Ranson et al. 1985, Sutton, Mingqi et al. 1986). Images can be obtained from various optical sources including macro scopes such as high-speed cameras, and microscopes, including scanning electron microscopes (McCormick and Lord 2010). The DIC technique can be applied not only to optical images but also to other datasets such as surface roughness maps and 2D surfaces of structures like tunnels. Basically, DIC techniques can be divided into 2D-DIC for in-plane deformation of nominal planar objects, 3D-DIC for surface 3D deformation of both planar and curved objects, and digital volume correlation (DVC) for internal full-field deformation of opaque solids or biological tissues. It should be mentioned that if the test object has a curved surface, or out-of-plane deformation occurs after loading, the 2D-DIC method is no longer applicable. The 3D-DIC was developed on the basis of the principle of binocular stereovision (Luo, Chao et al. 1993). The principle of DIC is to match the same pixel in two images (2D-DIC) or two image pairs recorded by two synchronized cameras (3D-DIC) recorded before and after deformation. The basic principle and theory of DIC are presented in Ref. (Sutton, Orteu et al. 2009), and a comprehensive review of DIC progress and applications can be found in Refs. (Pan, Qian et al. 2009, Pan 2011).

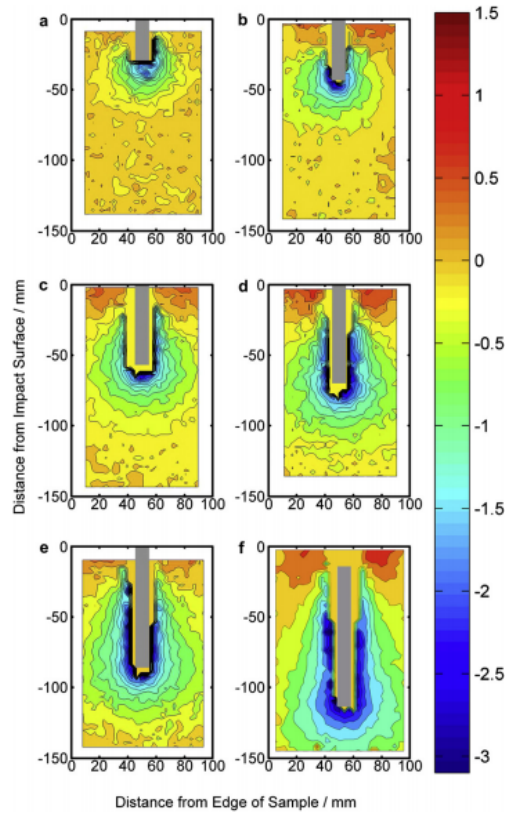
Typical use of high-speed 2D or 3D-DIC includes determination of the deformation field characterization of the deformation mechanism of various materials subjected to dynamic loading (Xiang, Zhang et al. 2007, Gilat, Schmidt et al. 2009, Koerber, Xavier et al. 2015) or vibration (Beberniss, Spottswood et al. 2011, Beberniss, Eason et al. 2012, Siebert and Crompton 2013), and identification of various dynamic parameters (e.g. fracture toughness) based on the computed displacement fields or strain fields (Garbowski, Gajewski et al. , Pierron, Sutton et al. 2011, Sanborn, Gunnarsson et al. 2014). Since the sensitivity is adjustable, the DIC method can be used across a variety of length scales from massive systems such as glaciers (Haug, Kääb et al. 2010) to micro- or nanoscale deformation (Berfield, Patel et al. 2007). One of difficult aspects of the application of the high-speed DIC

is purely photographic. In other words, how to guarantee the best quality images of the event can be recorded. Best quality means the best contrast with the minimal amount of noise (Reu and Miller 2008). With the constant emergence of high spatial resolution and high temporal resolution CMOS-based camera, the high-speed DIC method is promising optical measurement technology for dynamic experiments on geomaterials. A strain field of NSCB results is shown in Fig. 2.37.



**Fig. 2.37** Dynamic vertical strain fields of a NSCB specimen of Fangshan marble by DIC (Zhang and Zhao 2013)

High-speed X-ray photography processed by DIC has become more popular in recent years. This method gives detailed information on local displacements and internal displacements of opaque geomaterials without significantly disrupting or influencing the material behaviour. (Collins, Addiss et al. 2011) measured the internal flow fields in penetration of sand by long-rod projectiles with three different nose shapes at velocities up to 200 m/s as shown in Fig. 2.38. Impacts on concrete and gelatine were also performed to compare with sand. It was found that loose sand without confining responds in a noticeably different manner both to hydrodynamic materials and inhomogeneous solids. Therefore, sand cannot either be modelled as a fluid or as a conventional solid during ballistic penetration.

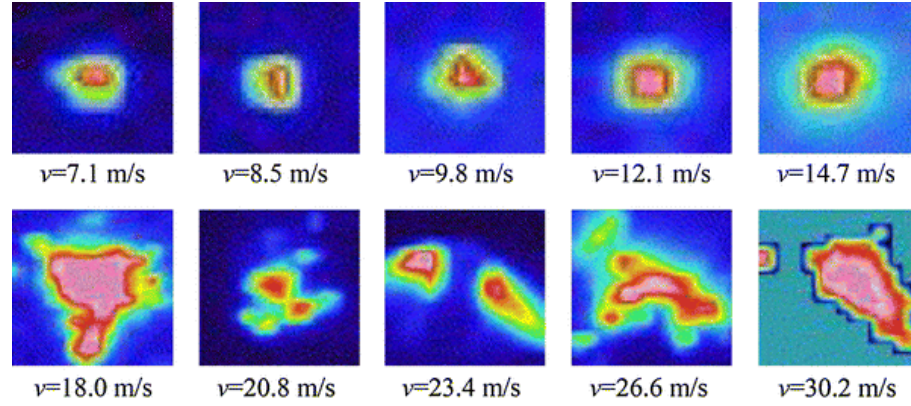


**Fig. 2.38** Contour plots of the longitudinal displacements (parallel to the projectile) for penetration of sand by flat-ended rod at 200 m/s. Colour bar denotes lateral displacement in mm. Time after impact: (a) 150 ms, (b) 250 ms, (c) 350 ms, (d) 450 ms, (e) 550 ms, and (f) 750 ms (Collins, Addiss et al. 2011).

#### 2.4.7 Infrared Thermography

Infrared radiation was discovered in 1790 by M. Pitke and rediscovered by Sir William Herschel in 1800 (Bramson 1968). Because the energy emitted by a body is mainly a function (Planck's law) of its surface temperature, IRT is considered as a means of 2D temperature

measurement (Meola and Carlomagno 2004). One of the applications is to measure temperature change in dynamic deformation and failure experiments (Moss and Pond 1975, Costin, Crisman et al. 1980, Hartley, Duffy et al. 1987, Marchand and Duffy 1988, Zehnder and Rosakis 1991, Zhou, Rosakis et al. 1996). It is noted that these studies were conducted on metallic materials, since these materials are expected to undergo higher temperature changes during high rate deformation (Crump, Dulieu-Barton et al. 2011). One of the hurdles of high-speed IRT development is that it can only be recorded by high-speed infrared cameras instead of standard high-speed cameras, and typical IR imaging systems can only run at television rates, 30 Hz. High frame rate IRT is limited to only a few groups which are equipped with bespoke detector systems capable of frame rates up to 1 MHz (Trojanowski, Macdougall et al. 1998, Zehnder, Guduru et al. 2000, Guduru, Rosakis et al. 2001). Recently, improvements in detector technology have led to the availability of commercial systems to acquire IR images at frame rates in the kHz range. This acquisition rate meets the requirements of studying the responses of a typical composite material at a strain rate of up to  $10^2 \text{ s}^{-1}$  (Fruehmann, Crump et al. 2013). Similar to normal digital high-speed cameras, the frame rate of high-speed infra camera is a compromise between three main parameters: the test duration, the thermal sensitivity and the number of detector elements (Fruehmann, Crump et al. 2011). The most advantages of IRT is no pre- or post-processing is needed because quantitative information in temperature is shown directly. Currently, this technique has not been widely applied in the research of rock dynamics due to the lack of adequate knowledge, high expense and difficulty in use (Meola and Carlomagno 2004). Fig. 2.39 shows transient target thermographs of a marble plate after impact at different impacting velocities (Shi, Wu et al. 2007). A thermal infrared imaging system, TVS-8100MKII, was used with a (theoretical) temperature sensitivity of  $0.025 \text{ }^\circ\text{C}$ , the fastest frame rate of 60 fps, and the spatial resolution of  $0.22 \text{ mm}^2$ . The geometric features and the radiant characteristics of the IRT in target region were extracted and regressively analysed against both the projectile's impacting velocity and kinetic energy. However, the accuracy of TIR measurements is influenced by many factors, for example, the calibration and evaluation of the emissivity of the target.



**Fig. 2.39** Transient target thermographs of marble plates impacted by SHPB at different impacting velocities (modified after (Shi, Wu et al. 2007))

## 2.5 CONCLUDING REMARKS

More than 130 years has passed since the birth of high-speed imaging technology (in 1878), and much progress has been made in the intervening years. High-speed imaging technology has been used for geomaterial research since the 1950s, and various imaging techniques have been applied in conjunction. For direct use of high-speed imaging in geomaterials, there is a need for high-speed colour cameras with long recording times and fast framing rates. Though introducing different grids of colour will increase the size of the data and decrease light sensitivity (As a colour filter array in front of the chip blocks approximately two-thirds of the incoming light), it offers the possibility to investigate the dynamic phenomena in geomaterials where different coloured grains are found. Another outlook for the direct use of high-speed cameras in geomaterial research is making comparative studies in an equivalent transparent material, such as the transparent soil mentioned in this review. Transparent soil and rock simulants generated by 3D printing (Jiang, Zhao et al. 2016) is another method which gives an excellent opportunity for high-speed cameras to record what happens inside a specimen. This method is in some ways more direct when compared to acoustic emission detection and is easier in terms of experimental setup than real-time X-Ray computed tomography. The persuasiveness of direct observation will open new perspectives of research in geomechanics.

For optical methods in combination with high-speed imaging, photoelastic coating, Moiré, HI, caustics, PIV, DIC and IRT for geomaterials were reviewed. Advantages and disadvantages of each optical method were discussed. In summary, these combined methods

## CHAPTER 2 REVIEW OF HIGH-SPEED IMAGING AND DIGITAL OPTICAL FULL-FIELD MEASUREMENT TECHNIQUES FOR GEOMATERIALS

are designed to obtain the wave propagation or stress/strain field at a certain moment. Due to the historic unavailability of the electronic camera and computer technology, photoelastic coatings, Moiré, HI and caustics played an important role in studies on geomaterial mechanics in the early days. However, just as film-based high-speed cameras have been replaced by digital high-speed cameras, the traditional optical methods have been replaced by digital processing methods like DIC and PIV. Another reason is that the principles of traditional optical methods such as photoelastic coating, Moiré, and HI, caustics are developed for transparent materials. To achieve good results, most experiments to investigate rock properties were conducted on transparent materials such as PMMA, epoxy or polyester which have similar fracturing properties to rocks. However, as the composition is different, it is only possible to make inferences about the behaviour in geomaterials, and the underlying physical mechanisms are generally not explained. With regard to DIC and PIV, a collection of recent literature was reviewed. The DIC and PIV methods are likely to be dominant for high-speed quantitative measurement in geomaterials for the foreseeable future. However, few papers have been dedicated to high-speed 3D-DIC. However, high-speed 3D-DIC inherits advantages from both DIC and stereovision, which is an outstanding method to study the fast full-field out-of-plane displacement. A further innovation in DIC is to analyse images obtained by high-speed synchrotron X-ray phase-contrast imaging (Parab, Guo et al. 2017). The various DIC methods can be divided into types according to different algorithms. One is to analyse the strain field in microscopic images ( $\mu$ DIC) by using the traditional continuum DIC method (Huang, Lu et al. 2016). The digital volume correlation (DVC) introduced by (Bay, Smith et al. 1999) has the ability to describe the individual particle movement by meshing the specimen into the same size. In this method, the rotational degrees of freedom of particles can be taken into consideration. This latter technique has been widely applied in mechanical research such as wood bending (Forsberg, Mooser et al. 2008), human bone (Zaue, Yeni et al. 2006) and Argillaceous rock (Lenoir, Bornert et al. 2007). The final DIC method is the discrete DIC method which reconstructs the particle with the original shape and size, meaning particles have no longer to be in contact, and large discontinuous deformation (fracture) can be defined in the DIC result (Nguyen, Hall et al. 2011). In high loading rate tests on geomaterials, the ability to measure particle movement and fracture propagation during failure can lead to a greater understanding of the micromechanics of

## CHAPTER 2 REVIEW OF HIGH-SPEED IMAGING AND DIGITAL OPTICAL FULL-FIELD MEASUREMENT TECHNIQUES FOR GEOMATERIALS

failure in rock, soil and concrete etc. Moreover, validation of finite element method (FEM) or theoretical analyses and the bridge between experiment, simulation and theory (e.g., the Virtual Fields Method (Pierron and Grédiac 2012)) has made extraordinary progress (Hild and Roux 2006, Avril, Bonnet et al. 2008).

It could be seen from the literature review that some research gaps still remain to be filled in the study of dynamic behaviour of rock with full-field and high-speed photography.

1. As the properties of high stiffness, brittleness and heterogeneity in most geomaterials, the displacement of rock under high-strain rate loading exhibits a relatively small deformation, posing challenges to the resolutions of high-speed cameras. Therefore, the 2D-DIC results in the previous study are neither in a high accuracy nor sufficient number of images. On the other hand, high-speed 3D-DIC technique has seldomly been implemented on the rock dynamics to investigate the 3D dynamic rock deformation problems.
2. Previously, the high-speed photography and digital optical measurements were mainly used to identify the crack development. The other dynamic deformation properties such as Young's modulus, Poisson's ratio and stress threshold of crack initiation are not directly measured.
3. As a direct and non-destructive measurement, the comparison of rock dynamic behaviour obtained between high-speed photography and other measurements (i.e. strain gauge) are rarely assessed.
4. The traditional application of high-speed and full-field measurement focusing on the rock dynamics under normal environment. The effect from intrinsic properties, such as rock type and grain size; the external effect, such as thermal and CO<sub>2</sub> treatment, on the rock dynamic behavior was not characterized with high-speed photography and digital optical measurement.
5. In the previous study on rock penetration, the high-speed photography mainly used to track the trajectory of projectile. The real-time damage process of rock target has not been well identified by full-field measurement.

## CHAPTER 2 REVIEW OF HIGH-SPEED IMAGING AND DIGITAL OPTICAL FULL-FIELD MEASUREMENT TECHNIQUES FOR GEOMATERIALS

### REFERENCES

- Adrian RJ (1991) Particle-imaging techniques for experimental fluid mechanics Annual Review of Fluid Mechanics 23:261-304
- Allen WA, Mayfield EB, Morrison HL (1957) Dynamics of a Projectile Penetrating Sand Journal of Applied Physics 28:370-376 doi:10.1063/1.1722750
- Amidror I, Amidror I, Amidror I, Amidror I (2000) The theory of the moiré phenomenon vol 38. vol LSP-BOOK-2000-001. Springer, Boston. doi:10.1007/978-1-84882-181-1
- Anastasi RF (1992) An Introduction to Moire Methods with Applications in Composite Materials. Army lab command watertown ma material technology lab,
- Anderson J, Schultz P, Heineck J (2000) A new view of ejecta curtains during oblique impacts using 3D particle imaging velocimetry. Paper presented at the Lunar and planetary science and exploration, Washington,
- Anderson JL, Schultz PH, Heineck JT (2003) Asymmetry of ejecta flow during oblique impacts using three - dimensional particle image velocimetry Journal of Geophysical Research: Planets 108
- Arakawa K, Drinnon Jr R, Kosai M, Kobayashi A (1991) Dynamic fracture analysis by moiré interferometry Experimental Mechanics 31:306-309 doi:10.1007/BF02325986
- Arbiter N, Harris C, Stamboltzis G (1969) Single fracture of brittle spheres Trans AIME 244:118-133
- Avril S et al. (2008) Overview of identification methods of mechanical parameters based on full-field measurements Experimental Mechanics 48:381-402 doi:10.1007/s11340-008-9148-y
- Ayatollahi M, Torabi A, Firoozabadi M (2015) Theoretical and experimental investigation of brittle fracture in V-notched PMMA specimens under compressive loading Engineering Fracture Mechanics 135:187-205 doi:10.1016/j.engfracmech.2015.01.005
- Bagnold RA (1941) The physics of wind blown sand and desert dunes Methuen, London 265
- Bagnold RA (2012) The physics of blown sand and desert dunes. Courier Corporation, New York. doi:10.1007/978-94-009-5682-7
- Bay BK, Smith TS, Fyhrie DP, Saad M (1999) Digital volume correlation: three-dimensional strain mapping using X-ray tomography Experimental Mechanics 39:217-226 doi:10.1007/BF02323555
- Bebniss T, Eason T, Spottswood S High-speed 3D digital image correlation measurements of long-duration random vibration; recent advancements and noted limitations. In: Proceedings, International Conference on Noise and Vibration Engineering (ISMA), Katholieke Universiteit Leuven, Belgium, 2012.
- Bebniss T, Spottswood M, Eason T (2011) High-speed digital image correlation measurements of random nonlinear dynamic response. In: Experimental and Applied Mechanics, Volume 6. Springer, pp 171-186. doi:10.1007/978-1-4614-0222-0\_22



## CHAPTER 2 REVIEW OF HIGH-SPEED IMAGING AND DIGITAL OPTICAL FULL-FIELD MEASUREMENT TECHNIQUES FOR GEOMATERIALS

- Berfield T, Patel J, Shimmin R, Braun P, Lambros J, Sottos N (2007) Micro-and nanoscale deformation measurement of surface and internal planes via digital image correlation *Experimental Mechanics* 47:51-62 doi:10.1007/s11340-006-0531-2
- Bieniawski ZT Mechanism of brittle fracture of rock: part I—theory of the fracture process. In: *International Journal of Rock Mechanics and Mining Sciences & Geomechanics Abstracts*, 1967a. vol 4. Elsevier, pp 395IN11405-11404IN12406. doi:10.1016/0148-9062(67)90030-7
- Bieniawski ZT (1967b) Mechanism of brittle fracture of rock: Part II—experimental studies *International Journal of Rock Mechanics and Mining Sciences & Geomechanics Abstracts* 4:407-423 doi:10.1016/0148-9062(67)90031-9
- Bieniawski ZT (1968) Fracture dynamics of rock *Int J Fract* 4:415-430 doi:10.1007/bf00186807
- Blair BE (1960) Use of high-speed camera in blasting studies vol 5584. US Dept. of the Interior, Bureau of Mines, USA
- Borg J, Morrissey M, Perich C, Vogler T, Chhabildas L (2013) In situ velocity and stress characterization of a projectile penetrating a sand target: experimental measurements and continuum simulations *International Journal of Impact Engineering* 51:23-35
- Borvik T, Gjørsvik OE, Langseth M (2007) Ballistic perforation resistance of high-strength concrete slabs *CONCRETE INTERNATIONAL-DETROIT*- 29:45
- Bourne N (2013) *Materials in mechanical extremes: Fundamentals and applications*. Cambridge University Press, Cambridge
- Bowden F, McOnie M Formation of cavities and microjets in liquids and their role in initiation and growth of explosion. In: *Proceedings of the Royal Society of London A: Mathematical, Physical and Engineering Sciences*, 1967. vol 1452. The Royal Society, pp 38-50
- Boys C (1892) On Electric Spark Photography; or, Photography of Flying Bullets, and so on, by the Light of the Electric Spark *Nature* 3:415
- Braithwaite C (2009) *High strain rate properties of geological materials*. University of Cambridge
- Brajer X, Forquin P, Gy R, Hild F (2003) The role of surface and volume defects in the fracture of glass under quasi-static and dynamic loadings *Journal of non-crystalline solids* 316:42-53 doi:10.1016/S0022-3093(02)01936-1
- Bramson MA (1968) *Infrared radiation. A handbook for applications* *Optical Physics and Engineering*, New York: Plenum Press, 1968 1
- Brara A, Camborde F, Klepaczko J, Mariotti C (2001) Experimental and numerical study of concrete at high strain rates in tension *Mechanics of materials* 33:33-45 doi:10.1016/S0167-6636(00)00035-1
- Brara A, Klepaczko JR (2006) Experimental characterization of concrete in dynamic tension *Mechanics of Materials* 38:253-267 doi:DOI: 10.1016/j.mechmat.2005.06.004
- Braslau D (1970) Partitioning of energy in hypervelocity impact against loose sand targets *Journal of Geophysical Research* 75:3987-3999 doi:10.1029/JB075i020p03987

## CHAPTER 2 REVIEW OF HIGH-SPEED IMAGING AND DIGITAL OPTICAL FULL-FIELD MEASUREMENT TECHNIQUES FOR GEOMATERIALS

- Brewster D (1815) Experiments on the depolarisation of light as exhibited by various mineral, animal, and vegetable bodies, with a reference of the phenomena to the general principles of polarisation Philosophical Transactions of the Royal Society of London 105:29-53
- Brewster D (1816) On the communication of the structure of doubly refracting crystals to glass, muriate of soda, fluor spar, and other substances, by mechanical compression and dilatation Philosophical Transactions of the Royal Society of London 106:156-178
- Cai M, Kaiser P, Suorineni F, Su K (2007) A study on the dynamic behavior of the Meuse/Haute-Marne argillite Physics and Chemistry of the Earth, Parts A/B/C 32:907-916
- Caverzan A, Peroni M, Solomos G (2016) Compressive behaviour of dam concrete at higher strain rates The European Physical Journal Special Topics:1-11 doi:10.1140/epjst/e2016-02628-5
- Chen J, Guo B, Liu H, Liu H, Chen P (2014a) Dynamic Brazilian Test of Brittle Materials Using the Split Hopkinson Pressure Bar and Digital Image Correlation Strain 50:563-570 doi:10.1111/str.12118
- Chen R, Xia K, Dai F, Lu F, Luo S (2009) Determination of dynamic fracture parameters using a semi-circular bend technique in split Hopkinson pressure bar testing Engineering Fracture Mechanics 76:1268-1276 doi:10.1016/j.engfracmech.2009.02.001
- Chen Z, Omidvar M, Iskander M, Bless S (2014b) Modelling of projectile penetration using transparent soils International Journal of Physical Modelling in Geotechnics 14:68-79
- Chia Y, Tong J, Tou C (1984) A study of dynamic holographic photoelasticity using ruby laser Canadian Society for Mechanical Engineering, Transactions 8:117-120
- Chin CT et al. (2003) Brandaris 128: A digital 25 million frames per second camera with 128 highly sensitive frames Review of scientific instruments 74:5026-5034
- Cho SH, Ogata Y, Kaneko K (2003) Strain-rate dependency of the dynamic tensile strength of rock International Journal of Rock Mechanics and Mining Sciences 40:763-777
- Chu T, Ranson W, Sutton M (1985) Applications of digital-image-correlation techniques to experimental mechanics Experimental mechanics 25:232-244 doi:10.1007/BF02325092
- Cintala MJ, Berthoud L, Hörz F (1999) Ejection - velocity distributions from impacts into coarse - grained sand Meteoritics & Planetary Science 34:605-623 doi:10.1111/j.1945-5100.1999.tb01367.x
- Cole RP (2010) Ballistic penetration of a sandbagged redoubt using silica sand and pulverized rubber of various grain sizes. University of South Florida
- Coleman KR, The photography of high temperature events. In: Proc. 4th Int. Kongress Kurzzeitphotographie, 1959. pp 32-39
- Collins A, Addiss J, Walley S, Promratana K, Bobaru F, Proud W, Williamson D (2011) The effect of rod nose shape on the internal flow fields during the ballistic penetration of sand International Journal of Impact Engineering 38:951-963
- Costin L, Crisman E, Hawley R, Duffy J On the localisation of plastic flow in mild steel tubes under dynamic torsional loading. In: Proc. 2 nd Conf. Mechanical Properties of Materials at High Rates of Strain, Oxford, England, Mar. 1979, 1980. pp 90-100

## CHAPTER 2 REVIEW OF HIGH-SPEED IMAGING AND DIGITAL OPTICAL FULL-FIELD MEASUREMENT TECHNIQUES FOR GEOMATERIALS

- Courtney-Pratt J (1973) Advances in High-Speed Photography 1957–1972. In, vol 82. vol 108. Springer Netherlands, pp 595-607. doi:10.1007/978-94-017-0445-8\_21
- Courtney-Pratt J (1986) Advances in High-Speed Photography: 1972–1982. In: Fast Electrical and Optical Measurements. Springer, pp 595-607. doi:10.1007/978-94-017-0445-8\_21
- Courtney-Pratt JS (1949) Photography of Fast Transients. Interferometric Study of Surfaces. University of Cambridge
- Cranz C, Schardin H (1929) Kinematographie auf ruhendem Film und mit extrem hoher Bildfrequenz Zeitschrift für Physik 56:147-183
- Crump D, Dulieu-Barton J, Fruehmann R (2011) Challenges in synchronising high speed full-field temperature and strain measurement. In: Thermomechanics and Infra-Red Imaging, Volume 7. Springer, pp 1-7. doi:10.1007/978-1-4614-0207-7\_1
- Culp FL, Hooper HL (1961) Study of Impact Cratering in Sand Journal of Applied Physics 32:2480-2484 doi:10.1063/1.1777095
- Daehnke A Stress wave and fracture propagation in rock. In: 9th ISRM Congress, 1999. International Society for Rock Mechanics,
- Dai F, Chen R, Xia K (2010) A semi-circular bend technique for determining dynamic fracture toughness Experimental Mechanics 50:783-791 doi:10.1007/s11340-009-9273-2
- Daniel I, Rowlands RE (1975) On wave and fracture propagation in rock media Experimental Mechanics 15:449-457 doi:10.1007/BF02318359
- De Ploey J, Savat J (1968) Contribution a l'étude de l'érosion par le splash Zeitschrift für Geomorphologie 12:174-193
- Dear J, Field J (1988) High - speed photography of surface geometry effects in liquid/solid impact Journal of Applied Physics 63:1015-1021 doi:10.1063/1.340000
- Denoual C, Cottenot CE (1998) Visualization of the damage evolution in impacted silicon carbide ceramics International journal of impact engineering 21:225-235 doi:10.1016/S0734-743X(97)00018-3
- Draxler VC (2005) High-Speed Diagnostics for Ballistics and Explosive Studies. In: High-Pressure Shock Compression of Solids VIII. Springer, pp 227-249. doi:10.1007/3-540-27168-6\_6
- Eastman G (1888) Camera, Patent US 388850 A. American Patent,
- Edgerton HE, Killian JR (1954) Flash!: Seeing the unseen by ultra high-speed photography. CT Branford Co., Massachusetts
- Einstein HH, Meyer T Müller lecture: puzzles in rock. In: 9th ISRM Congress, 1999. International Society for Rock Mechanics,
- Ellison W (1944) Studies of raindrop erosion Agricultural Engineering 25:131-136
- Epstein J, Dadkhah M (1993) Moire interferometry in fracture research Experimental Techniques in Fracture:427-508

## CHAPTER 2 REVIEW OF HIGH-SPEED IMAGING AND DIGITAL OPTICAL FULL-FIELD MEASUREMENT TECHNIQUES FOR GEOMATERIALS

- Fercher AF, Drexler W, Hitzenberger CK, Lasser T (2003) Optical coherence tomography-principles and applications Reports on progress in physics 66:239 doi:10.1088/0034-4885/66/2/204
- Field J, Proud W, Walley S (2009) Review of optical and X-ray techniques used at the Cavendish Laboratory The Imaging Science Journal 57:317-325
- Field J, Walley S, Proud W, Goldrein H, Siviour C (2004) Review of experimental techniques for high rate deformation and shock studies International Journal of Impact Engineering 30:725-775
- Fookes P (1991) Geomaterials Quarterly Journal of Engineering Geology and Hydrogeology 24:3-15
- Forquin P (2017) Brittle materials at high-loading rates: an open area of research Philosophical Transactions of the Royal Society A: Mathematical, Physical and Engineering Sciences 375 doi:10.1098/rsta.2016.0436
- Forsberg F, Mooser R, Arnold M, Hack E, Wyss P (2008) 3D micro-scale deformations of wood in bending: synchrotron radiation  $\mu$ CT data analyzed with digital volume correlation Journal of structural biology 164:255-262 doi:10.1016/j.jsb.2008.08.004
- Foster M, Love B, Kaste R, Moy P (2015) The rate dependent tensile response of polycarbonate and poly-methylmethacrylate Journal of Dynamic Behavior of Materials 1:162-175 doi:10.1007/s40870-015-0020-8
- Fourmeau M, Gomon D, Vacher R, Hokka M, Kane A, Kuokkala V-T (2014) Application of DIC technique for studies of Kuru Granite rock under static and dynamic loading Procedia Materials Science 3:691-697 doi:10.1016/j.mspro.2014.06.114
- Fourney W, Dally J, Holloway D (1976) Attenuation of strain waves in core samples of three types of rock Experimental Mechanics 16:121-126
- Fourney W, Holloway D, Dally J (1975) Fracture initiation and propagation from a center of dilatation International Journal of Fracture 11:1011-1029
- Fowler A, Scheu B, Lee W, McGuinness M A theoretical model of the explosive fragmentation of vesicular magma. In: Proceedings of the Royal Society of London A: Mathematical, Physical and Engineering Sciences, 2009. The Royal Society, p rspa20090382
- Fruehmann R, Crump D, Dulieu-Barton J (2011) The use of infrared thermography at high frame rates. In: Thermomechanics and Infra-Red Imaging, Volume 7. Springer, pp 9-15. doi:10.1007/978-1-4614-0207-7\_2
- Fruehmann R, Crump D, Dulieu-Barton J (2013) Characterization of an infrared detector for high frame rate thermography Measurement Science and Technology 24:105403
- Fuller PW (2005) Some highlights in the history of high-speed photography and photonics as applied to ballistics. In: High-Pressure Shock Compression of Solids VIII. Springer, pp 251-298. doi:10.1007/3-540-27168-6\_7
- Fuller PWW (1994) Aspects of high speed photography The Journal of Photographic Science 42:42-43

## CHAPTER 2 REVIEW OF HIGH-SPEED IMAGING AND DIGITAL OPTICAL FULL-FIELD MEASUREMENT TECHNIQUES FOR GEOMATERIALS

- Furbish DJ, Hamner KK, Schmeeckle M, Borosund MN, Mudd SM (2007) Rain splash of dry sand revealed by high - speed imaging and sticky paper splash targets *Journal of Geophysical Research: Earth Surface* 112 doi:10.1029/2006JF000498
- Gao G, Huang S, Xia K, Li Z (2015) Application of digital image correlation (DIC) in dynamic notched semi-circular bend (NSCB) tests *Experimental Mechanics* 55:95-104 doi:10.1007/s11340-014-9863-5
- Garbowski T, Gajewski T, Łodygowski T Identification of rate dependent material model parameters based on Split Hopkinson Pressure Bar test and high speed camera with Digital Image Correlation
- Gault DE, Moore HJ, Shoemaker EM (1963) Spray ejected from the lunar surface by meteoroid impact. National aeronautics and space administration,
- Giachetti A (2000) Matching techniques to compute image motion *Image and Vision Computing* 18:247-260 doi:10.1016/S0262-8856(99)00018-9
- Gilat A, Schmidt T, Walker A (2009) Full field strain measurement in compression and tensile split Hopkinson bar experiments *Experimental Mechanics* 49:291-302 doi:10.1007/s11340-008-9157-x
- Glenn L, Jaun H (1978) Crack propagation in rock plates loaded by projectile impact *Experimental Mechanics* 18:35-40
- Gong M, Jia J-p, Wang D-s (2005) A Review of Studies on the Blasting Model by Dynamic Photomechanics [J] *Blasting* 22:7-12
- Grady D, Benson D (1983) Fragmentation of metal rings by electromagnetic loading *Experimental Mechanics* 23:393-400
- Grady D, Kipp M The micromechanics of impact fracture of rock. In: *International Journal of Rock Mechanics and Mining Sciences & Geomechanics Abstracts*, 1979. vol 5. Elsevier, pp 293-302. doi:10.1016/0148-9062(79)90240-7
- Grange S, Forquin P, Mencacci S, Hild F (2008) On the dynamic fragmentation of two limestones using edge-on impact tests *International Journal of Impact Engineering* 35:977-991 doi:10.1016/j.ijimpeng.2007.07.006
- Grattan KT, Meggitt B (1995) *Optical fiber sensor technology* vol 1. vol 3. Springer, London. doi:10.1007/978-1-4757-6077-4
- Greated C, Skyner D, Bruce T Particle image velocimetry (PIV) in the coastal engineering laboratory. In: *Coastal Engineering Conference*, 1992. ASCE pp 212-212. doi:10.1061/9780872629332.016
- Guduru P, Rosakis A, Ravichandran G (2001) Dynamic shear bands: an investigation using high speed optical and infrared diagnostics *Mechanics of Materials* 33:371-402 doi:10.1016/S0167-6636(01)00051-5
- Guzman IL, Iskander M, Bless S (2015) Observations of projectile penetration into a transparent soil *Mechanics Research Communications* 70:4-11

## CHAPTER 2 REVIEW OF HIGH-SPEED IMAGING AND DIGITAL OPTICAL FULL-FIELD MEASUREMENT TECHNIQUES FOR GEOMATERIALS

- Hall J, Barigou M, Simmons M, Stitt E (2005) A PIV study of hydrodynamics in gas–liquid high throughput experimentation (HTE) reactors with eccentric impeller configurations *Chemical engineering science* 60:6403-6413 doi:10.1016/j.ces.2005.03.044
- Hariharan P, Oreb BF (1986) Stroboscopic holographic interferometry: application of digital techniques *Optics Communications* 59:83-86
- Hartley K, Duffy J, Hawley R (1987) Measurement of the temperature profile during shear band formation in steels deforming at high strain rates *Journal of the Mechanics and Physics of Solids* 35:283-301 doi:10.1016/0022-5096(87)90009-3
- Haug T, Kääb A, Skvarca P (2010) Monitoring ice shelf velocities from repeat MODIS and Landsat data—a method study on the Larsen C ice shelf, Antarctic Peninsula, and 10 other ice shelves around Antarctica *The Cryosphere* 4:161-178 doi:10.5194/tc-4-161-2010
- Heineck J, Schultz P, Anderson J (2002) Application of three-component PIV to the measurement of hypervelocity impact ejecta *Journal of visualization* 5:233-241
- Hertegård S, Larsson H, Wittenberg T (2003) High-speed imaging: applications and development *Logopedics Phoniatrics Vocology* 28:133-139 doi:10.1080/14015430310015246
- Hild F, Roux S (2006) Digital image correlation: from displacement measurement to identification of elastic properties—a review *Strain* 42:69-80 doi:10.1111/j.1475-1305.2006.00258.x
- Hino K (1956) Velocity of rock fragments and shape of shock wave *Journal of the industrial explosives society, Japan* 17:2-36
- Hogan J, Spray J, Rogers R, Vincent G, Schneider M (2014) Impact Failure of Planetary Materials *Experimental Mechanics* 54:665-675
- Hogan JD, Spray JG, Rogers RJ, Vincent G, Schneider M (2013a) Dynamic fragmentation of natural ceramic tiles: ejecta measurements and kinetic consequences *International Journal of Impact Engineering* 58:1-16
- Hogan JD, Spray JG, Rogers RJ, Vincent G, Schneider M (2013b) Dynamic fragmentation of planetary materials: ejecta length quantification and semi-analytical modelling *International Journal of Impact Engineering* 62:219-228
- Holloway D, Patacca A, Fourney W Application of holographic interferometry to a study of wave propagation in rock: *Exp mech*, V17, N8, Aug 1977, P314–384. In: *International Journal of Rock Mechanics and Mining Sciences & Geomechanics Abstracts*, 1978. vol 2. Pergamon, p A28. doi:10.1016/0148-9062(78)91719-9
- Hornemann U, Rothenhausler H, Senf H, Kalthoff J, Winkler S Experimental investigation of wave and fracture propagation in glass slabs loaded by steel cylinders at high-impact velocities. In: *Institute of Physics Conference Series*, 1984. vol 70. PLENUM PUBL CORP 233 SPRING ST, NEW YORK, NY 10013, pp 291-298
- Hu G, Ramesh K, Cao B, McCauley J (2011) The compressive failure of aluminum nitride considered as a model advanced ceramic *Journal of the Mechanics and Physics of Solids* 59:1076-1093 doi:10.1016/j.jmps.2011.02.003

## CHAPTER 2 REVIEW OF HIGH-SPEED IMAGING AND DIGITAL OPTICAL FULL-FIELD MEASUREMENT TECHNIQUES FOR GEOMATERIALS

- Huang J et al. (2016) Heterogeneity in deformation of granular ceramics under dynamic loading *Scripta Materialia* 111:114-118 doi:10.1016/j.scriptamat.2015.08.028
- Huang S, Luo S, Xia K Dynamic fracture initiation toughness and propagation toughness of PMMA. In: Proceedings of the SEM annual conference, Albuquerque, 2009. pp 1-4
- Huntley J, Field J (1989) High resolution moiré photography: application to dynamic stress analysis *Optical Engineering* 28:288926-288926- doi:10.1117/12.7977058
- Huston A (1978) High-speed photography and photonic recording *Journal of Physics E: Scientific Instruments* 11:601 doi:10.1088/0022-3735
- Ifju PG, Masters JE, Jackson WC (1995) The use of moiré interferometry as an aid to standard test-method development for textile composite materials *Composites science and technology* 53:155-163 doi:10.1016/0266-3538(95)00014-3
- Ilstad T, Elverhøi A, Issler D, Marr JG (2004a) Subaqueous debris flow behaviour and its dependence on the sand/clay ratio: a laboratory study using particle tracking *Marine Geology* 213:415-438
- Ilstad T, Marr JG, Elverhøi A, Harbitz CB (2004b) Laboratory studies of subaqueous debris flows by measurements of pore-fluid pressure and total stress *Marine Geology* 213:403-414 doi:10.1016/j.margeo.2004.10.016
- Islam MT, Bindiganavile V (2012) Stress rate sensitivity of Paskapoo sandstone under flexure *Canadian Journal of Civil Engineering* 39:1184-1192 doi:10.1139/l2012-101
- ISRM (1978) Suggested methods for determining tensile strength of rock materials *International Journal of Rock Mechanics and Mining Sciences* 15:99-103 doi:10.1016/0148-9062(78)90003-7
- Jacquot P (2008) Speckle interferometry: a review of the principal methods in use for experimental mechanics applications *Strain* 44:57-69 doi:10.1111/j.1475-1305.2008.00372.x
- Jiang C, Dong Z, Zhang Z (2015) Measurement of the movement parameters of saltating sand over a flat sand bed using a high-speed digital camera *Environmental Earth Sciences* 74:4865-4874
- Jiang C, Zhao G-F, Zhu J, Zhao Y-X, Shen L (2016) Investigation of Dynamic Crack Coalescence Using a Gypsum-Like 3D Printing Material *Rock Mechanics and Rock Engineering* 49:3983-3998 doi:10.1007/s00603-016-0967-3
- Jung W, Utagawa M, Ogata Y, Seto M, Katsuyama K, Miyake A, Ogawa T (2001) Effects of rock pressure on crack generation during tunnel blasting *Kayaku Gakkaishi/Journal of the Japan Explosives Society* 62:138-146
- Kimberley J, Ramesh K (2011) The dynamic strength of an ordinary chondrite *Meteoritics & Planetary Science* 46:1653-1669 doi:10.1111/j.1945-5100.2011.01254.x
- Kirk S (2014) Shock compression and dynamic fragmentation of geological materials. University of Cambridge
- Kiser T, Eigensatz M, Nguyen MM, Bompas P, Pauly M (2013) Architectural caustics—Controlling light with geometry. Springer, London. doi:10.1007/978-3-7091-1251-9\_7

## CHAPTER 2 REVIEW OF HIGH-SPEED IMAGING AND DIGITAL OPTICAL FULL-FIELD MEASUREMENT TECHNIQUES FOR GEOMATERIALS

- Klepaczko J, Brara A (2001) An experimental method for dynamic tensile testing of concrete by spalling *International Journal of Impact Engineering* 25:387-409
- Knauss W, Babcock C, Chai H (1980) Visualization of Impact Damage of Composite Plates by Means of the Moire Technique. DTIC Document,
- Koerber H, Xavier J, Camanho P, Essa Y, de la Escalera FM (2015) High strain rate behaviour of 5-harness-satin weave fabric carbon–epoxy composite under compression and combined compression–shear loading *International Journal of Solids and Structures* 54:172-182 doi:10.1016/j.ijsolstr.2014.10.018
- Koschatzky V, Moore P, Westerweel J, Scarano F, Boersma B (2011) High speed PIV applied to aerodynamic noise investigation *Experiments in fluids* 50:863-876 doi:10.1007/s00348-010-0935-8
- Kubota S, Ogata Y, Wada Y, Simangunsong G, Shimada H, Matsui K (2008) Estimation of dynamic tensile strength of sandstone *International Journal of Rock Mechanics and Mining Sciences* 45:397-406 doi:10.1016/j.ijrmms.2007.07.003
- Kutter H, Fairhurst C On the fracture process in blasting. In: *International Journal of Rock Mechanics and Mining Sciences & Geomechanics Abstracts*, 1971. vol 3. Elsevier, pp 181-202
- Lagarde A (2014) Static and dynamic photoelasticity and caustics: recent developments vol 290. Springer,
- Lasers for High Speed Imaging. <http://www.oxfordlasers.com/imaging/high-speed-imaging/>.
- Lauterborn W, Hentschel W (1985) Cavitation bubble dynamics studied by high speed photography and holography: part one *Ultrasonics* 23:260-268 doi:10.1016/0041-624X(85)90048-4
- Leith EN, Upatnieks J (1963) Wavefront Reconstruction with Continuous-Tone Objects\* *JOSA* 53:1377-1381
- Lenoir N, Bornert M, Desrues J, Bésuelle P, Viggiani G (2007) Volumetric digital image correlation applied to X - ray microtomography images from triaxial compression tests on argillaceous rock *Strain* 43:193-205 doi:10.1111/j.1475-1305.2007.00348.x
- Levy S, Molinari J-F (2010) Dynamic fragmentation of ceramics, signature of defects and scaling of fragment sizes *Journal of the Mechanics and Physics of Solids* 58:12-26 doi:10.1016/j.jmps.2009.09.002
- Li D, Wong LNY (2013) The Brazilian disc test for rock mechanics applications: review and new insights *Rock Mechanics and Rock Engineering* 46:269-287
- Li q, Yang R, Li J, Qiao C, Zhao Y, Ma Y (2005) Experimental study on propagation of dynamic cracks under blasting loading *Chinese Journal of Rock Mechanics and Engineering* 16:019
- Li X, Xie H, Kang Y, Wu X (2010) A brief review and prospect of experimental solid mechanics in China *Acta Mechanica Solida Sinica* 23:498-548 doi:10.1016/S0894-9166(11)60003-7
- Li Y, Yang Y, Yang R (1999) Study on effect of blasting in rock by laser holography *Journal of China University of Mining and Technology* 28:322-325



## CHAPTER 2 REVIEW OF HIGH-SPEED IMAGING AND DIGITAL OPTICAL FULL-FIELD MEASUREMENT TECHNIQUES FOR GEOMATERIALS

- Lima R et al. (2008) In vitro blood flow in a rectangular PDMS microchannel: experimental observations using a confocal micro-PIV system *Biomedical microdevices* 10:153-167
- Lindholm U (1964) Some experiments with the split hopkinson pressure bar *Journal of the Mechanics and Physics of Solids* 12:317-335 doi:10.1016/0022-5096(64)90028-6
- Litwiller D (2001) CMOS vs. CCD: Facts and fiction,” *Photonics Spectra*, Jan
- Locat J, Lee HJ (2005) Subaqueous debris flows. In: *Debris-flow Hazards and Related Phenomena*. Springer, pp 203-245
- Lohse D et al. (2004) Impact on soft sand: void collapse and jet formation *Physical review letters* 93:198003
- Lu H, Cary P (2000) Deformation measurements by digital image correlation: implementation of a second-order displacement gradient *Experimental mechanics* 40:393-400 doi:10.1007/BF02326485
- Luo H, Du Y, Hu Z, Lu H (2015) High-strain rate compressive behavior of dry mason sand under confinement. In: *Dynamic Behavior of Materials, Volume 1*. Springer, pp 325-333
- Luo P, Chao Y, Sutton M, Peters Iii W (1993) Accurate measurement of three-dimensional deformations in deformable and rigid bodies using computer vision *Experimental Mechanics* 33:123-132 doi:10.1007/BF02322488
- Maas H, Gruen A, Papantoniou D (1993) Particle tracking velocimetry in three-dimensional flows *Experiments in Fluids* 15:133-146 doi:10.1007/BF00190953
- Manogg P (1964) *Anwendungen der schattenoptik zur Untersuchung des zerreißvorgangs von platten*. Ernst-Mach-Inst,
- Marchand A, Duffy J (1988) An experimental study of the formation process of adiabatic shear bands in a structural steel *Journal of the Mechanics and Physics of Solids* 36:251-283 doi:10.1016/0022-5096(88)90012-9
- Mardoukhi A, Saksala T, Hokka M, Kuokkala V-T (2015) An experimental and numerical study of the dynamic Brazilian disc test on Kuru granite
- Marquez AM, Braithwaite CH, Weihs TP, Krywopusk NM, Gibbins DJ, Vecchio KS, Meyers MA (2016) Fragmentation and constitutive response of tailored mesostructured aluminum compacts *Journal of Applied Physics* 119:145903
- Mayne PW, Coop MR, Springman SM, Huang A-B, Zornberg JG *Geomaterial behavior and testing*. In: *Proc. 17th Int. Conf. on Soil Mechanics and Geotechnical Engineering*, 2009. IOS, pp 2777-2872
- McCormick N, Lord J (2010) Digital image correlation *Materials today* 13:52-54 doi:10.1016/S1369-7021(10)70235-2
- Meinhart C, Wereley S, Gray M (2000) Volume illumination for two-dimensional particle image velocimetry *Measurement Science and Technology* 11:809 doi:10.1088/0957-0233
- Meng X (1994) Application of dynamic reflection moire method in studying rock blasting mechanism *Explosion and Shock Waves*:193-198

## CHAPTER 2 REVIEW OF HIGH-SPEED IMAGING AND DIGITAL OPTICAL FULL-FIELD MEASUREMENT TECHNIQUES FOR GEOMATERIALS

- Meola C, Carlomagno GM (2004) Recent advances in the use of infrared thermography Measurement science and technology 15:R27
- Meyers MA (1994) Dynamic behavior of materials. John Wiley & Sons, USA. doi:10.1002/9780470172278
- Miguel A A-I, Bettina S, Donald B D (2011) Influence of the fragmentation process on the dynamics of Vulcanian eruptions: An experimental approach Earth and Planetary Science Letters 302:51-59 doi:10.1016/j.epsl.2010.11.045
- Min Y, Hong M, Xi Z, Jian L (2006) Determination of residual stress by use of phase shifting moiré interferometry and hole-drilling method Optics and Lasers in Engineering 44:68-79 doi:10.1016/j.optlaseng.2005.02.006
- Mindess S, Bentur A (1985) A preliminary study of the fracture of concrete beams under impact loading, using high speed photography Cement and Concrete Research 15:474-484
- Moeyersons J, De Ploey J (1976) Quantitative data on splash erosion, simulated on unvegetated slopes Zeitschrift für Geomorphologie Suppl 25:120-131
- Mollenhauer D, Iarve EV, Kim R, Langley B (2006) Examination of ply cracking in composite laminates with open holes: a moiré interferometric and numerical study Composites Part A: Applied Science and Manufacturing 37:282-294 doi:10.1016/j.compositesa.2005.06.004
- Moss GL, Pond RB (1975) Inhomogeneous thermal changes in copper during plastic elongation Metallurgical Transactions A 6:1223-1235 doi:10.1007/BF02658532
- Muybridge E (1878) The horse in motion. Library of Congress Prints and Photographs Division <http://hdl.loc.gov/locnpn/cph3a45870>, [online accessed 08 August 2014]
- Nagao M, Terada T, Somekawa H, Singh A, Mukai T (2014) Deformation Behavior of Binary Mg-Y Alloy Under Dynamic Compression Loading JOM 66:305-311 doi:10.1007/s11837-013-0854-2
- Nguyen TL, Hall SA, Vacher P, Viggiani G (2011) Fracture mechanisms in soft rock: identification and quantification of evolving displacement discontinuities by extended digital image correlation Tectonophysics 503:117-128 doi:10.1016/j.tecto.2010.09.024
- Nicoletto G (1991) Moiré interferometry determination of residual stresses in the presence of gradients Experimental Mechanics 31:252-256
- Nicoletto G, Post D, Smith C Moire interferometry for high sensitivity measurements in fracture mechanics. In: SESA/JSME Jt Conf Exp Mech, Oahu-Maui, HI, 1982.
- Freeze Frame Eadweard Muybridge's Photography of Motion: National Museum of American History (NMAH) (2001).
- Ohtani K, Numata D, Kikuchi T, Sun M, Takayama K, Togami K (2006) A study of hypervelocity impact on cryogenic materials International journal of impact engineering 33:555-565 doi:10.1016/j.ijimpeng.2006.09.025
- Pan B (2011) Recent progress in digital image correlation Experimental Mechanics 51:1223-1235 doi:10.1007/s11340-010-9418-3

## CHAPTER 2 REVIEW OF HIGH-SPEED IMAGING AND DIGITAL OPTICAL FULL-FIELD MEASUREMENT TECHNIQUES FOR GEOMATERIALS

- Pan B, Qian K, Xie H, Asundi A (2009) Two-dimensional digital image correlation for in-plane displacement and strain measurement: a review *Measurement science and technology* 20:062001 doi:10.1088/0957-0233
- Pan B, Xie H, Wang Z (2010) Equivalence of digital image correlation criteria for pattern matching *Applied optics* 49:5501-5509 doi:10.1364/AO.49.005501
- Parab ND et al. (2014) Experimental assessment of fracture of individual sand particles at different loading rates *International Journal of Impact Engineering* 68:8-14 doi:10.1016/j.ijimpeng.2014.01.003
- Parab ND et al. (2017) In situ observation of fracture processes in high-strength concretes and limestone using high-speed X-ray phase-contrast imaging *Philosophical Transactions of the Royal Society A: Mathematical, Physical and Engineering Sciences* 375 doi:10.1098/rsta.2016.0178
- Parker R, Jones D (1988) The use of holographic interferometry for turbomachinery fan evaluation during rotating tests *Journal of turbomachinery* 110:393-400 doi:10.1115/1.3262209
- Patorski K (1993) *Handbook of the moiré fringe technique*. Elsevier Science, Amsterdam
- Pedrin G, Osten W, Gusev ME (2006) High-speed digital holographic interferometry for vibration measurement *Applied Optics* 45:3456-3462 doi:10.1364/AO.45.003456
- Peres MR (2013) *The Focal Encyclopedia of Photography*. Taylor & Francis,
- Perkins R, Green S (1968) High speed photography in dynamic materials testing *Review of Scientific Instruments* 39:1209-1210 doi:10.1063/1.1683621
- Persson P-A, Holmberg R, Lee J (1993) *Rock blasting and explosives engineering*. CRC press,
- Peters W, Ranson W (1982) Digital imaging techniques in experimental stress analysis *Optical engineering* 21:213427 doi:10.1117/12.7972925
- Pierron F, Cheriguene R, Forquin P, Moulart R, Rossi M, Sutton M Performances and limitations of three ultra high-speed imaging cameras for full-field deformation measurements. In: *Applied Mechanics and Materials*, 2011a. Trans Tech Publ, pp 81-86
- Pierron F, Forquin P (2012) Ultra - High - Speed Full - Field Deformation Measurements on Concrete Spalling Specimens and Stiffness Identification with the Virtual Fields Method *Strain* 48:388-405 doi:10.1111/j.1475-1305.2012.00835.x
- Pierron F, Grédiac M (2012) The virtual fields method: extracting constitutive mechanical parameters from full-field deformation measurements. Springer Science & Business Media, London. doi:10.1007/978-1-4614-1824-5
- Pierron F, Sutton M, Tiwari V (2011b) Ultra high speed DIC and virtual fields method analysis of a three point bending impact test on an aluminium bar *Experimental Mechanics* 51:537-563 doi:10.1007/s11340-010-9402-y
- Post D, Han B, Ifju P (2012) *High sensitivity moiré: experimental analysis for mechanics and materials*. Springer Science & Business Media, London. doi:10.1007/978-1-4612-4334-2

## CHAPTER 2 REVIEW OF HIGH-SPEED IMAGING AND DIGITAL OPTICAL FULL-FIELD MEASUREMENT TECHNIQUES FOR GEOMATERIALS

- Post D, Han B, Ifju PG (2000) Moiré methods for engineering and science—Moiré interferometry and shadow moiré. In: Photomechanics. Springer, pp 151-196. doi:10.1007/3-540-48800-6\_5
- Prasad AK (2000) Particle image velocimetry CURRENT SCIENCE-BANGALORE- 79:51-60
- Qin YW (1981) Application of Faraday's effect in static and dynamic holographic photoelasticity Experimental Mechanics 21:389-393 doi:10.1007/BF02324801
- Raffel M, Willert CE, Kompenhans J (2013) Particle image velocimetry: a practical guide. Springer, London. doi:10.1007/978-3-540-72308-0
- Ramesh K, Hogan JD, Kimberley J, Stickle A (2015) A review of mechanisms and models for dynamic failure, strength, and fragmentation Planetary and Space Science 107:10-23 doi:10.1016/j.pss.2014.11.010
- Rastogi P (2015) Digital Optical Measurement Techniques and Applications. Artech House,
- Rastogi PK (2000) Principles of holographic interferometry and speckle metrology. In: Photomechanics. Springer, pp 103-151
- Rastogi PK, Hack E (2012) Optical methods for solid mechanics: a full-field approach. John Wiley & Sons, Germany
- Ravi-Chandar K (2004) Dynamic fracture. Elsevier, UK
- Ray SF (2006) High Speed Photography and Photonics vol PM120. SPIE Press, United States
- Rayleigh L (1874) XII. On the manufacture and theory of diffraction-gratings The London, Edinburgh, and Dublin Philosophical Magazine and Journal of Science 47:81-93 doi:10.1080/14786447408640996
- Reu PL High/Ultra-high speed imaging as a diagnostic tool. In: Applied Mechanics and Materials, 2011. Trans Tech Publ, pp 69-74
- Reu PL, Miller TJ (2008) The application of high-speed digital image correlation The Journal of Strain Analysis for Engineering Design 43:673-688 doi:10.1243/03093247JSA414
- Righi A (1887) Sui fenomeni che si producono colla sovrapposizione di due peticoli e sopra alcune loro applicazioni Il Nuovo Cimento (1877-1894) 21:203-228
- Riley W, Dally J (1969) Recording dynamic fringe patterns with a Cranz-Schardin camera Experimental Mechanics 9:27N-33N
- Rossmannith H, Fourney W (1982) Fracture initiation and stress wave diffraction at cracked interfaces in layered media I. brittle/brittle transition Rock mechanics 14:209-233
- Rossmannith H, Knasmillner R, Daehnke A, Mishnaevsky Jr L (1996) Wave propagation, damage evolution, and dynamic fracture extension. Part II. Blasting Materials Science 32:403-410 doi:10.1007/BF02538964
- Sanborn B, Gunnarsson C, Foster M, Weerasooriya T (2014) Quantitative Visualization of Human Cortical Bone Mechanical Response: Studies on the Anisotropic Compressive Response and Fracture

## CHAPTER 2 REVIEW OF HIGH-SPEED IMAGING AND DIGITAL OPTICAL FULL-FIELD MEASUREMENT TECHNIQUES FOR GEOMATERIALS

Behavior as a Function of Loading Rate *Experimental Mechanics*:1-15 doi:10.1007/s11340-015-0060-y

Schuler H, Mayrhofer C, Thoma K (2006) Spall experiments for the measurement of the tensile strength and fracture energy of concrete at high strain rates *International Journal of Impact Engineering* 32:1635-1650 doi:10.1016/j.ijimpeng.2005.01.010

Schultz PH, Heineck JT, Anderson JLB (2000) Using 3-D PIV in laboratory impact experiments. Paper presented at the Lunar Planetary Science Conference XXXI, Houston, TX, USA, Mar 01

Seah CC, Børvik T, Remseth S, Pan T-C (2011) Penetration and perforation of rock targets by hard projectiles *Advances in Rock Dynamics and Applications*:143

Settles G (2006) High-speed Imaging of Shock Waves, Explosions and Gunshots New digital video technology, combined with some classic imaging techniques, reveals shock waves as never before *American Scientist* 94:22-31 doi:10.1511/2006.1.22

Sharma SP, Ruffin SM, Meyer SA, Gillespie WD, Yates LA (1993) Density measurements in an expanding flow using holographic interferometry *Journal of thermophysics and heat transfer* 7:261-268 doi:10.2514/3.415

Sharpe WN (2008) *Springer handbook of experimental solid mechanics*. Springer Science & Business Media, USA. doi:10.1007/978-0-387-30877-7\_3

Shi W, Wu Y, Wu L (2007) Quantitative analysis of the projectile impact on rock using infrared thermography *International Journal of Impact Engineering* 34:990-1002

Shockey DA, Curran DR, Seaman L, Rosenberg JT, Petersen CF Fragmentation of rock under dynamic loads. In: *International Journal of Rock Mechanics and Mining Sciences & Geomechanics Abstracts*, 1974. vol 8. Elsevier, pp 303-317. doi:10.1016/0148-9062(74)91760-4

Shukla A (1991) Dynamic photoelastic studies of wave propagation in granular media *Optics and Lasers in Engineering* 14:165-184

Shukla A, Damania C (1987) Experimental investigation of wave velocity and dynamic contact stresses in an assembly of disks *Experimental mechanics* 27:268-281

Siebert T, Crompton MJ (2013) Application of high speed digital image correlation for vibration mode shape analysis. In: *Application of Imaging Techniques to Mechanics of Materials and Structures*, Volume 4. Springer, pp 291-298. doi:10.1007/978-1-4419-9796-8\_37

Song Y, Li M, Wang X, Li X, Fu X (2015) Experimental test on marble containing two pre-existing cracks under loading and unloading conditions based on high-speed photography *Journal of Rock Mechanics and Engineering* 43:773-781 doi:10.13722/j.cnki.jrme.2013.1718

Song Y, Li M, Wang X, Liu X, Fu X (2014) Experimental test on marble containing single pre-existing cracks under loading and unloading conditions based on high-speed photography *Journal of China University of Mining & Technology*

Stetson KA, Powell RL (1965) Interferometric hologram evaluation and real-time vibration analysis of diffuse objects *JOSA* 55:1694-1695 doi:10.1364/JOSA.55.001694

## CHAPTER 2 REVIEW OF HIGH-SPEED IMAGING AND DIGITAL OPTICAL FULL-FIELD MEASUREMENT TECHNIQUES FOR GEOMATERIALS

- Strassburger E, Senf H, Rothenhäusler H (1994) Fracture propagation during impact in three types of ceramics *Le Journal de Physique IV* 4:C8-653-C658-658 doi:10.1051/jp4:1994899
- Surrel Y (2003) *Optique C1-18851 Images optiques; mesures 2D et 3D* Polycopié de cours vol 8. Conservatoire National des Arts et Métiers.
- Sutton M, Mingqi C, Peters W, Chao Y, McNeill S (1986) Application of an optimized digital correlation method to planar deformation analysis *Image and Vision Computing* 4:143-150 doi:10.1016/0262-8856(86)90057-0
- Sutton M, Yan J, Tiwari V, Schreier H, Orteu J (2008) The effect of out-of-plane motion on 2D and 3D digital image correlation measurements *Optics and Lasers in Engineering* 46:746-757 doi:10.1016/j.optlaseng.2008.05.005
- Sutton MA, Orteu JJ, Schreier H (2009) *Image correlation for shape, motion and deformation measurements: basic concepts, theory and applications*. Springer Science & Business Media,
- Theocaris PS, Gdoutos E (1972) An optical method for determining opening-mode and edge sliding-mode stress-intensity factors *Journal of Applied Mechanics* 39:91-97 doi:10.1115/1.3422676
- Thomson KC, Ahrens TJ, Toksöz MN (1969) Dynamic photoelastic studies of p and s wave propagation in prestressed media *Geophysics* 34:696-712
- Thoroddsen ST, Etoh TG, Takehara K (2008) High-Speed Imaging of Drops and Bubbles *Annual Review of Fluid Mechanics* 40:257-285 doi:10.1146/annurev.fluid.40.111406.102215
- Tieng SM, Lai WZ (1992) Temperature measurements of reacting flowfield by phase-shifting holographic interferometry *Journal of thermophysics and heat transfer* 6:445-451 doi:10.2514/3.381
- Tiwari V, Sutton M, McNeill KO, Fourney W, Bretall D On studying improvised explosive devices (IEDs) using digital image correlations. . In: *Proc. 2007 SEM Annu. Conf. Exposition Exp. Appl. Mech*, MA, USA, January 2007. Springfield,
- Tong W (2005) An evaluation of digital image correlation criteria for strain mapping applications *Strain* 41:167-175 doi:10.1111/j.1475-1305.2005.00227.x
- Trojanowski A, Macdougall D, Harding J (1998) An improved technique for the experimental measurement of specimen surface temperature during Hopkinson-bar tests *Measurement Science and Technology* 9:12
- Trolinger J, Hsu J Flowfield Diagnostics by Holographic Interferometry and Tomography. In: *Fringe*, 1993. pp 423-439
- True DG (1975) Penetration of projectiles into seafloor soils. DTIC Document,
- Tuzi Z (1928) *Photographic and Kinematographic Study of Photo-Elasticity* Scientific Papers of the Institute of Physical and Chemical Research 8:247-267
- Van Dijk A, Meesters A, Bruijnzeel L (2002) Exponential distribution theory and the interpretation of splash detachment and transport experiments *Soil Science Society of America Journal* 66:1466-1474 doi:10.2136/sssaj2002.1466
- Versluis M (2013) High-speed imaging in fluids *Experiments in Fluids* 54:1-35

## CHAPTER 2 REVIEW OF HIGH-SPEED IMAGING AND DIGITAL OPTICAL FULL-FIELD MEASUREMENT TECHNIQUES FOR GEOMATERIALS

- Walley S (2014) An Introduction to the Properties of Silica Glass in Ballistic Applications Strain 50:470-500 doi:10.1111/str.12075
- Wang D, Wang Y, Yang B, Zhang W, Lancaster N (2008) Statistical analysis of sand grain/bed collision process recorded by high - speed digital camera Sedimentology 55:461-470 doi:10.1111/j.1365-3091.2007.00909.x
- Wang H, Liu Da, Gong W, Li L (2015) Dynamic analysis of granite rockburst based on the PIV technique International Journal of Mining Science and Technology 25:275-283 doi:10.1016/j.ijmst.2015.02.017
- Wang Y, Wang D, Wang L, Zhang Y (2009) Measurement of sand creep on a flat sand bed using a high - speed digital camera Sedimentology 56:1705-1712 doi:10.1111/sed.12232
- Weinstein LA (1969) Open resonators and open waveguides. The Golem Press, Boulder, Colorado, USA
- White D, Take W, Bolton M (2003) Soil deformation measurement using particle image velocimetry (PIV) and photogrammetry Geotechnique 53:619-631
- Whittles D, Kingman S, Lowndes I, Jackson K (2006) Laboratory and numerical investigation into the characteristics of rock fragmentation Minerals engineering 19:1418-1429 doi:10.1016/j.mineng.2006.02.004
- Willert C, Gharib M (1992) Three-dimensional particle imaging with a single camera Experiments in Fluids 12:353-358 doi:10.1007/BF00193880
- Willmott G, Field J (2006) A high-speed photographic study of fast cracks in shocked diamond Philosophical Magazine 86:4305-4318
- Wong L, Einstein H (2009a) Crack coalescence in molded gypsum and Carrara marble: part 1. Macroscopic observations and interpretation Rock Mechanics and Rock Engineering 42:475-511
- Wong L, Einstein H (2009b) Using high speed video imaging in the study of cracking processes in rock Geotechnical Testing Journal 32:1 doi:10.1520/GTJ101631
- Wong LN, Einstein H Fracturing behavior of prismatic specimens containing single flaws. In: Golden Rocks 2006, The 41st US Symposium on Rock Mechanics (USRMS), Colorado, 21 June 2006. American Rock Mechanics Association,
- Wong LNY, Zou C, Cheng Y (2014) Fracturing and failure behavior of Carrara marble in quasistatic and dynamic Brazilian disc tests Rock mechanics and rock engineering 47:1117-1133 doi:10.1007/s00603-013-0465-9
- Wu S, Chau K, Yu T (2004) Crushing and fragmentation of brittle spheres under double impact test Powder technology 143:41-55 doi:10.1016/j.powtec.2004.04.028
- Wu Z, Lu J, Han B (1998) Study of residual stress distribution by a combined method of Moire interferometry and incremental hole drilling, part II: implementation Journal of applied mechanics 65:844-850

## CHAPTER 2 REVIEW OF HIGH-SPEED IMAGING AND DIGITAL OPTICAL FULL-FIELD MEASUREMENT TECHNIQUES FOR GEOMATERIALS

- Wyant JC, Koliopoulos CL, Bhushan B, George OE (1984) An optical profilometer for surface characterization of magnetic media ASLE transactions 27:101-113 doi:10.1080/05698198408981550
- Xiang G, Zhang Q, Liu H, Wu X, Ju X (2007) Time-resolved deformation measurements of the Portevin–Le Chatelier bands Scripta Materialia 56:721-724
- Xu S, Huang J, Wang P, Zhang C, Zhou L, Hu S (2015) Investigation of rock material under combined compression and shear dynamic loading: An experimental technique International Journal of Impact Engineering 86:206-222 doi:10.1016/j.ijimpeng.2015.07.014
- Xu W, Yao X, Yeh H, Jin G (2005) Fracture investigation of PMMA specimen using coherent gradient sensing (CGS) technology Polymer testing 24:900-908 doi:10.1016/j.polymertesting.2005.06.005
- Yang B, Wang Y, Zhang Y (2009a) The 3-D spread of saltation sand over a flat bed surface in aeolian sand transport Advanced Powder Technology 20:303-309 doi:10.1016/j.apr.2008.11.002
- Yang L, Xu P, Gao X, Sun J (2014) Digital Laser High-speed Photography System and Its Application in Photomechanical Tests with Blast Loading Science & Technology Review 32:013 doi:10.3981/j.issn.1000-7857.2014.32.002
- Yang R, Wang Y, Ding C (2016a) Laboratory study of wave propagation due to explosion in a jointed medium International Journal of Rock Mechanics and Mining Sciences 81:70-78
- Yang R, Xu P, Yue Z, Chen C (2016b) Dynamic fracture analysis of crack–defect interaction for mode I running crack using digital dynamic caustics method Engineering Fracture Mechanics 161:63-75 doi:10.1016/j.engfracmech.2016.04.042
- Yang R, Yang L, Yue Z, Xiao T, Dong J, Niu X (2009b) Dynamic caustics experiment of crack propagation in material containing flaws under blasting load Journal of China Coal Society 34
- Yang R, Yue Z, Dong J, Gui L, Xiao T (2008a) Dynamic Caustics Experiment of Blasting Crack Propagation in Discontinuous Jointed Material [J] Journal of China University of Mining & Technology 4:006
- Yang R, Yue Z, Sun Z, Xiao T, Guo D (2009c) Dynamic fracture behavior of rock under impact load using the caustics method Mining Science and Technology (China) 19:79-83
- Yang R, Yue Z, Xiao T, Dong J, Yang L (2008b) Dynamic caustics experiment on crack propagation of jointed medium fracture with controlled blasting Chinese Journal of Rock Mechanics and Engineering 2:005
- Yao X, Xu W (2011) Recent application of caustics on experimental dynamic fracture studies Fatigue & Fracture of Engineering Materials & Structures 34:448-459
- Yao X, Xu W, Arakawa K, Takahashi K, Mada T (2005) Dynamic optical visualization on the interaction between propagating crack and stationary crack Optics and lasers in engineering 43:195-207 doi:10.1016/j.optlaseng.2004.06.003
- Yao X, Xu W, Xu M, Arakawa K, Mada T, Takahashi K (2003) Experimental study of dynamic fracture behavior of PMMA with overlapping offset-parallel cracks Polymer testing 22:663-670 doi:10.1016/S0142-9418(02)00173-3



## CHAPTER 2 REVIEW OF HIGH-SPEED IMAGING AND DIGITAL OPTICAL FULL-FIELD MEASUREMENT TECHNIQUES FOR GEOMATERIALS

- Yao XF, Jin GC, Arakawa K, Takahashi K (2002) Experimental studies on dynamic fracture behavior of thin plates with parallel single edge cracks *Polymer testing* 21:933-940 doi:10.1016/S0142-9418(02)00037-5
- Yao Y, Bonakdar A, Faber J, Gries T, Mobasher B (2014) Distributed cracking mechanisms in textile-reinforced concrete under high speed tensile tests *Materials and Structures*:1-18 doi:10.1617/s11527-015-0685-4
- Yin Z, Ma H, Hu Z, Zou Y (2014a) Effect of Static-Dynamic Coupling Loading on Fracture Toughness and Failure Characteristics in Marble *Journal of Engineering Science and Technology Review* 7:169-174
- Yin Z, Wang L, Ma H, Hu Z, Jin J (2014b) Application of Optical Measurement Method in Brazilian Disk Splitting Experiment Under Dynamic Loading *Sensors & Transducers* 171:176-182
- Younis N (2012) Experimental Strain Investigation of Bolt Torque Effect in Mechanically Fastened Joints
- Yu-wen Q (1979) Application of faraday's effect in the holographic photoelasticity *Acta Mechanica Sinica* 3:008
- Yu L, Pan B (2015) The errors in digital image correlation due to overmatched shape functions *Measurement Science and Technology* 26:045202 doi:10.1088/0957-0233
- Zael R, Yeni Y, Bay B, Dong X, Fyhrie D (2006) Comparison of the linear finite element prediction of deformation and strain of human cancellous bone to 3D digital volume correlation measurements *Journal of biomechanical engineering* 128:1-6 doi:10.1115/1.2146001
- Zehnder AT, Guduru PR, Rosakis AJ, Ravichandran G (2000) Million frames per second infrared imaging system *Review of Scientific Instruments* 71:3762-3768 doi:10.1063/1.1310350
- Zehnder AT, Rosakis AJ (1990) Dynamic fracture initiation and propagation in 4340 steel under impact loading *International Journal of Fracture* 43:271-285 doi:10.1007/BF00035087
- Zehnder AT, Rosakis AJ (1991) On the temperature distribution at the vicinity of dynamically propagating cracks in 4340 steel *Journal of the Mechanics and Physics of Solids* 39:385-415 doi:10.1016/0022-5096(91)90019-K
- Zhang C (2014a) Application of digital image correlation in dynamic testing. Univeristy of Science and Technology of China
- Zhang J, Tao B, Katz J (1997) Turbulent flow measurement in a square duct with hybrid holographic PIV *Experiments in Fluids* 23:373-381 doi:10.1007/s003480050124
- Zhang QB (2014b) Mechanical Behaviour of Rock Materials under Dynamic Loading. École Polytechnique Fédérale de Lausanne
- Zhang QB, Braithwaite CH, Zhao J (2017) Hugoniot equation of state of rock materials under shock compression *Philosophical Transactions of the Royal Society A: Mathematical, Physical and Engineering Sciences* 375

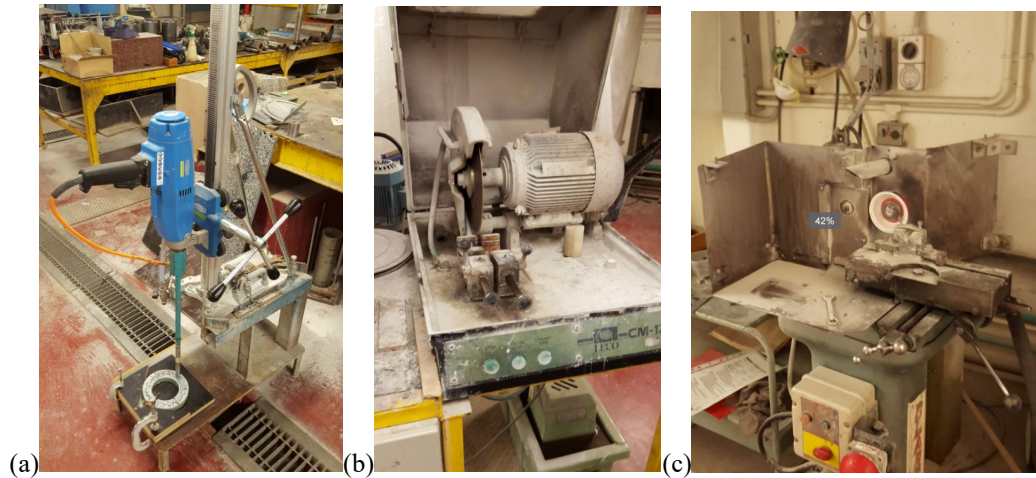
## CHAPTER 2 REVIEW OF HIGH-SPEED IMAGING AND DIGITAL OPTICAL FULL-FIELD MEASUREMENT TECHNIQUES FOR GEOMATERIALS

- Zhang QB, Zhao J (2013a) Determination of mechanical properties and full-field strain measurements of rock material under dynamic loads *Int J Rock Mech Min* 60:423-439 doi:10.1016/j.ijrmms.2013.01.005
- Zhang QB, Zhao J (2013b) Effect of loading rate on fracture toughness and failure micromechanisms in marble *Engineering Fracture Mechanics* 102:288-309
- Zhang QB, Zhao J (2014a) Quasi-static and dynamic fracture behaviour of rock materials: phenomena and mechanisms *International Journal of Fracture* 189:1-32 doi:10.1007/s10704-014-9959-z
- Zhang QB, Zhao J (2014b) A review of dynamic experimental techniques and mechanical behaviour of rock materials *Rock Mechanics and Rock Engineering* 47:1411-1478 doi:10.1007/s00603-013-0463-y
- Zhang R, Guo R, Wang S (2014a) Mixed mode fracture study of PMMA using digital gradient sensing method *Engineering Fracture Mechanics* 119:164-172 doi:10.1016/j.engfracmech.2014.02.020
- Zhang W, Wang Y, Lee S-J (2007) Two-phase measurements of wind and saltating sand in an atmospheric boundary layer *Geomorphology* 88:109-119 doi:10.1016/j.geomorph.2006.10.017
- Zhang X, Sun Z, Hu X (2014b) Low temperature fracture toughness of PMMA and crack-tip conditions under flat-tipped cylindrical indenter *Polymer Testing* 38:57-63 doi:10.1016/j.polymertesting.2014.06.009
- Zhang Y, Wang Y, Jia P (2014c) Measuring the kinetic parameters of saltating sand grains using a high-speed digital camera *Science China Physics, Mechanics & Astronomy* 57:1137-1143 doi:10.1007/s11433-013-5284-1
- Zhang Z, Kou S, Jiang L, Lindqvist P-A (2000) Effects of loading rate on rock fracture: fracture characteristics and energy partitioning *International Journal of Rock Mechanics and Mining Sciences* 37:745-762 doi:10.1016/S1365-1609(00)00008-3
- Zhou M, Rosakis A, Ravichandran G (1996) Dynamically propagating shear bands in impact-loaded prenotched plates—I. Experimental investigations of temperature signatures and propagation speed *Journal of the Mechanics and Physics of Solids* 44:981-1006 doi:10.1016/S1365-1609(00)00008-3
- Zhou YX, Zhao J (eds) (2011) *Advances in rock dynamics and applications*. CRC Press,
- Zhou Z, Li X, Zou Y, Jiang Y, Li G (2014) Dynamic Brazilian tests of granite under coupled static and dynamic loads *Rock mechanics and rock engineering* 47:495-505
- Zou C, Wong LNY Study of Mechanical Properties and Fracturing Processes of Carrara Marble in Dynamic Brazilian Tests by Two Optical Observation Methods. In: *Rock Mechanics and Its Applications in Civil, Mining, and Petroleum Engineering*, 2014. ASCE, pp 20-29. doi:10.1061/9780784413395.004
- Zou X-Y, Wang Z-L, Hao Q-Z, Zhang C-L, Liu Y-Z, Dong G-R (2001) The distribution of velocity and energy of saltating sand grains in a wind tunnel *Geomorphology* 36:155-165 doi:10.1016/S0169-555X(00)00038-6

## CHAPTER 3 EXPERIMENTAL SET-UP

### 3.1 MATERIAL PREPARATION

The rock specimens in this study were cored from rock block with no obvious layer or bedding into cylinders with diameters of 48 mm, as shown in Fig. 3.1(a). The rock core was afterwards cutted into 48 mm-length cylinders for dynamic compression tests, 100 mm-length cylinders for quasi-static compression tests and 24 mm-length cylinders for BD test. The leco cutter is shown in Fig. 3.1(b). Specimen surfaces were grinded by the grinder (Fig. 3.1(c)) ensuring two ends of the specimen were ground to be flat to 0.02 mm tolerance and not depart from perpendicularity to its axis by more than 0.001 rad as suggested by International Society for Rock Mechanics (ISRM) for rock mechanical tests (Zhou, Xia et al. 2012).



**Fig. 3.1** Specimen manufacturing machine: (a) Coring machine (b) Diamond cutter and (c) Surface grinder

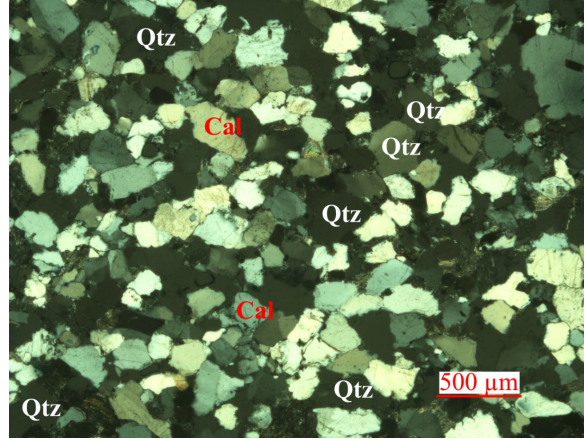
### 3.2 MATERIAL SPECIFICATION

Three types of rocks were investigated including Hawkesbury sandstone, Cararra marble and Impala black gabbro, as shown in Fig. 3.2.

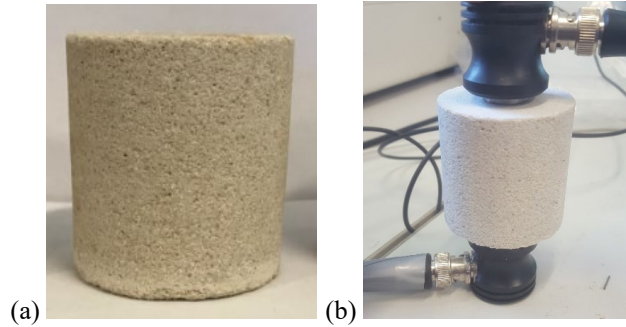


Fig. 3.2 Photograph of marble, sandstone and gabbro

The Hawkesbury sandstone from early Triassic age is quarried from Gosford basin in Sydney, Australia. The white-grey coloured sandstone block for this study has a medium grain size varying from 0.04 to 1 mm, belonging to the silicate cemented group with a high percentage of quartz mineral (90% quartz, 5% calcite, 2% kaolinite, and other clay minerals). The petrographic thin sections of rock specimen, as shown in Fig. 3.3, were prepared and observed under cross polarised light (XPL) using a Zeiss at the School of Earth, Atmosphere and Environment, Monash University. The wave velocity of rock specimen was detected by the ultrasonic scanning transducers (Olympus Model V103) at a frequency of 1 MHz, as shown in Fig.3.4. A spike pulse was excited by the PXI-5412 waveform generator and amplified by a Trek piezo pre-amplifier (Model 2100HF) while the signal of the receiver was amplified by an Olympus preamplifier (Model 5660B). The sampling rate of the system was 10MHz to achieve a high enough accuracy. The couplant was applied between the transducers and rock for efficient wave transmission. The wave velocity of each specimen was examined ensuring the agreement in properties. The sandstone specimens are homogeneous with the properties: density  $\rho = 2.21 \text{ g/cm}^3$ , P-wave velocity  $V_p = 2110 \text{ m/s}$ , S-wave velocity  $V_s = 1210 \text{ m/s}$ , elastic modulus  $E = 8.39 \text{ GPa}$ , and UCS  $\sigma = 41 \text{ MPa}$ .



**Fig. 3.3** Microscopic images of thin sections of medium-grained sandstones



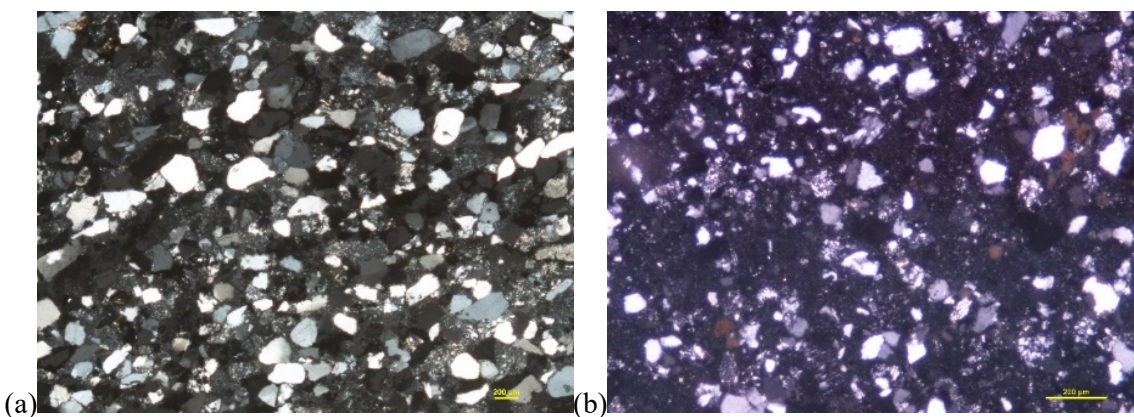
**Fig. 3.4(a)** A medium-grained Hawkesbury sandstone specimen **(b)** Ultrasonic wave method to determine the wave velocity

In addition to medium grain-sized (MG) sandstone, coarse-grained (CG) and fine-grained (FG) sandstone, as shown in Fig. 3.5, were studied as well. The grain size is 200~500  $\mu\text{m}$  for CG sandstone and 55~120  $\mu\text{m}$  for FG sandstone, respectively. The thin sections of CG and FG sandstone grain distribution are shown in Fig. 3.6.



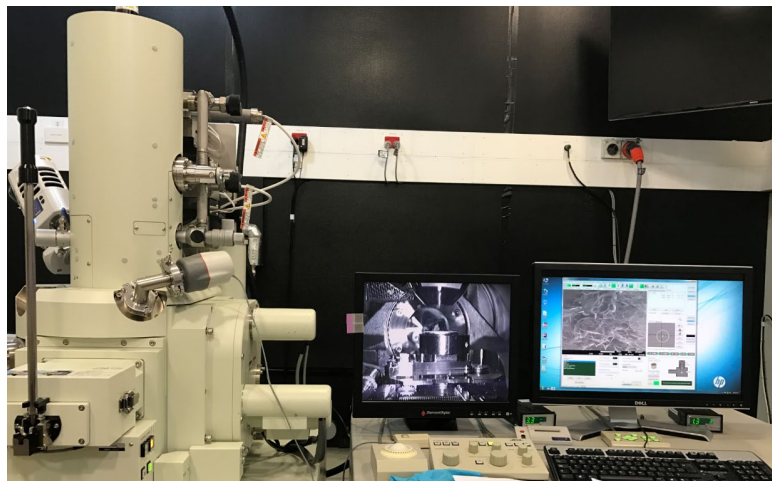
**Fig. 3.5** Photographs of sandstones of three grain sizes (left to right: CG, MG and FG sandstone)





**Fig. 3.6** Microscopic images of thin sections of (a)CG and (b)FG (right) sandstone

The dominant grain in those three sandstones is quartz, however, FG sandstone has a considerable amount of clay minerals. The microscopic topography of grain and clay distribution was obtained by JEOL JSM-7001F scanning electron microscopy (SEM) at Monash Centre for Electron Microscopy as shown in Fig. 3.7. The recipe for the scanning was 10 nA current, 15 kV voltage, and 10mm working distance. The SEM images in Fig. 3.8 show that the CG sandstone has a clear grain boundary, however the quartz grains are surrounded by clay minerals in FG sandstone.



**Fig. 3.7** JEOL JSM-7001F scanning electron microscopy (SEM) at Monash Centre for Electron Microscopy

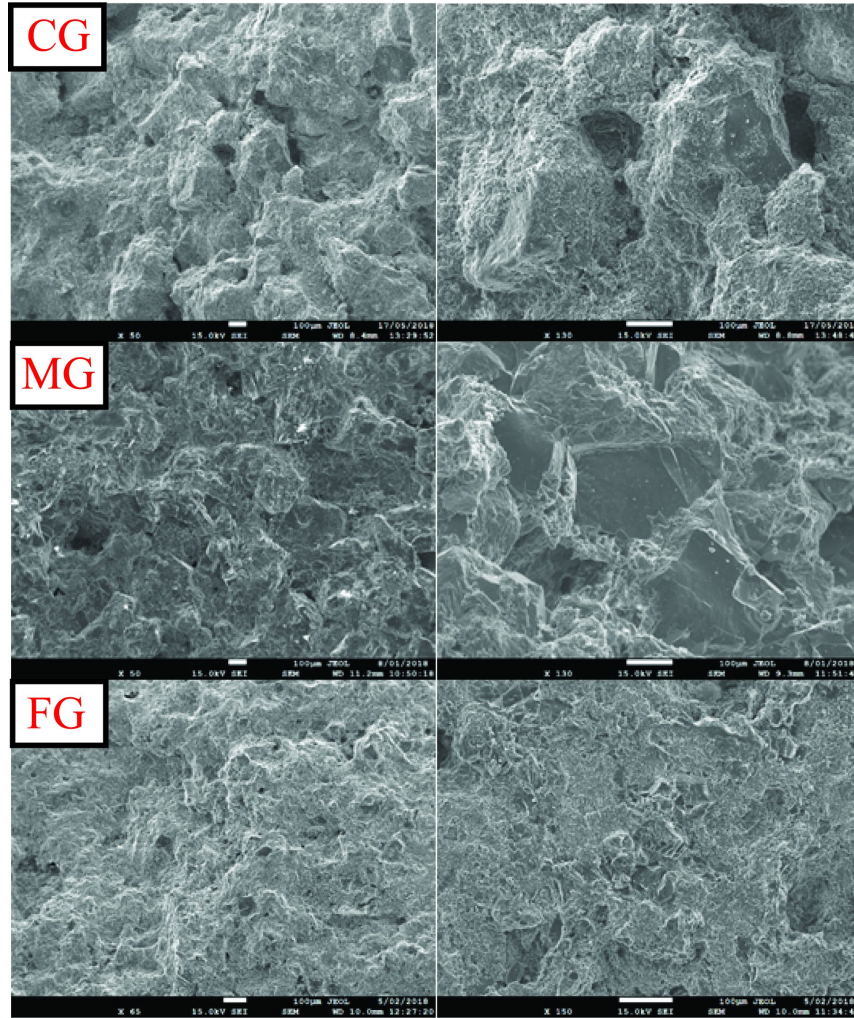


Fig. 3.8 SEM images of CG, MG and FG sandstone

Impala black gabbro, also as known as Impala Dark, is a gabbro rock from South Africa. This rock is part of the Precambrian Bushveld igneous complex which is about 2 billion years old. This rock has no preferred grain orientations nor deformations, with an average grain size from 1 to 3 mm. The mineral composition, shown as Fig. 3.9(a), mainly consists of plagioclase (60%), orthopyroxene (25%), clinopyroxene (10%), with traces of amphibole (~5%). The density of gabbro is 2.90 g/cm<sup>3</sup>, P-wave velocity is 6821 m/s, elastic modulus is 63.6 GPa, and UCS is 284 MPa.

Carrara marble is quarried in the city of Carrara located in the province of Massa and Carrara in the Lunigiana, the northernmost tip of modern-day Tuscany, Italy. This marble is famously known as construction material for sculptures and historical buildings. The rock block is pure white by observation, with no visible impurities or dykes. The thin section in Fig. 3.9(b)



shows that it is almost pure calcite (99%) with an average grain size between 0.2 to 0.4mm, which makes the physical properties of this rock quite homogeneous. The marble has a density of 2.68 g/cm<sup>3</sup>, P-wave velocity of 5340 m/s, elastic modulus of 40.0 GPa and UCS of 112 MPa.

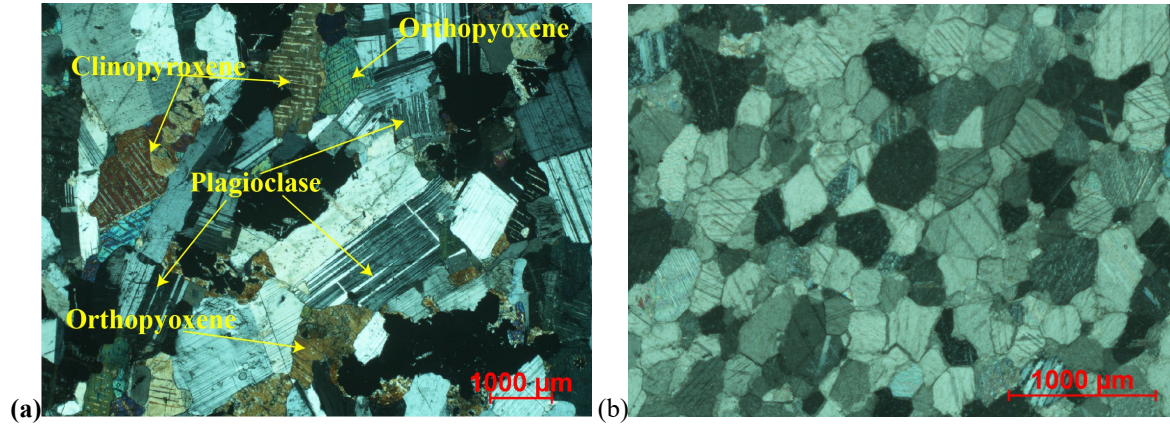


Fig. 3.9 Microscopic images of the thin sections of (a)gabbro and (b)marble

### 3.3 LOADING DEVICE

#### 3.3.1 Quasi-static system

The quasi-static behaviour of the rock specimens are tested by 300 kN Shimadzu AGS-X Series testing machine, as shown in Fig. 3.10. The stress-strain curve in uniaxial compression test (Fig.3.11(a)) is interpreted from the load (kN)-displacement (mm) according to the length and area of the specimen. Young's modulus is the slope of stress-strain curve, Poisson's ratio is sign ratio of lateral strain to axial strain where the lateral strain is measured by strain gauge attached horizontally to the specimen surface.





Fig. 3.10 Shimadzu 100 KN compression machine

The quasi-static tensile strength is determined by BD test, as shown in Fig. 3.11(b). The principle of BD test comes from the fact that rocks are much weaker in tension than in compression. The diametrically-loaded rock disc sample fails first due to the tension along the loading diameter near the center. The tensile strength  $\sigma_t$  determined from the BD test is derived by,

$$\sigma_t = \frac{2P_{max}}{\pi DB} \quad (3.1)$$

where the  $P_{max}$  is the load when the failure occurs, D and B are the diameter and thickness of the specimen, respectively.

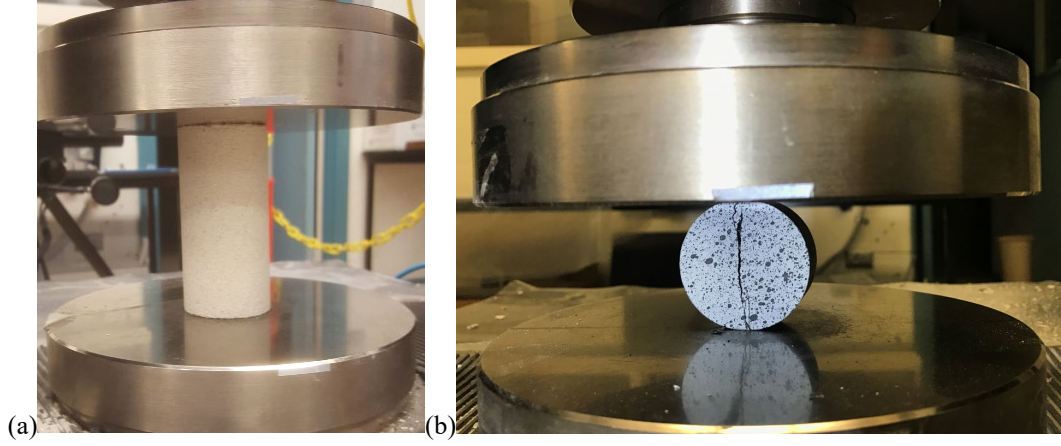


Fig. 3.11(a) photograph of the quasi-static compression and (b) BD test

### 3.3.2 SHPB system

The dynamic loading in this project is operated by SHPB testing method. The principle of SHPB is based on the theory of one-dimensional (1D) stress wave propagation, and the dynamic pressure on the incident ( $P_1$ ) and transmitted ( $P_2$ ) ends of specimen are (Kolsky 1949, Zhao and Gary 1996, Gray III 2000):

$$P_1 = \frac{A_B}{A_s} E_B (\varepsilon_i + \varepsilon_r), \quad P_2 = \frac{A_B}{A_s} E_B \varepsilon_t \quad (3.2)$$

where  $E_B$  is Young's modulus of bars;  $A_B$  and  $A_s$  are the cross-sectional area of the bar and specimen;  $\varepsilon_i$ ,  $\varepsilon_r$  and  $\varepsilon_t$  are the incident, reflected and transmitted strain signals, respectively.

The velocities at the incident bar end ( $v_1$ ) and the transmitted bar end ( $v_2$ ) are:

$$v_1 = C_B (\varepsilon_i - \varepsilon_r), \quad v_2 = C_B \varepsilon_t \quad (3.3)$$

where  $C_B$  is the wave velocity of the bar.

The average engineering strain rate  $\dot{\varepsilon}$  and strain  $\varepsilon$  in the specimen are calculated as:

$$\dot{\varepsilon} = \frac{v_1 - v_2}{L_s} = \frac{C_B}{L_s} (\varepsilon_i - \varepsilon_r - \varepsilon_t), \quad \varepsilon = \int_0^t \dot{\varepsilon} dt = \frac{C_B}{L_s} \int_0^t (\varepsilon_i - \varepsilon_r - \varepsilon_t) dt \quad (3.4)$$

where  $t$  is time and  $L_s$  is the length of the specimen.

When the pressures on both ends of two bars reach an equilibrium, namely  $P_1 = P_2$ , Eq. 3.3 leads to:

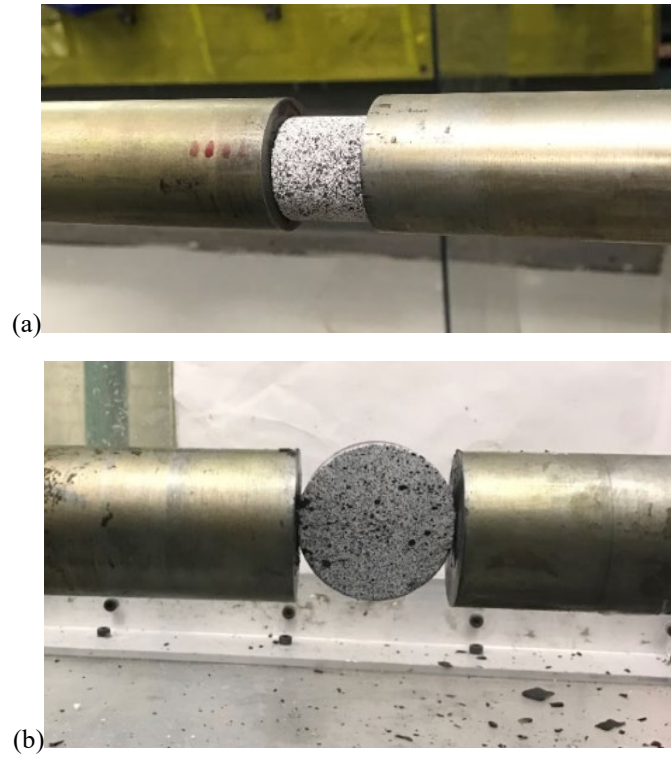
$$\varepsilon_i + \varepsilon_r = \varepsilon_t \quad (3.5)$$

Eq. 3.4 and 3.5 can thus be simplified as follows,

$$\dot{\varepsilon} = -2 \frac{C_B}{L_s} \varepsilon_r, \varepsilon = -2 \frac{C_B}{L_s} \int_0^t \varepsilon_r dt \quad (3.6)$$

For dynamic BD test, the dynamic tensile strength is determined as  $\sigma(t) = \frac{2P(t)}{\pi DB}$ , where  $P(t) = \frac{A_B}{A_s} E_B (\varepsilon_i + \varepsilon_r)$ , the loading rate is determined by  $\dot{\sigma} = \frac{\partial \sigma}{\partial t}$ .

Close views of the dynamic compression and BD tests in SHPB system are shown in Fig. 3.12.



**Fig. 3.12(a)** photograph of the dynamic compression and **(b)** BD test

The schematic of the SHPB used in this project is shown in Fig. 3.13. SHPB system consists of a gas gun, a striker (0.4 m), an incident bar (2.4 m), a transmitted bar (1.4 m) and a momentum bar (0.8 m). The striker and bars made with high strength 40Cr steel, and share the diameter of 50 mm and have a nominal yield strength of 800 MPa, the P-wave velocity of 6100 m/s, and elastic modulus of 208 GPa. The striker launched by the gas gun impacts the incident bar to generate a compressive wave which propagates through the specimen and afterwards to the transmitted bar. The strains induced by the wave on the bars are measured

by two sets of strain gauges attached on the incident and transmitted bars; the voltage signals from strain gauges were then amplified by a differential amplifier through a Wheatstone bridge (half bridge circuits).

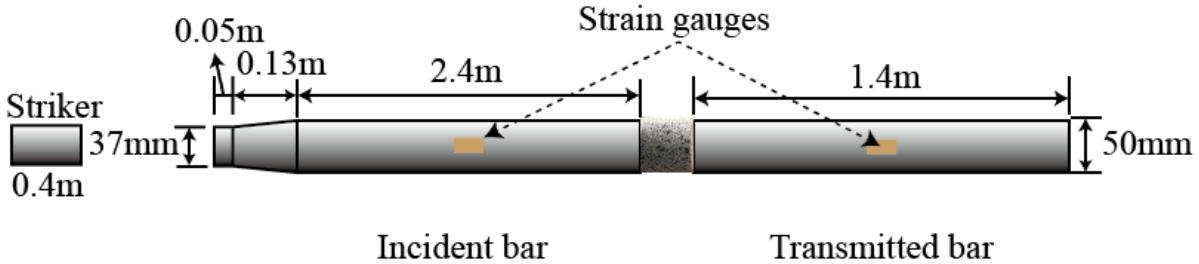


Fig. 3.13 Geometry of the SHPB

The contact surfaces between the specimen and the bars are lubricated with molybdenum disulphide grease to minimize friction. The rubber with the dimension of 10 mm×0.2 mm (diameter × thickness) was attached to the impact face of the incident bar as a pulse shaper.

### 3.4 ACQUISITION SYSTEM

National Instrument data acquisition (DAQ) system, as shown in Fig. 3.14, is integrated into the SHPB test. The velocity of the striker is calculated with the duration of passing two beams of lasers, as shown in Fig. 3.15, where its voltage signal was acquired by a multifunction DAQ card (NI PXIe-6361). The voltage signals from strain gauges are digitised and recorded by a 1 MHz and 12-bit analogue-to-digital converters (NI PXIe-5105) with a low-pass filter at a threshold frequency of 10 kHz. Synchronous transistor-transistor logic (TTL) signals to trigger high-speed cameras are generated by a digital trigger provider (NI BNC-2090A) when striker passed the laser beam.



Fig. 3.14 Data acquisition and signal generator system.

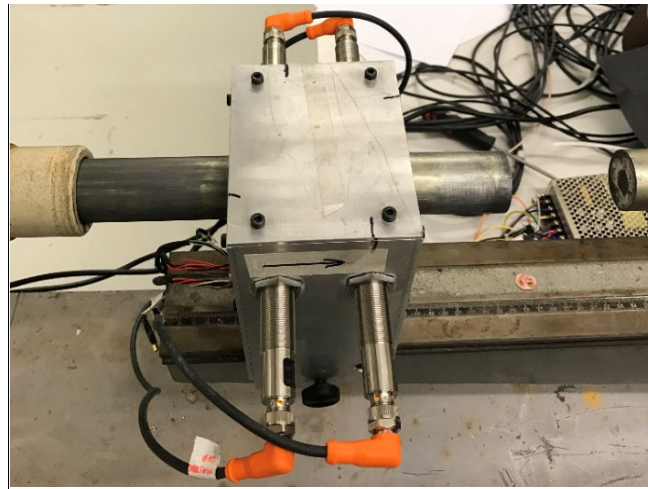


Fig. 3.15 Laser beams to measure striker velocity

The process of SHPB test with voltage signals acquisition is as follows,

1. Connect the BNC cables from the amplifier to the oscilloscope. Check the right channels and connect them. Make sure the amplifier and oscilloscope are grounded. Turn ON the amplifier and oscilloscope and pre-heat for about 30 minutes to achieve a stable working condition.
2. The excitation voltage and gain are set to 2V and 10 respectively. Set the voltage levels, trigger position, data duration time (2 ms to 4 ms), for all the channels in NI DAQ system. Specify the bandwidth of the channel. Balance the Wheatstone bridge for all the channels by turning the reset button. Specify reference position, for instance, a value of 25.0 means 25% of the acquired data will be pre-trigger samples and 75%

will be post-trigger samples. Set the filter type including low pass filter, high pass filter, band pass filter, band stop filter and smoothing filter.

3. Check whether the bars are well aligned or not, and also the projectile should be well aligned to the impact end of the incident bar. Then make sure that the bars are moving freely. It is recommended to test the alignment and contact of bars by impacting the bars without specimen. There should be no reflective wave and the incident wave is consistent to the transmitted wave if the alignment and contact between bars are good. This step can also ensure the strain gauge signal recording is well.
4. Select the striker according to required strain rate and wave length. Strain rate can be varied by using different pressures and different striker bars. Clean the interfaces of the bars and the projectile with acetone. Push the projectile to the end of the barrel of gas gun. Lubricate both faces of the test specimen with Molybdenum disulfide lubricant and sandwich the specimen between the bars and align the specimen with respect to bar center. Place the pulse shaper at the impact end of the incident bar and align it with respect to bar center. Release the nitrogen gas from the gas tank into the gas gun chamber until the required pressure level is achieved. Once again, ensure that the specimen is well aligned between the bars and verify the status of the trigger before pressing the solenoid valve release button. Press control box button to release the projectile. Save captured data for further analysis. After the experiment is completed, turn off the cylinder and make sure all the left-over nitrogen gas in the gas chamber is released.

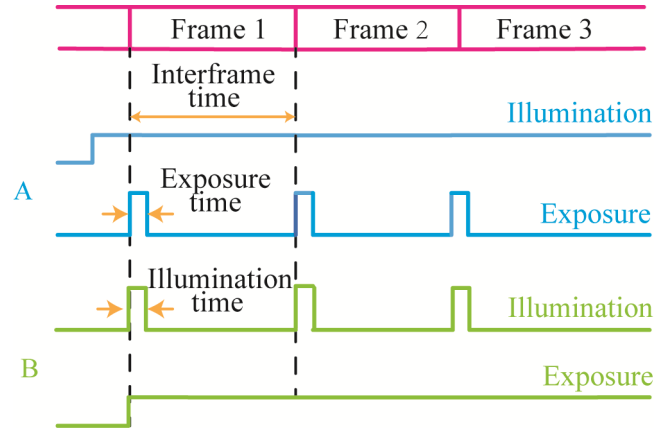
### **3.5 FULL-FIELD MEASUREMENT**

#### **3.5.1 High-speed photography**

##### **(a) Frame rate, exposure time and resolution**

The frame rate, refers to the number of frames taken per second. The reciprocal function of the frame rate is approximately the interframe time (depending on whether the exposure time is included in the calculations or not), simply the time between frames, and essentially defines the temporal resolution of the system. Fig. 3.16 is a schematic representation of the definitions of frame rate, interframe time, exposure time, and illumination time in a series of successive frames. It illustrates two different high-speed photography methods, firstly a long

illumination and short exposures controlled by the camera, and secondly a long camera exposure illuminated by short bursts of illumination.



**Fig. 3.16** Illustration of interframe time, exposure time and illumination time. A: a long illumination and short exposures controlled by the camera, and B: a long camera exposure illuminated by short bursts of illumination (after Versluis 2013).

The optimum frame rate for the observation  $f$  can be estimated from:

$$f = N \cdot u / l \quad (3.7)$$

where  $N$  represents the required number of samples, a minimum value of 2, but a typical value of 5-10 would be more appropriate,  $u$  is a typical velocity, and  $l$  is a typical length scale. According to Eq. 3.7, the required frame rates for some common experimental setups are listed in Table 3.1.

**Table 3.1** Some common high strain-rate tests of geomaterials and their required frame rates.

Application	Frame Rate (kfps)
Blast effect	5-50
Projectile penetrating	25-75
Shock tube work	25-100
Hopkinson bar test	100-1,000
High rate fracture	300-1,000
Explosive detonation initiation	1,000

For SHPB test, a typical wave propagation velocity in the geomaterial sample is several kilometres per second (i.e., millimetres per microsecond). Thus, millimetre sized samples require microsecond interframe times or approximately a frame rate of hundreds of kfps. In this study, 100 to 200 kfps is appropriate for measuring the dynamic behaviour of rock in SHPB test.



The exposure time is the time for which light is collected for an image. In order to build up a sequence of still images (without motion blur) that show the change in a scene with time, the exposure time is typically shorter than the interframe time. One criterion for the necessary exposure time is the time taken for an object to move its own length rather than the object's speed (Ray 2006). Therefore, the smaller the object is, like sand, the shorter the exposure time is likely to be in many situations. As seen in Fig. 3.17, the impact of a steel ball into fine very loose sand is well defined by short exposure time (Lohse, Bergmann et al. 2004). Standard shutter time for digital camera is  $1\mu\text{s}$ , but can also be as short as hundreds of nanoseconds (ns), however, such options are often export controlled. Specialized double-frame particle imaging velocimetry (PIV) cameras are capable of having exposure times of 200 ns, while an intensified CCD camera can have an exposure time as short as 250 ps owing to the fast electronic gating of the image intensifier which converts photons imaged onto a photocathode to electrons (Versluis 2013). The short-pulse laser illumination developed by the Oxford Laser Company can enhance camera performance by reducing the effective exposure time to  $1/40,000,000$  of a second (25 ns).



Fig. 3.17 An oblique impact of a steel ball into fine very loose sand creates a splash followed by a jet in the backward direction (Lohse, Bergmann et al. 2004).

In this study, the aperture is set as its maximum value and the exposure time is chosen the minimum value under all resolution which was around  $4\mu\text{s}$ .

Digital high-speed imaging is always memory hungry because thousands or millions of photos have been captured even in one second which means large memory and throughput ability are required at the same time. The size of one picture can be obtained by the following equation,



$$\text{Size/frame (bytes)} = \text{Horizontal pixel} \times \text{Vertical pixel} \times \text{Bit depth}/8 \quad (3.8)$$

$$\text{Size (bytes)} = \text{Horizontal pixel} \times \text{Vertical pixel} \times \text{Bit depth}/8 \times \text{frames} \quad (3.9)$$

where the bit depth determines the maximum number of gray scale levels that the sensor can see. The 12-bit cameras can clarify 12 levels of gray i.e.  $2^{12}$  or 4,096 levels of gray. In general, the larger the bit depth is the better the images are, but the larger the file size will be. Taking a photo of 1,280×800 resolution with 12-bit color depth as an example, the size per frame will be 1.5Mb. If the frame rate is 5000 fps, it will generate 7.3 Gigabytes (GB) recording data in one second, no matter for acquisition or data stream it is a huge figure. The available on-board memory is typically from 8 to 288 GB, when the internal memory (RAM) is fixed, there must be a trade-off between resolution and recording time (frames) according to Eq. 3.9.

In addition to the coupling of resolution and recording time (frames), there is another coupling between frame rates and resolution due to the limitation of the total throughput rate of the digitizer. Because the capacity of the A/D convertor of imaging chip is finite, typically up to several tens of billion pixels per second. Since the internal memory is temporary and not large enough, the data will be transferred to the external memory in a reduced speed up to one billion pixels per second by flash SSD memory through USB, FireWire or more commonly Ethernet cable before the next recording. However, one second of HD 1,000 fps recording takes up 2 GB memory and 4-second recording may take more than 8 minutes to save onto the external drive which wastes a lot of time between shots. To solve this problem, most high-speed camera companies developed a second RAM-like memory, which has a maximum memory of 2TB, and is a little slower in transferring speed than the original RAM but much faster than that of external drive. Played as a buffer, the same shot mentioned above will be removed from the RAM and saved to the second RAM-like memory in 8 seconds making the camera able to take next shot quickly. At the same time, the data in the second-RAM like memory will be downloaded to the external memory using GB Ethernet or optional fiber-based 10 GB Ethernet. Commonly, a series of experiment will take up to several TB data and one-second recording in 5,000 fps needs nearly 4 minutes to review at a speed of 25 fps. Therefore, several weeks could be consumed to analyze the pictures recorded in several

seconds. In this study, the frame rate is determined as 100-200 kfps. The resolution is expected between  $520 \times 320$  pixels and  $256 \times 256$  pixels to ensure the accuracy of displacement calculation in DIC. The accuracy of the displacement calculation in DIC which will be discussed in the Section 3.5.2.

### **(b) Illumination**

The difficulties encountered in lighting high-speed photography can often be influenced by the limiting factor in the quality of the data obtained, rather than the camera itself (Courtney-Pratt 1957). Since the number of photons impinging on the detector is strongly restricted in a short exposure time, a good deal of photons is required to begin with. This problem is becoming acute when colour images are captured, as the need for three colour filters generally increases the light required by at least a factor of 2.

Various types of lighting available for high-speed photography are summarized in Table 3.2. Nowadays, the light-emitting diodes (LEDs) are becoming more popular as a lighting source in high-speed photography, replacing the older technologies of traditional filament-based flash units. It is possible to vary the output intensity, synchronize with the camera, trigger externally or provide a pulsed output. Moreover, LEDs offer continual light output in addition to flashes, which can be done at short intervals owing the LEDs not requiring a preheat time. However, if one uses LED lights, a high-quality DC power supply is essential to avoid flickering. Another light option is laser pulse, in which a typical high frequency pulsed laser can offer shutter speeds ranging from 30 ns to 250 ns at frequencies up to around 50 kHz without the need for an image intensifier. Both LED and laser systems share an advantage over conventional lighting that they are “cold light” and do not generate high temperatures which could affect some sample types, for example plastics. Laser illumination has the unique advantage of single wavelength illumination, and help with imaging processes which emit light, such as burning. It also allows for interferometric measurements to be made, holography, or PIV measurements through focusing of the beam on a thin sheet.

Based on the above considerations, two 84-watt LED lights (GS Vitec MultiLED LT, shown in Fig. 3.18) provided 15,400 Lumen in total are chosen as the illumination source in the study of rock dynamics.

**Table 3.2** Types of lighting available for high-speed photography (Fuller 2009)

Source	Typical duration (s)
Sunlight	continuous
Tungsten filament lamps	continuous
Continuous arc sources and gas discharge lamps	continuous
Flash bulbs	$0.5-5 \times 10^{-3}$
Electronic flash	$10^{-3}-10^{-6}$
Argon bomb	$10^{-6}-10^{-7}$
Electrical spark	$10^{-6}-10^{-9}$
X-ray flash	$10^{-7}-10^{-9}$
Pulsed laser	$10^{-6}-10^{-12}$
Super radiant light sources	$10^{-9}$
LED	continuous or up to $5 \times 10^{-7}$



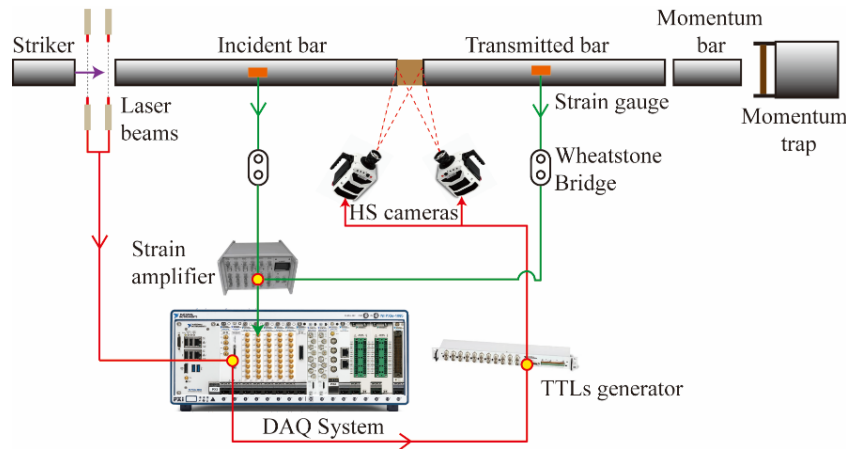
**Fig. 3.18** GS Vitec Multi LED Light

### (c) Triggering

For high-speed imaging, triggering largely influence the success or failure of the recording of interest due to the limited number of frames captured within extremely short time. Triggering is also essential, since other measurements like strain gauges and acoustic emission recordings need to have a common zero to aid post-experimental analysis. There are several triggering methods commonly used, such as manually (i.e., pushing a button), through triggering a computer interface, and by a signal from a delay/pulse generator. Generally, a generator takes a variety of inputs and depends on the type of optical, acoustical and magnetic signals that can be transferred into electrical trigger. The transistor-transistor logic (TTL) signal is widely used for high-speed camera. It should be noted that the transportation of trigger signal needs time, which can be considerable in relation to the framing time in ultra-high-speed imaging, and causes a delayed trigger. Programmable delays on selected input and output triggers are usually accurate to a few nanoseconds. Some camera systems will introduce an unavoidable delay of their own, for example, rotating prism

cameras need a period of time to accelerate up to a wanted framing rate before recording. If standard flash lamps are used, the warm-up time will also need to be incorporated into a delay sequence to avoid dark photos. When continuous recording is available (i.e., images are recorded to a buffer which is continuously overwritten), further triggering options become available. If the start of an event is important or an event before triggering is of interest, one may adopt pre-triggered acquisition where the trigger tells the camera to keep the frames recorded before a certain point.

For the rock dynamic test with SHPB system, two synchronous transistor-transistor logic (TTL) signals are applied to trigger two high-speed cameras generated by a digital trigger provider (NI BNC-2090A) when striker passed the laser beam. A schematic of TTL triggering signals integrated in SHPB is shown in Fig. 3.19.



**Fig. 3.19** Schematic of TTL triggering signals integrated in SHPB

#### (d) High-speed camera selection

There are two types of high-speed camera based on CMOS and CCD sensor types. CMOS and CCD technologies were developed roughly at the same time (1963 and 1969, respectively). Both components are based on the photoelectric effect, the discovery of which won the Nobel Prize in Physics in 1921. The main difference between them is how the value of the electric charge of each cell in the image is read. In CCD architecture, as shown in Fig. 3.20(a), after each exposure, the charges in every row of pixel are moved into the buffer device successively and then are guided to the amplifier on the edge of the CCD. Finally, an output is generated from an analogue to digital converter (ADC) in sequence. In most CMOS

devices, as shown in Fig. 3.20(b), there are several transistors at each pixel that amplify and move the charge using more traditional wires. Based on these differences, the CCD architecture allows high-quality, low-noise images. Conversely, CMOS enables parallel and partial readout of subareas of the sensor at higher rates. However, as the CMOS architecture tends to be utilised in consumer devices and therefore receives more development, the line between CCD and CMOS image quality has become more blurred.

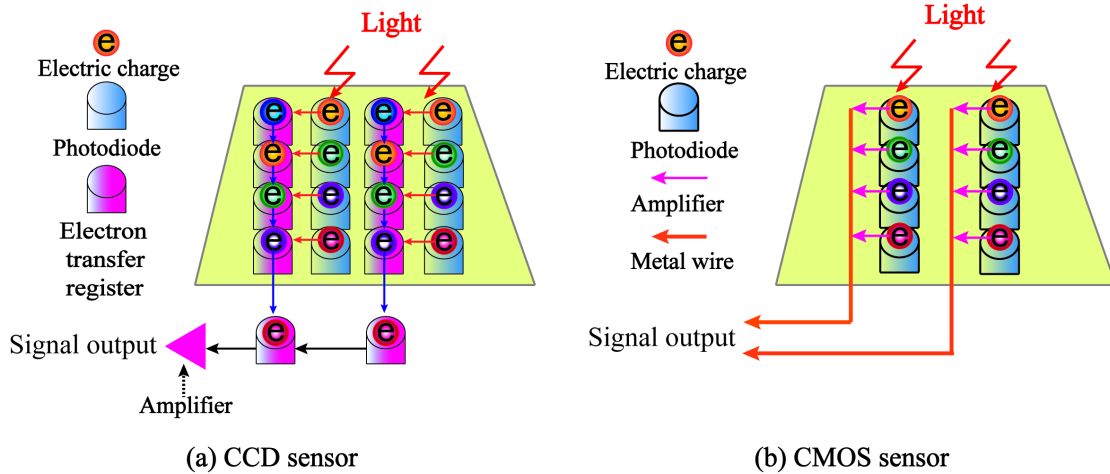


Fig. 3.20 Schematic of (a) CCD sensor and (b) CMOS sensor

A diagram showing the performance of currently available CMOS and CCD-based digital cameras is shown in Fig. 3.21. As can be seen, there is a large gap between the frame rate/record length of the CMOS-based cameras and that of the CCD-based cameras. The CMOS-based cameras normally have a frame rate limitation of around Mfps (except Kirana and Shimadzu HPV) with a relatively small resolution. However, the number of frames easily exceed 50,000. In terms of CCD-based cameras, the frame rate can be more than 100 Mfps with a large resolution but less than 100 images can be captured. Meanwhile, the maximum resolution for CMOS-based camera decreases with the increase of frame rate, but not for CCD-based cameras. The high frame rate of CMOS-based camera relies on the high detector sensitivity and fast data transfer rate of a single detector. The maximum throughput of this design is stationary, which means a higher frame rate needs to sacrifice the resolution per image and vice versa. The design of CCD-based camera follows that of original film-based rotating mirror or beam splitter device, where the image is relayed onto a number of distinct detectors or spatially separated areas on a single detector. As a result, the resolution and

## CHAPTER 3 EXPERIMENTAL SET-UP

frame rate are independent. The gap in the middle zone are series of intermediate-rate experiments that are currently not adequately covered by a high-speed camera.

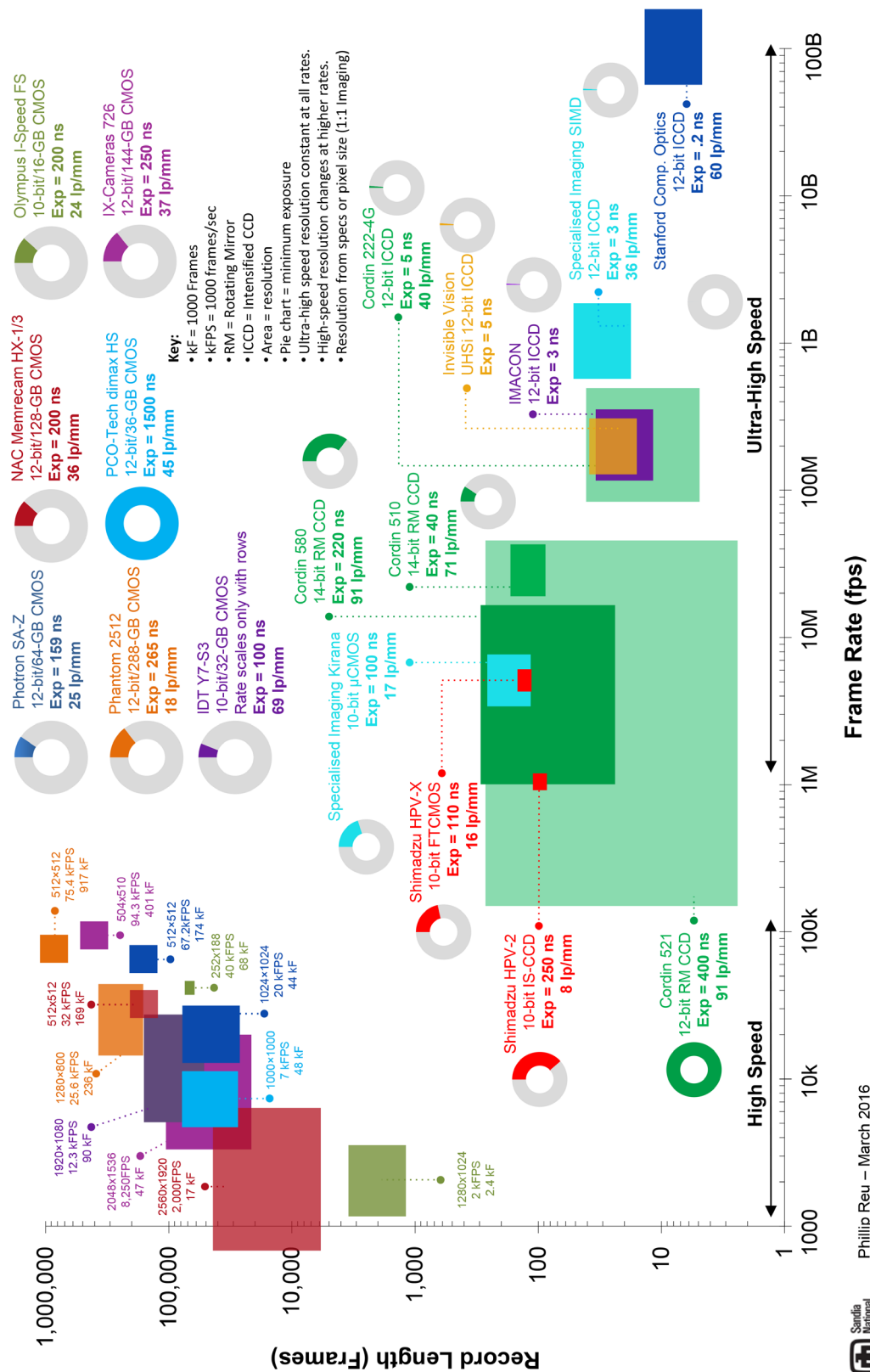


Fig. 3.21 Survey of current HS cameras based on CMOS and CCD technologies (the maximum resolution is proportional to the area of the representative rectangle of each camera), courtesy of Dr. Reu. (Reu and Miller 2008)

Although the frame rate and resolution can be at a high level at the same time for CCD camera, but the total frames it can achieve is not enough for rock dynamics analysis. The short recording time of CCD high-speed camera also poses challenges in the trigger which has to be very accurate by signals to pre-trigger which increases the complexities in rock dynamic experiments. By considering above pros and cons of different commercial high-speed cameras, Phantom V2511 CMOS ultra-high-speed camera is selected in this study, as shown in Fig. 3.22. Phantom V2511 is one of the fastest megapixel digital high-speed cameras on the market, V2511 is 12 bits capable of taking over 25,000 frames-per-second (fps) at full resolution of  $1280 \times 800$  pixels.



Fig. 3.22 Phantom V2511 ultra-high-speed camera

With the FAST option, up to 1,000,000 fps at reduced resolution can be achieved for 7.6 seconds recording time. Programmable trigger location (pre/post trigger recording) is available from image-based auto-trigger standard, trigger from software, hardware trigger BNC. It has the 15ns timing accuracy in synchronization which is important to stereovision establishment. 10 Gb Ethernet is offered for control and data transfer.



### 3.5.2 High-speed 3D-DIC

DIC belongs to a class of non-contact methods that acquire images of an object, store images in digital form and perform image analysis to extract full-field shape, deformation or motion measurements (Sutton, Orteu et al. 2009). The principle of DIC is a matching of the same two-pixel points from reference and deformed images to determine the desired displacement. For simplicity, the matching of the same two pixels from two images to determine the desired displacement is schematically illustrated in Fig. 3.23. In order to obtain the displacement of a point  $P$ , a square subset centred at a point  $P(x_0, y_0)$  is chosen as the reference subset. Then the DIC algorithms search its corresponding subset in the deformed image as the target subset, after which the center point of the target subset is the point  $P(x'_0, y'_0)$  in the deformed image. The DIC algorithms are also known as the correlation criterion for evaluation of the similarity degree between the reference subset and the target subset. Although different definitions of correlation criteria can be found in the literature, these correlation criteria can be categorized into two groups, namely CC criteria and SSD correlation criteria. More information about the correlation criterion can be found in (Giachetti 2000, Tong 2005). Once the displacement of the center of a subset is determined by  $u$  and  $v$  in the horizontal and vertical directions respectively, then another deformed pixel  $(x'_i, y'_i)$  can be obtained by the first-order shape function from the pixel  $(x_i, y_i)$  in the reference subset:

$$x'_i = x_i + u + \frac{\partial u}{\partial x} \Delta x + \frac{\partial u}{\partial y} \Delta y, \quad y'_i = y_i + v + \frac{\partial v}{\partial x} \Delta x + \frac{\partial v}{\partial y} \Delta y \quad (3.10)$$

where  $\Delta x$  and  $\Delta y$  are the horizontal and vertical distances from the subset center to point respectively. The first-order shape function allowing translation, rotation, shear, normal strains and their combinations of the subset is most commonly used. However, when apparent non-homogeneous deformation presents, the twelve-parameter second-order shape function capable of depicting more complex local deformation has been demonstrated to provide high accuracy (Lu and Cary 2000, Yu and Pan 2015).

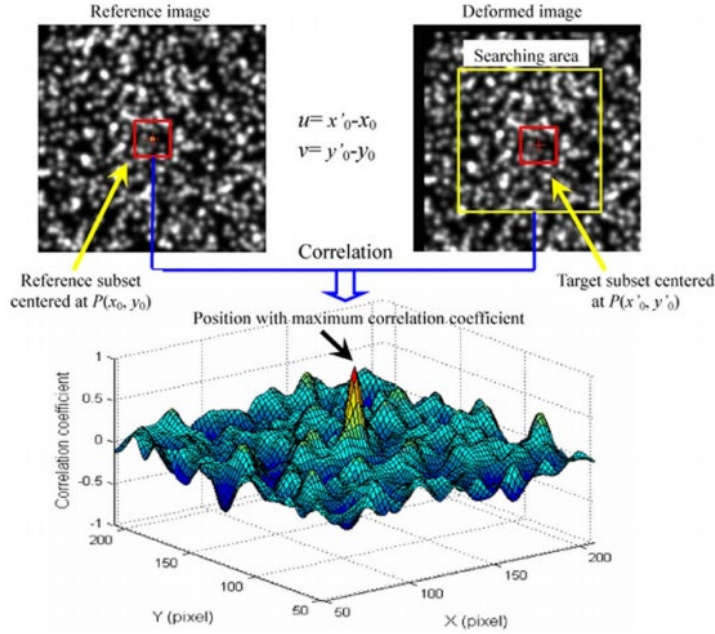


Fig. 3.23 Schematic of a reference subset before deformation and a target subset after deformation. The center position of the target subset is obtained through searching the peak position of the distribution of the correlation coefficient (Pan, Xie et al. 2010).

To reveal the three dimensional displacements, 3D-DIC based on the principle of binocular stereovision (Luo, Chao et al. 1993) was developed. For simplicity, the principle of the binocular stereovision is illustrated in Fig. 3.24. When pixel  $M_1$  moved to  $M_2$ , its projection on left camera is the same which means one camera cannot detect the depth. However, when another camera exists, the projection coordinate of  $M_2$  in right camera is  $m_2$  instead of  $m_1$ , on the other hand, the intersection of line  $O_2m_2$  and  $O_1m_0$  is one and only at the unique point  $M_2$ . The detailed binocular stereovision principle and algorithm are discussed in (Ayache and Hansen 1988). Two cameras are necessary to establish the stereovision by calibrating the space coordinates to reconstruct the 3D position from transformation matrices.

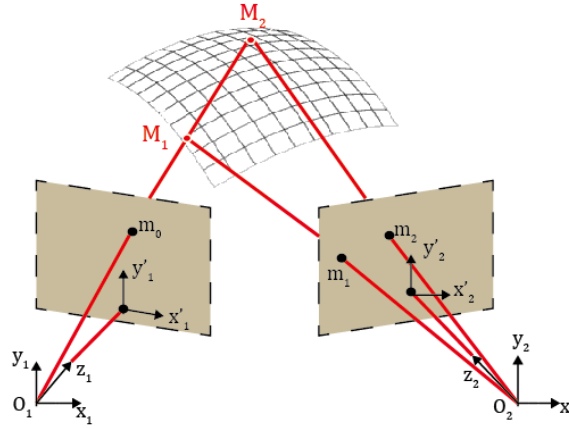


Fig. 3.24 Binocular stereovision illustration. (O1, O2 are origins of left and right cameras; M1 and M2 are reference and deformed points in the 3D space, respectively)

Once calibration is finished, image pairs from two synchronized cameras are firstly processed to determine ‘x’ and ‘y’ coordinate (2D-DIC process). The 3D shape is finally established after the ‘z’ coordinate being determined by binocular stereovision principle between two deformed images. The displacement is obtained through the subtraction of a pair of neighbouring 3D shapes. Strain fields are constructed after a differentiation on displacement fields and a further differentiation on strain field gives the strain rate fields. An illustration of 3D-DIC process is shown in Fig. 3.25.

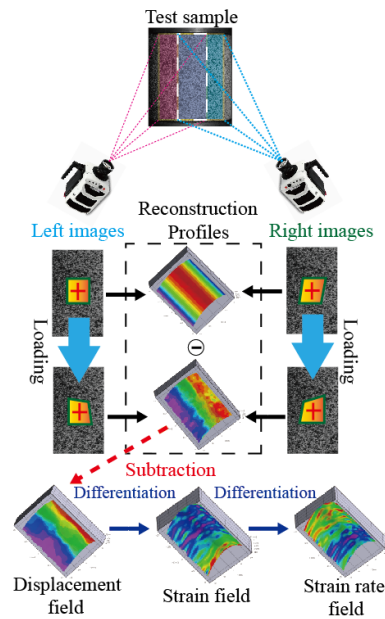


Fig. 3.25 Schematic of 3D-DIC and deformation field determination

DIC technique is regarded as one of the most promising and ideal means to measure the dynamic deformation of materials because of its accuracy, applicability and operability (Pan, Yu et al. 2017). A brief summary of application of high-speed 3D-DIC in dynamic tests is listed in Table 3.3.

**Table 3.3** Brief summary of high-speed 3D-DIC in dynamic tests

Material	High-speed camera	Testing method	Frame rate (fps)	Resolution (pixels)	AOI (mm <sup>2</sup> )	Reference
TC4 Alloy	N/A	Direct tension	100,000	208 × 96	18 × 5	(Fan, Wei et al. 2015)
Polymeric foams	Photron SA-X2	Compression	100,000	384 × 264	42 × 39	(Koohbor, Kidane et al. 2016)
Carbon/epoxy composite	Photron SA1	Implosion	50,000	1024 × 1024	76 × 51	(Pinto, Gupta et al. 2015)
Reinforced carbon	Phantom v7	Ballistic impact	26,900	256 × 256	355 × 355	(Schmidt, Tyson et al. 2005)
Aluminium and steel	Phantom v1610	Airblast	21,000	896 × 800	4000 × 4000	(Aune, Fagerholt et al. 2016)
Braided composite	(Photron SA5	Ballistic impact	15,000	896 × 560	Ø 120	(Pan, Yu et al. 2016)
Steel	Photron APX-RS	Double Lap Shear	10,000	1024 × 1280	600 × 22	(Raurova, Berggreen et al. 2010)

When it comes to geomaterial, Zhang and Zhao (Zhang and Zhao 2013) presented a detailed experimental procedure of high-speed 2D-DIC to determine the mechanical properties and full-field strain of rock under dynamic loads. Strain localization and the onset of fracture were examined under three loading conditions: NSCB, BD, and uniaxial compression (UC). Afterwards, a number of SHPB tests on geomaterials in conjunction with high-speed DIC technology have been conducted. A summary of high-speed DIC applied to rock materials is shown in Table 3.4.

It can be seen from Table 3.4 that 3D-DIC analysis was seldom conducted with two high-speed cameras, except the analysis of the dynamic BD test on Kuru granite experiment conducted by (Mardoukhi, Saksala et al. 2015). In geometries, such as UC where out of plane displacement is a particular problem, however, no 3D-DIC has been applied in dynamic UC tests on geomaterials. It can also be seen from Table 3.4 that most experiments were conducted with CMOS-based digital high-speed cameras which have sufficient performance for dealing with DIC (Tiwari, Sutton et al. 2007).

Gao et.al. (Gao, Huang et al. 2015) used an ICCD type camera to record the NSCB test on Laurentian granite for DIC analysis. However, ICCD has the drawbacks of beam splitting or image intensifying, which decreases the dynamic range and increases noise levels. The errors in DIC using an ICCD high-speed camera are described in detail by (Tiwari, Sutton et al. 2007). Fourmeau et.al. (Fourmeau, Gomon et al. 2014) used a rotating-mirror type CCD camera to capture Kuru Granite in BD test, thus avoiding some of the ICCD problems. The errors in DIC from rotating mirror camera images is described by (Kirugulige and Tippur 2009). ISIS-CCD high-speed cameras are also well suited to DIC but have not been applied in dynamic tests on geomaterials yet. Rotating prism high-speed cameras have not been used successfully for the 3D-DIC due to the image misalignments caused by the rotating prism (Reu and Miller 2008). Details about distortions in high-speed cameras and their corrections related to image correlation are discussed in (Tiwari V, Sutton M et al. 2007)

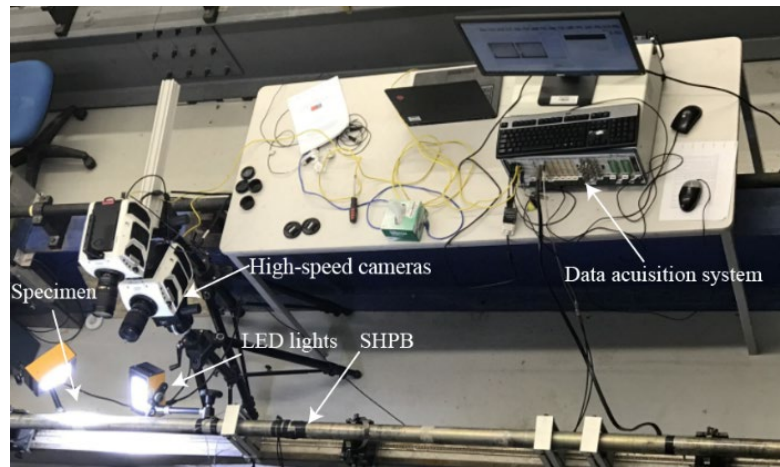
# CHAPTER 3 EXPERIMENTAL SET-UP

**Table 3.4** Summary of the main results on high-speed DIC application to rock materials with SHPB test

Loading Method	Testing Methods	Geomaterial type	High-speed camera type	Frame rate(fps)	Spatial resolution (pixels array size)	Reference
<b>Tension</b>	BD test	Fangshan Marble	Photron Fastcam SA1.1 (CMOS)	60,000	448×192	(Zhang and Zhao 2013)
	BD test	Granite	Photron Fastcam SA5 (CMOS)	100,000	320×192	(Chen, Guo et al. 2014)
	BD test	Kuru Granite	Two Photron Fastcam SA-X2 (CMOS)	160,000	256×176	(Mardoukhi, Saksala et al. 2015)
	BD test	Kuru Granite	Cordin 535 (Rotating mirror CCD)	200,000	Full field	(Fourmeau, Gomon et al. 2014)
	BD test	Sandstone	Photron Fastcam SA1.1 (CMOS)	10,000	192×192	(Yin, Wang et al. 2014)
	BD test	Carrara Marble	Not mentioned	100,000	270×70	(Zou and Wong 2014)
	DT test	Textile-reinforced concrete	Phantom v7.3 (CMOS)	10,000	Not mentioned	(Yao, Bonakdar et al. 2014)
<b>Compression</b>	UC test	Fangshan Marble	Photron Fastcam SA1.1 (CMOS)	60,000	256×256	(Zhang and Zhao 2013)
	UC test	Dam concrete	IDT-Y4 (CMOS)	17,000	225×725	(Caverzan, Peroni et al. 2016)
<b>Combined compression and shear</b>	UC and shear coupling test	Granite	Phantom-675 (CMOS)	74,000	240×208	(Xu, Huang et al. 2015)
	UC and shear coupling test	Granite	Phantom V12.1 (CMOS)	71,400	240×208	(Zhang 2014)
<b>Bending</b>	NSCB test	Fangshan Marble	Photron Fastcam SA1.1 (CMOS)	125,000	256×144	(Zhang and Zhao 2013)01
	NSCB test	Laurentian granite	Ultra UHSi 12/24 IVV Imprint™ (ICCD)	180,000	1,082×974	(Gao, Huang et al. 2015)
	NSCB test	Fangshan Marble	Photron Fastcam SA1.1 (CMOS)	125,000	256× 128	(Yin, Ma et al. 2014)

Full field means the spatial resolution of the camera is capable of recording the full image of specimen

In this study, for a cylindrical rock specimen, two cameras were configured to be symmetrical along the axial to achieve a regular view of interest in DIC analysis; therefore, two V2511 ultra-high-speed cameras were mounted by tripods as an up-down position aiming at the specimen with good focus. Two cameras were equipped with the lenses of Nikon AF-S DX Nikkor 18-105 mm F/3.5-5.6G ED. For dynamic compression test, according to the scale of the actual image size ( $59\text{mm} \times 59\text{mm}$ ) to the resolution, each pixel length represented 0.23 mm. The DIC matching accuracy is controlled as 5% of the pixel length (0.0115 mm) in this work, which corresponds to 0.00237 % (23 micro strain) in engineering strain. To avoid distortion, no transparent shelter was set in front of the cameras. Two LED lights with high-strength glass were set close to the sample, which protect high-speed cameras from the flying debris. In addition, an UV filter as an extra protector for camera was applied which has no disturbance to the raw image. The setup of SHPB coupled with two high-speed cameras system is shown in Fig. 3.26.



**Fig. 3.26** Photo of the SHPB and high-speed imaging system

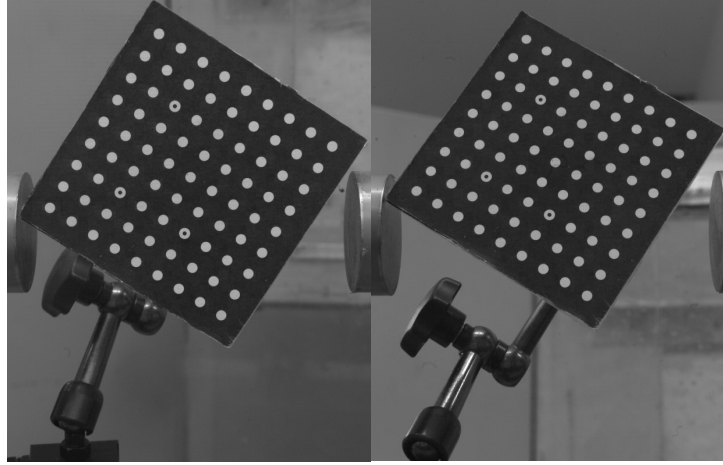
According to the principles of DIC measurement, the quality of speckle patterns significantly affects the accuracy of measurement results (Reu 2014, Reu 2014). The speckle pattern should be randomly distributed in a proper density with good contrast and each speckle must be at least three pixels in size. Rock specimens were speckled by spray painting in this study, as shown in Fig. 3.27.



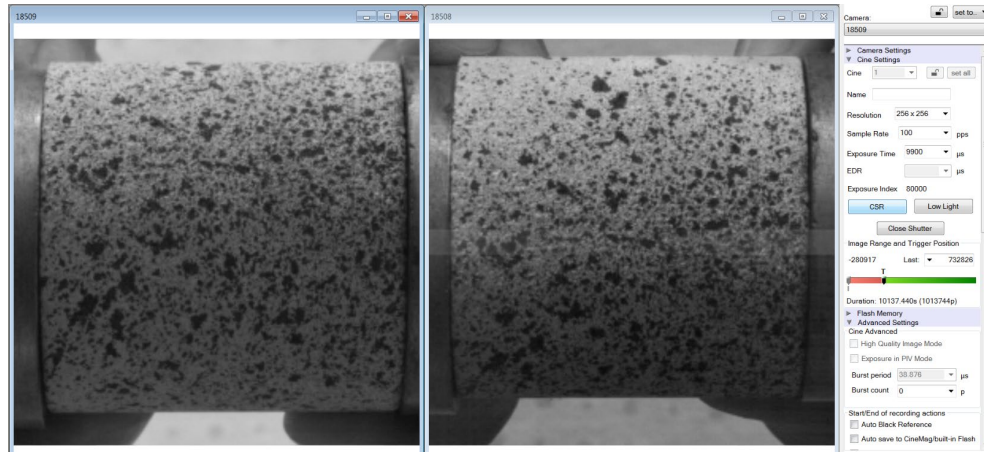
**Fig. 3.27** A typical well-speckled sandstone specimen

After position, aperture and focus of two cameras are configured, the calibration was conducted under the maximum resolution to achieve the best performance. By moving, tilting and rotating the calibration target, totally twenty pairs of images of target were captured to calibrate the upper and lower cameras. The calibration target was a plastic board (100 mm  $\times$  100 mm) with black base and  $9 \times 9$  white grids (grid space 10 mm), as shown in Fig. 3.28. The standard deviation of residuals in calibration in the tests were below 0.10 (in pixels) indicating the calibration was adequate for measuring (Sutton, Orteu et al. 2009). The tripod supporting the camera might still be hit by the flying debris, therefore after every single impact the calibration score was checked ensuring within the acceptable range by inputting a new pair of images of the calibration board. New calibration must be conducted if the latest score exceeds the tolerance. After calibration was completed, image pairs were recorded at the desired frame rate and resolution by two synchronised cameras, as shown in Fig. 3.29. The cropping adjustment function in the software can recognise the actual resolution and apply a modified calibration to the speckle images.





**Fig. 3.28** A typical calibration process by capturing standard grid target



**Fig. 3.29** Synchronized views of specimens in two cameras

The configurations of DIC in this study are as follows: subset: 17, step: 1, subset weights: Gaussian weights, interpolation: optimised 8-tap, correlation criterion: zero-normalized squared differences (ZNSD). During the correlation, the confidence margins (error tolerance during the matching) were under 0.05 pixel by a computing threshold. Because the duration from wave propagation to fracturing in the specimen is around 200  $\mu\text{s}$  and the interval time for each image is 5  $\mu\text{s}$ , roughly 40 pairs of images were valuable for the post processing.

The whole procedure for 3D-DIC establishment in SHPB test is as follows,

Set up the tripods, mount two cameras up and down to have a perpendicular view on the target which can directly provide a normal coordinate. Turn on the cameras and pre-heat for 30 minutes to have a stable working condition. Set the resolution as the expected one but

leave the exposure time and frame rate at low value. Adjust the position of the camera and lens to have a good focus on the speckle. Set the frame rate and exposure time to the experiment ones and set up the LED light until rock specimen has a good contrast in high-speed photography. Turn off the LED light and set the full resolution with low frame rate and high exposure time for better recognition by calibration algorithm. By moving, tilting and rotating the calibration target, totally twenty pairs of images of target are suggested to be captured. Check the calibration score. Once the calibration is good, cameras are not allowed to move anymore, or the cameras have to be calibrated again. Set the frame rate, resolution and exposure time to the expected ones and prepare the triggering mode and position. After the capture is completed, the video is recommended to cut to a smaller size with useful information, because the on-board memory will be deleted when a new capture begins. The clip is further converted to a sequence of images for DIC to calculate.

### 3.6 SUMMARY

The basics of high-speed photography, such as the frame rate, the exposure time, and illumination are introduced with suggested method to evaluate the proper parameters above. It is noted that LEDs have become more and more popular in high-speed imaging illumination, due to their adaptability and cold light. The currently available digital high-speed cameras were summarized. Fig. 3.21 clearly shows that the CCD-based high-speed cameras are dominant in terms of the frame rate and spatial resolution, but have a smaller frame number. CMOS-based cameras have the trade-off of temporal and spatial resolution but could be solved with the development of sensor and memory. It is likely to see CMOS high-speed camera will become the dominant technology in the future due to the inherent drawbacks of CCDs. Triggering is extremely important for use of high-speed cameras. Programmable delay on selected input and output triggers is usually in nanoseconds, and good triggering design is essential for the success of the experiment.

## REFERENCES

- Aune, V., et al. (2016). "Experimental study on the response of thin aluminium and steel plates subjected to airblast loading." *International journal of impact engineering* 90: 106-121.
- Ayache, N. and C. Hansen (1988). Rectification of images for binocular and trinocular stereovision. *Pattern Recognition*, 1988., 9th International Conference on, IEEE.
- Caverzan, A., M. Peroni and G. Solomos (2016). "Compressive behaviour of dam concrete at higher strain rates." *The European Physical Journal Special Topics*: 1-11.
- Chen, J., B. Guo, H. Liu, H. Liu and P. Chen (2014). "Dynamic Brazilian Test of Brittle Materials Using the Split Hopkinson Pressure Bar and Digital Image Correlation." *Strain* 50(6): 563-570.
- Collins, A., J. Addiss, S. Walley, K. Promratana, F. Bobaru, W. Proud and D. Williamson (2011). "The effect of rod nose shape on the internal flow fields during the ballistic penetration of sand." *International Journal of Impact Engineering* 38(12): 951-963.
- Fan, Y., et al. (2015). "On the application of digital image correlation testing technology in hopkinson bar loading." *Journal of Experimental Mechanics (Chinese)* 30(5): 591-598.
- Field, J. E., et al. (2004). "Review of experimental techniques for high rate deformation and shock studies." *Int J Impact Eng* 30(7): 725-775.
- Fourmeau, M., D. Gomon, R. Vacher, M. Hokka, A. Kane and V.-T. Kuokkala (2014). "Application of DIC technique for studies of Kuru Granite rock under static and dynamic loading." *Procedia Materials Science* 3: 691-697.
- Gao, G., S. Huang, K. Xia and Z. Li (2015). "Application of digital image correlation (DIC) in dynamic notched semi-circular bend (NSCB) tests." *Experimental Mechanics* 55(1): 95-104.
- Giachetti, A. (2000). "Matching techniques to compute image motion." *Image and Vision Computing* 18(3): 247-260.
- Gray III, G. T. (2000). "Classic split Hopkinson pressure bar testing." *ASM Handbook Vol 8, Mechanical testing and evaluation*. ASM Int, Materials Park OH 8: 15.
- Kirugulige, M. and H. Tippur (2009). "Measurement of Fracture Parameters for a Mixed - Mode Crack Driven by Stress Waves using Image Correlation Technique and High - Speed Digital Photography." *Strain* 45(2): 108-122.
- Kolsky, H. (1949). "An investigation of the mechanical properties of materials at very high rates of loading." *Proceedings of the Physical Society. Section B* 62(11): 676.
- Koohbor, B., et al. (2016). "Investigation of the dynamic stress-strain response of compressible polymeric foam using a non-parametric analysis." *International journal of impact engineering* 91: 170-182.
- Lu, H. and P. Cary (2000). "Deformation measurements by digital image correlation: implementation of a second-order displacement gradient." *Experimental Mechanics* 40(4): 393-400.
- Luo, P., et al. (1993). "Accurate measurement of three-dimensional deformations in deformable and rigid bodies using computer vision." *Experimental Mechanics* 33(2): 123-132.

- Mardoukhi, A., T. Saksala, M. Hokka and V.-T. Kuokkala (2015). "An experimental and numerical study of the dynamic Brazilian disc test on Kuru granite."
- Pan, B., et al. (2010). "Equivalence of digital image correlation criteria for pattern matching." *Applied optics* 49(28): 5501-5509.
- Pan, B., et al. (2016). "Full-field transient 3D deformation measurement of 3D braided composite panels during ballistic impact using single-camera high-speed stereo-digital image correlation." *Composite Structures* 157: 25-32.
- Pan, B., et al. (2017). "Review of single-camera stereo-digital image correlation techniques for full-field 3D shape and deformation measurement." *SCIENCE CHINA Technological Sciences*.
- Pinto, M., et al. (2015). "Study of implosion of carbon/epoxy composite hollow cylinders using 3-D digital image correlation." *Composite Structures* 119: 272-286.
- Raurova, I., et al. (2010). A dual 3D DIC-system application for DSL strain and displacement measurements. *EPJ Web of Conferences*, EDP Sciences.
- Reu, P. (2014). "All about speckles: speckle size measurement." *Experimental Techniques* 38(6): 1-2.
- Reu, P. L. and T. J. Miller (2008). "The application of high-speed digital image correlation." *The Journal of Strain Analysis for Engineering Design* 43(8): 673-688.
- Schmidt, T. E., et al. (2005). Full-field dynamic deformation and strain measurements using high-speed digital cameras. 26th International Congress on High-Speed Photography and Photonics, International Society for Optics and Photonics.
- Sutton, M., J. Yan, V. Tiwari, H. Schreier and J. Orteu (2008). "The effect of out-of-plane motion on 2D and 3D digital image correlation measurements." *Optics and Lasers in Engineering* 46(10): 746-757.
- Sutton, M., et al. (2008). "The effect of out-of-plane motion on 2D and 3D digital image correlation measurements." *Optics and Lasers in Engineering* 46(10): 746-757.
- Sutton, M. A., et al. (2009). *Image correlation for shape, motion and deformation measurements: basic concepts, theory and applications*, Springer Science & Business Media.
- Tiwari V, Sutton M, K. O. McNeill, Fourney W and Bretall D (2007). On studying improvised explosive devices (IEDs) using digital image correlations. *Proc. 2007 SEM Annu. Conf. Exposition Exp. Appl. Mech*, MA, USA, Springfield.
- Tiwari, V., M. Sutton and S. McNeill (2007). "Assessment of high-speed imaging systems for 2D and 3D deformation measurements: methodology development and validation." *Experimental mechanics* 47(4): 561-579.
- Tong, W. (2005). "An evaluation of digital image correlation criteria for strain mapping applications." *Strain* 41(4): 167-175.
- Xing, H. Z., et al. (2017). "High-Speed Photography and Digital Optical Measurement Techniques for Geomaterials: Fundamentals and Applications." *Rock Mechanics and Rock Engineering*: 1-49.

- Xu, S., J. Huang, P. Wang, C. Zhang, L. Zhou and S. Hu (2015). "Investigation of rock material under combined compression and shear dynamic loading: An experimental technique." *International Journal of Impact Engineering* 86: 206-222.
- Yao, Y., A. Bonakdar, J. Faber, T. Gries and B. Mobasher (2014). "Distributed cracking mechanisms in textile-reinforced concrete under high speed tensile tests." *Materials and Structures*: 1-18.
- Yin, Z., H. Ma, Z. Hu and Y. Zou (2014). "Effect of Static-Dynamic Coupling Loading on Fracture Toughness and Failure Characteristics in Marble." *Journal of Engineering Science and Technology Review* 7(2): 169-174.
- Yin, Z., L. Wang, H. Ma, Z. Hu and J. Jin (2014). "Application of Optical Measurement Method in Brazilian Disk Splitting Experiment Under Dynamic Loading." *Sensors & Transducers* 171(5): 176-182.
- Yu, L. and B. Pan (2015). "The errors in digital image correlation due to overmatched shape functions." *Measurement Science and Technology* 26(4): 045202.
- Zhao, H. and G. Gary (1996). "On the use of SHPB techniques to determine the dynamic behavior of materials in the range of small strains." *Int J Sol Struct* 33(23): 3363-3375.
- Zhang, C. (2014). Application of digital image correlation in dynamic testing. Master, University of Science and Technology of China.
- Zhang, Q. B. and J. Zhao (2013). "Determination of mechanical properties and full-field strain measurements of rock material under dynamic loads." *Int J Rock Mech Min* 60: 423-439.
- Zhou, Y. X., et al. (2012). "Suggested methods for determining the dynamic strength parameters and mode-I fracture toughness of rock materials." *Int J Rock Mech Min* 49: 105-112.
- Zou, C. and L. N. Y. Wong (2014). Study of Mechanical Properties and Fracturing Processes of Carrara Marble in Dynamic Brazilian Tests by Two Optical Observation Methods. *Rock Mechanics and Its Applications in Civil, Mining, and Petroleum Engineering*, ASCE.



## **CHAPTER 4 DYNAMIC PROPERTIES AND FRACTURE PATTERNS OF ROCK BY FULL-FIELD MEASUREMENT**

Much of the materials in this chapter have been included in the publication by Xing et al. (2018) in International Journal of Impact Engineering (Vol.113, pp.61-72), titled ‘Full-field measurement and fracture characterisations of rocks under dynamic loads using high-speed three-dimensional digital image correlation’ and the publication by Xing et al. (2018) in Rock Mechanics and Rock Engineering (Vol.51, pp.945-951), titled ‘Stress Thresholds of Crack Development and Poisson’s Ratio of Rock Material at High Strain Rate’.

### **4.1 INTRODUCTION**

Rock deformation and mechanical properties under dynamic loading have a significant impact on various rock engineering areas such as tunneling (Hajiabdolmajid and Kaiser 2003), anti-seismic research (Mavko, Mukerji et al. 2009), hydraulic fracturing (Hubbert and Willis 1972) and mining (Dehkhoda and Hood 2014). The deformation characteristics of rock at high strain rate play a major role in rock engineering safety or efficiency such as rockburst prevention (Cook 1965) and hard-rock cutting (Dehkhoda 2011). The SHPB technique has been recognised as the most successful loading method for determining dynamic properties of various materials (Lindholm 1964, Li and Meng 2003, Gama, Lopatnikov et al. 2004, Zhou, Xia et al. 2012, Zhang and Zhao 2014, Xia and Yao 2015) since its modern design developed in 1949 (Kolsky 1949). The early application of SHPB on rock was reported by Hauser (Hauser 1966) in which a stress-strain curve of rock was derived. After that, testing methods with SHPB were expanded to investigate various dynamic properties of rock such as tensile strength (Dutta and Kim 1993), bending strength (Dai, Chen et al. 2010), shear strength (Xu, Huang et al. 2015) and fracture toughness (Zhang and Zhao 2013). The effects of external factors such as confining pressure (Li, Zhou et al. 2008), water saturation (Huang, Xia et al. 2010) and thermal treatment (Kumar 1968) on the rock dynamic behaviour were also of interest to researchers. The optimisation of the experimental design and bar modification (Li, Lok et al. 2000, Frew, Forrestal et al. 2002, Song and Chen 2006, Frew, Akers et al. 2010) has always been concerned for achieving constant strain rate and stress equilibrium in rock-like materials.

With regard to the deformation characteristics, investigation is more challenging than that of stress on the specimen in SHPB experiments (Chen and Song 2010). The application of high-speed photography in SHPB made it possible to visualise the real-time deformation of the specimen. The initial application of high-speed photography technology in SHPB tests of rock was made by Perkins and Green (Perkins and Green 1968) in 1968 on Solenhofen limestone at the strain rate of  $10 \text{ s}^{-1}$ . The combination of high-speed photography and digital optical measurements allowed the detection of the quantitative information on the specimen surface. To the best of author's knowledge, the study of the full-field deformation of rock materials under dynamic uniaxial compression has not been studied up to now. Therefore, the actual strain evolution on a rock specimen and its difference with the strain calculated from one-dimensional wave propagation theory is not clear. As SHPB has no servo system to adjust the applied loading according to the feedback from the specimen, the loading status of brittle materials like rock is uncertain during post-peak stage. Some deformation properties of the rock under dynamic loading remains indirect calculation.

### (1) Dynamic deformation properties

One of the underrated dynamic deformation properties which plays an undeniably important role in rock deformation under static or dynamic loading is Poisson's ratio. The main reason is the narrow range of its value which people tend to refer to a typical one. Additionally, Poisson's ratio is largely dependent on the loading rate, temperature and stress state which can hardly be predicted accurately. For example, the value of Poisson's ratio for the rock mass in numerical simulation was larger than the value for the intact rock, even  $\nu > 0.5$  were obtained (Bauer and Conley 1987, Bhasin and Høeg 1998, Min and Jing 2003), indicating the anisotropy induced by the joints could affect Poisson's ratio. In some cases, negative Poisson's ratio was reported due to highly anisotropy (Hardy 1976). Although Poisson's ratio has no effect on plane elasticity problems when no body forces involved, in three-dimensional stress conditions, the impact of Poisson's ratio can be fatal. It has been reported many times about the relationship between the geomaterial fracturing and Poisson's ratio. Investigations (Bieniawski 1967, Swamy 1971) have also shown that Poisson's ratio has a significant role to play in studying the formation and propagation of micro-cracks, and in studying the fracture mechanism of geomaterial.



The last reason for Poisson's ratio being underrated is the difficulty in its measurement (Swamy 1971). In terms of the static Poisson's ratio, direct and indirect methods are proposed to carry out the results. For indirect method, determined from the derivation of other elastic constants like elastic modulus  $E$ , shear modulus  $G$  which can be more easily to obtain. However, an error of 2% in the experimental determinations of  $E$  and  $G$  may give an error of up to 20% in the Poisson ratio. When  $G$  is close to  $0.5E$ ,  $\nu$  varies very rapidly which can explain why in many cases negative Poisson's ratio is obtained when  $2G > E$  (Burshtein 1968). With regards to direct method, axial strain was generally recorded by the pressure machine, strain gauge or linear variable displacement transformer (LVDT). The lateral strain is relatively harder to accurately acquire (Swamy 1971). The strain gauge is the most widely used method by attaching horizontally to the axial of the specimen. But large strains will generate when the stress is past the peak which cannot be measured with resistance strain gauges. Moreover, due to the influences of localized failure, it is desirable to measure the volumetric strain as an average over a part instead of one point of the specimen. Such measurements include chain extensometer (Leeman and Grobbelaar 1957), or by fluid level change in fluid-field vessel (Crouch 1970). However, these contact methods will more or less give a confinement. As for dynamic Poisson's ratio, until now only the indirect measurement was introduced such as impulse excitation of vibration (ASTM 1876), sonic resonance (ASTM 1875) or interpreted by the longitudinal and transverse wave velocity. There are also some studies (King 1983, b Heerden 1987, Eissa and Kazi 1988) trying to establish the empirical relationships between the static and dynamic Nevertheless, Poisson's ratio are not conclusive and largely depends on the status of rock and loading condition (Zhang and Bentley 2005). To overcome the disadvantages above, non-contact optical techniques are more preferable. DIC as a digital optical measurement has been proved powerful in dealing with multiple deformation conditions. Success has been achieved in some studies. (Pritchard, Lava et al. 2013, Pan, Yu et al. 2015, Cui, Tang et al. 2016) used 2D-DIC to investigate the axial and transverse strain of composite material or alloy with thin-section shape in static tests. In those cases, 2D-DIC are acceptable due to the out-plane displacement has little effects on the measurement. When it comes to rock uniaxial tests, out-plane displacement must be considered. Therefore, a precise measurement of Poisson's ratio is required.

(2) Dynamic fracturing pattern

When deformation continues to a certain degree, the initiation of the crack is induced by the stress concentration whose progress finally leads to the failure of rock. In underground rock engineering such as tunnel, slope and mine, it is vulnerable to encounter with high strain-rate loadings from explosion, impact or seismic activity. The crack evolution under dynamic loading can cause the instability of construction but fracturing is encouraged as much as possible in the excavation or reservoir stimulation. The identification of the dynamic crack development can provide more optional indexes to quantify the damage degree of rock under high strain-rate loading.

The fracturing characterization of rock has been widely investigated by the laboratory tests for more than fifty years (Brace 1963, Wawersik and Fairhurst 1970, LAJTAI and LAJTAI 1974). A consensus in those studies is that the crack process has several stages based on the stress-strain curves expressed as axial or lateral deformation recorded during uniaxial or triaxial tests. A typical stress-strain diagram showing the stages of crack development is illustrated as Fig. 4.1. In this type of classification, there are five stages: (1) crack closure, (2) linear elastic deformation, (3) crack initiation and stable crack growth, (4) critical energy release and unstable crack growth, and (5) failure and post-peak behaviour. It could be noted that, the critical stresses are determined by the certain volumetric and crack strains. It is generally accepted that a stress-volumetric strain curve is the most sensitive indicator of initiation and subsequent growth of cracks in laboratory tests (Brace, Paulding et al. 1966). The relationship between the volumetric strain and crack progress was also supported by the interpretation of acoustic emission (AE) event counts (Eberhardt, Stead et al. 1998) and 3D location (Zhao, Cai et al. 2013). (Xue, Qin et al. 2014) summarized the results of uniaxial compression tests on different rocks reported in previous studies, to evaluate similarities and differences of stress thresholds among igneous, metamorphic, and sedimentary rocks. Using the volumetric strain-stress and petrographic technology, (Nicksiar and Martin 2013) discussed the relationship between the mineral composition and crack initial stress. To determine the volumetric strain in laboratory test, the axial, radial and lateral strains are required to be obtained and summed up (radial strain equals to lateral strain under axially symmetric loading).

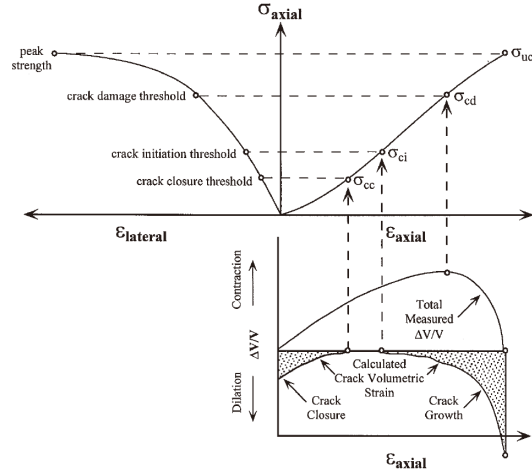


Fig. 4.1 Stress-strain diagrams showing the stages of crack development (Martin 1993). ( $\Delta V$ , change in volume;  $V$ , initial volume).

With regard to the fracture patterns, efforts were made, for example, to observe the residual pieces of the fractured specimen with naked eyes or the electron microscope; and to link its failure patterns and mechanisms with the strain rate or pre-stress state (Lindholm 1974, Li, Lok et al. 2005, Doan and Gary 2009, Zhang and Zhao 2014). The application of high-speed photography in SHPB made it possible to visualise the real-time fracturing process of the specimen, however, the grey scale image and relatively low resolution make it hard to locate the initial cracks. The combination of high-speed photography and digital optical measurements allowed the detection of the quantitative information on the fracturing pattern. A summary of the application of high-speed DIC on rock was given in Table 3.4. However, a 3D deformation and fracturing patterns of rock at high strain-rate compression are still unknown.

To solve above-mentioned issues, this chapter aims at identifying the full-field strain and strain rate fields directly on the rock specimen in SHPB tests by high-speed 3D-DIC method. The strain and strain rate results determined by DIC method and one-dimensional wave theory were discussed. The error between 2D- and 3D-DIC was investigated. The dynamic Poisson's ratio and Young's modulus were directly identified with their strain-rate sensitivity. Stress and strain thresholds of crack development in rock under different high strain rates were investigated. The full-field fracturing evolution such as initiation, branching, and coalescence are revealed.

## 4.2 EXPERIMENTAL SET-UP

Hawkesbury sandstone was tested in the experiments. Totally 15 specimens tested in dynamic tests at the strain rates ranging from 66 to 132 s<sup>-1</sup>. The dynamic compression test was conducted with the SHPB introduced in Section 3.3. The quasi-static behaviour of the sandstone specimens were tested by 300 kN Shimadzu AGS-X Series testing machine at the strain rate of 10<sup>-4</sup> s<sup>-1</sup>. High-speed 3D-DIC measurement was used to characterize the fracturing process during dynamic testing with a resolution of 256×256 pixels (209×129 pixels for the area of interest), frame rate of 200,000 fps and exposure time of 4 μs. The setup of the SHPB and high-speed imaging system is shown in Fig. 4.2(a). The deformation and fracturing in quasi-static test were studied by 3D-DIC, as shown in Fig. 4.2(b), at a resolution of 2448×2050 pixels and frame rate of 10 fps.

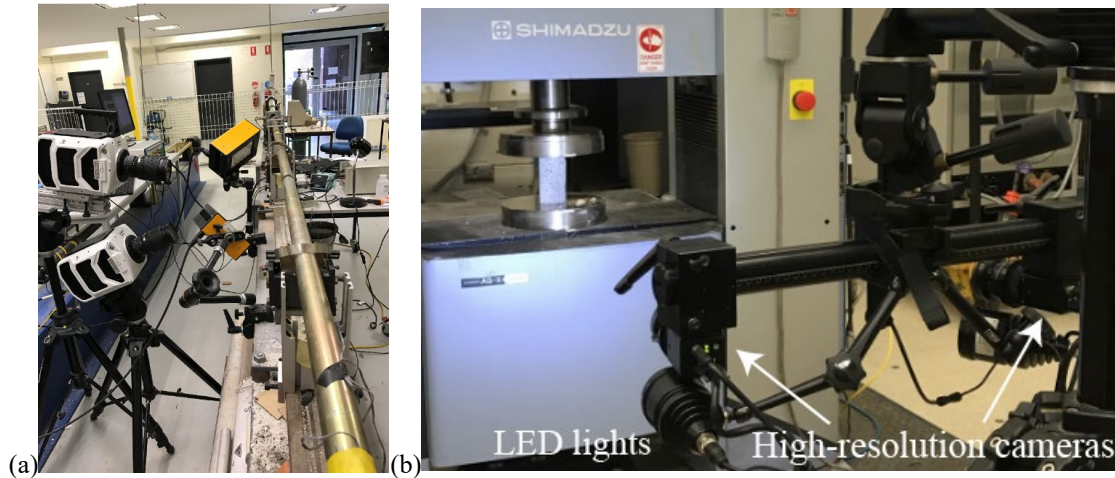


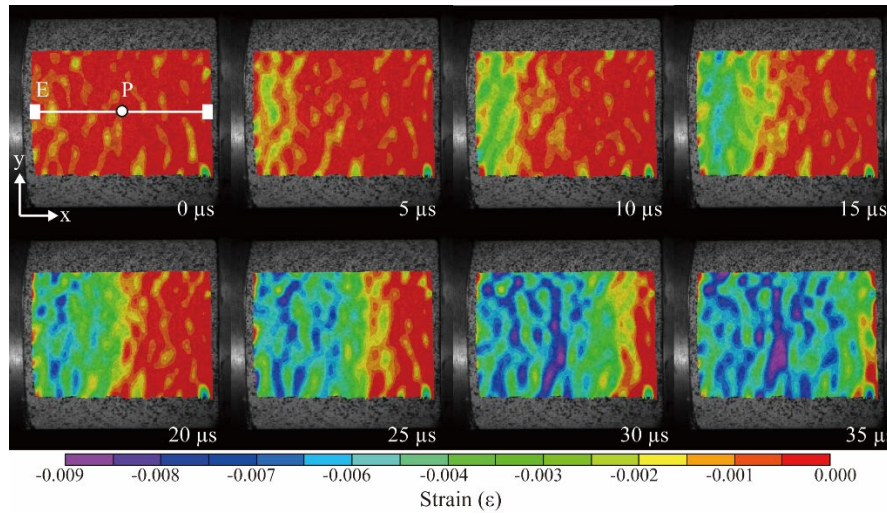
Fig. 4.2(a) Setup of the SHPB system (b) static compression machine and high-resolution cameras system

## 4.3 FULL-FIELD DEFORMATION MEASUREMENT

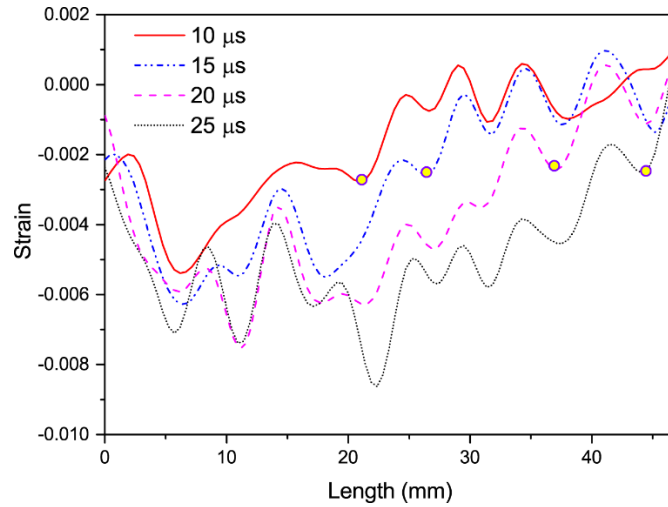
### 4.3.1 Strain and strain rate pattern

The area of interest (AOI) in DIC was defined as a portion of the specimen located within the overlap between two cameras views, as illustrated in Fig. 4.3, and the AOI corresponds to a 47 mm × 33 mm rectangular in the real scale. A virtual extensometer ‘E’ was attached within the AOI to obtain the average strain and strain rate along the centre axis of the specimen, and point ‘P’ represents the centre point. In Fig. 4.3 the stress wave propagation was visualised by the negative strain field movement in *x* direction (compression is negative in DIC). The absolute strain in the wavefront is smaller than the wave body revealing the

pressure rising in the waveform. The average wave velocity is determined by the wavefront movement on the surface as  $C_L^m = 2034 \text{ m/s} \approx 0.96 C_L$ . This indicates that the specimen does not deform homogeneously within the cross section where the particle motion along core is faster than that along surface. The surface without confinement has the largest radial inertia effect, which consumes part of the input energy in the form of transverse kinetic energy for lateral movement, resulting in lower axial wave velocity. Fig. 4.4 shows the strain distribution along the middle line of AOI in x direction from 10 to 25  $\mu\text{s}$  at a strain rate of  $120 \text{ s}^{-1}$ . Circles indicate the same point in the stress wave profile, where, behind the circle, the rising period extends and vibrates more times as wave propagates over distance, proving the existence of dispersion effect in the rock specimen. The dispersion is caused by the radial inertia effect since the high-frequency wave has the lower velocity than the low-frequency one; this velocity difference disperses the waveform and accumulates as wave propagates over the distance.



**Fig. 4.3** Compressive wave propagating within the sandstone at a strain rate of  $120 \text{ s}^{-1}$  ('E' is the virtual extensometer along the centre axis, and 'P' is the centre point of the AOI).



**Fig. 4.4** Strain distribution along middle line of AOI in x direction from 10 to 25  $\mu\text{s}$  at a strain rate of  $120 \text{ s}^{-1}$

A constant strain rate is one of the main assumptions in SHPB test, which is highly desirable to present the mechanical behaviour during dynamic testing. The strain rates were determined by both strain gauge signals and DIC method. In this section, highest strain rates obtained by strain gauges are 70, 93 and  $120 \text{ s}^{-1}$ , respectively. Fig. 4.5 shows the strain rate field in the test with the strain rate of  $120 \text{ s}^{-1}$ ; the strain field was found reflecting back and forth after reaching the interface between the rock and the bar. The strain rate field on the specimen proves that the strain rate distribution is different at any time, the maximum value was over  $600 \text{ s}^{-1}$  at 35  $\mu\text{s}$  which is more than five times than the peak strain rate obtained by strain gauges based on the one-dimensional stress wave propagation theory.

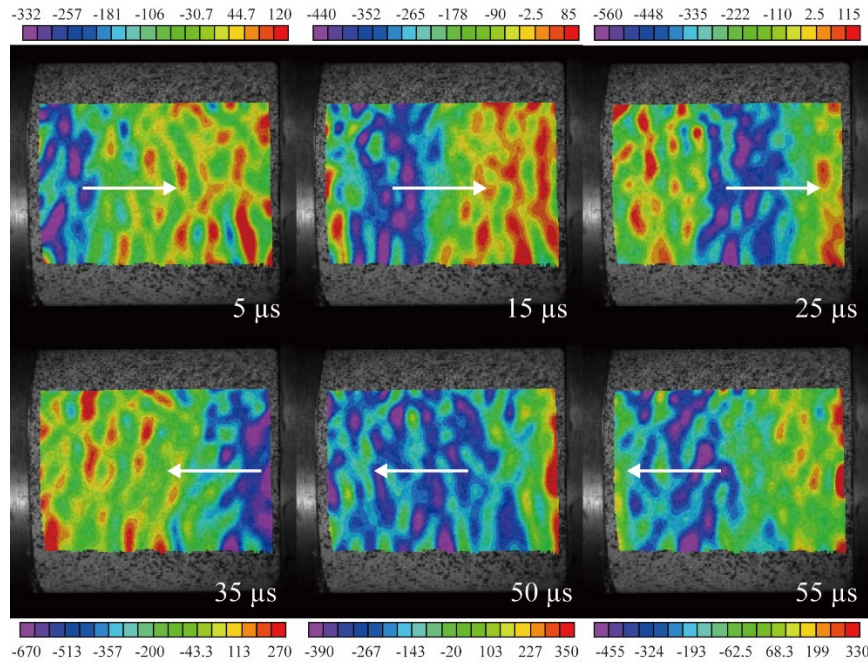
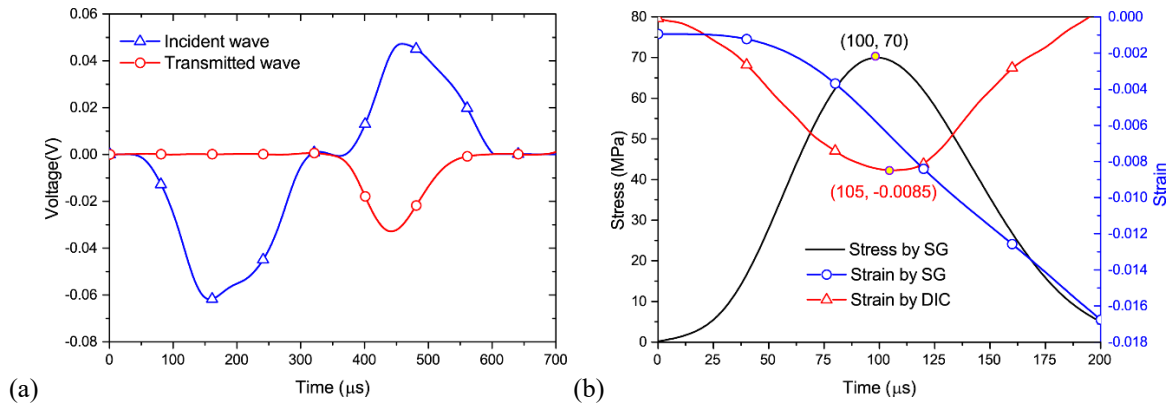


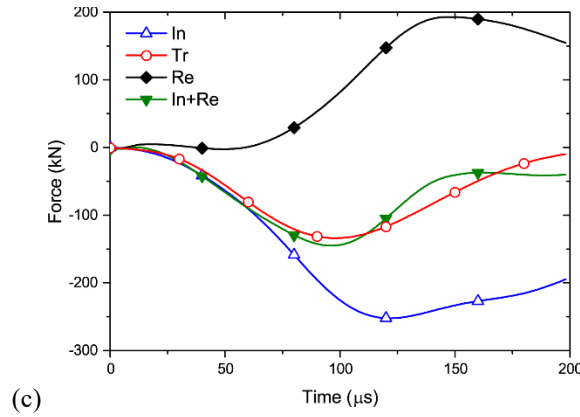
Fig. 4.5 Strain rate field distribution through sandstone specimen at the strain rate of  $120 \text{ s}^{-1}$ .

#### 4.3.2 Comparison between 3D-DIC and strain-gauge method

Fig. 4.6(a) shows the raw voltage signal from the strain gauge at a strain rate of  $120 \text{ s}^{-1}$ . According to Eq. 3.4, the stress and strain history curves are obtained (Fig. 4.6(b)) and the dynamic force equilibrium was further checked (Fig. 4.6(c)).







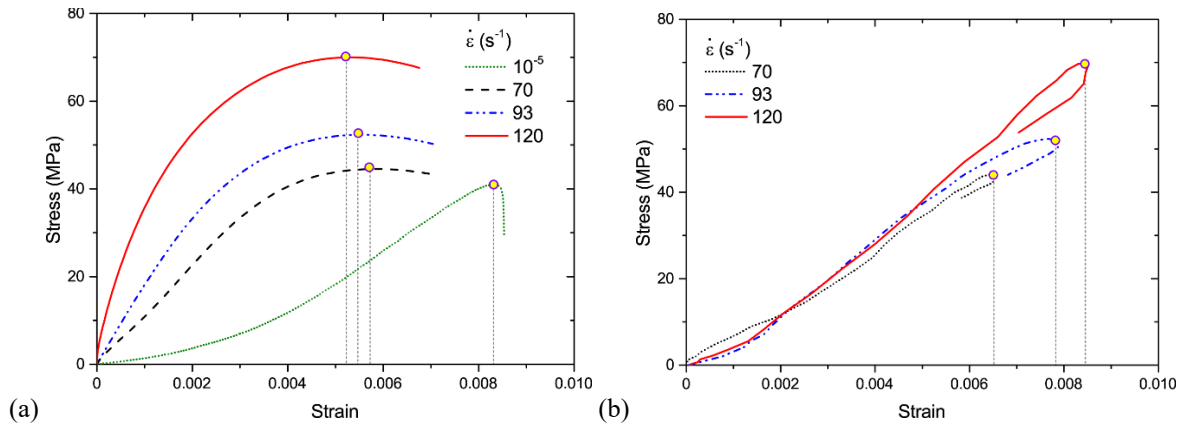
**Fig. 4.6** Typical experimental data at the strain rate of  $120 \text{ s}^{-1}$ : **(a)** raw voltage data from oscilloscope, **(b)** stress and strain history derived by strain gauge signals and the 3D-DIC, and **(c)** Dynamic equilibrium check

By identifying the wave propagation in the strain field, we define the starting time of wave transmission into the specimen and synchronise it with the timeline of the stress and strain history obtained by strain gauges. Strain histories at a strain rate of  $120 \text{ s}^{-1}$  obtained by the DIC virtual extensometer is shown in Fig. 4.6(b). Compared with the strain history obtained from the strain gauge, the strain value in DIC increased faster and larger at first but once the peak stress reached the strain from DIC started to decrease. The fundamental reason causing the difference is the strains measured by DIC and strain gauge come from two different sources. The strain determined by the strain gauge signals is a calculated one (time integration of the strain rate derived from reflected wave). This method is based on the assumptions as follows: (i) one-dimensional elastic wave propagation in the bars and (ii) homogeneous deformation of the sample (Kolsky 1963). First assumption ignored the radial inertial effect of the bar which will consume part of the strain energy from the reflected wave. That leads to the calculated axial strain being less than the actual one. For the second assumption, unlike metal whose deformation is more homogenous, the brittle material like rock experiences rather short or even no elastic period in dynamic loading. Therefore, the strain localisation begins to accumulate at the very beginning which leads to a faster increase in the axial strain than the homogenous compression. Moreover, the inertial effects and the interfacial friction effect although are expected to be minimize through different ways but hard to be eliminated especially in brittle material. Both friction and inertial effect will contribute to the strain energy causing the underestimation of the axial strain calculated by theory. The axial inertial effect causes a larger strain rate than the ultimate value in the beginning, resulting in fast



increase in strain. The difference in the strain history shape (inflexion point) in the post-peak stage has been widely studied in static UCS test (Rummel and Fairhurst 1970, Wawersik and Fairhurst 1970, Hudson, Brown et al. 1971). The results suggested that rock could be classified into two categories: class I where the post-peak strain continues to increase and fracture propagation is stable; and class II where the post-peak strain decrease and fracture propagation is unstable. A closed-loop servo-controlled loading system can only capture the class I curve and both class I and II curve can be obtained depending on the brittleness of the rock without this arrangement (Hudson, Brown et al. 1971). (Munoz, Taheri et al. 2016) also reported a class II curve obtained by 3D-DIC in static UCS test on sandstone. In our SHPB test, strain by DIC refers to class II and strain by strain gauge refers to class I. From mechanics perspective, peak stress coincides with the specimen losing its bearing capacity and stability, leading to unloading of the stored elastic part of the strain and the extension of the strain detected by DIC. However, there is no servo system in SHPB adjusting the bar to deform synchronously and coordinately as the specimen distorts. As a result, the extended specimen cannot press the bar after failure due to incompact contact at the interface of specimen and bars, hence is unable to give a compression signal in the reflected wave as well as the decrease in strain history. Fig. 4.7 shows two different groups of stress-strain curves in which the stress histories were both derived from strain gauge signal. The curve patterns where the strain determined by the strain gauges shows that Young's modulus and the critical strain (the strain to the maximum stress) increase with an increase of strain rate; this observation is generally accepted in rock-like materials (Bischoff and Perry 1991). However, the stress-strain curves by strain gauges show a ductile property after peak stress (Fig. 4.7(a)) which is different with the static one. The curves by DIC (Fig. 4.8(b)) demonstrate that the modulus at three strain rates are unaffected by the strain rate at 9.58 GPa (14% higher than the static one), and the higher the strain rate, the larger is the strain at the peak stress. Such result was also reported in (Frew, Forrestal et al. 2001). It is obvious that improper measurement of strains can lead to an inaccurate characterization of the post-peak behaviour of rock which is used to quantify post-peak fracture energy (Bažant 1989, Markeset and Hillerborg 1995, Jansen and Shah 1997) as well as rock brittleness property (Tarasov and Potvin 2013). The strain obtained by the voltage signals on the bar not only relies on several assumptions discussed above but also influenced by the environmental noise, hardware

quality and interpretation method. DIC method is more reliable, here, as it is a direct measurement of specimen deformation, controlled by the calculation threshold. Some attempts have also been made by optical full-field measurements and/or numerical simulations to correct and determine stress–strain curves in compression (Zhao and Gary 1996), spalling (Pierron and Forquin 2012) and tensile-shear (Peirs, Verleysen et al. 2011) tests. Therefore, the stress-strain curve should be carefully examined to reveal the true dynamic modulus and post-peak stress-strain property of brittle material in high strain rate tests.



**Fig. 4.7** Stress-strain curves: the strain histories obtained by (a) strain gauges and (b) a virtual extensometer.

By averaging the strain rate along the middle axial of AOI, the strain rate histories by DIC are determined (Fig. 4.8). Comparison of this strain rate history with the strain gauge interpretation shows that the DIC result increases dramatically in the beginning to a top value which is larger than the constant rate; this phenomenon demonstrates that the axial inertial effect is large when the stress firstly transmits into the specimen. After several times vibration, the strain rate was gradually inclined to a stable value. It is clear that the average strain rate history by DIC in the test of  $70 \text{ s}^{-1}$  vibrated three times before it reached a constant around  $47 \text{ s}^{-1}$  at  $88 \mu\text{s}$  and kept constant for  $62 \mu\text{s}$ . The average strain rate in  $93 \text{ s}^{-1}$  test vibrated three times and reached  $77 \text{ s}^{-1}$  at  $75 \mu\text{s}$  for a short period and then decreased gradually. However, the strain rate in  $120 \text{ s}^{-1}$  test declined dramatically without showing a constant strain rate after two vibrations at  $57 \mu\text{s}$ . Since at higher strain rates, the strain localisation is generated earlier than the peak stress, the unstable stress state distribution prevents the strain rate from reaching balance. Therefore, the pulse shaper is essential in the SHPB tests, especially in high strain-

rate test, to expand the duration prior to the peak stress, allowing more time for stabilising strain rate.

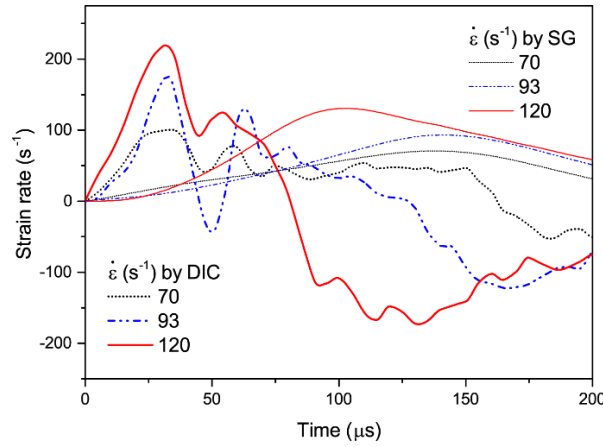


Fig. 4.8 Average strain rates along the middle line within AOI by 3D-DIC and strain rates by strain gauge (compressive strain rate is positive in this chart).

We suggest that before conducting a high strain-rate test, the strain rate history could be examined by DIC at lower strain-rate test to identify the fixed vibration duration before a constant strain rate is achieved (115  $\mu\text{s}$  in this study); DIC could also be used to determine the minimum pressure rising time as a reference in selecting the pulse shaper. It is also noted that the strain rate history derived from strain gauge signals does not reflect on the vibration pattern; they exhibit a relatively constant curve near the peak which means traditional analysis can not determine whether the strain rate reaches a constant value or not.

#### 4.3.3 Comparison between 3D-DIC and 2D-DIC

To clarify to what extent the out-of-plane displacement affects the in-plane deformation in the dynamic uniaxial compression testing of rocks, the same images in the lower camera were employed to conduct the 2D-DIC with the same configuration as the 3D-DIC. The strain, strain rate history and strain distributions in the same position of AOI are discussed under three strain rates. According to the comparison in Fig. 4.9, the general curve pattern is similar between 2D- and 3D-DIC in strain and strain rate history. In terms of the value of the strain or strain rate, the errors corresponding to different strain rates are shown in Table 4.1. The error of strain in 2D-DIC caused by the out-of-plane displacement can be as high as 32% at the strain rate of 120  $\text{s}^{-1}$  and 14% for other two strain rates. The peak strain in 2D-DIC is different from 1% to 14% with the 3D results and the error in the time, when peak strain is

reached, varies from 5  $\mu\text{s}$  to 15  $\mu\text{s}$ . The error for the constant portion of the strain rate is 21%, the starting time for constant strain rate has the difference of 43  $\mu\text{s}$ . There is no obvious relationship between the error and strain rates, but the errors in the evolution of strain and strain rate will mislead to an incorrect stress-strain curve and incorrect interpretation of the dynamic property.

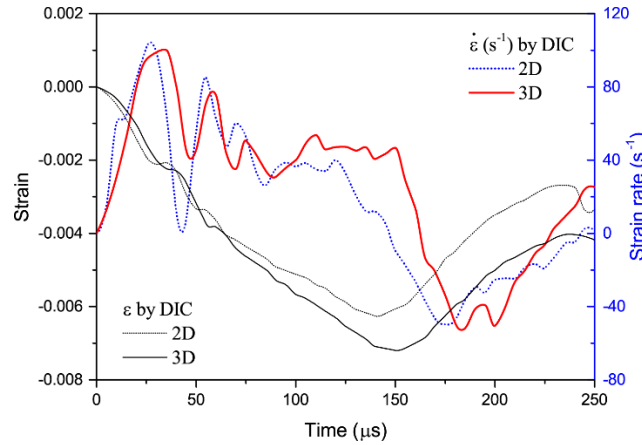


Fig. 4.9 Strain history from extensometer by high-speed 2D-DIC and 3D-DIC at a strain rate of 70  $\text{s}^{-1}$ .

**Table 4.1** Errors in 2D to 3D-DIC (positive time means postpone and vice versa)

Strain rate	Max strain error in the whole process	Strain error at peak	Time error at peak strain
70 $\text{s}^{-1}$	-14 %	-14%	- 15 $\mu\text{s}$
93 $\text{s}^{-1}$	-14 %	-7%	+10 $\mu\text{s}$
120 $\text{s}^{-1}$	+32 %	+1%	-5 $\mu\text{s}$

Apart from the evolution of the strain and strain rate, the distribution is also different in 2D- and 3D-DIC. Fig. 4.10 shows the axial ( $\epsilon_{xx}$ ) and radial ( $\epsilon_{yy}$ ) strain distributions along the centre line of AOI at 50  $\mu\text{s}$  under the strain rate of 70  $\text{s}^{-1}$ . It is apparent that the strain distribution pattern is different in two methods, the maximum strain differences at the same position can be 0.001 and 0.0018 in axial and radial directions, respectively. The error will be accumulated to a large value when the incremental correlation is adopted in the correlation process.

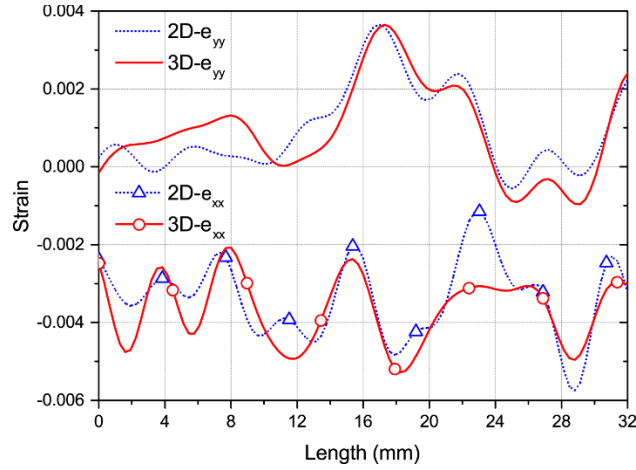


Fig. 4.10 Strain distribution at 50  $\mu$ s along the centre line of AOI by 2D- and 3D-DIC at a strain rate of 70  $s^{-1}$ .

#### 4.4 IDENTIFICATION OF DYNAMIC PROPERTIES

The dynamic elastic modulus was obtained with the ratio of the increment of stress to axial strain ( $\Delta\sigma / \Delta\epsilon_x$ ). The dynamic elastic modulus was compared under five different strain rates in the stable crack development stage (between  $\sigma_{ci}$  and  $\sigma_{cd}$ ) which has a strong linearity. Results show that, the modulus in each strain rate is around  $9.4 \pm 0.2$  GPa. It indicates the modulus is unaffected by the strain rate but still 14% higher than the one in static test.

According to the definition of the dynamic Poisson's ratio, it is determined by the sign ratio of lateral strain to axial strain ( $-\epsilon_y / \epsilon_x$ ). Fig. 4.11 shows the results of Poisson's ratios evolution under different strain rates. At the beginning of axial, Poisson's ratios in all strain rates showed a negative value which means the shrinkage happened in the lateral direction. This unusual phenomenon in rock was also reported in other studies (Hardy 1976, Homand-Etienne and Houpert 1989, TU and YANG 2008). A cross section from front view by X-ray tomography is obtained, shown in Fig. 4.12(a) supporting the common view that when the crack closes in the first stage the grains would rotate inward causing the decrease in both axial and lateral direction, as shown in Fig. 4.12(b). It is a behaviour of the anisotropy in the scale of rock microstructure rather than a main mechanical property of rock material.

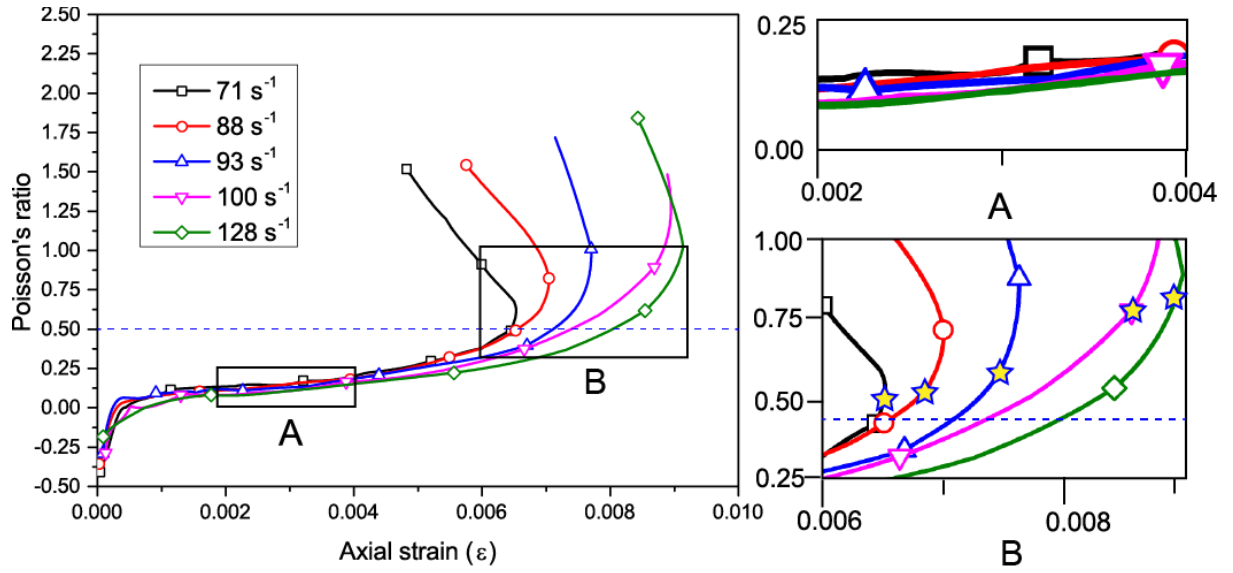


Fig. 4.11 Poisson's ratio evolution of sandstone with different strain rates (star indicates peak strain position)

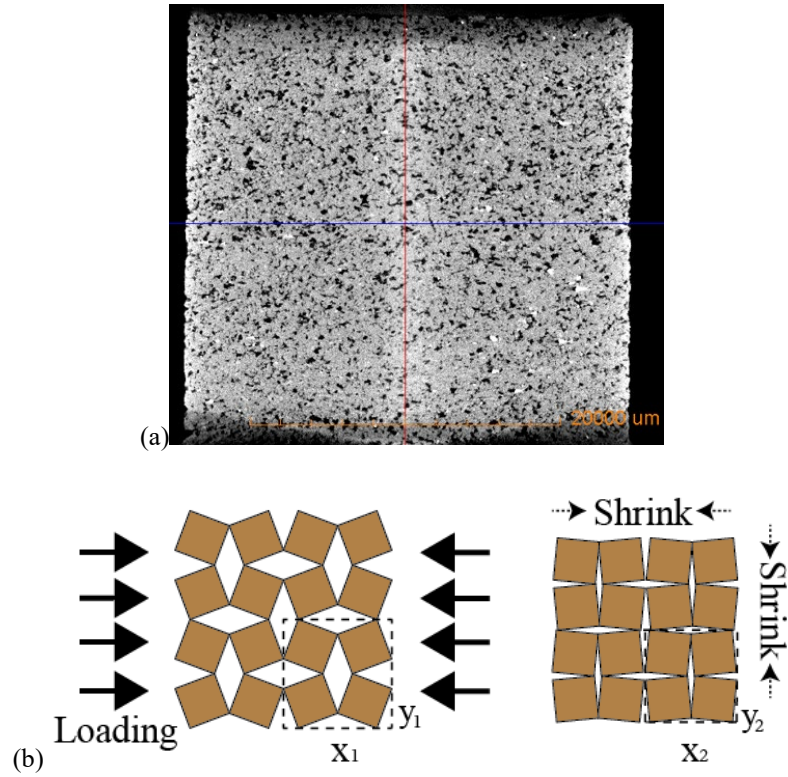


Fig. 4.12(a) Cross section from front view by X-ray tomography (b) Grain rotation model

After Poisson's ratio quickly rise above zero, it reached a relatively stable period which remains growing but in a slow speed. The average value in different strain rate is shown in Table 4.2 which is less than 0.21. It shows that the actual Poisson's ratio on the specimen

under dynamic loading is different than the one determined by high-frequency ultrasound method calculated as following,

$$\nu = \frac{1}{2} \frac{(V_p/V_s)^2 - 2}{(V_p/V_s)^2 - 1} \quad (4.1)$$

where the P-wave velocity  $V_p = 2110$  m/s, S-wave velocity  $V_s = 1210$  m/s. (Bieniawski 1967) proposed that Poisson's ratio of the rock which is constant during the linear elastic deformation, starts to increase due to initiation of new micro cracks or extension of existing ones. Therefore, no constant Poisson's ratio confirms no elastic deformation existed again.

**Table 4.2** Poisson's ratio and Young's modulus vs strain rates

Strain rate	Poisson's ratio	Dynamic Young's modulus
71 s <sup>-1</sup>	0.22	9.4 ± 0.2 GPa
88 s <sup>-1</sup>	0.21	
93 s <sup>-1</sup>	0.20	
120 s <sup>-1</sup>	0.18	
128 s <sup>-1</sup>	0.13	

Moreover, it could be found that lower strain rate had a larger Poisson's ratio than the higher one. Because rock experiences rather short or even no elastic period in dynamic loading. Upon the wave completely propagates through the specimen (35 μs for 120 s<sup>-1</sup> strain rate loading in this work), the stable crack begins to emerge which contributes to a faster increase in the axial strain. The higher the strain rate is, the sooner the strain localisation accumulates, which results in a larger axial strain and insufficient lateral deformation. It indicates that a smaller loading rate allows a more sufficient lateral deformation than larger one at the same axial strain. On the other hand, this differences also proved there is no elastic stage in which Poisson's ratio should be rate independent. After the axial strains exceeded the unstable crack development threshold, Poisson's ratios began to increase significantly even higher than 0.5 which was regarded as the upper limit of Poisson's ratio. This trend was also discovered in quasi static tests (Zhiwei and Zongze 2000, Jianming, Bingye et al. 2001). Moreover, the value of Poisson's ratio for the rock mass in numerical simulation was larger than the value for the intact rock, a value larger than 0.5 were obtained (Bauer and Conley 1987, Bhasin and Høeg 1998, Min and Jing 2003), indicating the anisotropy induced by the joints could affect

Poisson's ratio. In the post-peak stage, Poisson's ratio grows dramatically identifying the lateral damage is very violent.

As above, the Poisson ratio is rate dependent and changing all the time. A constant value is applicable in numerical simulation before unstable crack development but after which Poisson's ratio increases more and more significantly even over 0.5 before peak. In the post-peak stage, Poisson's ratio grows dramatically indicating the failure deformation is stronger in lateral direction than the axial one.

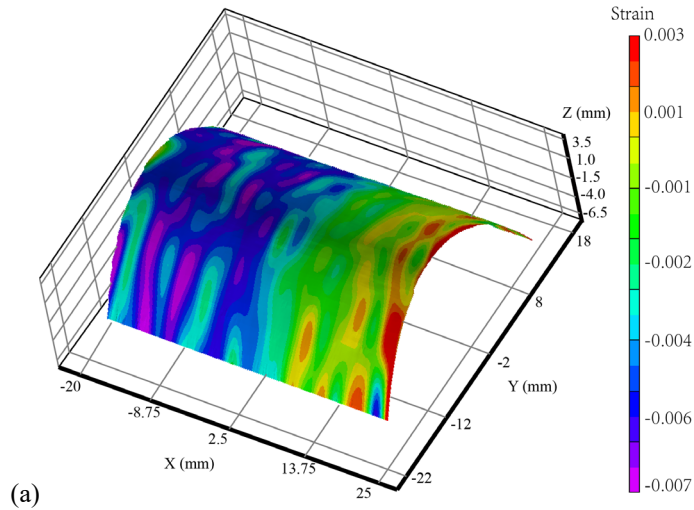
## 4.5 STRESS THRESHOLD FOR FRACTURE

### 4.5.1 Identification of dynamic stress thresholds

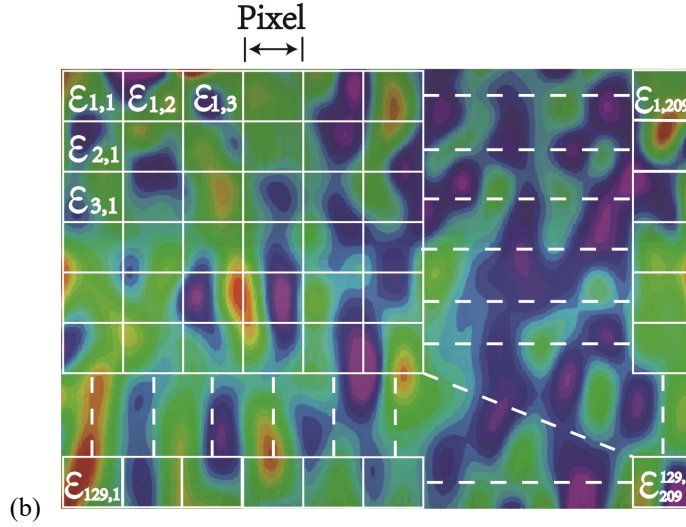
The volumetric strain is a sum up of strains in axial ( $\varepsilon_x$ ), lateral ( $\varepsilon_\theta$ ) and radial ( $\varepsilon_r$ ) directions where  $\varepsilon_r = \varepsilon_\theta$  under axially symmetric loading. A typical axial strain field on the 3D shape of the specimen at  $30 \mu\text{s}$  with the strain rate of  $120 \text{ s}^{-1}$  is shown in Fig. 4.13(a). The axial and lateral strain of the specimen were extracted in axial ( $e_{xx}$ ) and lateral ( $e_{yy}$ ) strain fields based on DIC results (Fig. 4.13(b)) as follows,

$$\varepsilon_x, \varepsilon_\theta = \frac{\sum_{j=1}^{129} \sum_{i=1}^{209} \varepsilon_{i,j}}{129 \times 209} \quad (4.2)$$

where the  $\varepsilon_{i,j}$  refers to the strain within the pixel in row  $i$  and column  $j$ .







**Fig. 4.13(a)** Reconstructed 3D shape and strain field of a specimen at 30  $\mu\text{s}$  at the strain rate of 120  $\text{s}^{-1}$ , **(b)** Illustration of averaging the strain value in a field, (pixel size was enlarged for illustration)

The crack strain is determined *by* subtracting the elastic volumetric strain from the total volumetric strain, where the elastic volumetric strain  $\varepsilon_{VE}$  is as following,

$$\varepsilon_{VE} = \frac{1-2\nu}{E} \sigma_{\text{dyn}} \quad (4.3)$$

where  $\nu$  is Poisson's ratio,  $E$  is elastic modulus and  $\sigma_{\text{dyn}}$  is the axial stress derived from the signals of strain gauges on the bars with the one-wave method (Zhang and Zhao 2014). By identifying the first compressive strain occurred on the specimen, the strain and stress were synchronized. The dynamic Poisson's ratio to determine the elastic volumetric strain was 0.21.

Fig. 4.14 shows a typical stress thresholds diagram of sandstone loaded at the strain rate of 120  $\text{s}^{-1}$ . The patterns of volumetric and crack strains are similar to those in quasi-static tests (Martin 1993). The first stage was the crack closure period in which the crack strain decreased to zero. However, once the crack strain decreased to zero, it began to develop immediately which means no elastic stage existing in a dynamic condition. This phenomenon was also predicted by (Liang, Li et al. 2012) with an increasing strain rate in the quasi-static test. However, this stage still exhibited a strong linearity in modulus because of the slow crack initiation speed according to the crack history. At that moment, there was no strain localisation emerging on the surface of the specimen. When the volumetric strain reached its

peak, the dilatancy took place, namely, the beginning of unstable crack development. The crack kept growing until the stress reaching the peak.

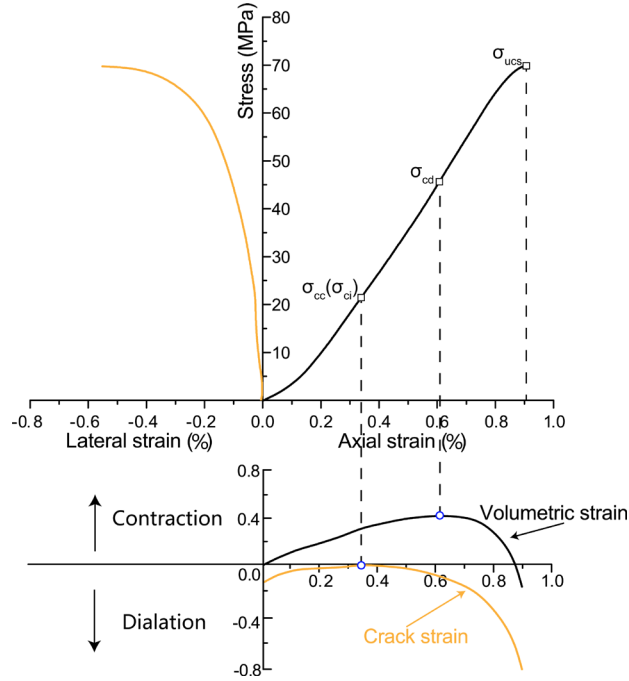


Fig. 4.14 Volumetric strain corresponding to stress thresholds of sandstone under strain rate of  $120 \text{ s}^{-1}$

#### 4.5.2 Strain rate effect

Three stress, strain thresholds and normalised critical stresses corresponding to five typical strain rates were listed in Table 4.3. Fig. 4.15 illustrated the threshold pattern against the strain rate, where the error bar indicated the result range in other strain-rate tests. It can be seen, all stress thresholds and corresponding strains increased with the growth of strain rate. In terms of the normalised stress thresholds of every two of the critical stress (crack initiation stress,  $\sigma_{ci}$ ; the crack damage stress,  $\sigma_{cd}$ ; and the peak stress or UCS,  $\sigma_{UCS}$ ):  $\sigma_{ci}/\sigma_{UCS}$  fell between 20% and 31%,  $\sigma_{cd}/\sigma_{UCS}$  had a range of 50% to 67%, and  $\sigma_{ci}/\sigma_{cd}$  varied from 40% to 51%. However, these normalised stresses had no obvious relationship with strain rate. Compared with the  $\sigma_{cd}/\sigma_{UCS}$  in static tests (69%), the dynamic value was lower and also lower than those ( $78\% \pm 11\%$ ) of sedimentary rocks summarised by (Xue, Qin et al. 2014). It proves that the dynamic loading increases the strength but shifts the thresholds of unstable cracking earlier.

**Table 4.3** Thresholds of stresses (MPa) and corresponding strains ( $\epsilon$ ) under different strain rates

Strain rate	$\sigma_{ci}$	$\epsilon_{ci}$	$\sigma_{cd}$	$\epsilon_{cd}$	$\sigma_{ucs}$	$\epsilon_{ucs}$	$\sigma_{ci} / \sigma_{ucs}$	$\sigma_{cd} / \sigma_{ucs}$	$\sigma_{ci} / \sigma_{cd}$
$10^{-4} \text{ s}^{-1}$	13.5	0.00162	28.3	0.00264	41.0	0.00363	0.33	0.69	0.36
$71 \text{ s}^{-1}$	8.9	0.00180	22.1	0.00359	44.5	0.00657	0.2	0.50	0.40
$88 \text{ s}^{-1}$	12.1	0.00211	30.3	0.00424	50.5	0.00684	0.24	0.54	0.40
$93 \text{ s}^{-1}$	14.2	0.00227	34.2	0.00439	52.3	0.00746	0.27	0.65	0.42
$100 \text{ s}^{-1}$	19.6	0.00339	38.3	0.00540	64.2	0.00869	0.31	0.60	0.51
$128 \text{ s}^{-1}$	22.0	0.00343	47.0	0.00618	70.0	0.00905	0.31	0.67	0.47

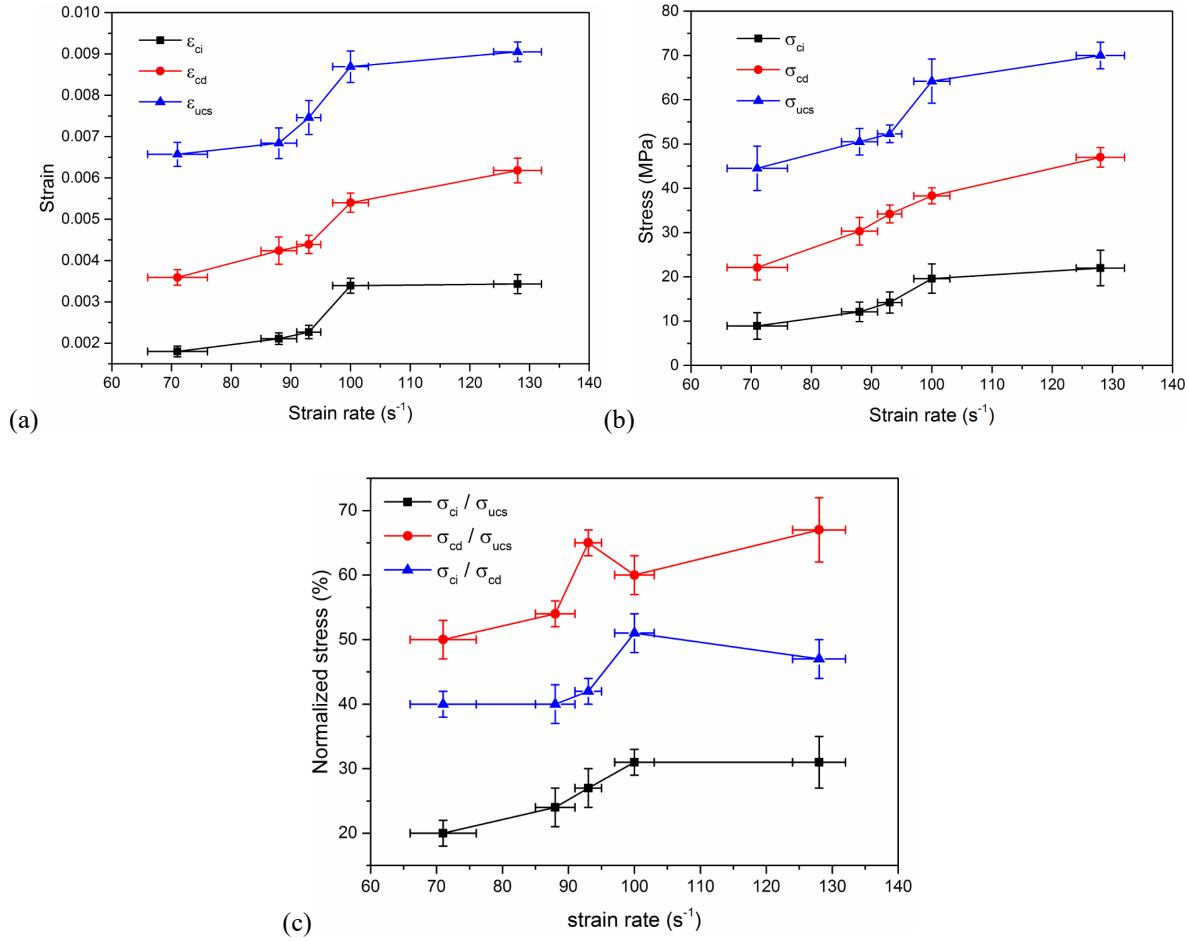


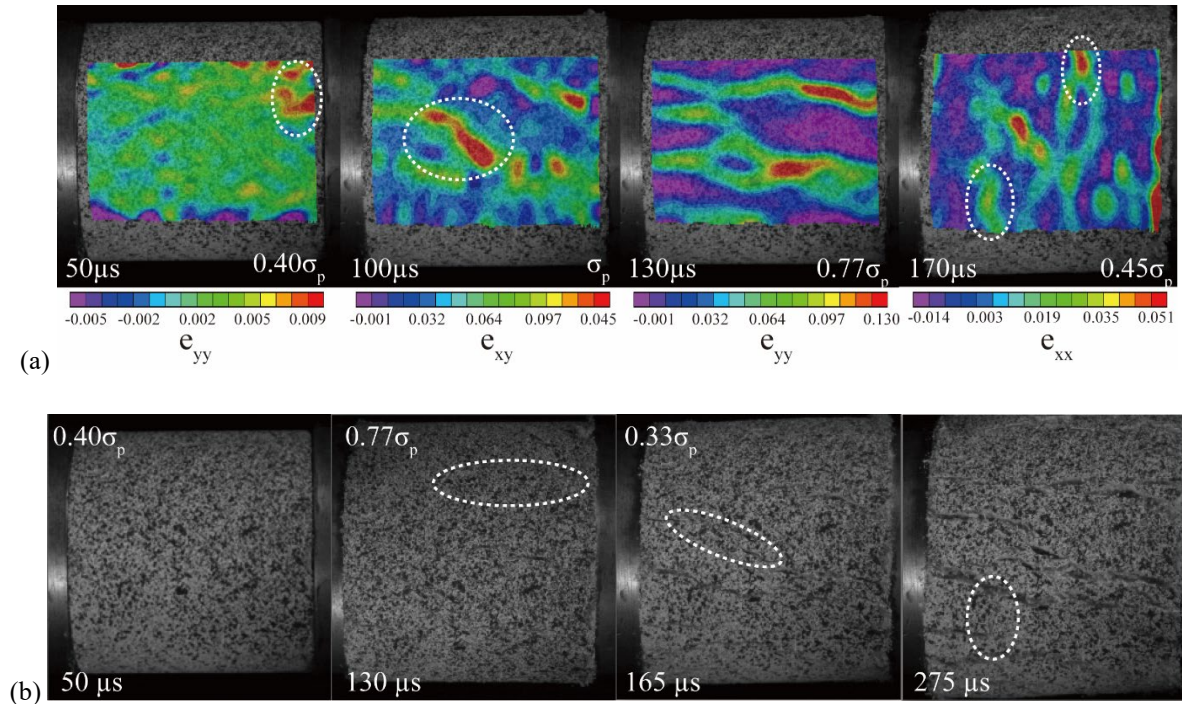
Fig. 4.15 Critical (a) strains, (b) stresses and (c) normalised stresses in dynamic loading tests

## 4.6 STRAIN LOCALISATION AND FRACTURE CHARACTERISTICS

### 4.6.1 Strain localisation and fracture evolution

Fig. 4.16(a) shows the strain fields under the strain rate of  $120 \text{ s}^{-1}$  in axial ( $e_{xx}$ ), vertical ( $e_{yy}$ ) and shear ( $e_{xy}$ ) directions at different stages. The strain localisation firstly appeared at  $50 \mu\text{s}$  in the vertical strain field when the stress was 40% of peak stress, it was formed horizontally

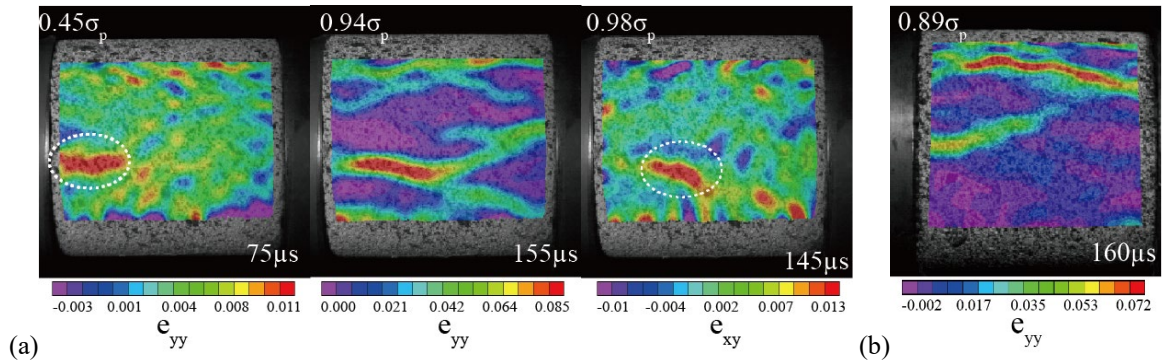
at the edge of the specimen due to radial expanding, while there are no visible cracks on the surface (Fig. 4.16(b)). After that, more horizontal strain localisations emerged from both edges and extended towards the centre. Shear strain localisation then appeared on the surface in the middle of the specimen at 100  $\mu\text{s}$  connected though the previous horizontal strain localisations. Not until 130  $\mu\text{s}$  did the horizontal cracks emerge where the strain was localised; in other words, the surface will not fracture before the stress reaches its peak. However, the modules in the stress-strain curve became gentle before the peak, indicating cracks must have been initiated inside the rock. The visible shear crack emerged at 165  $\mu\text{s}$  when the stress unloaded to 30% of the peak stress. One should note that there was also vertical strain localisation in axial strain field near the top and bottom of the specimen since 170  $\mu\text{s}$  and transited to a crack at 275  $\mu\text{s}$ . This is a spalling crack attributed to the tensile wave generated after the reflection of the compressive wave at the interface. As a result, the fragmentation is more significant as well as the fragments are smaller due to the new cracks generation as the strain rate rises.



**Fig. 4.16(a)** Strain field evolution and **(b)** images of the evolution of visible cracks at a strain rate of 120  $\text{s}^{-1}$ .

When the strain rate decreased to 93  $\text{s}^{-1}$  (Fig. 4.17(a)), the first strain localisation appeared horizontally at 75  $\mu\text{s}$  from the edge of AOI when the stress is 45% of the peak stress. The

shear localisation showed up 70  $\mu\text{s}$  later when the stress was 0.98 peak stress, after which the visible tensile crack and shear crack emerged on the specimen surface at 155  $\mu\text{s}$  (10  $\mu\text{s}$  after peak stress) and 225  $\mu\text{s}$  with the stress corresponding to 0.94 and 0.42 of peak stress. In terms of the strain rate of 70  $\text{s}^{-1}$  (Fig. 4.17(b)), there is no vertical strain localisations developed in  $e_{xx}$  fields; the horizontal strain localisation in  $e_{yy}$  field and first crack was generated at 85 and 160  $\mu\text{s}$  with the stress of 0.56 and 0.89 of peak stress. The shear strain localisation in  $e_{xy}$  field and corresponding cracks were also generated at, respectively, 155 and 235  $\mu\text{s}$  at stress of 0.99 and 0.59 of peak stress. In all three strain rates, the strain localisation degree (Table 4.4) that triggered the first visible crack are 0.072, 0.085 and 0.130 with increase of the strain rate.



**Fig. 4.17** Strain fields at different stages in different directions at strain rate of (a) 93  $\text{s}^{-1}$  and (b) 70  $\text{s}^{-1}$ .

**Table 4.4** Critical normalised stress, strain difference and time ( $\mu\text{s}$ ) for strain localisation or visible crack

Strain rate	Peak stress time	NS for horizontal SL / time	NS for shear SL / time	NS for first crack/time	Strain at the first visible crack
70 $\text{s}^{-1}$	143	0.56 / 85	0.99 / 155	0.89 / 160	0.072
93 $\text{s}^{-1}$	135	0.45 / 75	0.98 / 145	0.94 / 155	0.085
120 $\text{s}^{-1}$	100	0.40 / 50	1.00 / 100	0.77 / 130	0.130

(NS: Normalised stress; SL: Strain localisation)

In conclusion, at all strain rates, a horizontal strain localisation firstly appeared from the edge of the specimen in y direction of the strain field before the stress reached its peak; then the shear strain localisation developed at or shortly after the time when the stress reached its peak. The generations of visible cracks followed the order of tensile, shear and spalling ones at strain rates of 93  $\text{s}^{-1}$  and 120  $\text{s}^{-1}$ ; only tensile and shear cracks existed at the strain rate of 70  $\text{s}^{-1}$ . The higher the strain rate, the lower is the critical stress (after normalised to peak stress)



required for strain localisation to occur. Same pattern exists in time scale, the localisation took place earlier for the higher strain rate when normalised to the peak stress time. Likewise, the critical normalised stress for first crack opening is rate independent, the durations prior to the crack initiation, from the time when the strain first localised is almost  $80 \mu\text{s}$  at all three strain rates. Therefore, the crack development from strain localisation is rate-independent but also depends on its intricate mechanical property.

When the fracturing process is connected with the stress threshold using the same stress history, as shown in Fig. 4.18. According to the strain field (I and II) by 3D-DIC, the crack closure stage corresponded to the first-time wave propagation process and finished when wave thoroughly propagated. At that moment, the tensile strain localisation (III) firstly generated horizontally from the edge of the specimen in lateral strain field axial ( $e_{yy}$ ). Therefore, the unstable crack development threshold is a milestone when both surface and inner start to fracture. As the stress growing to the peak, the shear strain localisation emerged (IV).

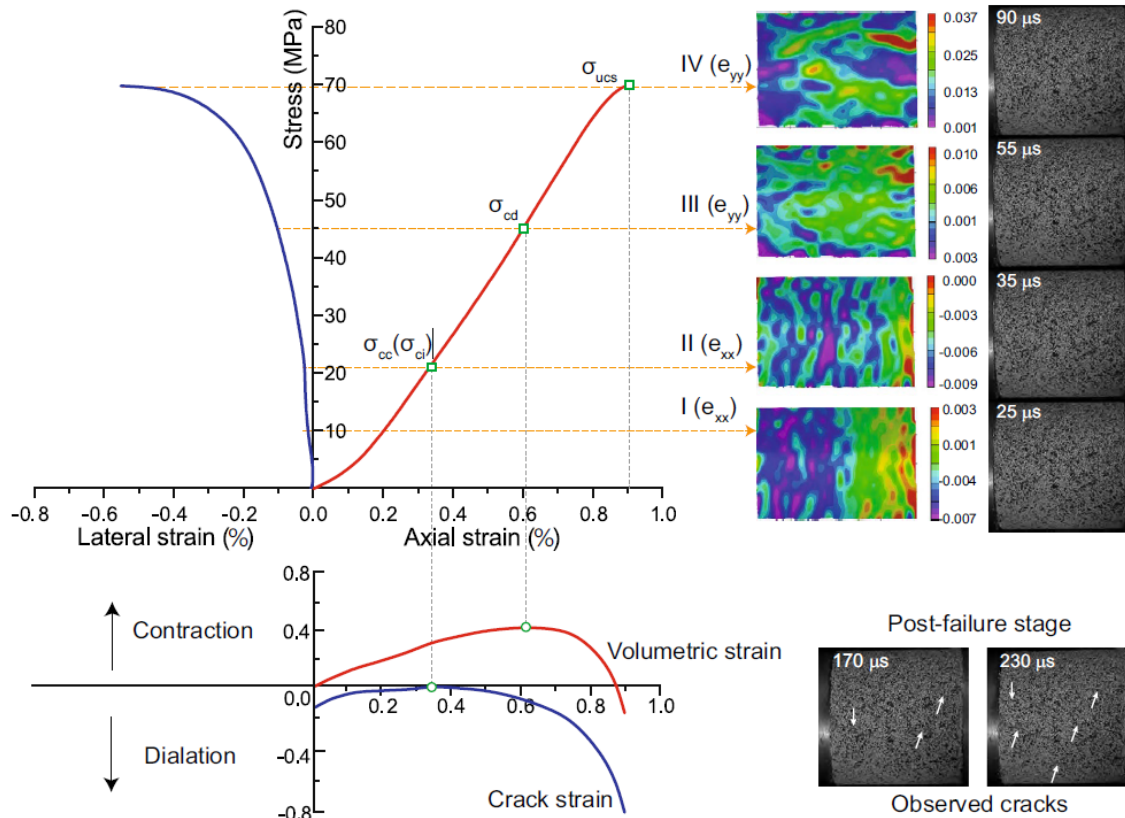
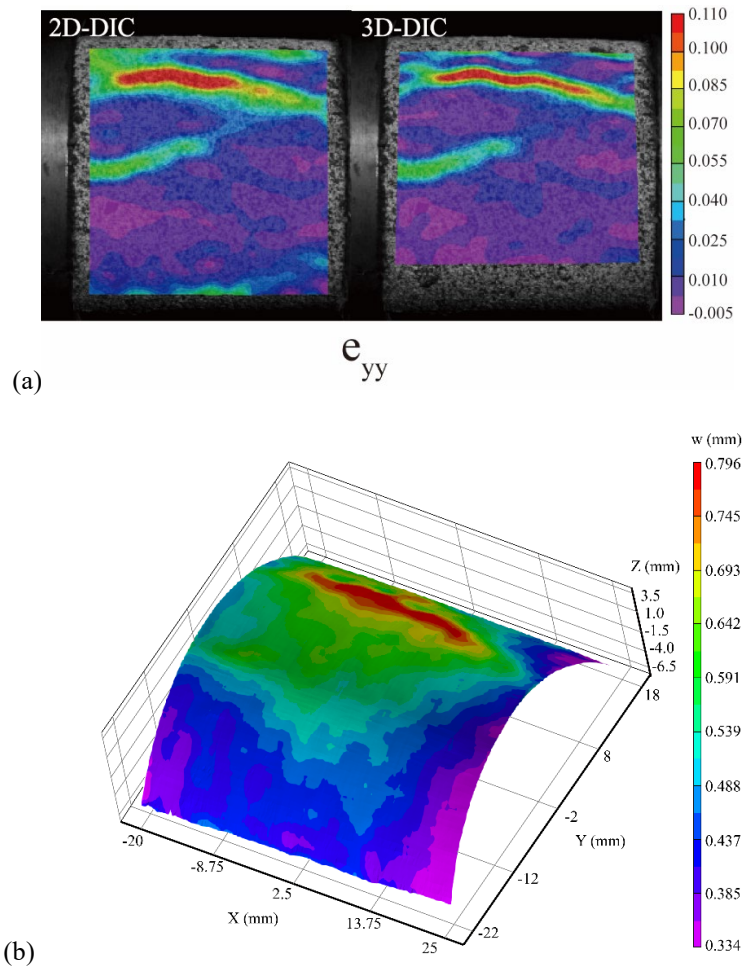


Fig. 4.18 Stress thresholds and corresponding strain fields of sandstone under strain rate of  $120 \text{ s}^{-1}$

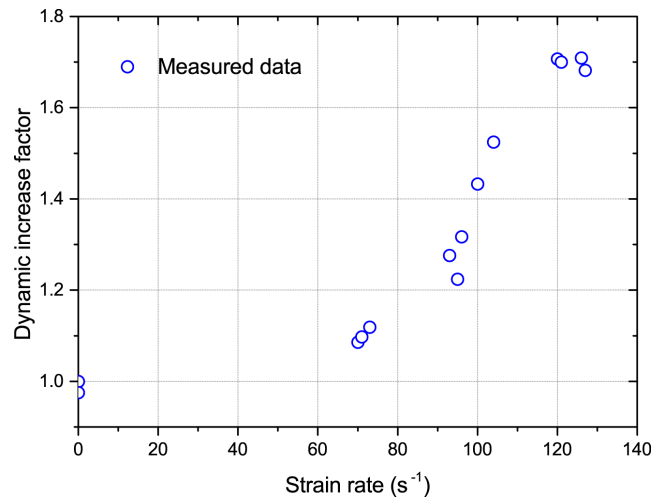
With regards to the strain field, although the degree of the strain is different, the number, location and initial time of strain localisation are roughly similar as seen in Fig. 4.19(a). As a result, it is applicable to use 2D-DIC to detect the qualitative strain localisation pattern such as location and number when only one high-speed camera is available. However, quantitative information can only be approximated from the 2D-DIC in the dynamic uniaxial compression as the error in strain or strain rate is considerable to be neglected. Fig. 4.19(b) shows the out-of-plane displacement field on a reconstructed 3D specimen at  $220\ \mu\text{s}$  with the strain rate of  $70\ \text{s}^{-1}$  which is not able to be measured by the 2D-DIC. The lateral expansion can be easily read from the field and the localisation indicates the non-uniform expansion generated during shear dilation.



**Fig. 4.19(a)** Strain fields at  $220\ \mu\text{s}$  by high-speed 2D- and 3D-DIC at the strain rate of  $70\ \text{s}^{-1}$  **(b)** 3D shape and out-of-plane displacement field at  $220\ \mu\text{s}$  with the strain rate of  $70\ \text{s}^{-1}$

#### 4.6.2 Post-failure characteristics

Fragmentation pattern after the loading depends on the strain rate (Li, Lok et al. 2005, Cai, Kaiser et al. 2007, Doan and Gary 2009), which is also influenced by the dynamic strength of the specimen (Masuda, Mizutani et al. 1987, Olsson 1991, Zhao, Li et al. 1999). The dynamic increase factor (DIF,  $\sigma_{ucd} / \sigma_{ucs}$ ) and its relationship with the strain rate are illustrated as Fig.4.20 for this study; which are 1.09, 1.28 and 1.71 for the three chosen tests with strain rate of  $70 \text{ s}^{-1}$ ,  $93 \text{ s}^{-1}$  and  $120 \text{ s}^{-1}$ , respectively. Fig. 4.21 shows the main part of the residual pieces of the sandstone after static and dynamic loadings. The residual parts remain relatively intact due to the friction of the interface between the specimen and bar. Although the grease was used to minimise the friction, the sandstone still has a considerable roughness which induced a confining pressure on the end causing the shear failure rather than splitting, and, as a result, leading to more significant fragmentation. At all the strain rates, the lower the strain rate is, the more intact the residual part will be; and double cones were symmetric from the middle of the length, the differences among them is the angle of the slope. The angles of the slope to the horizon are  $75^\circ$ ,  $73^\circ$ ,  $70^\circ$  and  $59^\circ$  as the strain rate increases, verifying that the radial inertial force determined by the strain rate will influence the maximum shear stress plane.



**Fig. 4.20** Dynamic increase factor (DIF) as a function of strain rate.



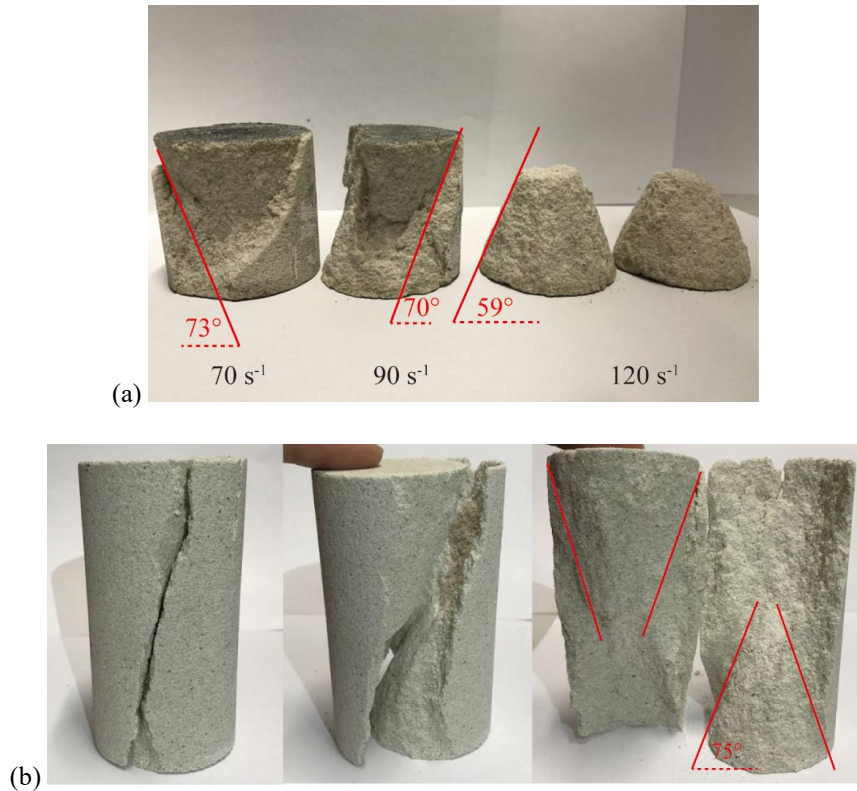


Fig. 4.21 Main part of residual pieces after tests of (a) dynamic loading (b) quasi-static loading.

As a consequence, the dynamic failure mode at the strain rates of 70, 93 and 120 s<sup>-1</sup> is shear dominant, similar to failure mode of static loading condition. The failed sections adjacent to both ends of the specimen (Fig. 4.21(b)) are thin due to the shear plane, explaining why the tensile cracks firstly appeared from the edge where there is less bonding. The whole fracture process begins with the internal shear crack generation as the resultant forces of axial, radial stress and inertial force reach the maximum shear strength. Afterwards, the surface tensile crack develops due to lateral expansion from the edge to the centre where the bonding is increasing. Once the stress reaches its peak, the dominant shear crack will occur on the surface connecting edge cracks. If the strain rate is high enough, the spalling cracks are generated creating greater fragmentation.

#### 4.7 RECOMMENDATIONS FOR FURTHER WORK

Although the real-time deformation and fracture pattern of full-field specimen surface were analysed, the internal fracture characteristics of the specimen remain unknown. To fully identify the dynamic fracture process of rock, it is necessary to understand the evolution,

distribution, energy and mechanism of the fracture development inside the specimen. The combination of the surface deformation, internal fracturing and fragments could provide an overall picture of the whole process of rock dynamic failure. To achieve the internal deformation measurement, some options are X-Ray (Chen, Hudspeth et al. 2014), digital volume correlation (DVC) and acoustic emission (AE). Among them, AE, due to its high sampling rate, promises to have the most potential for internal examination and detection of failures in dynamic testing of rocks. There have been several studies (Liu, Li et al. 2015, Woo and Kim 2016) using AE sensor to detect the AE events and energy in SHPB tests. However, in those tests only one channel was adopted for parameter-based analysis which could not determine the spatial and temporal development of fracture. Therefore, in the future, multi-channel, i.e. waveform-based, AE test is required to analyse the internal crack evolution, distribution, energy and mechanism in rock subjected to the dynamic loading.

#### 4.8 SUMMARY

High-speed 3D-DIC was succeeded to characterize the stress thresholds corresponding to cracks development and the fracture characteristics of the rock under dynamic loads were investigated under different strain rates for the first time. The main conclusions of this paper are as follows:

- The 256×256 pixels resolution and 200,000 fps frame rate are proven to be good in the high-speed 3D-DIC measurement of rock material in SHPB test to obtain sufficient information with the enough accuracy. The strain field during the pre-failure stage shows the wave propagation and dispersion proving the existence of the radial inertial effect on the specimen. The strain rate field on the specimen presents a significant vibration pattern which is caused by the axial inertial effect. The strain extracted from DIC has an elastic recovery after peak which is not reflected by one-dimensional wave method. Hence, the actual strain on the brittle material especially after the peak stress cannot be accurately revealed by strain gauge signals.
- The strain and strain rate history developed from 2D- and 3D-DIC are different and the maximum error of 2D-DIC can be up to 32% and 21% respectively for strain and strain rate measurements (during the constant period). The distribution of strain in the same position shows a different pattern with the maximum strain error of 0.18%.

- The dynamic Poisson's ratio is changing during the loading and can be negative at the beginning due to the high anisotropy. No complete constant Poisson's ratio exists because there is no elastic stage. Within the relatively stable period, the average value is lower than that obtained by ultrasound method. The dynamic Poisson's ratio is rate-dependent where the lower strain rate had a larger Poisson's ratio than the higher one indicating a smaller loading rate allows a more sufficient lateral deformation than larger one. The value can rise above 0.5 before peak stress and goes up dramatically afterwards. These non-traditional phenomenon and values should be taken into consideration when numerical computation is implemented.
- The normalized stress threshold is independent on the strain rate. Compared with the quasi-static condition ( $78\% \pm 11\%$ ), the normalized stress threshold of unstable crack development is earlier ( $58\% \pm 8\%$ ).
- When the interfacial friction is high, the failure of the sandstone in SHPB test is shear mode. After the shear crack generated inside the rock causing the stress redistribution, the tensile strain localisation firstly appears horizontally from the edge of the surface prior to the stress reached peak. The shear localisation on surface happens closely after the peak stress. The higher the strain rate, the lower the normalised stress threshold for the strain localisation initiation. The initiation of dynamic fracture from strain localisation is rate-independent but dependent on a fixed duration since the strain localisation took place.

## REFERENCES

- Aune V, Fagerholt E, Hauge K, Langseth M, Børvik T (2016) Experimental study on the response of thin aluminium and steel plates subjected to airblast loading *International Journal of Impact Engineering* 90:106-121
- Ayache N, Hansen C Rectification of images for binocular and trinocular stereovision. In: *Pattern Recognition*, 1988., 9th International Conference on, 1988. IEEE, pp 11-16
- Bažant ZP (1989) Identification of strain-softening constitutive relation from uniaxial tests by series coupling model for localization *Cement and Concrete Research* 19:973-977
- Bieniawski, Z. and M. Bernede (1979). Suggested methods for determining the uniaxial compressive strength and deformability of rock materials: Part 1. Suggested method for determining deformability of rock materials in uniaxial compression. *International Journal of Rock Mechanics and Mining Sciences & Geomechanics Abstracts*, Elsevier.

## CHAPTER 4 DYNAMIC PROPERTIES AND FRACTURE PATTERNS OF ROCK BY FULL-FIELD MEASUREMENT

Bischoff P, Perry S (1991) Compressive behaviour of concrete at high strain rates *Materials and structures* 24:425-450

Brace, W., B. Paulding and C. Scholz (1966). "Dilatancy in the fracture of crystalline rocks." *Journal of Geophysical Research* 71(16): 3939-3953.

Brace, W. F. (1963). *Brittle fracture of rocks*, Massachusetts Institute of Technology, Industrial Liaison Program.

Cai, M., P. Kaiser, F. Suorineni and K. Su (2007). "A study on the dynamic behavior of the Meuse/Haute-Marne argillite." *Physics and Chemistry of the Earth, Parts A/B/C* 32(8): 907-916.

Chen J, Guo B, Liu H, Liu H, Chen P (2014) Dynamic Brazilian Test of Brittle Materials Using the Split Hopkinson Pressure Bar and Digital Image Correlation Strain 50:563-570 doi:10.1111/str.12118

Chen WW, Song B (2010) *Split Hopkinson (Kolsky) bar: design, testing and applications*. Springer Science & Business Media,

Chen, W. W., M. C. Hudspeth, B. Claus, N. D. Parab, J. T. Black, K. Fezzaa and S. N. Luo (2014). "In situ damage assessment using synchrotron X-rays in materials loaded by a Hopkinson bar." *Philosophical Transactions of the Royal Society A: Mathematical, Physical and Engineering Sciences* 372(2015).

Dai F, Chen R, Xia K (2010) A semi-circular bend technique for determining dynamic fracture toughness *Experimental Mechanics* 50:783-791 doi:10.1007/s11340-009-9273-2

Dehkhoda S (2011) *Experimental and Numerical Study of Rock breakage by Pulsed Water Jets*. PhD Thesis, Brisbane, Australia University of Queensland

Dehkhoda S, Hood M (2014) The internal failure of rock samples subjected to pulsed water jet impacts *International Journal of Rock Mechanics and Mining Sciences* 66:91-96

Doan, M.-L. and G. Gary (2009). "Rock pulverization at high strain rate near the San Andreas fault." *Nature Geoscience* 2(10): 709-712.

Dutta PK, Kim K (1993) High-strain-rate tensile behavior of sedimentary and igneous rocks at low temperatures. DTIC Document,

Eberhardt, E., D. Stead, B. Stimpson and R. Read (1998). "Identifying crack initiation and propagation thresholds in brittle rock." *Canadian Geotechnical Journal* 35(2): 222-233.

Fan Y, Wei Y, Xue Y, Chen J (2015) On the application of digital image correlation testing technology in hopkinson bar loading *Journal of Experimental Mechanics (Chinese)* 30:591-598

Field JE, Walley SM, Proud WG, Goldrein HT, Siviour CR (2004) Review of experimental techniques for high rate deformation and shock studies *Int J Impact Eng* 30:725-775 doi:10.1016/j.ijimpeng.2004.03.005

Fourmeau M, Gomon D, Vacher R, Hokka M, Kane A, Kuokkala V-T (2014) Application of DIC technique for studies of Kuru Granite rock under static and dynamic loading *Procedia Materials Science* 3:691-697

Frew D, Forrestal MJ, Chen W (2001) A split Hopkinson pressure bar technique to determine compressive stress-strain data for rock materials *Experimental mechanics* 41:40-46

## CHAPTER 4 DYNAMIC PROPERTIES AND FRACTURE PATTERNS OF ROCK BY FULL-FIELD MEASUREMENT

Frew D, Forrestal MJ, Chen W (2002) Pulse shaping techniques for testing brittle materials with a split Hopkinson pressure bar *Experimental mechanics* 42:93-106

Frew DJ, Akers SA, Chen W, Green ML (2010) Development of a dynamic triaxial Kolsky bar *Meas Sci Technol* 21:105704 doi:10.1088/0957-0233/21/10/105704

Gama BA, Lopatnikov SL, Gillespie JW (2004) Hopkinson bar experimental technique: A critical review *Appl Mech Rev* 57:223-250 doi:10.1115/1.1704626

Gao G, Huang S, Xia K, Li Z (2015) Application of digital image correlation (DIC) in dynamic notched semi-circular bend (NSCB) tests *Experimental Mechanics* 55:95-104 doi:10.1007/s11340-014-9863-5

Gray III GT (2000) Classic split Hopkinson pressure bar testing *ASM Handbook Vol 8, Mechanical Testing and Evaluation ASM Int, Materials Park OH* 8:15

Hajiabdolmajid V, Kaiser P (2003) Brittleness of rock and stability assessment in hard rock tunneling *Tunneling and Underground Space Technology* 18:35-48

Hauser FE (1966) Techniques for measuring stress-strain relations at high strain rates *Experimental Mechanics* 6:395-402

Huang S, Xia K, Yan F, Feng X (2010) An experimental study of the rate dependence of tensile strength softening of Longyou sandstone *Rock mechanics and rock engineering* 43:677-683

Hubbert MK, Willis DG (1972) *Mechanics of hydraulic fracturing*

Hudson J, Brown E, Fairhurst C (1971) Optimizing the control of rock failure in servo-controlled laboratory tests *Rock Mechanics and Rock Engineering* 3:217-224

Jansen DC, Shah SP (1997) Effect of length on compressive strain softening of concrete *Journal of Engineering Mechanics* 123:25-35

Kolsky H (1949) An investigation of the mechanical properties of materials at very high rates of loading *Proceedings of the Physical Society Section B* 62:676

Kolsky H (1963) *Stress waves in solids vol 1098*. Courier Corporation,

Koohbor B, Kidane A, Lu W-Y, Sutton MA (2016) Investigation of the dynamic stress-strain response of compressible polymeric foam using a non-parametric analysis *International Journal of Impact Engineering* 91:170-182

Kumar A (1968) The effect of stress rate and temperature on the strength of basalt and granite *Geophysics* 33:501-510

LAJTAI, E. Z. and V. N. LAJTAI (1974). "The evolution of brittle fracture in rocks." *Journal of the Geological Society* 130(1): 1-16.

Li, X., T. Lok and J. Zhao (2005). "Dynamic characteristics of granite subjected to intermediate loading rate." *Rock Mechanics and Rock Engineering* 38(1): 21-39.

Li QM, Meng H (2003) About the dynamic strength enhancement of concrete-like materials in a split Hopkinson pressure bar test *Int J Sol Struct* 40:343-360 doi:10.1016/s0020-7683(02)00526-7

## CHAPTER 4 DYNAMIC PROPERTIES AND FRACTURE PATTERNS OF ROCK BY FULL-FIELD MEASUREMENT

Li X, Lok T, Zhao J, Zhao P (2000) Oscillation elimination in the Hopkinson bar apparatus and resultant complete dynamic stress–strain curves for rocks *International Journal of Rock Mechanics and Mining Sciences* 37:1055-1060

Li X, Zhou Z, Lok T-S, Hong L, Yin T (2008) Innovative testing technique of rock subjected to coupled static and dynamic loads *International Journal of Rock Mechanics and Mining Sciences* 45:739-748

Liang, C. Y., X. Li, S. Wang, S. Li, J. He and C. Ma (2012). "Experimental investigations on rate-dependent stress–strain characteristics and energy mechanism of rock under uniaxial compression." *Chinese Journal of Rock Mechanics and Engineering* 31(9): 1830-1838.

Lindholm U (1964) Some experiments with the split hopkinson pressure bar *Journal of the Mechanics and Physics of Solids* 12:317-335 doi:10.1016/0022-5096(64)90028-6

Lindholm U (1974) Review of dynamic testing techniques and material behavior. In: *Mechanical properties at high rates of strain*.

Liu, X.-l., X.-b. Li, L. Hong, T.-b. Yin and M. Rao (2015). "Acoustic emission characteristics of rock under impact loading." *Journal of Central South University* 22(9): 3571-3577.

Luo P, Chao Y, Sutton M, Peters Iii W (1993) Accurate measurement of three-dimensional deformations in deformable and rigid bodies using computer vision *Experimental Mechanics* 33:123-132 doi:10.1007/BF02322488

Martin, C. D. (1993). The strength of massive Lac du Bonnet granite around underground openings. Doctoral, University of Manitoba.

Markeset G, Hillerborg A (1995) Softening of concrete in compression—localization and size effects *Cement and Concrete Research* 25:702-708

Masuda, K., H. Mizutani and I. Yamada (1987). "Experimental study of strain-rate dependence and pressure dependence of failure properties of granite." *Journal of Physics of the Earth* 35(1): 37-66.

Mavko G, Mukerji T, Dvorkin J (2009) *The rock physics handbook: Tools for seismic analysis of porous media*. Cambridge university press,

Munoz H, Taheri A, Chanda E (2016) Pre-peak and post-peak rock strain characteristics during uniaxial compression by 3D digital image correlation *Rock Mechanics and Rock Engineering* 49:2541-2554

Nicksiar, M. and C. Martin (2013). "Crack initiation stress in low porosity crystalline and sedimentary rocks." *Engineering Geology* 154: 64-76.

Olsson, W. (1991). The compressive strength of tuff as a function of strain rate from 10<sup>-6</sup> to 10<sup>3</sup>/sec. *International Journal of Rock Mechanics and Mining Sciences & Geomechanics Abstracts*, Elsevier.

Pan B, Yu L, Yang Y, Song W, Guo L (2016) Full-field transient 3D deformation measurement of 3D braided composite panels during ballistic impact using single-camera high-speed stereo-digital image correlation *Composite Structures* 157:25-32

Pan B, Yu L, Zhang QB (2017) Review of single-camera stereo-digital image correlation techniques for full-field 3D shape and deformation measurement *Science China Technological Sciences*

## CHAPTER 4 DYNAMIC PROPERTIES AND FRACTURE PATTERNS OF ROCK BY FULL-FIELD MEASUREMENT

Peirs J, Verleysen P, Van Paepegem W, Degrieck J (2011) Determining the stress–strain behaviour at large strains from high strain rate tensile and shear experiments *International Journal of Impact Engineering* 38:406-415

Perkins R, Green S (1968) High speed photography in dynamic materials testing *Review of Scientific Instruments* 39:1209-1210 doi:10.1063/1.1683621

Pierron F, Forquin P (2012) Ultra-High-Speed Full-Field Deformation Measurements on Concrete Spalling Specimens and Stiffness Identification with the Virtual Fields Method *Strain* 48:388-405

Pinto M, Gupta S, Shukla A (2015) Study of implosion of carbon/epoxy composite hollow cylinders using 3-D digital image correlation *Composite Structures* 119:272-286

Raurova I, Berggreen C, Eriksen R A dual 3D DIC-system application for DSL strain and displacement measurements. In: *EPJ Web of Conferences*, 2010. EDP Sciences, p 31005

Reu P (2014a) All about speckles: aliasing *Experimental Techniques* 38:1-3

Reu P (2014b) All about speckles: speckle size measurement *Experimental Techniques* 38:1-2

Rummel F, Fairhurst C (1970) Determination of the post-failure behavior of brittle rock using a servo-controlled testing machine *Rock mechanics* 2:189-204

Schmidt TE, Tyson J, Galanulis K, Revilock DM, Melis ME Full-field dynamic deformation and strain measurements using high-speed digital cameras. In: *26th International Congress on High-Speed Photography and Photonics*, 2005. International Society for Optics and Photonics, pp 174-185

Song B, Chen W (2006) Energy for Specimen Deformation in a Split Hopkinson Pressure Bar Experiment *Experimental Mechanics* 46:407-410 doi:10.1007/s11340-006-6420-x

Sutton M, Yan J, Tiwari V, Schreier H, Orteu J (2008) The effect of out-of-plane motion on 2D and 3D digital image correlation measurements *Optics and Lasers in Engineering* 46:746-757

Sutton MA, Orteu JJ, Schreier H (2009) *Image correlation for shape, motion and deformation measurements: basic concepts, theory and applications*. Springer Science & Business Media,

Tarasov B, Potvin Y (2013) Universal criteria for rock brittleness estimation under triaxial compression *International Journal of Rock Mechanics and Mining Sciences* 59:57-69

Wawersik, W. and C. Fairhurst (1970). A study of brittle rock fracture in laboratory compression experiments. *International Journal of Rock Mechanics and Mining Sciences & Geomechanics Abstracts*, Elsevier.

Woo, S.-C. and T.-W. Kim (2016). "High strain-rate failure in carbon/Kevlar hybrid woven composites via a novel SHPB-AE coupled test." *Composites Part B: Engineering* 97: 317-328.

Xia K, Yao W (2015) Dynamic rock tests using split Hopkinson (Kolsky) bar system—A review *Journal of Rock Mechanics and Geotechnical Engineering* 7:27-59

Xing HZ, Zhang QB, Braithwaite CH, Pan B, Zhao J (2017) High-Speed Photography and Digital Optical Measurement Techniques for Geomaterials: Fundamentals and Applications *Rock Mechanics and Rock Engineering*:1-49 doi:10.1007/s00603-016-1164-0

## CHAPTER 4 DYNAMIC PROPERTIES AND FRACTURE PATTERNS OF ROCK BY FULL-FIELD MEASUREMENT

Xu S, Huang J, Wang P, Zhang C, Zhou L, Hu S (2015) Investigation of rock material under combined compression and shear dynamic loading: An experimental technique *International Journal of Impact Engineering* 86:206-222

Xue, L., S. Qin, Q. Sun, Y. Wang, L. M. Lee and W. Li (2014). "A study on crack damage stress thresholds of different rock types based on uniaxial compression tests." *Rock Mechanics and Rock Engineering* 47(4): 1183-1195.

Yin, Z., L. Wang, H. Ma, Z. Hu and J. Jin (2014). "Application of Optical Measurement Method in Brazilian Disk Splitting Experiment Under Dynamic Loading." *Sensors & Transducers* 171(5): 176.

Zhang Q, Zhao J (2013a) Effect of loading rate on fracture toughness and failure micromechanisms in marble *Engineering Fracture Mechanics* 102:288-309

Zhang Q, Zhao J (2014a) A review of dynamic experimental techniques and mechanical behaviour of rock materials *Rock mechanics and rock engineering* 47:1411-1478

Zhang QB, Zhao J (2013b) Determination of mechanical properties and full-field strain measurements of rock material under dynamic loads *Int J Rock Mech Min* 60:423-439 doi:10.1016/j.ijrmms.2013.01.005

Zhang QB, Zhao J (2014b) A review of dynamic experimental techniques and mechanical behaviour of rock materials *Rock Mechanics and Rock Engineering* 47:1411-1478 doi:10.1007/s00603-013-0463-y

Zhao, J., H. Li, M. Wu and T. Li (1999). "Dynamic uniaxial compression tests on a granite." *International Journal of Rock Mechanics and Mining Sciences* 36(2): 273-277.

Zhao H, Gary G (1996a) On the use of SHPB techniques to determine the dynamic behavior of materials in the range of small strains *Int J Sol Struct* 33:3363-3375 doi:10.1016/0020-7683(95)00186-7

Zhao H, Gary G (1996b) On the use of SHPB techniques to determine the dynamic behavior of materials in the range of small strains *International Journal of Solids and structures* 33:3363-3375

Zhao, X., M. Cai, J. Wang and L. Ma (2013). "Damage stress and acoustic emission characteristics of the Beishan granite." *International Journal of Rock Mechanics and Mining Sciences* 64: 258-269.

Zhou, Y., K. Xia, X. Li, H. Li, G. Ma, J. Zhao, Z. Zhou and F. Dai (2012). "Suggested methods for determining the dynamic strength parameters and mode-I fracture toughness of rock materials." *International Journal of Rock Mechanics and Mining Sciences* 49: 105-112.

Zhou, Z.-l., Z. Yuan, Y.-h. Jiang, Z. Yang, C. Xin and D.-y. Li (2017). "Dynamic behavior of rock during its post failure stage in SHPB tests." *Transactions of Nonferrous Metals Society of China* 27(1): 184-196.

Zou, C. and L. N. Y. Wong (2014). Study of Mechanical Properties and Fracturing Processes of Carrara Marble in Dynamic Brazilian Tests by Two Optical Observation Methods. *Rock Mechanics and Its Applications in Civil, Mining, and Petroleum Engineering*: 20-2



## CHAPTER 5 INTRINSIC AND EXTERNAL EFFECTS ON DYNAMIC BEHAVIOUR OF ROCK

Part of the materials in this chapter is based on the publication by Xing et al. (2019) in International Journal of Rock Mechanics and Mining Sciences (Vol.50, pp.1611-1659), titled 'Fracture and mechanical characteristics of CO<sub>2</sub>-saturated sandstone at extreme loading condition'.

### 5.1 INTRODUCTION

It has been well known that the grain composition, distribution and size have the significant effect on the mechanical properties of the rock since the different microstructure would entirely change the characteristics of rock behaviour. Meanwhile, the utilization of underground spaces, where high temperature and fluid environment may occur, is more and more important. For example, energy such as geothermal power is extracted by the enhanced geothermal system (EGS), in which either water (Tester, Anderson et al. 2006) or supercritical CO<sub>2</sub> (Brown 2000) interacts with hot rock, creates a subsurface fracture system and subsequently brings the heat out. In terms of resources, a good example is the exploitation of CH<sub>4</sub> (Cui, Bustin et al. 2004), shale gas (Middleton, Carey et al. 2015) and oil (Hamouda and Tabrizy 2013) from the reservoir via the fracture and replacement by CO<sub>2</sub> which achieves carbon capture and sequestration (CCS) at the same time. The thermal and fluid effect on the rock mechanics will influence the safety of the rock engineering or the efficiency of the rock excavation. Geo-energy extraction often interacts with fluid, typically water, brine and CO<sub>2</sub>, which would affect the physical and chemical aspects of mineralogical structure and composition. On the other hand, the underground structure may suffer dynamic loading from earthquake and impact, where the mechanical properties of rock differ significantly due to strain rate effect. However, temperature or fluid have opposite effects on the mechanical properties against strain rate effect. Decreasing the strain rate, increasing the temperature or presence of fluid such as water, carbon dioxide and brine will lead to lower stress levels, but higher values of strain (Zhang and Zhao 2014). Therefore, the understanding of the coupled effect between intrinsic, external factors and strain rate on the dynamic behaviour of rocks is essential.

In this chapter, the intrinsic effect mainly focuses on the grain size and rock type aspect. The external effect concentrates on the high temperature and brine/water/CO<sub>2</sub>. The dynamic properties and fracture patterns of rock under coupled effect are investigated by SHPB tests with high-speed 3D-DIC. The mechanism of the intrinsic and external effect is revealed by microscopic analysis such as XRD and SEM.

## **5.2 BACKGROUND**

### **5.2.1 Grain size effect**

Sandstone, as a porous and permeable geomaterial composed by grains vary from 0.0625 mm to 2 mm, plays an important role in geo-resource such as the enhanced oil recovery, CO<sub>2</sub> storage (Benson 2015) and enhanced geothermal system. However, to ensure the sustainable access to the geo-energy, the rock mechanics is the key to providing a safe working environment and efficient engineering operation. One of the most concerning issues is the dynamic behaviour of rock under a high-strain rate loading.

Investigations have been extensively made by researchers on the relationships between mechanical properties and mean grain size of rock. The early studies focused on the qualitative relationship, and a consensus was that the mechanical properties decrease with the increase of mean grain size (Brace 1961, Mendes, Aires-Barros et al. 1966, Willard and McWilliams 1969). Afterwards, much efforts were made to find the regression equations between mechanical properties and grain size. Linear regression equations were established between the weight mean grain size and ultimate strength (Hugman III and Friedman 1979, Åkesson, Lindqvist et al. 2001, Yusof and Zabidi 2016), Los Angeles (LA) value (Räisänen 2004) and aggregate impact value (AIV) (French, Kermani et al. 2001, Lundqvist and Göransson 2001). Other regression equation were also found on inverse square root (Wong, Chau et al. 1996), logarithm (Přikryl 2001) and exponential relationship (Hareland, Polston et al. 1993). In numerical study, the description of coarse or medium grain size was adopted by inputting the homogeneity indexes (Wang, et.al., 2014). The result showed that the homogeneity indexes apparently affected the crack initiation and development. Although there have been many correlations between mechanical properties and grain size, most of them only test in a fixed strain rate. An increase of strain rate induces a change in mechanical

properties and fracture behaviour (Zhang and Zhao 2014). A fundamental difference between quasi-static and high strain-rate tests is that inertia effects will be considerable enough that affecting the stress wave propagation and deformation (Xing, Zhang et al. 2018). Micro-measurements also revealed that the fracture mechanism will change corresponding to different strain rates. A rougher surface with mostly inter-granular fracture was displayed in quasi-static test, but a flatter fracture surface with more trans-granular fracture generated in the high strain rate loading (Zhang and Zhao 2014). (Wasantha, Ranjith et al. 2015) investigated the sandstone specimens with different grain sizes under uniaxial compression at a range of strain rates of  $10^{-6}$ ,  $10^{-5}$ ,  $10^{-4}$  and  $10^{-3} \text{ s}^{-1}$ . The sensitivity of the grain size on strain rate effect was discussed and an unusual behaviour was observed for coarse grained sandstone which has the maximum strength at the slowest strain rate, reversing the general decreasing trend of strength with decreasing strain rate. (Yu, Wei et al. 2017) investigated the dynamic tensile strength of sandstone with different loading rates and grain sizes through the BD tests on SHPB. The relationship between the dynamic tensile strength and loading rates was built through a linear equation.

It can be seen that the effect of grain size on the mechanical behaviour is seldom reported with the strain rate effect, especially under the high strain-rate loadings. Previous investigations focused more on the mechanical properties rather than the fracture pattern. The micro-measurement was rarely applied to investigate the mechanism of the coupled effect between strain rate and grain size.

### 5.2.2 Rock type effect

Although grain size effect on rock mechanics and fracturing attracted great attentions, the grain composition and distribution effect were few studied. In this section, dynamic BD test with high-speed DIC is implemented to examine dynamic behavior of different rock type.

BD test, as an indirect testing method to determine tensile strength, has been widely applied on brittle materials especially geomaterial such as rock and concrete. More than 7500 research papers related to BD test are published in the last two years according to the data from google scholar. To determine the dynamic tensile strength, BD test are operated on SHPB. The dynamic BD test was firstly employed on ceramic by Nojima and Ogawa (1989), on concrete by Ross et al. (1989) and Tedesco et al. (1989) and on rock by Dutta and Kim

(1993). In the last two decades, the development in the dynamic BD test mainly focused on the improvement of loading method, integration of innovative measurement and environmental factors. In terms of the improvement of loading method, four typical loading configurations of the loading platens were proposed successively. They are flat loading platens, flat loading platens with two small-diameter steel rods, flat loading platens with cushion, curved loading jaws and the flattened disc (Wang, Jia et al. 2004). The improvement all came from the validity of BD test which is the location of the failure initiation. According to the theoretical analysis based on the Griffith criteria, the failure should start from the center of the disc. However, Hudson et al. (1972) found that failure always initiated directly under the loading points in BD test if only flat steel platens were used to load the specimens in a servo-controlled testing machine. Based on three-dimensional (3D) finite element method (FEM) numerical analysis, Yu (2005) reported that BD test was not suitable to measure the tensile strength of rock-like materials, because the largest equivalent stress was always at the loading interface rather than the center of the disc. Noting that, specially designed steel rod or cardboard cushions between a flat loading platen and the specimen were suggested in the BD test (ASTM 2008). Curved loading jaws were proposed to guarantee a reasonable failure mode of rock discs. Erarslan et al. (Erarslan, Liang et al. 2012) investigated the difference between standard Brazilian jaws and various loading arc angles for BD test on Brisbane tuff by experimental and numerical studies. But the design and manufacture of above special loading platens are complex, and different specimen sizes require different loading platens. With regards to the measurement development in dynamic BD test, the milestone is the application of high-speed imaging with digital optical measurements monitoring the deformation of the specimen. Wong et al. (Wong, Zou et al. 2014) observed the cracking processes in static and dynamic BD test of Carrara marble by high-speed video footage captured at a frame rate of 100,000 fps. Rock-like material was investigated by dynamic BD test with high-speed photography as well. Zhou and Zhu studied the tensile behavior of five types of 3D printing material by BD test with the aid of (Zhou and Zhu 2017) a high-speed camera at 100,000 fps to monitor the fracturing process. Colback applied high-speed photography to observe the photoelastic patterns induced in birefringent layers to determine the fracture initiation point and subsequent propagation (Colback 1966). The digital image correlation (DIC) method was firstly employed by Zhang and Zhao to calculate the strain

fields of specimen to observe the failure initiation and propagation (Zhang and Zhao 2013). Microscopic observation was applied as a post failure analysis means to investigate the mechanism of the fracture after BD test. Li, Hui, et al. used X-ray diffraction (XRD) (Li, Lai et al. 2017) to estimate the mineralogy and total organic content (TOC) after the sample failed. Zhang and Zhao (Zhang and Zhao 2013) applied thin section to study the relationship between crack path and grain boundary. Scanning electron microscopy (SEM) was also applied to investigate the topography of the fractured surface of fragments after BD test. The environmental effects studies carried out with BD test include the saturation of water (Huang, Xia et al. 2010), , thermal (Liu, Xu et al. 2016), bedding effect (Tavallali and Vervoort 2010) and the pre-stress (Zhou, Li et al. 2014).

### 5.2.3 Thermal effect

The thermal effect on the rock dynamics has attracted extensively attentions from researchers. The dynamic fracture toughness of Fangshan gabbro subjected to high temperature was measured by (Zhang, Yu et al. 2001) with the short rod (SR) method on SHPB. It was found that temperature variation affected the dynamic fracture toughness of the two rocks to a limited extent within the temperature range tested. This was different from the results obtained under the static loading condition. (Yin, Li et al. 2012) investigated the effect of thermal treatment on the dynamic fracture toughness of Laurentian granite (LG) through NSCB test. The micro-cracks in the rock samples induced by thermal treatment were examined by SEM. They found that at temperatures below 250°C, the thermal expansion of grains led to an increase in the rock toughness. When treatment temperatures were above 450 °C, the sources of weakness such as grain boundaries and phase transition of silicon were depleted, and resulted in the decrease in fracture toughness. Similar pattern was also found in tensile strength in BD tests done by (Yin, Li et al. 2015) with LG after being treated with high temperature. The dynamic tensile strength first increased and then decreased with a linear increase in loading rate. (Liu and Xu 2014) employed SHPB method to conduct uniaxial compression and split tensile tests on the Qinling biotite granite samples, which were treated under high temperatures and then cooled naturally to room temperature. The effect of high temperature on the dynamic tensile and compressive strength was concluded. (Huang and Xia 2015) used CT to quantify the damage induced by the heat-treatment and correlated it with the dynamic compressive strength of Longyou sandstone. (Liu and Xu 2015) carried

out the investigations of the influences of coupled temperature-strain-rate effect on dynamic behaviours of sandstone. They found that the increase ratios of dynamic compressive strength, peak strain, and energy absorption ratio of rock under high temperature had no obvious strain rate effects. The research was also examined on granite by (Fan, Wu et al. 2017). The results showed that the dynamic energy absorption capacity increased below 400 °C but then decreased as the temperature increased to 800 °C. The thermal effects on energy absorption capacity were more obvious for granite under a smaller impact pressure. The dynamic mechanical behaviours of coal exposed to elevated temperatures were tested by SHPB with anthracite specimens preheated up to 500°C in an oxygen-free environment (Yu, Zhang et al. 2017). They found that the coal gradually lost its dynamic bearing and anti-deformation capacities with increase in temperature, especially after 300°C.

However, in the previous study, only mechanical properties after or under heat treatment, such as strength and elastic modulus, were investigated. The dynamic fracture pattern like stress threshold for crack initiation and full-field crack propagation mode are still of uncertainty.

#### **5.2.4 Fluid effect**

Many efforts have been made by researchers to investigate the fluid effect on the mechanical behaviour of rock. The uniaxial compressive strength (UCS) and triaxial compressive strength (TCS) of rock affected by water saturation were studied on different types of rock under different saturation levels (Colback and Wiid 1965, Broch 1974, 1978, Hawkins and McConnell 1992, Li, Wong et al. 2012). In those studies, all UCS and TCS results showed reduced value in saturated rock. Rathnaweera et al. investigated the effect of NaCl brine of different concentrations on the stress-strain curve pattern as well as the failure stages of sandstone in UCS (Rathnaweera, Ranjith et al. 2014) and TCS test (Rathnaweera, Ranjith et al. 2015). The strength was lower in the brine-saturated specimen, but showed to be decreasing and then increasing at the concentration threshold of 10%. The AE count generated in high brine saturated rocks showed a more significant and brittle pattern due to the crush of NaCl crystal and the conductivity of brine. In TCS test the presence of NaCl in pore was found to enhance the friction angle, cohesion and dilatancy strength but reduced the post-peak dilation. Investigation of the presence and absence of CO<sub>2</sub> saturation in sandstone samples in UCS tests were studied. Results showed that the introduction of CO<sub>2</sub>

further weakened the sandstone combined with water or brine saturation, and the failure type was transformed from shear failure to splitting, which is more brittle (Rathnaweera, Ranjith et al. 2015). An investigation of TCS characteristics of the sandstone treated by CO<sub>2</sub> and brine was also discussed in (Perera, Rathnaweera et al. 2016). Experiments conducted on CO<sub>2</sub> injecting in silicate and carbonate-cemented sandstone samples have shown that the effect of CO<sub>2</sub> varies with the different mineralogical composition of rock (Rathnaweera, Ranjith et al. 2017). The silicate-cemented sandstone showed an increase in UCS with increasing injection pressure, but the trend was the opposite for the carbonate-cemented sandstone. Water effect on the fracture pattern of rock are widely investigated in hydraulic fracturing problems (Wang, et al., 2013).

In dynamic cases, Lomov et al. (Lomov, Hiltl et al. 2001) conducted a plate impact test on the dry and wet sandstone to verify a constitutive model for rock, in which the behaviour of the water-saturated material was addressed with a modified effective stress model. Huang et al. (Huang, Xia et al. 2010) conducted dynamic BD tests on dry and saturated sandstone to study the tensile strength softening by water saturation. The tensile strength of the saturated specimen showed a less strength but the gap was decreasing with the increase of the strain rate, which indicated that the saturated sandstone had a higher rate sensitivity. Kim et al. (Kim and de Oliveira 2015) studied Young's modulus, maximum stress and strain of Red and Buff sandstones with different porosities under dried and fully saturated conditions by SHPB. It was found that the maximum stress was greater in the dry samples, but maximum strain has the opposite pattern. The porosity had a more hydro-sensitivity influence on Young's modulus and maximum strain than maximum stress. The water effect on the dynamic tensile strength of coal with bedding was studied by Zhao et al. (Zhao, Liu et al. 2016) through BD test with SHPB. They reported that saturated coal specimens had higher indirect tensile strength and loading rate dependency than dry ones. A relationship between water content (during both saturation and drying process) and dynamic strength of fine-grained sandstone was discussed by Zhou et al. (Zhou, Cai et al. 2016). The result showed that treatment with the same water content in different processes could lead to different dynamic tensile strength but same compressive strength. The combined effect of strain and saturation in a fine-grained sandstone was also investigated by Zhou et al. (Zhou, Xin et al. 2016) with a range of strain rate from 70 s<sup>-1</sup> to 230 s<sup>-1</sup> for dry and saturated specimens. They

found a critical strain rate of  $180 \text{ s}^{-1}$  above which the compressive strength of saturated specimens is higher than that of dry ones. Fracture toughness is a symbolised parameter to represent the fracturing behaviour of rock (Ayatollahi and Aliha 2007, Aliha and Ayatollahi 2014). It was found that, compared with the dry specimen, the saturated specimen owned a higher rate dependency of the dynamic fracture initiation, propagation toughness and a lower rate dependency of crack propagation velocity (Zhou, Cai et al. 2019).

The investigation of the fluid effect on dynamic behaviour of rock at high strain rate was limited to water saturation condition. The effect of brine,  $\text{CO}_2$ , and their combination on the rock mechanics was studied only in static range. The previous studies predominantly focused on the relationship between strength and fluid treatment. The fracturing behaviour such as stress threshold and morphology of crack initiation and propagation was however seldom studied.

### 5.3 GRAIN SIZE EFFECT

In this section, the coupled effect between grain size and strain rate on the dynamic mechanical properties and fracture patterns of sandstone was investigated by SHPB compression test. Full-field deformation and fracturing information were identified by high-speed 3D-DIC. The mechanism was explained from the perspective of microscopic investigation.

Coarse-grained, medium-grained and fine-grained Hawkesbury sandstones, as described in Section 3.2, were studied in this section. The mechanical properties of three different grain-size sandstones are listed in Table 5.1.

**Table 5.1** Mechanical properties for sandstones of different grain sizes

Grain size	Density ( $\text{kg/m}^3$ )	UCS (MPa)	Young's modulus (GPa)	P-wave Velocity (m/s)	Poisson's ratio
coarse	2165	13	1.9	3116	0.27
medium	2214	41	6.9	2110	0.21
fine	2331	47	7.2	4128	0.20

The results of dynamic strength of three sandstone at different strain rates are listed in Table 5.2 and illustrated in Fig. 5.1. Because each sandstone has the different wave impedance



which will affect the incident and transmitted wave. As a result, the same projectile velocity resulted in different strain rates on different rocks. When the strain rate was under  $100 \text{ s}^{-1}$ , the FG sandstone had the highest strength followed by the MG and the CG sandstone whose order was as same as the static condition. However, when the strain rate was above  $100 \text{ s}^{-1}$  the MG sandstone became the strongest. This could also be interpreted from the strain rate sensitivity in which the MG sandstone had the largest the sensitivity followed by the CG and FG sandstone, respectively. In terms of the dynamic increase factor (DIF), although the CG sandstone had the weakest strength but its DIF was the largest among three types of rock.

Table 5.2 Strength of CG, MG and FG under different strain rates

ID	Strain rate ( $\text{s}^{-1}$ )	Strength (MPa)	DIF	Strain rate sensitivity ( $\text{MPa}\cdot\text{s}$ )
CG-01	92	16	1.14	0.35
CG-02	104	20	1.43	
CG-03	115	24	1.71	
MG-00	70	45	1.10	0.5
MG-01	93	52	1.27	
MG-02	100	64	1.56	
MG-03	120	70	1.70	0.18
FG-01	67	51	1.09	
FG-02	73	54	1.15	
FG-03	100	57	1.21	

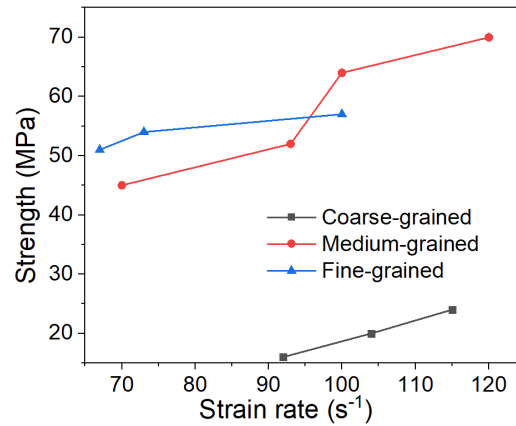


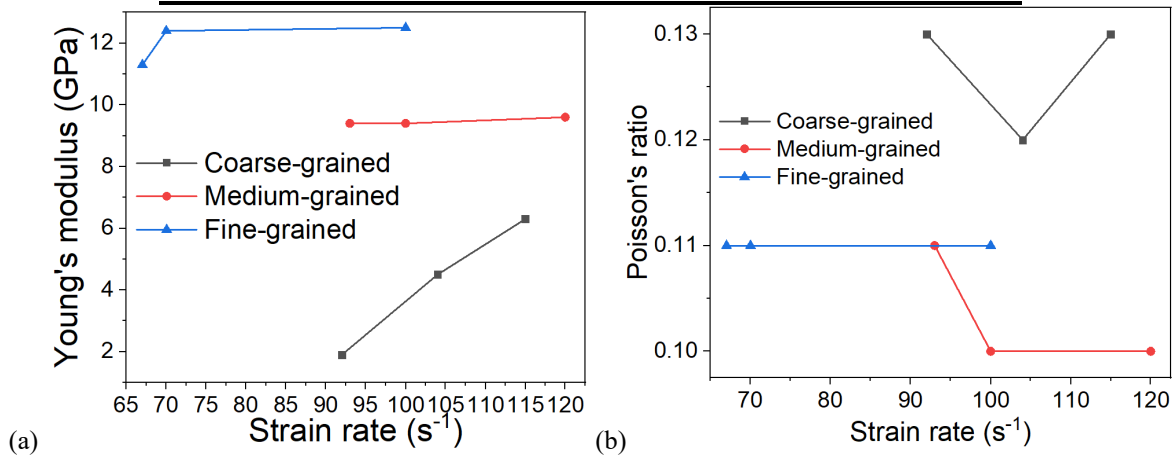
Fig. 5.1 Strength of CG, MG and FG under different strain rates

The dynamic elastic modulus was obtained with the ratio of the increment of stress to axial strain ( $\Delta\sigma / \Delta\epsilon_x$ ) during the quasi-linear stage in the stress-strain curve. The dynamic Poisson's ratio was determined by the sign ratio of lateral strain to axial strain ( $-\epsilon_y / \epsilon_x$ ). The

axial and lateral strain of the specimen were determined by axial ( $e_{xx}$ ) and lateral ( $e_{yy}$ ) strain fields averaged by pixels based on DIC results. According to Table 5.3 and Fig. 5.2, the FG sandstone had the largest Young's modulus followed by the MG and CG sandstone. The FG and MG was less rate dependent than the CG in Young's modulus. All types of sandstones increased its Young's modulus compared to static condition especially for the CG sandstone which increased more than 3 times at  $115 \text{ s}^{-1}$ . On the other hand, the CG sandstone had the highest Poisson's ratio, FG ranked second and MG least, but the differences in Poisson's ratio were not considerable at high strain rates. Compared with the static condition, all types of sandstones decreased more than half of the static Poisson's ratio which indicates the lateral expansion was largely limited at high strain rates.

**Table 5.3** Young's modulus and Poisson's ratio of CG, MG and FG at different strain rates

Specimen	Strain rate ( $\text{s}^{-1}$ )	Young's modulus (GPa)	Poisson's ratio
CG-01	92	1.9	0.13
CG-02	104	4.5	0.12
CG-03	115	6.3	0.13
MG-01	93	9.4	0.11
MG-02	100	9.4	0.10
MG-03	120	9.6	0.10
FG-01	67	11.3	0.11
FG-02	73	12.4	0.11
FG-03	100	12.5	0.11

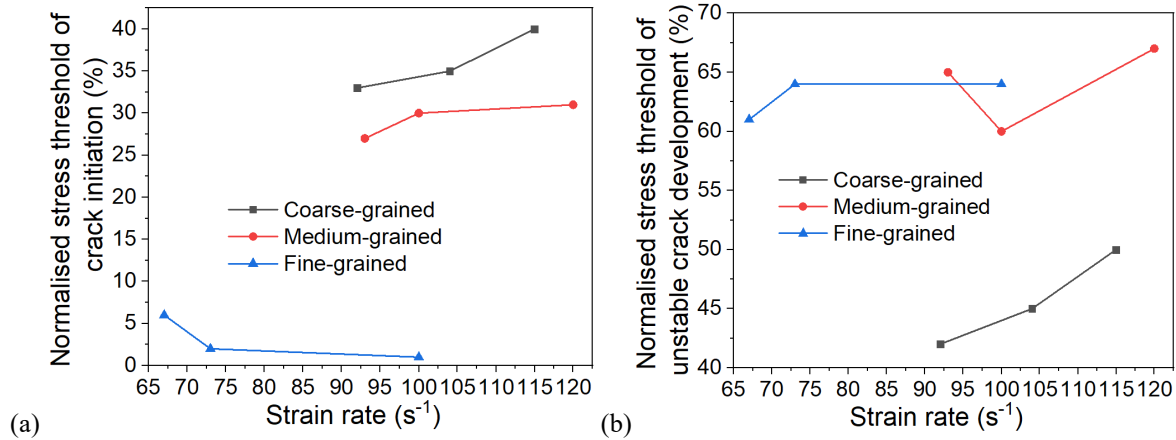


**Fig. 5.2(a)** Young's modulus and **(b)** Poisson's ratio versus different grain size and strain rates

Table 5.4 and Fig. 5.3 show that the stress threshold for crack initiation, unstable crack development increase with the growth of the strain rates for MG and CG sandstone. In terms of normalised stress threshold for crack initiation, CG and MG increase with the increase of strain rate but FG sandstone has the opposite trend. The value for the FG sandstone is significantly small around 5%, which means as soon as the dynamic loading applied on the material it triggers the crack initiation after a short crack closure stage. When it comes to normalised stress threshold, the FG and CG sandstone increase as the strain rating rising, the MG sandstone is somehow strain rate independent.

**Table 5.4** Stress thresholds of CG, MG and FG under different strain rates

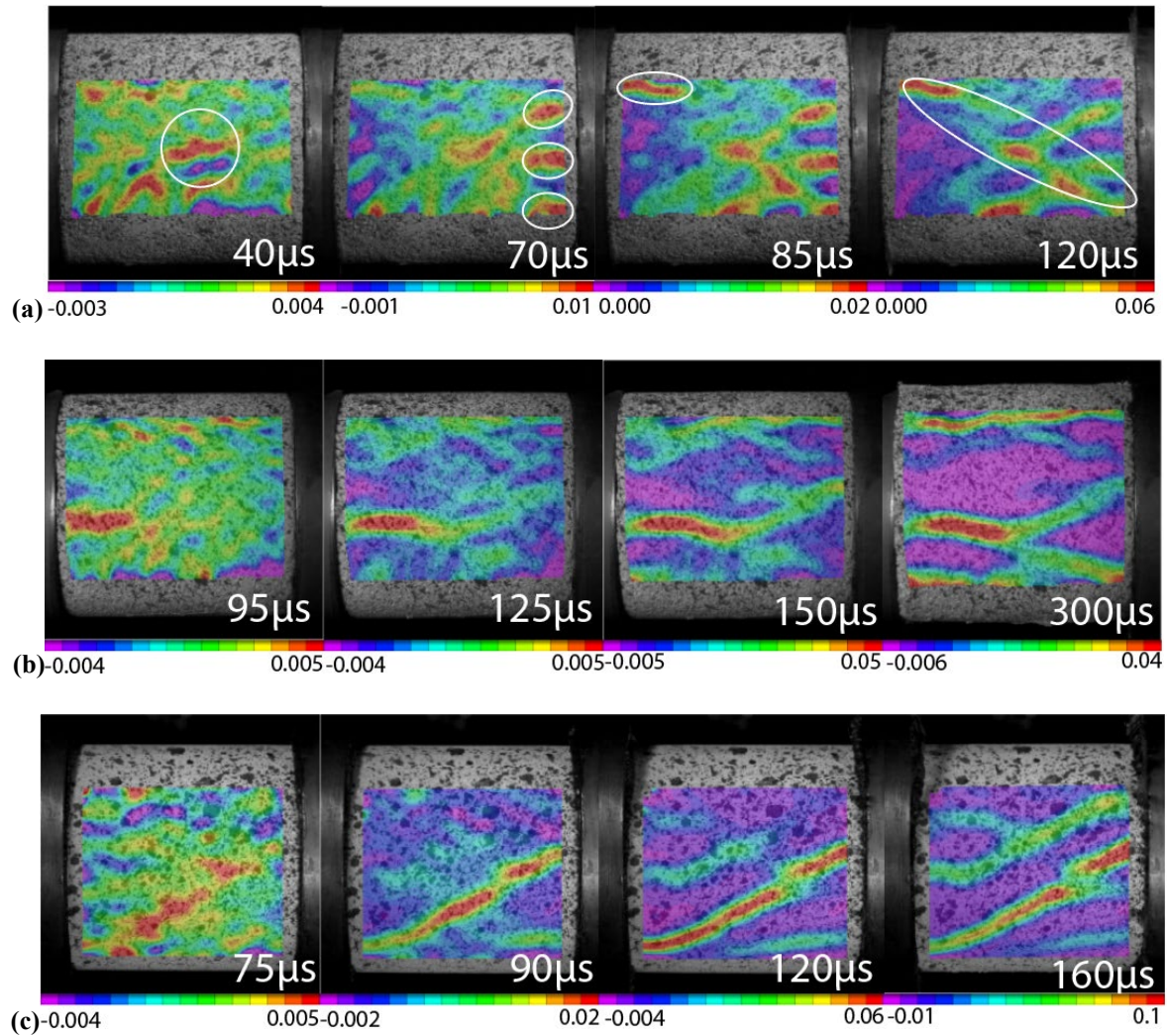
ID	Strain rate ( $s^{-1}$ )	$\sigma_{ci}$ (MPa)	$\sigma_{cd}$ (MPa)	$\sigma_{ucs}$ (MPa)	$\sigma_{ci}/\sigma_{ucs}$	$\sigma_{cd}/\sigma_{ucs}$
CG-01	92	5.3	6.7	16	33%	42%
CG-02	104	6.9	8.9	20	35%	45%
CG-03	115	9.7	11.9	24	40%	50%
MG-01	93	14.2	34.2	52.3	27%	65%
MG-02	100	19.6	38.3	64.2	30%	60%
MG-03	120	22.0	47.0	70.0	31%	67%
FG-01	67	3.3	31.2	51	6%	61%
FG-02	73	1.1	34.8	54	2%	64%
FG-03	100	0.8	36.2	57	1%	64%



**Fig. 5.3 (a)** Normalised stress threshold of crack initiation and **(b)** unstable development verses different grain size and strain rates

A strain field of specimen can provide the distribution and evolution of the strain localization indicating where the crack will happen. The strain localisation development in CG-02, MG-02 and FG-03 are shown in Fig. 5.4, where the strain rates are very close at around  $100 s^{-1}$

making them comparable. The first image in each figure corresponds to the initiation of the strain localisation. The strain localisation initiation in CG sandstone was sooner than FG and MG sandstone. The strain localisation initiated at the center of the specimen in CG-02 but at the edge in MG-02. With regards to FG-02, a span of strain localization suddenly appeared across the specimen with an angle.



**Fig. 5.4** Strain localisation development in (a) CG 02 (b) MG 02 and (c) FG 03.

During the crack development, the CG sandstone had several strain localisations generated at the edge, branched gradually and finally coalesced with a dominant crack inclined to the axis. The development of fracturing in MG-02 tended to be a splitting mode, in which the strain localisation extended from the initiation place with a nearly horizontal path to another

edge. That fracturing pattern is quite similar in FG-03 that a dominant crack extends from the initiation location but in an inclined direction.

## 5.4 ROCK TYPE EFFECT

This section, rock type effect on the dynamic tensile behavior was investigated with three types of rock representing igneous, metamorphic and sedimentary rock. The initiation and propagation of crack were discussed by high-speed 3D-DIC results. The fracturing feature was understood from the perspective of mineral composition and distribution obtained by thin section and SEM.

Three types of rocks were investigated with BD test which are Hawkesbury sandstone, Cararra marble and Impala black gabbro, as described in Section 3.2. The quasi-static BD test was controlled as a constant displacement of 0.2 mm/min. The dynamic loading was generated by the projectile at velocity around 8.5 m/s. High-speed cameras were employed to capture the deformation and fracturing process of the specimens. Two cameras were mounted up and down by tripods to establish a stereovision for the 3D-DIC. The resolution was set as 256×256 pixels and the frame rate was 200,000 fps with 4  $\mu$ s exposure time. The specimen ID and its corresponding loading condition are listed together with the tensile strength in Table 5.5. It can be seen from Table 5.5 that even the projectile velocity has a small standard deviation, the loading rate generated in three rock types may be dramatically different. Therefore, the loading rate not only depends on the incident wave or the geometry of the specimen and bar but also depends on the properties of rock. More commissioning tests have to be done if similar loading rates are required between different rocks for comparison. In terms of the tensile strength features, the strengthening effect of the loading rate exists for each rock type. The dynamic increase factor is 1.34, 1.9 and 2.0 for gabbro, marble and sandstone, respectively, which has the opposite order with the tensile strength.

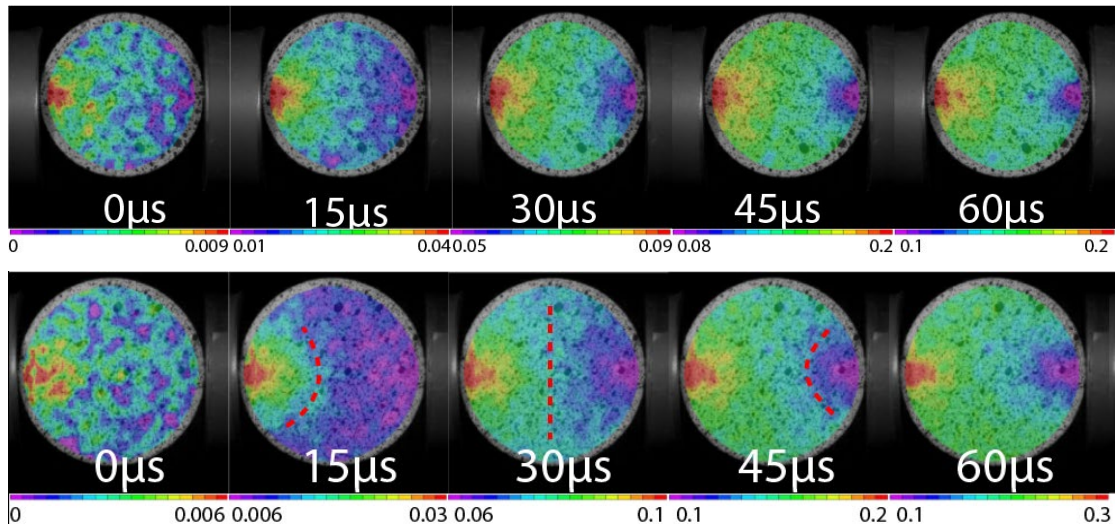
**Table 5.5** Specimen ID, loading condition and the tensile strength

Rock type	Impedance (MPa·s)	Loading type	Loading condition*	ID	Tensile strength (MPa)	Loading rate (Gpa/s)
<b>Gabbro</b>	2.02	static	0.2mm/min	G1	13.5	
				G2	12.7	
				G3	13.8	
		dynamic	8.4 $\pm$ 0.4 m/s	G4	17.7	430
				G5	17.8	479
				G6	18.2	488
<b>Marble</b>	1.46	static	0.2mm/min	M1	6.4	

<b>Sandstone</b>	0.44	dynamic	$8.6 \pm 0.4$ m/s	M2	6.6	334
				M3	5.5	
				M4	13.1	
				M5	11.9	
				M6	10.2	
				S1	2.8	
	0.44	static	0.2mm/min	S2	3.2	119
				S3	3.0	
				S4	5.5	
		dynamic	$9.0 \pm 0.1$ m/s	S5	6.1	
				S6	6.5	

\*Condition refers to loading speed for static tests and projectile velocity for dynamic tests.

Fig. 5.5 shows the horizontal displacement within the  $60 \mu\text{s}$  in all three types of rock indicating the stress wave propagation within the disc. It can be seen from the contour that the horizontal displacements of three types of rock firstly concentrated at the interface between the bar and the disc. Afterwards, it gradually propagated through the specimen with an arc front (indicated by red dash) which was symmetrical to the vertical axis. When the wave propagated across the center of the specimen, the arc front became vertical then turned back to arc again but with an opposite curvature. Finally, most of the specimen shared similar displacements while the edges had the largest and least displacements. The characteristics of the displacement is the interaction between the spherical wave (caused by point loading source) and the boundary of the disc. Because the gabbro has the largest wave velocity, the horizontal displacement propagates and reaches the end of the specimen with the shortest time followed with marble and sandstone.





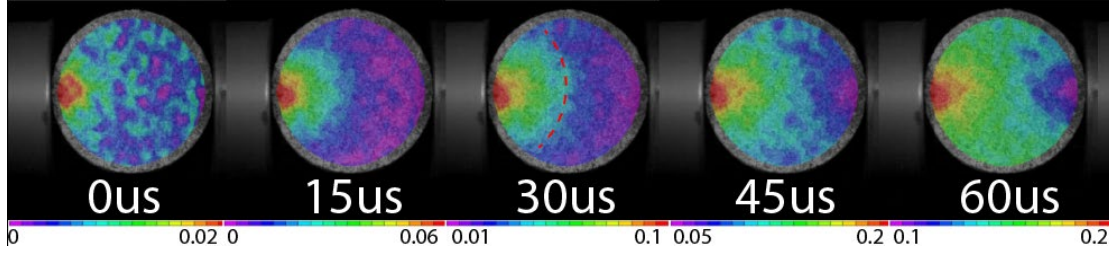


Fig. 5.5 Horizontal displacement (mm) in gabbro, marble and sandstone (up to down)

The vertical displacement is shown in Fig. 5.6 where the upper and lower semi-circle apparently has the opposite directions along with the horizontal axis after the loading. However, the speed and the patterns of the separation showed the difference. Gabbro and marble had the similar vertical displacement pattern that the separation of two semis started from the loading edge with an angle and propagate through the horizontal axis symmetrically. The separation of two semis finished at 30  $\mu$ s for gabbro and 50  $\mu$ s for marble. The vertical displacement of sandstone disc started at the edge with an angle close up to the center line of the disc with the separation time of 60  $\mu$ s.

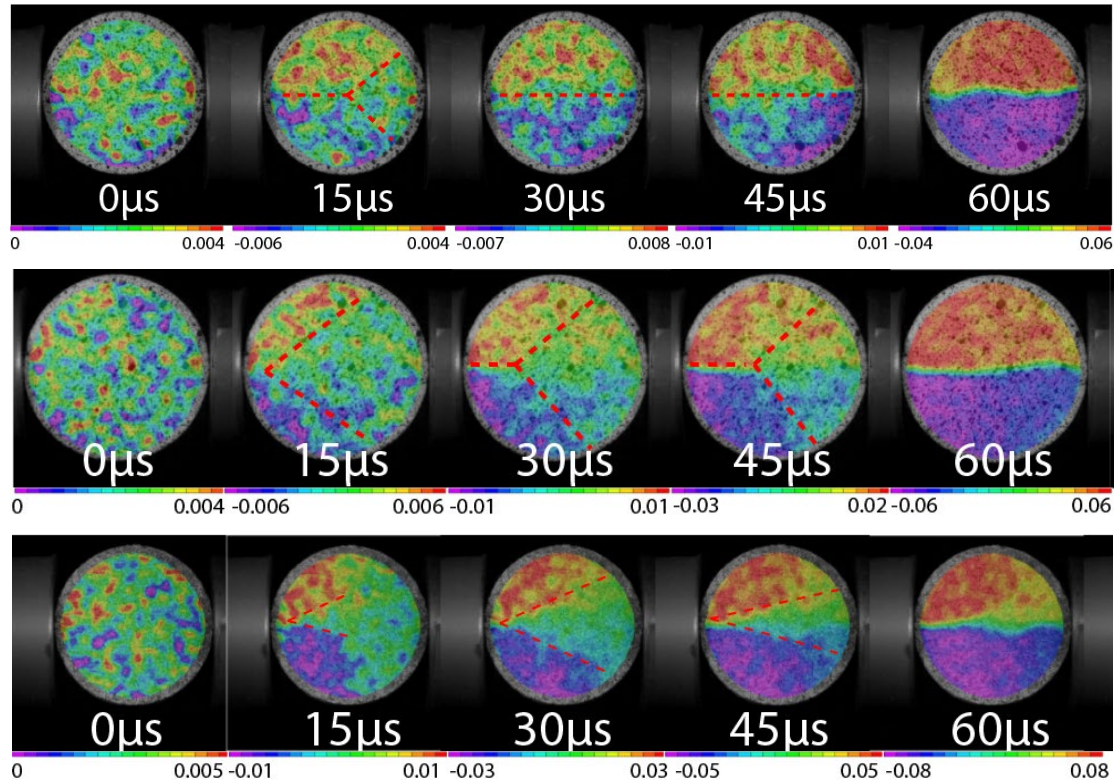


Fig. 5.6 Vertical displacement (mm) in gabbro, marble and sandstone (up to down)

The out-of-plane displacement at edge, shown in Fig. 5.7, is explained as the shear failure. The displacement firstly appeared at  $40\ \mu\text{s}$  at the end of the disc for gabbro which is opposite to the case of marble and sandstone. The out-of-plane displacement showed earliest in sandstone at  $20\ \mu\text{s}$  with significant degree due to the lowest shear strength. The rest part of the specimen had less out-of-plane displacement but not symmetric between upper and lower semi-circles for gabbro and marble which indicating that the deformation was not consistent through the z direction. This may be caused by the heterogeneity or manufacturing error in thickness direction. The 3D reconstructed surface is illustrated in Fig. 5.8, it is clear that the shear failure caused an uplifted shape on the edge of the BD disc. The maximum out-of-plane displacement is 0.23 mm, 0.16mm, 0.19mm for gabbro, marble and sandstone, respectively. Gabbro has the largest out-of-plane displacement but least area, sandstone has the largest shear failure zone.

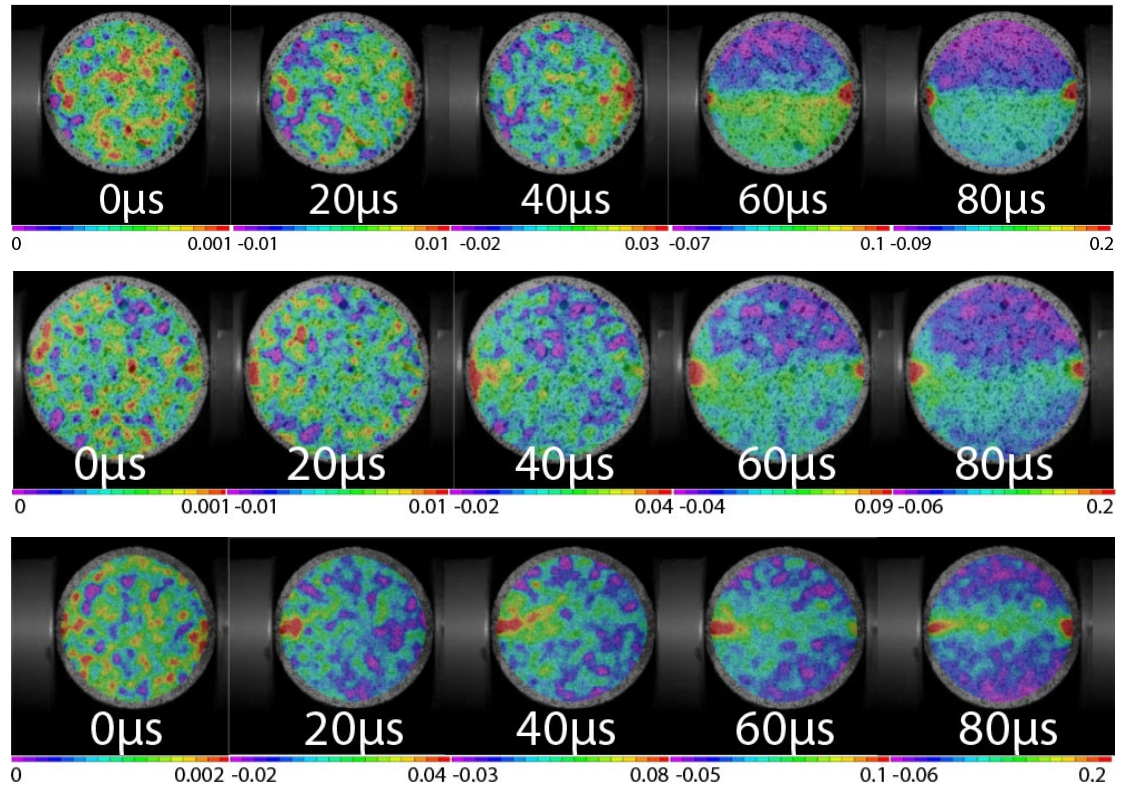


Fig. 5.7 Out-of-plane displacement (mm) in gabbro, marble and sandstone (up to down)



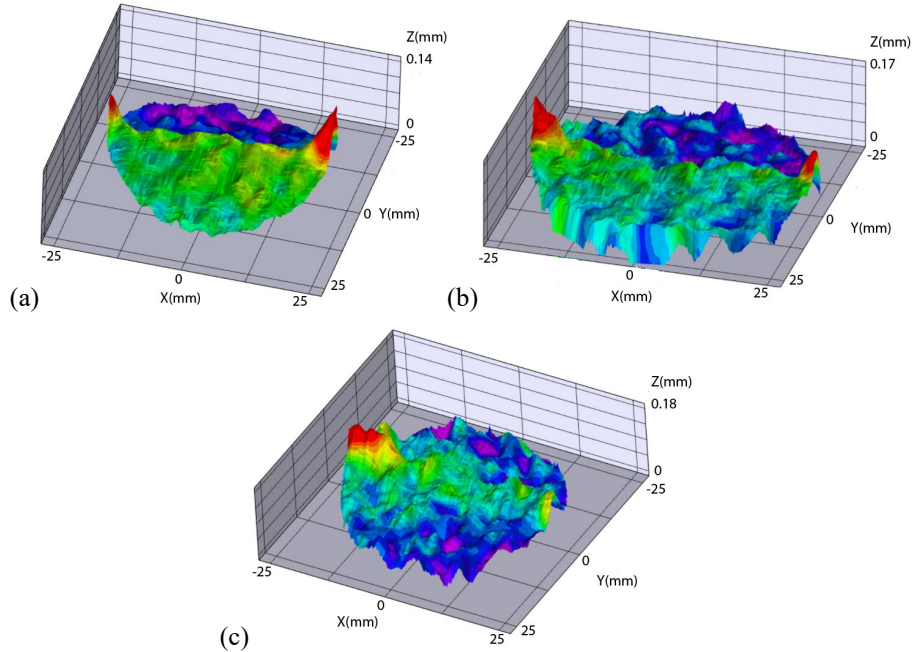


Fig. 5.8 3D view of the surface of (a) gabbro (b) marble and (c) sandstone at  $60 \mu\text{s}$

Fig. 5.9 shows the vertical strain localisation development in three types of rock. The first photo represents the initiation of the strain localisation. The strain localisation initiated from the end of the loading interface only happened in gabbro, both marble and sandstone initiated from the loading edge. This trend is same as the out-of-plane displacement. Therefore, the location of the strain localization in BD test with flat platen depends on where shear failures. The tensile stress afterwards dramatically concentrates on the strain localization and pull two semi-circles apart along the center axis. The duration for the strain localization was  $20 \mu\text{s}$ ,  $50 \mu\text{s}$  and  $90 \mu\text{s}$  for gabbro, marble and sandstone which has the same scale with the wave impedance in Table 5.5. Therefore, the propagation velocity of the strain localization (as well as crack) is dependent on the wave impedance of the rock which represents the resistance of rock against momentum transfer. Because the strain localization did not appear at the center, the tensile strength cannot represent the maximum tensile strength of the rock according to Griffith theory. It confirms that the plane platen can hardly obtain a good stress distribution in dynamic tests to find out the tensile strength of the rock.

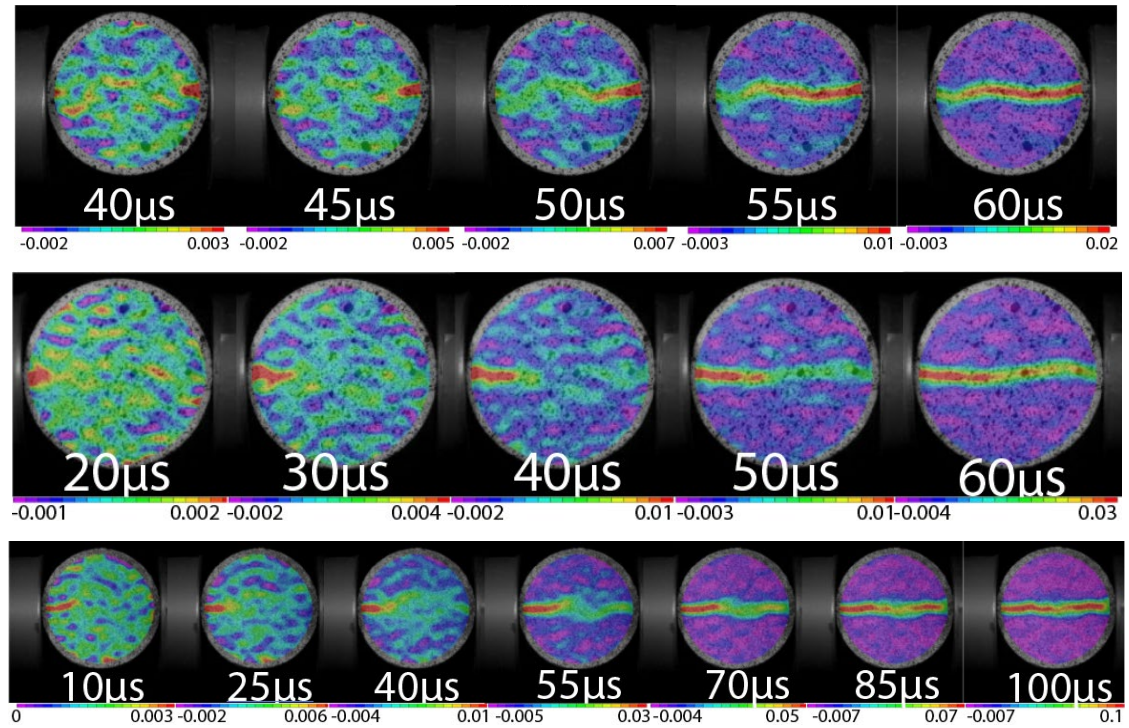


Fig. 5.9 vertical strain field ( $\epsilon_{yy}$ ) in gabbro, marble and sandstone (up to down)

The fractured surface of the BD discs were investigated under SEM, as shown in Fig. 5.10. According to the thin section images in Fig. 3.8, the gabbro is an intrusive igneous rock with coarse-sized mineral grains that formed as a result of slow cooling, which makes the grains well-formed and interlocked. When the tension is applied on the rock, most mineral grains would bear the stress and finally fracture intergranularly generating a high tensile strength, as shown in Fig. 5.10(a). The mineral grains in marble are with the similar sizes and fitted tightly. The grain surface is clear that most fractures were trans-granular, only a small part was intergranular as shown in Fig. 5.10(b). Because the quartz grain in sandstone is connected to each other by clay mineral such as Kaolinite, most fracture happened along the clay boundary. As can be seen in Fig. 5.10(c), the grain is still intact without tensile mark on its surface. As a result, the sandstone has the lowest tensile strength. Based the above ideas, a flow chart estimating the strength of the rock from the microscopic view is proposed in Fig. 5.11. The fragments of the BD disc in the static and dynamic tests are shown in Fig. 5.12. The shear failure is more significant in dynamic loading than that in static one.

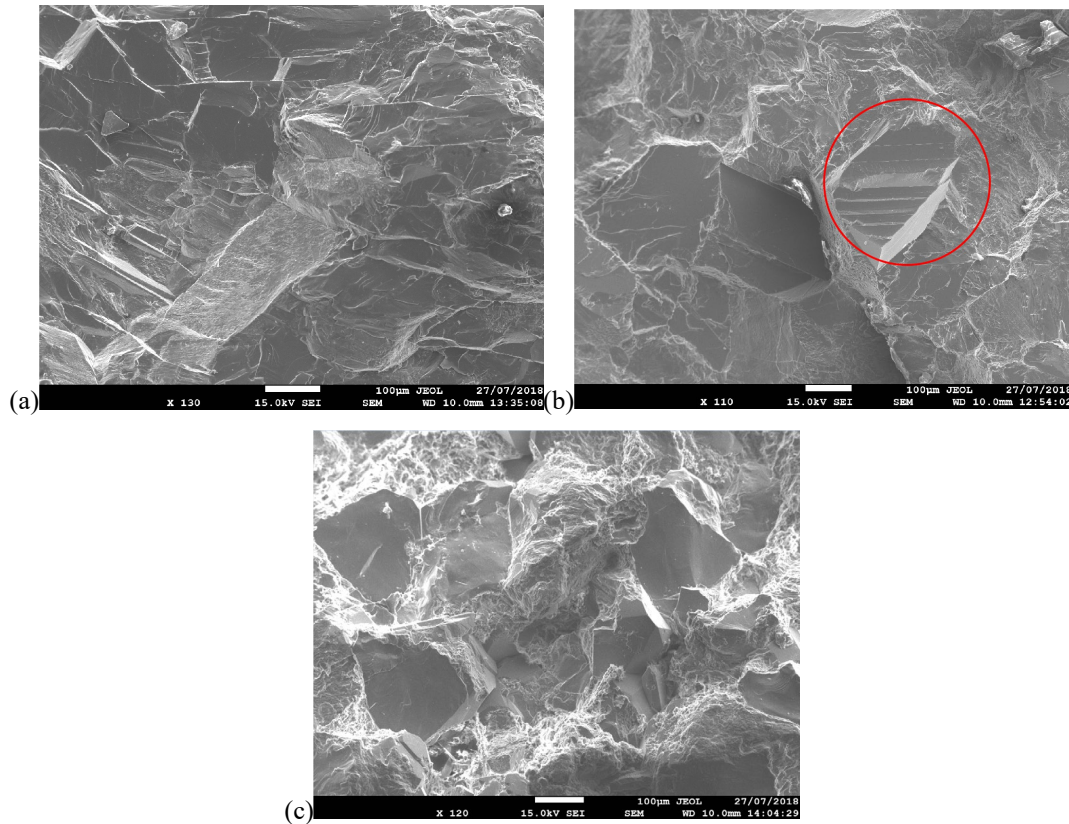


Fig. 5.10 Topography of the fracture surface of (a) gabbro, (b) marble and (c) sandstone after dynamic loading by SEM

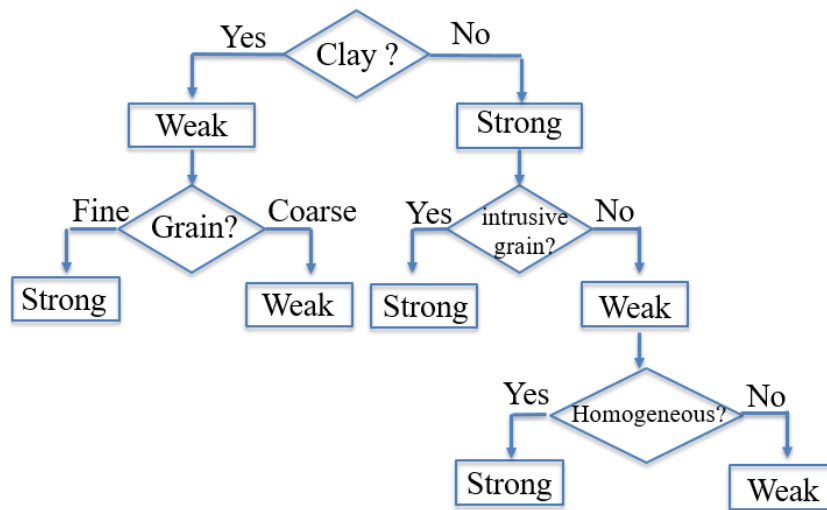
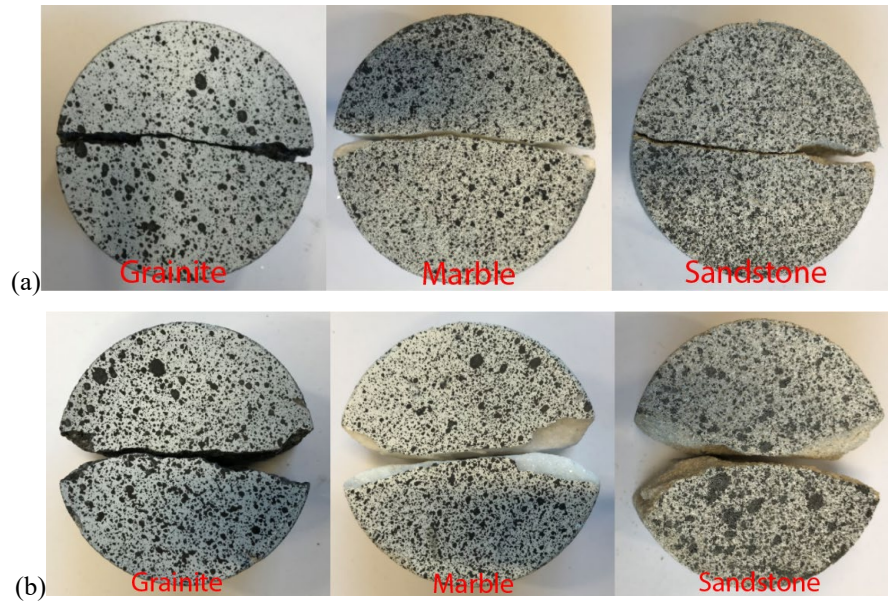


Fig. 5.11 Flow chart estimating the strength of the rock



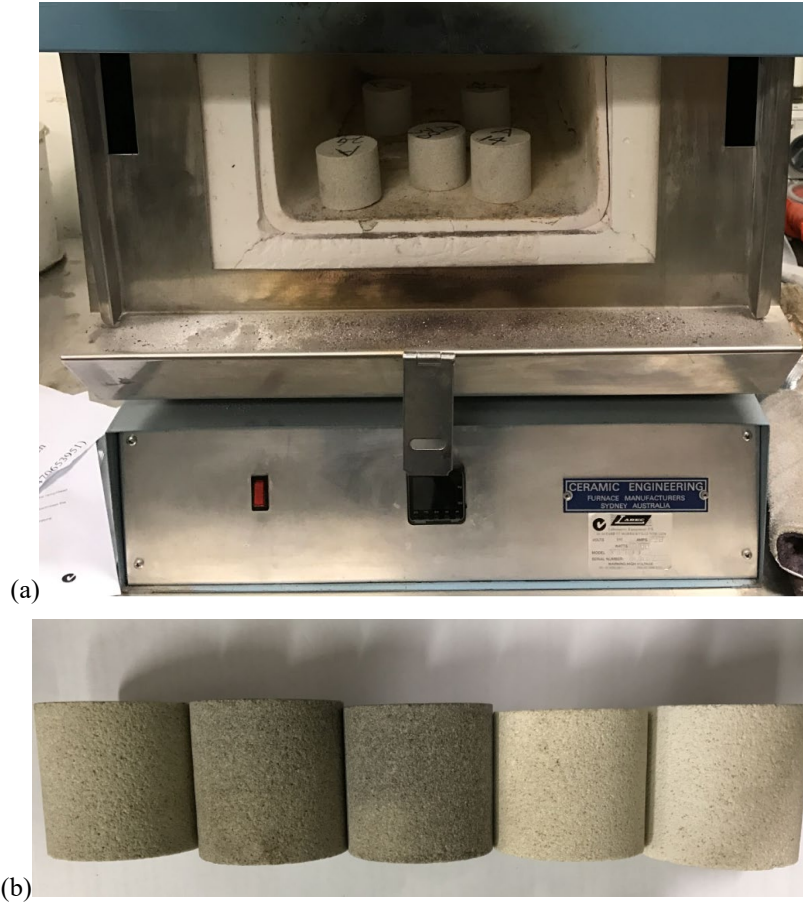
**Fig. 5.12** Post-failure fragments of gabbro, marble and sandstone in **(a)** quasi-static test and **(b)** dynamic test

The sandstone shows the most horizontal fracture path followed by marble and gabbro in Fig. 5.12. Because the crack propagated through the weakest path. In sandstone the weakest plane is clay mineral which has the smallest size. For non-clay mineral rock, the crack propagation path will be affected by the grain size.

## 5.5 THERMAL EFFECT

Hawkesbury sandstone was used for dynamic compression test and BD tests after high-temperature treatment. The specimens were heated by a muffle furnace, as shown in Fig. 5.13(a), to 200 °C, 400 °C, 800 °C and 1200 °C with the heating rate of 2°C /min to avoid heat shock (Ding, Ju et al. 2016). A soaking time of 6 hours was given to achieve the thermal steady state, followed by cooling down at the rate of 2°C /min. Fig. 5.13(b) shows the sandstone after different heat treatments and the colours appear a positive shift from green towards red with increasing temperature, i.e. sandstones become more reddish after heating. This colour change is mostly attributed to the iron-bearing minerals. A minor amount of ferrous minerals such as goethite or hematite can oxidise and turn the colour of sandstone to red.





**Fig. 5.13(a)** Muffle furnace to heat the sandstone **(b)** Colour change of Hawkesbury sandstone with increasing temperature (specimens from left to right were at 20 °C, 200 °C, 400 °C, 800 °C, 1200 °C)

In this study, SHPB was used to characterize the dynamic behavior of specimens. Two high-speed CMOS cameras (Phantom V2511) were adopted with the resolution of  $256 \times 256$  pixels, frame rate of 200,000 fps and exposure time of 4  $\mu$ s. High-speed 3D-DIC was used to characterize the full-field displacement.

Physical and mechanical results corresponding to different strain rates and temperatures are listed in Table 5.6. Fig. 5.14(a) shows the relationship between density, wave velocity and different temperature treatments. The densities did not change significantly since the samples did not lose any mass during heat treatment, a light decrease was due to the evaporation of constitution water. However, the wave velocity reduced significantly, up to 78% with regards to 1200 °C treatment. Even the mass did not change, the grain structure and distribution changed drastically due to the heat effect. Fig. 5.14(b) shows the relationship between dynamic tensile strength and thermal treatment. The strength firstly increased and reached the highest at the temperature of 400 °C, after which it decreased to 1.93 MPa which was

only 50% of strength at room temperature. In terms of the dynamic compressive strength shown in Fig. 5.14(c) the strain rate effect on the strength enhancement still exists for heat treated sandstone. The 400 °C group still has the highest compressive strength among all strain rates, followed by 200 °C, 20 °C, 800 °C and 1200 °C treatment. The reduction in the strength of 1200 °C group can exceed 70% compared with the room temperature strength. This pattern in dynamic compression is same as the tensile strength, which means that there is a critical temperature between 400 °C and 800 °C. Under that critical temperature the strength is positive to the increase of temperature, which is mainly due to the closing of various micro cracks inside the rock, the evaporation of water and the improvement of the friction relationship among the particles. Fig. 5.14(d) shows the strain rate sensitivity coefficient of dynamic compressive strength variation with temperature. The strain rate sensitivity coefficient is defined as the following:

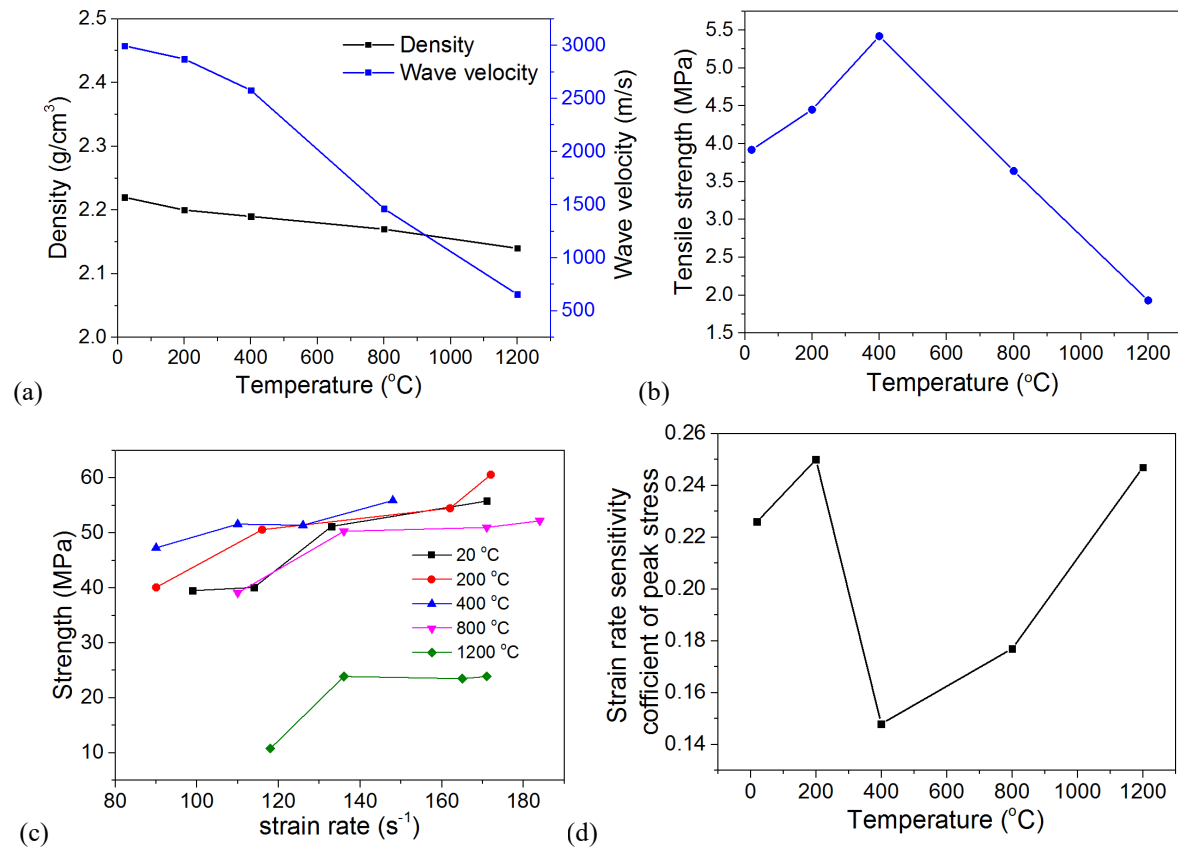
$$\tau_{\sigma} = \frac{\sigma_{max} - \sigma_{min}}{\dot{\epsilon}_{max} - \dot{\epsilon}_{min}} \quad (5.1)$$

where  $\sigma_{max}$ ,  $\sigma_{min}$  are the compressive strength at the highest ( $\dot{\epsilon}_{max}$ ) and lowest ( $\dot{\epsilon}_{min}$ ) strain rates, respectively. According to Fig. 5.14(d), at room temperature, the strain rate sensitivity coefficient of dynamic compressive strength is 0.23. With the increase of temperature, it changes in volatility. From 200 °C to 1200 °C, the strain rate sensitivity coefficients are 0.25, 0.15, 0.18 and 0.25, respectively. 200 °C and 1200 °C have the highest strain rate sensitivity coefficient over room temperature, indicating that under these conditions the strain rate effect on dynamic compressive strength is the most significant; 400 °C group which has the highest strength, however, has the weakest strain rate effect.

**Table 5.6** Compression and tensile strength corresponding to different strain rates and temperatures

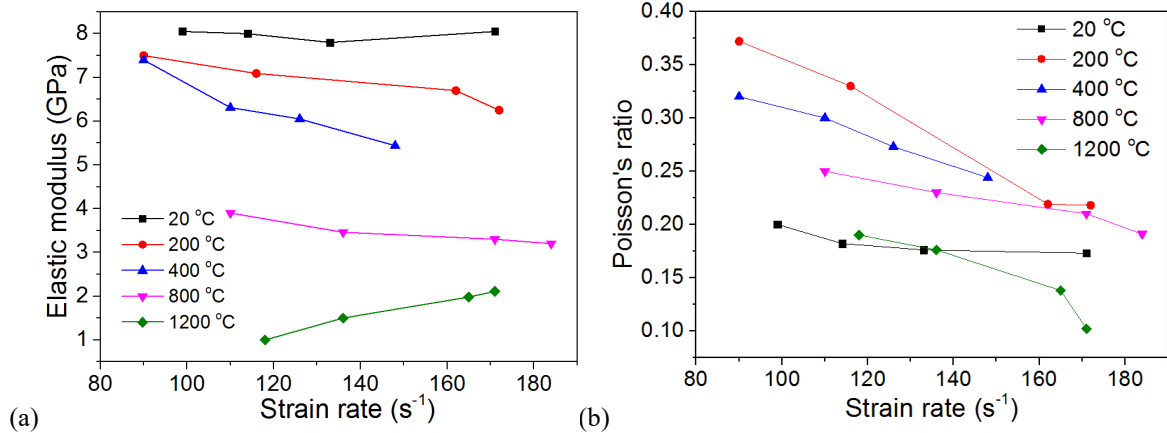
Impact pressure	Temperature treated (°C)	Density (g/cm <sup>3</sup> )	P-wave velocity(m/s)	Strain rate	Dynamic UCS(MPa)	Dynamic BD (MPa)
0.25 MPa	20	2.21	2972	99	39.5	3.92
	200	2.22	2840	90	40.1	4.45
	400	2.18	2380	90	47.3	5.42
	800	2.18	1462	110	39.1	3.64
	1200	2.13	660	118	10.8	1.93
0.30 MPa	20	2.21	2973	114	40.1	

	200	2.18	2875	116	50.6
	400	2.20	2587	110	51.6
	800	2.18	1453	136	50.3
	1200	2.15	653	136	23.9
	20	2.22	3069	133	51.2
0.35 MPa	200	2.19	2875	162	54.5
	400	2.20	2609	126	51.4
	800	2.16	1460	171	51.0
	1200	2.13	650	165	23.5
	20	2.24	2972	171	55.8
0.42 MPa	200	2.20	2899	172	60.6
	400	2.19	2738	148	55.9
	800	2.16	1478	184	52.2
	1200	2.13	660	171	23.9



**Fig. 5.14**(a) variation in density and wave velocity of rocks with treatment temperature; (b) variation in dynamic tensile strength with treatment temperature; (c) dynamic compressive strength versus strain rate at different temperatures; (d) strain rate sensitivity coefficient of dynamic compressive strength at different temperatures.

The dynamic elastic modulus was determined by the ratio of the increment of stress to axial strain ( $\Delta\sigma / \Delta\epsilon_x$ ) during the quasi-linear stage of the stress-strain curve. The dynamic Poisson's ratio is determined by the sign ratio of lateral strain to axial strain ( $-\epsilon_y / \epsilon_x$ ) during the quasi-linear stage of the stress-strain curve. The stress is obtained by the strain gauge signals, while the strain is determined from the axial and lateral strain fields averaged by pixels based on DIC results. Fig. 5.15(a) shows that at a similar strain rate, along with the increase of the temperature the Young's modulus decreases significantly. When the temperature is fixed, the strain-rate effect on modulus is not obvious for room temperature group but a slight decrease trend for 200 °C, 400 °C and 800 °C and increase trend for 1200 °C. Fig. 5.15(b) illustrates the dynamic Poisson's ratio variation with the strain rate at different temperatures. It can be noted that the larger the strain rate is the lower dynamic Poisson's ratio will be for each temperature. However, Poisson's ratios in 200 °C, 400 °C and 800 °C are larger than that of room temperature, which means a larger lateral expansion is allowed to generate at higher temperature. Instead, the 1200 °C treatment reduced Poisson's ratio compared with the room temperature one, to some extent, it transforms the rock into a more brittle state.



**Fig. 5.15(a)** Elastic modulus versus strain rate at different temperatures, **(b)** Poisson's ratio versus strain rate at different temperatures

In the dynamic loading conditions, stress thresholds for rock fracture can be divided into, (1) crack closure, (2) crack initiation, (3) unstable crack growth, and (4) post-peak behaviour (Xing, Zhang et al. 2018). Crack closure occurs during the initial stages of loading prior to the time when crack strain back to zero. Crack initiation (stable crack) stress threshold  $\sigma_{ci}$  corresponds to crack strain starting to increase from zero. The symbol of unstable crack



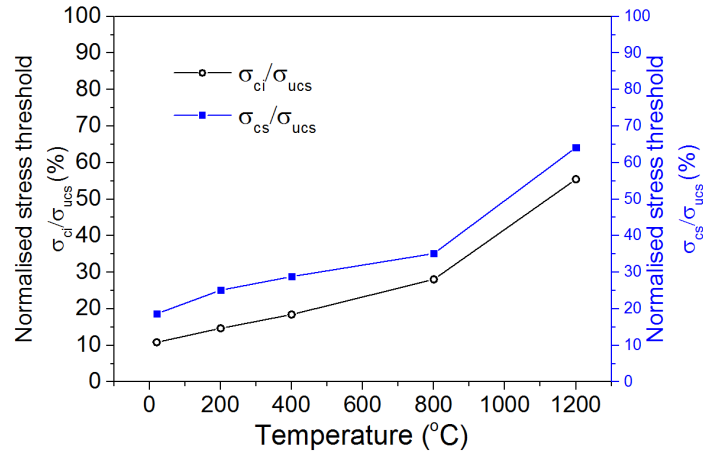
growth stress threshold  $\sigma_{cd}$  is the point the volumetric strain reaches its maximum value. The volumetric strain  $\varepsilon_V$ , elastic volumetric strain  $\varepsilon_{VE}$  and crack strain  $\varepsilon_c$  are determined as following,

$$\varepsilon_V = e_{xx} + 2e_{yy}, \varepsilon_{VE} = \frac{1-2\nu}{E} \sigma_{dyn}, \varepsilon_c = \varepsilon_V - \varepsilon_{VE} \quad (5.2)$$

According to the above equations, the stable and unstable crack stress thresholds for different temperatures with similar strain rates are listed in Table 5.7. The normalized stress threshold versus different temperatures are illustrated in Fig. 5.16. Because the strain rate has less effect on the normalized stress threshold (Xing, Zhang et al. 2018), the difference of strain rates can be ignored in temperature effect analysis. Fig. 5.16 shows that normalized stress threshold increases both for stable crack and unstable crack with the increase of temperature. When the loading rate is same, a larger normalized stress threshold means later crack initiation or losing instability. In terms of the gap between stable and unstable stress thresholds, 200 °C and 400 °C has the largest ones which means they has a longer quasi-linear stress-strain curve before losing the stability.

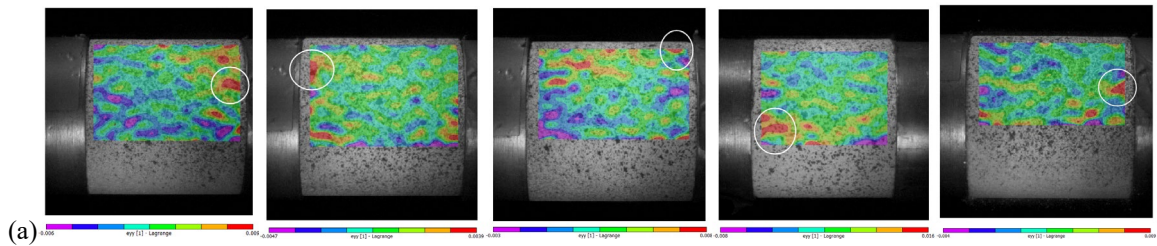
**Table 5.7** Normalized stable and unstable crack stress thresholds corresponding to different temperatures

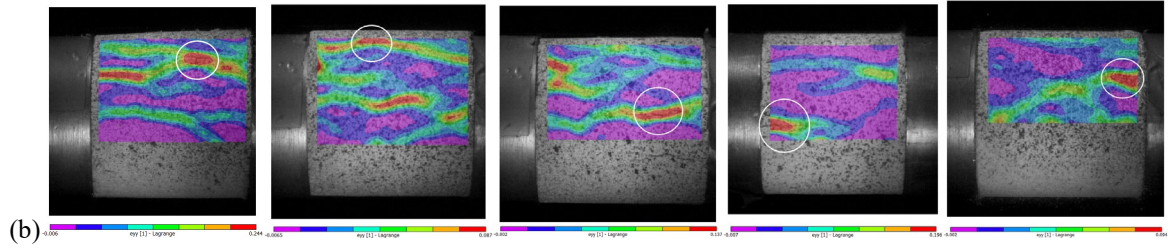
Temperature (°C)	Strain rate (s <sup>-1</sup> )	$\sigma_{ci}$ (MPa)	$\sigma_{cd}$ (MPa)	$\sigma_{ucs}$ (MPa)	$\sigma_{ci} / \sigma_{ucs}$	$\sigma_{cd} / \sigma_{ucs}$
20	171	6.05	10.40	55.8	10.9%	18.6%
200	172	8.89	15.21	60.6	14.7%	25.1%
400	148	10.30	16.12	55.9	18.4%	28.8%
800	171	14.30	17.92	51.0	28.0%	35.1%
1200	171	13.25	15.32	23.9	55.4%	64.1%



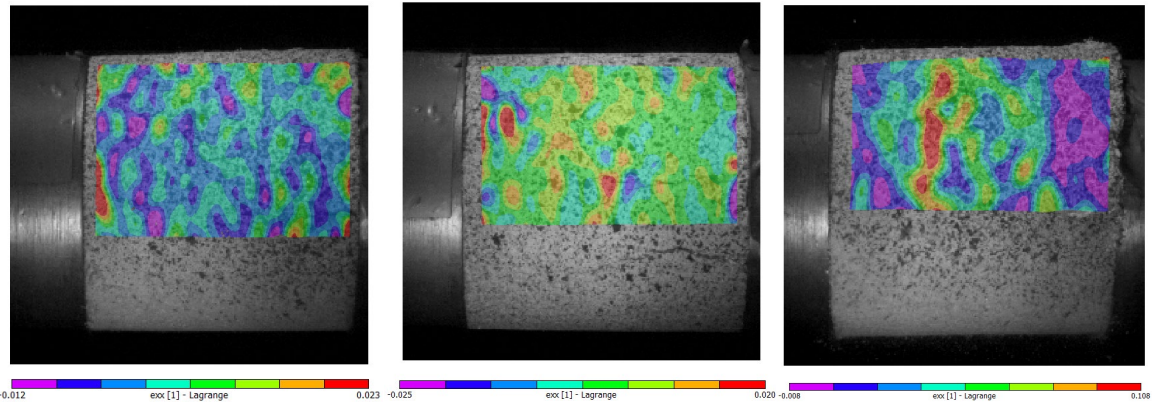
**Fig. 5.16** Variation in normalized stable ( $\sigma_{ci}$ ) and unstable stress ( $\sigma_{cs}$ ) of rocks with treatment temperatures

The strain field especially strain localization provides a direct understanding of the deformation and fracturing patterns of rock before visible crack formation. Fig. 5.17(a) shows the strain localization initiation by high-speed 3D-DIC under different temperatures with similar strain rates. The localizations all initiated from the edge of the specimen and the strain localization was around 0.01 for each temperature treatment. The vertical strain fields after peak stress of different temperature treatments are shown in Fig. 5.17(b), in which 20 °C, 200 °C and 400 °C treatments have more strain localizations and branching than 800 °C and 1200 °C conditions. The peak strain localizations highlighted by the circles are in the middle of the specimen in 20 °C, 200 °C and 400 °C treatments, however, the peak localizations in 800 °C and 1200 °C are at the edge of the specimen. The results indicate that the crack propagation is attenuated due to the high temperature. The post-peak horizontal strain fields ( $\epsilon_{xx}$ ) of 20 °C, 400 °C and 1200 °C are shown in Fig. 5.18.



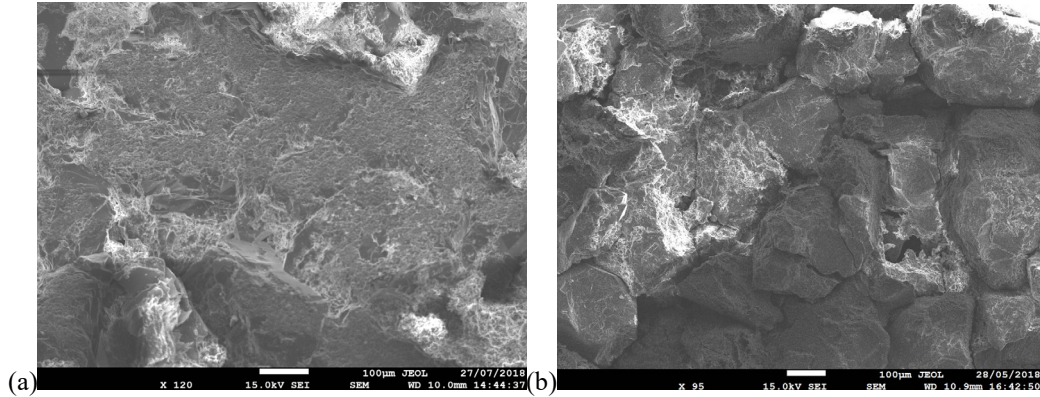


**Fig. 5.17(a)** Vertical strain fields ( $e_{yy}$ ) of the initiation of strain localisation at different temperature treatments, left to right temperature: 20 °C to 1200 °C, strain rate: 114, 116, 110, 110 and 118 s<sup>-1</sup> **(b)** Vertical strain fields ( $e_{yy}$ ) of fractured rock at post-peak stages with different temperature treatments, left to right temperature: 20 °C to 1200 °C, strain rate: 114, 116, 110, 110 and 118 s<sup>-1</sup>



**Fig. 5.18** Horizontal strain fields ( $e_{xx}$ ) of fractured rock with different temperature treatments, left to right temperature: 20 °C, 400 °C and 1200 °C, strain rate: 114, 110 and 118 s<sup>-1</sup>

The horizontal strain localization is contributed by the reflection of the compressive wave on the edge, which may cause violent fragmentations after the impact. The horizontal strain localization appeared at 1200 °C but hardly be seen in the cases of 20 °C and 400 °C. The mechanical and fracturing features in different temperature-treated specimens are attributed to the micro-structure alternation. Fig. 5.19 shows the grain topography in 400 °C and 1200°C treated specimen, where the thermal expansion of grains can be seen from 400 °C specimen leading to an increase in the mechanical properties such as strength of the rock. While the grain damage by the extreme high temperature can be observed from Fig. 5.19(b) causing the decrease in the mechanical properties.

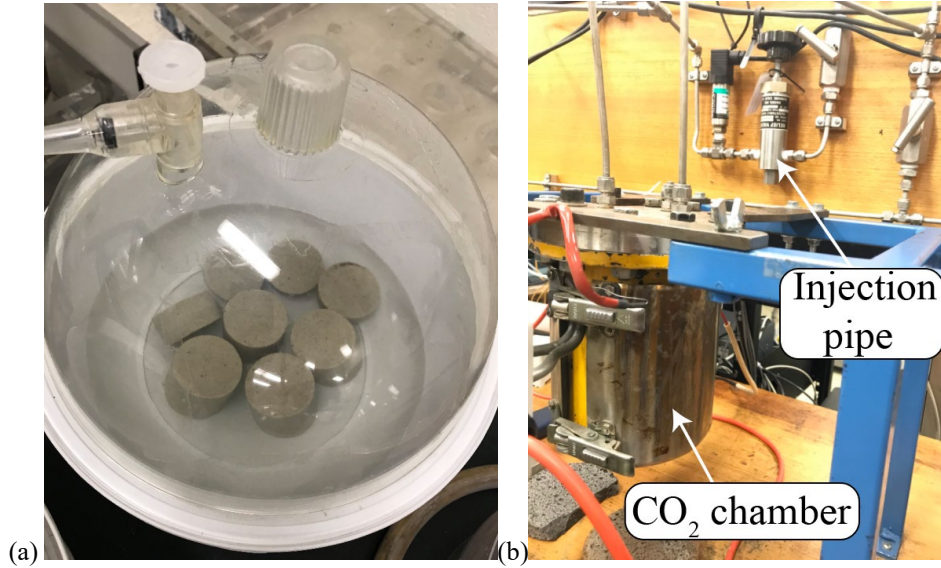


**Fig. 5.19** SEM images of the grain in (a) 400°C and (b) 1200 °C treated sandstone specimen

## 5.6 CARBON DIOXIDE EFFECT

### 5.6.1 Experimental set-up

The specimens are Hawkesbury sandstone tested by dynamic compression and BD methods. Before saturation, the specimens were dried in the oven, at 80 °C for 24 hours with the heating rate of 2°C /min. The dried specimens were categorised into seven sets: dry specimens with and without scCO<sub>2</sub> injection, water saturation (5% water content) with and without scCO<sub>2</sub> injection, brine saturation (6% NaCl) with and without scCO<sub>2</sub> injection and high NaCl concentration brine (20% NaCl) saturation set. To achieve the full saturation of water or brine without CO<sub>2</sub>, the specimens were soaked in the desiccators under vacuum for one month, as shown in Fig. 5.20(a). In terms of the sets with CO<sub>2</sub> injection, the saturation was performed in the high-pressure chamber, as shown in Fig. 5.20(b). The specimens were firstly fully-saturated with water or brine in the vacuumed desiccators (except dry specimen with CO<sub>2</sub>), after which the specimens were put into the chamber filled with the corresponding water or brine at 50 °C, and the CO<sub>2</sub> was injected at 8 MPa for four months. A summary of the treatment condition and specimen number is listed in Table 5.8.



**Fig. 5.20(a)** Desiccators for water saturation **(b)** Chamber for high-pressure CO<sub>2</sub> injection

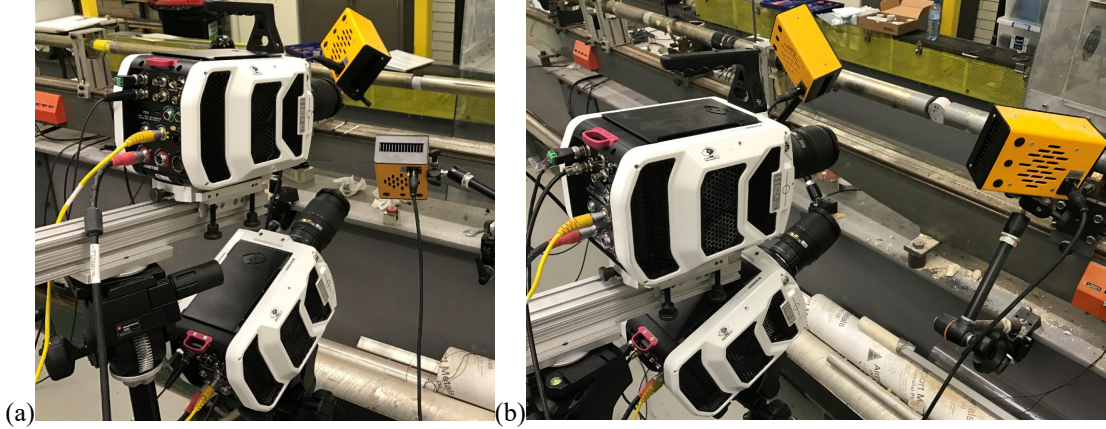
To avoid the loss of saturation, apart from dry and dry + CO<sub>2</sub> specimens, the saturated specimens were kept in the water or brine desiccators before being sandwiched between the loading bars.

**Table 5.8** Summary of treatment conditions and specimen number

Treatment	Saturation conditions (Temperature, injection pressure)	Wave velocity (m/s)	Sample number
Dry	20°C	3020 ± 146	4 UCS +3 BD
Water	20°C, vacuum	3645 ± 76	4 UCS +3 BD
Dry +CO <sub>2</sub>	50°C, 8 MPa	2860 ± 48	4 UCS +3 BD
Water + CO <sub>2</sub>	50°C, 8 MPa	3580 ± 102	3 UCS +3 BD
6% NaCl	20°C, vacuum	3660 ± 67	3 UCS +3 BD
6% NaCl + CO <sub>2</sub>	50°C, 8 MPa	3600 ± 55	3 UCS +3 BD
20% NaCl	20°C, vacuum	3655 ± 45	3 UCS +3 BD

In this study, the dynamic loading is applied by the SHPB introduced in Chapter.3. The experimental setup is shown in Fig. 5.21.





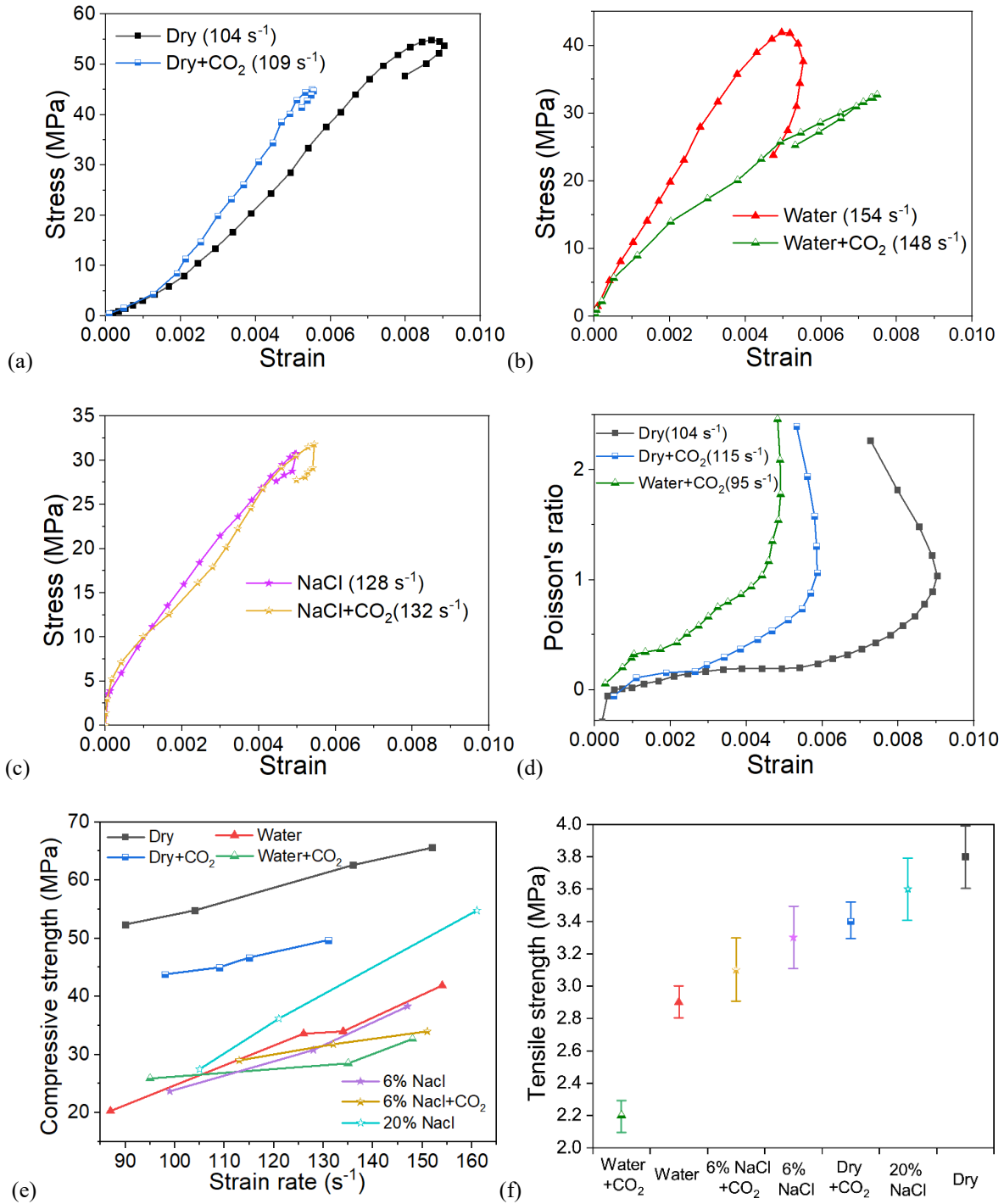
**Fig. 5.21** Photograph of the setup for (a) dynamic compression and (b) dynamic tension test

In this study, two high-speed CMOS cameras (Phantom V2511) were operated with an image resolution of  $256 \times 256$  pixels, frame speed of 200,000 fps and exposure time of  $4 \mu\text{s}$ . The field of view of DIC is  $128 \times 188$  pixels corresponding to an area of interest of  $31.3 \times 45.1 \text{ mm}^2$ , as a result, each pixel length represents 0.24 mm. The accuracy threshold is controlled as 5% of the pixel length which is 0.012 mm, corresponds to 0.0024% (24 micro-strain) in engineering strain. The configurations of DIC are as follows: subset:  $17 \times 17$  pixels, step size: 1 pixel, subset weights: Gaussian weights, interpolation: optimised 8-tap, correlation criterion: zero-normalised squared differences (ZNSD).

### 5.6.2 Results

In this section, Young's modulus, Poisson's ratio, compressive and tensile strength were studied. According to the previous study on the dynamic compression of rock, there is no pure elastic stage for rock under high strain rates. The dynamic Young's modulus was obtained in the quasi-linear part of the stress-strain curve in the stable crack development stage (between  $\sigma_{ci}$  and  $\sigma_{cd}$ ). The dynamic Poisson's ratio was determined from the relatively stable part of the sign ratio of lateral strain to axial strain ( $-\epsilon_y/\epsilon_x$ ). The stress above is obtained by the strain gauge signals. While the strain in the above equations is calculated from the axial and lateral strain fields averaged by pixels based on DIC results. The axial and lateral strain of the specimen were determined by axial ( $e_{xx}$ ) and lateral ( $e_{yy}$ ) strain fields averaged by pixels based on DIC results. Six typical stress-strain curves of dry, water and brine saturation with and without  $\text{CO}_2$  at close strain rates are illustrated in Fig. 5.22 (a) ~ (c). The compressive and tensile strength in the sandstone with or without  $\text{CO}_2$  at different strain rates

are shown in Fig. 5.22(e) and Fig. 5.22(f), respectively. A summary of all dynamic mechanical properties results is listed in Table 5.9.



**Fig. 5.22** Typical stress-strain curves of (a) dry vs dry +CO<sub>2</sub>, (b) water vs water +CO<sub>2</sub>, (c) NaCl vs NaCl +CO<sub>2</sub>, (d) Poisson's ratio evolution in dry, dry+CO<sub>2</sub> and water + CO<sub>2</sub>, (e) Compressive strength variation against strain rate in all treatments, (f) Tensile strength in all treatments at loading rate of 100 ± 3 GPa/s

In terms of the dynamic Young's modulus, according to Fig. 5.22(a) ~ (c) and Table 5.9, the presence of CO<sub>2</sub> in the Dry sandstone increases the modulus. An increase of modulus is observed up to 19% between D3 and DC4 at a strain rate around 135 s<sup>-1</sup>. However, CO<sub>2</sub> has a decreasing effect on Young's modulus of sandstone saturated with water. The attenuation of Young's modulus is significant that there is a 30% reduction in modulus in WC2 compared with W2 at strain rate around 123 s<sup>-1</sup>. When the environment is saline, CO<sub>2</sub> has a negligible effect on the dynamic Young's modulus. But the results of 6% and 20% NaCl brine shows that the increase of the saline concentration could enhance Young's modulus under the high strain rate loading. For dry specimens, when the strain rate is increased, the dynamic modulus showed no obvious rate dependency. However, when the specimen is treated with water, brine or CO<sub>2</sub>, Young's modulus becomes dependent on the strain rate where the higher strain rates lead to a larger Young's modulus. The rate sensitivities were calculated according to the ratio of the difference (between the maximum and minimum value) of modulus to the difference of strain rates, which were 20.8 and 61.0 MPa/s<sup>-1</sup> for the water with and without CO<sub>2</sub>, respectively; 15.8 and 37.5 MPa/s<sup>-1</sup> for the 6% NaCl brine with and without CO<sub>2</sub>, respectively. Therefore, the existence of CO<sub>2</sub> in water and brine reduces the strain rate enhancement effect on Young's modulus.

**Table 5.9** Mechanical properties of different treated samples under different strain rates

Type	ID	Compressive strain rate (s <sup>-1</sup> )	Compressive strength (MPa)	Poisson's ratio	DIF	Young's modulus (GPa)
<b>Dry</b>	D0	10 <sup>-4</sup>	48.0	0.21	N/A	8.4
	D1	90	52.4	0.20	1.09	9.0
	D2	104	54.8	0.19	1.14	8.4
	D3	136	62.6	0.19	1.30	9.0
	D4	152	65.6	0.18	1.37	9.4
<b>Dry + CO<sub>2</sub></b>	DC0	10 <sup>-4</sup>	42	0.31	N/A	8.2
	DC1	98	43.8	0.20	1.04	9.0
	DC2	109	45.0	0.16	1.07	8.9
	DC3	115	46.7	0.15	1.11	10.3
	DC4	131	49.7	0.15	1.18	10.7
<b>Water</b>	W0	10 <sup>-4</sup>	18.3	0.28	N/A	4.4
	W1	87	20.3	0.24	1.11	4.9



	W2	126	33.6	0.22	1.84	7.2
	W3	134	34	0.22	1.86	8.5
	W4	154	41.9	0.21	2.29	9.0
	WC0	10 <sup>-4</sup>	16.4	0.32	N/A	3.5
<b>Water</b>	WC1	95	25.9	0.36	1.58	4.1
<b>+ CO<sub>2</sub></b>	WC2	135	28.5	0.21	1.74	4.9
	WC3	148	32.7	0.20	1.99	5.2
	N0	10 <sup>-4</sup>	19.7	0.32	N/A	4.0
<b>6%</b>	N1	99	23.7	0.27	1.20	4.3
<b>NaCl</b>	N2	128	30.8	0.23	1.56	4.9
	N3	147	38.3	0.21	1.94	6.1
	NC0	10 <sup>-4</sup>	18.8	0.37	N/A	3.6
<b>6%</b>	NC1	113	29.0	0.32	1.54	3.7
<b>NaCl</b>	NC2	132	31.8	0.23	1.69	4.2
<b>+ CO<sub>2</sub></b>	NC3	151	34.0	0.22	1.80	4.3
	NN0	10 <sup>-4</sup>	21.8	0.31	N/A	4.3
<b>20%</b>	NN1	105	27.5	0.30	1.26	4.5
<b>NaCl</b>	NN2	121	36.2	0.25	1.66	6.5
	NN3	161	54.8	0.24	2.51	6.7

\* DIF: dynamic increase factor (dynamic strength / static strength)

Three typical evolution of Poisson's ratio and results of each treatment are shown in Fig. 5.22(d) and Table 5.9, respectively. Poisson's ratio starts from negative for D2 and DC2 which is due to the rotation of grains during crack closure causing the decrease in both axial and lateral directions. WC1 does not exhibit this since the pore is filled with water whose pressure would restrain the crack closure. When it comes to a relatively stable stage, the water-saturated sandstone with CO<sub>2</sub> has a larger Poisson's ratio than that without CO<sub>2</sub>. The gap between two Poisson's ratios gets small when the strain rates increase. The introduction of CO<sub>2</sub> to dry sandstone, however, reduces Poisson's ratio of untreated dry specimen up to 21% (D3 and DC4 at around 135 s<sup>-1</sup>), which displays a more brittle behaviour. Poisson's ratio of 6% NaCl brine with and without CO<sub>2</sub> are quite close which is not affected by the CO<sub>2</sub> saturation. All types of treatments show a strain rate effect on Poisson's ratio where the ratio decreases as the increase of the strain rate. It indicates that a smaller loading rate allows a more sufficient lateral deformation.

According to Table 5.9 and Fig. 5.22(e), the CO<sub>2</sub> weakens the dynamic compressive strength of sandstone in both dry and water-saturated condition. A 14% reduction is found between D1 and DC1 at a strain rate around 94 s<sup>-1</sup> and 22% reduction for W4 and WC3 at a strain rate around 151 s<sup>-1</sup>. The strength of sandstone saturated in brine is not affected by the presence of CO<sub>2</sub>, but the increase of concentration from 6% to 20% enhances the dynamic compressive strength. For example, an 18% increase at the strain rate around 124 s<sup>-1</sup>. As can be seen from the stress-strain curves, the strain at peak strength is affected differently by CO<sub>2</sub> in sandstone of dry and water environment. The CO<sub>2</sub> extended the peak strain of water saturated sandstone but has an opposite trend for the dry CO<sub>2</sub>. A ductile behaviour is promoted by CO<sub>2</sub> for water saturated sandstone, whereas a more brittle pattern developed on dry sandstone by CO<sub>2</sub>. The CO<sub>2</sub> does not show an effect on the deformability for the sandstone saturated in brine. The strain rate enhancing the effect on the compressive strength still existed after all types of treatments. The dynamic increase factor (DIF) in Table 5.9 indicates the strain rate sensitivity of compressive strength. By comparing the dry, water and brine saturated sandstone with and without CO<sub>2</sub>, it is found that the presence of CO<sub>2</sub> will decrease the DIF for dry and water saturated sandstone, in another word, reducing the strain rate enhancing effect on the compressive strength. Brine-saturated sandstone has less influence on DIF by CO<sub>2</sub> but the increase of the salinity promotes the DIF.

The tensile strengths are shown in Table 5.10 and illustrated in Fig. 5.22 (f) at the loading rate of 100 ± 3 GPa/s. Water and brine saturation cause the reduction in dynamic tensile strength, and the presence CO<sub>2</sub> further attenuates the strength in dry and water saturated sandstone but not obvious in the sandstone in brine condition. CO<sub>2</sub> creates 11% and 24% reduction in the dynamic tensile strength of dry and water-saturated sandstone, respectively. The high concentration of salinity slightly recovers the tensile strength.

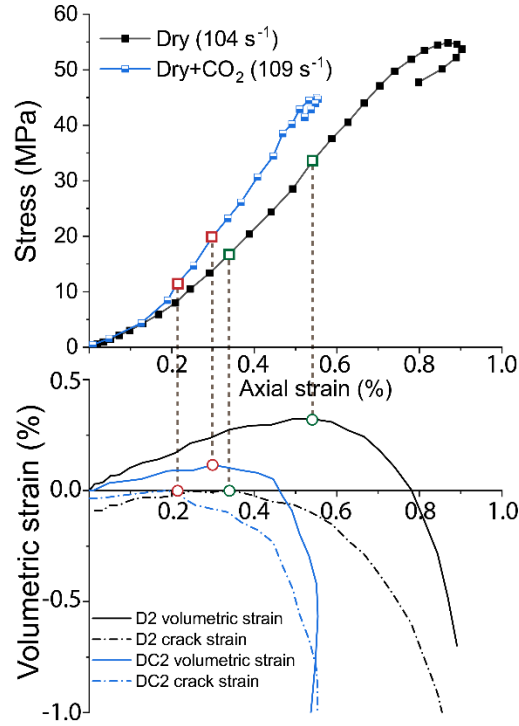
**Table 5.10** Tensile strength of different treated samples

Type	ID	Loading rate (GPa/s)	Average (GPa/s)	Tensile strength (MPa)	Average (MPa)
<b>Dry</b>	TD1	103		4.0	
	TD2	101	$100 \pm 3$	3.7	$3.8 \pm 0.2$
	TD3	97		3.6	
<b>Dry + CO<sub>2</sub></b>	TDC1	103		3.5	
	TDC2	101	$101 \pm 2$	3.4	$3.4 \pm 0.1$
	TDC3	99		3.4	
<b>Water</b>	TW1	98		2.9	
	TW2	99	$99 \pm 2$	2.9	$2.9 \pm 0.1$
	TW3	101		3.0	
<b>Water + CO<sub>2</sub></b>	TWC1	100		2.3	
	TWC2	100	$99 \pm 2$	2.1	$2.2 \pm 0.1$
	TWC3	97		2.2	
<b>6% NaCl</b>	TN1	98		3.1	
	TN2	100	$99 \pm 1$	3.5	$3.3 \pm 0.2$
	TN3	99		3.1	
<b>6% NaCl + CO<sub>2</sub></b>	TNC1	100		2.9	
	TNC2	103	$102 \pm 2$	3.3	$3.1 \pm 0.2$
	TNC3	102		3.2	
<b>20% NaCl</b>	TNN1	99		3.5	
	TNN2	100	$100 \pm 2$	3.6	$3.6 \pm 0.2$
	TNN3	103		3.8	

According to the theory, the crack closure threshold ( $\sigma_{cc}$ ) is where the crack strain is decreased to zero. At Young's stage, the crack strain keeps zero. The crack initiation stress ( $\sigma_{ci}$ ) represents the stress level necessary for micro-fracturing to begin. This is marked as the point, where the crack strain begins to increase again. As the loading continues, unstable crack growth emerges whose stress level ( $\sigma_{cd}$ ) is at the point of reversal in the volumetric strain curve and is also known as dilation point.

In dynamic loading conditions, stress thresholds for rock fracture is divided into, (i) crack closure, (ii) crack initiation, (iii) unstable crack growth, and (iv) post-peak behaviour. The

axial and lateral strains of the specimen were then extracted in axial and lateral strain fields using the 3D-DIC. A typical identification of stress thresholds of D2 and DC2 from axial and volumetric evolution is illustrated in Fig. 5.23 and all results are listed in Table 5.11.



**Fig. 5.23** Crack and volumetric strain evolutions and identification of the stress thresholds in D2 and DC2

According to Table 5.11, the stress thresholds for both crack initiation and propagation in each treatment condition follow the same pattern with the compressive strength. This means the treated rock with weaker strength would have a smaller stress threshold for crack initiation and propagation. The patterns are different when stress threshold is normalised to the compressive strength ( $\sigma_{ucs}$ ) in which a smaller value means an earlier initiation or propagation of crack. In terms of the normalised crack initiation stress threshold ( $\sigma_{ci}/\sigma_{ucs}$ ),  $\text{CO}_2$  slightly reduces the threshold when it is saturated in dry specimen. However,  $\text{CO}_2$  brings the crack initiation threshold forward greatly for sandstone saturated in water. For example, at the strain rate of  $135 \text{ s}^{-1}$ , the threshold in W3 is 31.7% of peak strength, but WC2 is 14.9%, which means the crack initiates almost simultaneously as the loading. The threshold of brine saturated sandstone is not sensitive to the existence of  $\text{CO}_2$  but sensitive to the salinity. A higher salinity brings forward the crack initiation threshold. However, the change of salinity does not affect the normalised unstable crack propagation stress threshold ( $\sigma_{cd}/\sigma_{ucs}$ ), whereas

the presence of CO<sub>2</sub> reduces this threshold for dry, water and brine-saturated sandstone. This reduction is significant when CO<sub>2</sub> being injected into the sandstone saturated by water, in which the unstable normalised stress threshold is below 50% of peak strength. It should be noted that the strain rate has no influences on the normalised stress threshold for crack initiation and unstable development.

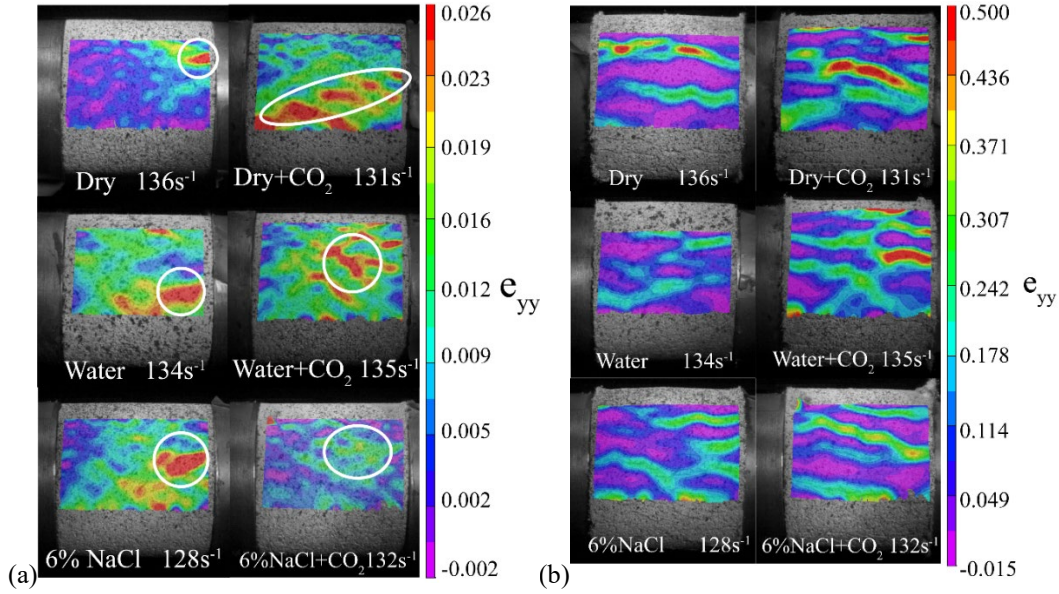
**Table 5.11** Normalised stable and unstable crack stress thresholds corresponding to different treatments

Type	ID	Strain rate (s <sup>-1</sup> )	$\sigma_{ci}$ (MPa)	$\sigma_{cd}$ (MPa)	$\sigma_{ci}/\sigma_{ucs}$ (%)	$\sigma_{cd}/\sigma_{ucs}$ (%)
<b>Dry</b>	D1	90	12.1	34.7	23.0	66.2
	D2	104	16.5	33.4	30.1	61.0
	D3	136	14.7	35.7	23.5	57.1
	D4	152	21.2	39.5	32.4	60.2
<b>Dry + CO<sub>2</sub></b>	DC1	98	9.6	23.5	21.8	53.6
	DC2	109	12.0	24.4	25.3	51.7
	DC3	115	13.4	30.2	27.2	61.5
	DC4	131	10.8	28.7	20.2	53.7
<b>Water</b>	W1	87	7.2	10.6	35.6	52.3
	W2	126	9.4	17.9	27.9	53.2
	W3	134	10.8	18.9	31.7	55.6
	W4	154	14.3	22.0	34.1	52.5
<b>Water + CO<sub>2</sub></b>	WC1	95	3.8	12.3	14.7	47.4
	WC2	135	4.2	11.5	14.9	40.3
	WC3	148	5.7	8.9	17.3	27.1
<b>6% NaCl</b>	N1	99	8.5	11.5	36.0	48.7
	N2	128	11.1	16.3	36.2	52.9
	N3	147	10.4	15.3	27.1	40.0
<b>6% NaCl + CO<sub>2</sub></b>	NC1	113	10.5	12.2	36.2	42.1
	NC2	132	10.0	12.6	31.4	39.6
	NC3	151	15.0	18.3	29.3	36.2
<b>20% NaCl</b>	NN1	105	7.1	14.9	26.0	54.1
	NN2	121	7.4	19.9	20.4	54.9
	NN3	161	11.7	22.5	21.3	41.0

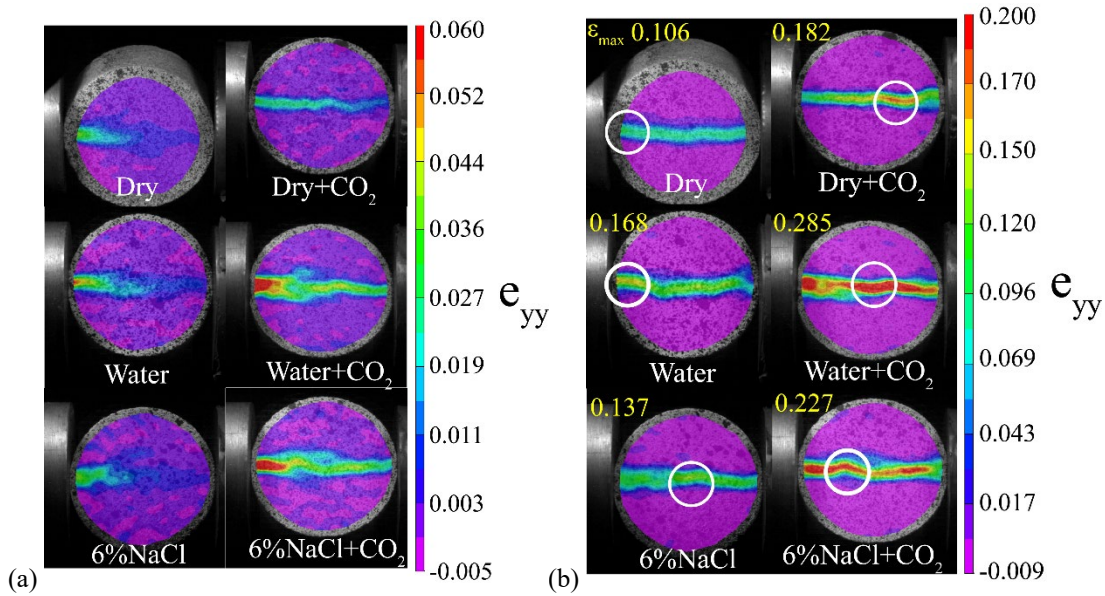
The strain field captured from 3D-DIC provides means for direct understanding of rock deformation and fracturing patterns before any visible cracks are formed. Fig. 5.24(a) shows

the initiation of strain localisation in vertical strain fields for different treated specimens. According to Fig. 5.24(a), the strain localisations all initiate from the edges for non-CO<sub>2</sub> saturated specimens since the tensile stress concentration reached its maximum at the edge. However, the strain localisations in specimens saturated with CO<sub>2</sub> shift to the middle part of the specimen. The fracturing patterns in the post failure stage (250  $\mu$ s after loading) of each treated specimen were shown in Fig. 5.24(b). The results indicate the water saturated specimen with the smallest degree of strain localisation has the least number of fractures. 6% NaCl brine saturated specimen has a fracturing pattern with more branches, but less degree of strain localisation compared with the dry type. Strain fields of the CO<sub>2</sub> treated specimen in dry, water and brine environment are shown on the right of Fig. 5.24(b). It is clear that the introduction of CO<sub>2</sub> dramatically intensifies the dynamic fracturing process of the sandstone.

The fluid effect on the single fracturing process was investigated through BD tests as shown in Fig. 5.25. Fig. 5.25(a) compares the strain localisation at 50  $\mu$ s for each treated sample. The strain localisation starts at the impact edge of the samples. CO<sub>2</sub>-riched specimens showed an apparent stronger degree of tensile strain localisation and faster propagation speed than the samples without CO<sub>2</sub> injection. The accumulation of the strain localisation leads to visible cracks which are shown in Fig. 5.25(b). White circles in this figure indicate the maximum strain localisation along the fracture. It is clear that the CO<sub>2</sub> deteriorates the sample by altering the crack initiation position and the fracturing process in dry, water and brine conditions.



**Fig. 5.24** Vertical strain fields ( $e_{yy}$ ) of the (a) initiation of strain localisation at 60  $\mu$ s since wave propagating into the specimen (circles indicate where strain localisations initiate) (b) the post-failure at 250  $\mu$ s since wave propagating into the specimen corresponding to different treatments



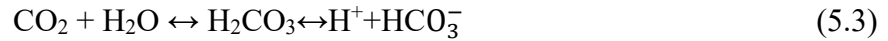
**Fig. 5.25** Vertical strain fields ( $e_{yy}$ ) of BD test (a) at 50  $\mu$ s and (b) the maximum strain of BD test on each sample at 100  $\mu$ s. (circles indicate the maximum strain localisation)

### 5.6.3 Discussion

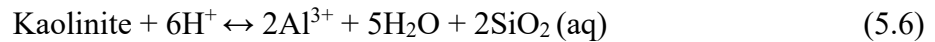
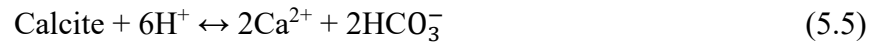
The effect of CO<sub>2</sub> saturation in dry/water/brine saturated sandstone on the fracture and mechanical characteristics at extreme loading conditions mainly comes from two aspects which are chemical or physical alternation in microstructure of sandstone and the free water effect.

**(1) Chemical and physical alternation**

In general, the chemical or physical alternation changes the distribution and composition of the minerals where the former factor affects more in terms of strength and fracture the latter one alters the deformation behaviour. (Kaszuba, Janecky et al. 2003) systematically explained the reactions between CO<sub>2</sub> and host fluid, where the most fundamental reaction between the CO<sub>2</sub> and water phase produces carbonic acid with the release of H<sup>+</sup> ions developing an acidic medium, as described in Eq. 5.3.



Once the free H<sup>+</sup> ions exist, some minerals may dissolve during the exposure, affecting the mineral composition and microstructure distribution. Main reactions for mineral dissolution in the majority of the minerals (90%~95%) are given in Eq. 5.4 to 5.6

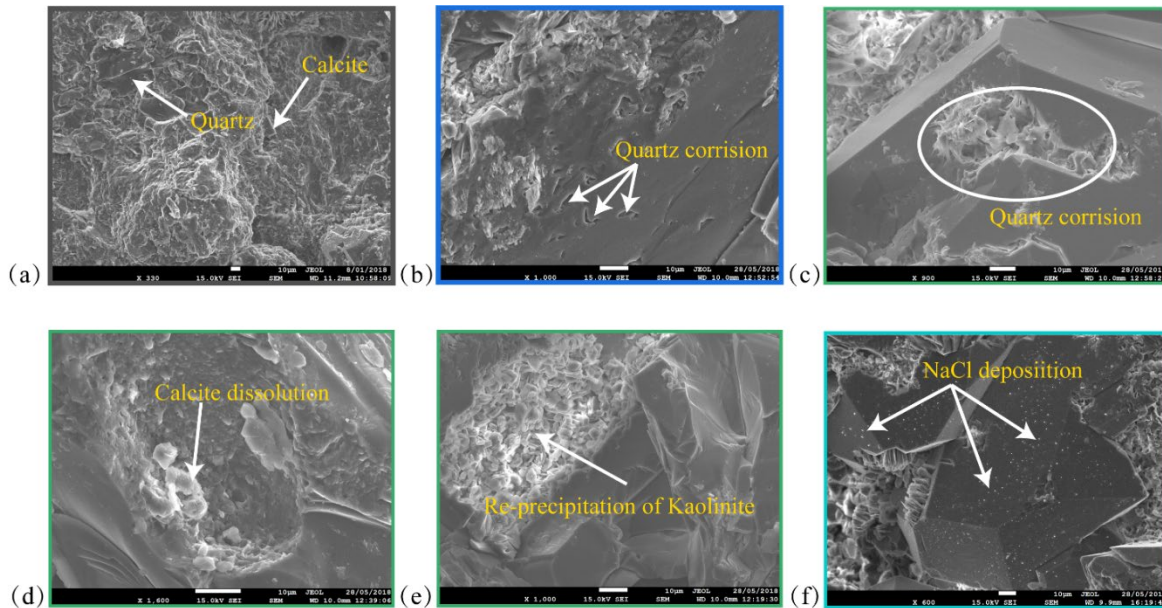


Those reactions can go both sides of the equilibrium at any time depending on the condition of the environment, where the final status is a dynamic balance of multiple ions at a certain concentration. During the dynamic balancing period, the mineral that was initially dissolved can be re-precipitated as the pH value changes.

The microstructure changes in sandstone were studied using a JEOL 7001 FEGSEM SEM at 15 kV. The specimens before and after the treatments were manufactured into 1 mm slices to reduce the charging effect. The slices were coated with a thin layer of Iridium around 2 nm to conduct electrons. The micrograph of untreated sandstone is shown in Fig. 5.26(a) confirming that the specimen mainly consists of quartz, with a minority of calcite and kaolinite cementation. The boundary of the quartz grain can be seen clearly. The quartz grains are intact without crack and uniformly surrounded by the small amount of clay mineral. Fig. 5.26(b) shows the quartz corrosion in the set of dry specimens saturated with CO<sub>2</sub>. Clusters of small corrosion spots of 5 μm in length can be seen on the surface of the quartz grain. Greater quartz corrosion was observed in the set of water saturation with CO<sub>2</sub> as shown in



Fig. 5.26(c). The corrosion size was approximately  $70\ \mu\text{m} \times 30\ \mu\text{m}$  in dimension, filled with the re-precipitation of the clay mineral. The presence of either water or brine triggers and accelerates the mineral corrosion reactions. At the same time the dissolution of calcite (Fig. 5.26(d)) and the cementation of the Kaolinite notably appeared among the quartz mineral grains as shown in Fig. 5.26(e). Fig. 5.26(f) shows a considerable amount of NaCl crystals deposited in the rock pores after the sandstone was saturated in a 20% brine. The reactions also destroyed the original clay matrix that was uniformly surrounded the grain, and as a result, the newly re-precipitated clay mineral was scattered next to the quartz grain. These changes smoothed the grain surface and weakened the bonding and the friction effect between grains.



**Fig. 5.26** Typical SEM images of (a) dry specimen without treatment, (b) Quartz corrosion in the set of dry+CO<sub>2</sub> saturation, (c) Quartz corrosion and clay mineral precipitation in the set of pure water saturation with CO<sub>2</sub>, (d) Calcite dissolution in the set of pure water saturation with CO<sub>2</sub>, (e) Secondary precipitation of Kaolinite clay in the set of water saturation with CO<sub>2</sub>, and (f) NaCl re-crystallisation in the set of 20% NaCl saturation

The mineral corrosion, dissolution and re-precipitation due to the CO<sub>2</sub> saturation (in dry and water saturated specimen) damages bonding and friction between grains and reduce the quartz grain intactness. As a result, the dynamic compressive and tensile strength is attenuated. In dry samples, since there is no water for CO<sub>2</sub> dissolution and further ionisation, CO<sub>2</sub> has to directly interact with rock mineral which has a less decreasing effect on strength compared to water-saturated sandstone. On the other hand, water itself has significantly

changed the mechanical properties even when the proportion is small due to the clay mineral is highly water sensitive (Shukla, Ranjith et al. 2013).

In terms of the saline environment, since the dissolution of CO<sub>2</sub> in brine is less than in water as the salting-out effect take over. Besides, the NaCl crystallisation in the pore space compensates a part of the attenuation from the CO<sub>2</sub>. This result is quite different from the static results where the brine weakens the sandstone in terms of strength (Rathnaweera, Ranjith et al. 2015). Therefore, the damage severity depends on not only the rock mineralogy and the composition of brine but also strain rate. In terms of fracturing behaviour, the damage of the microstructure shifts the location of the strain localisations initiation. For example, initiation started from the middle part of the specimen rather than the edge. Accordingly, the stress threshold of crack initiation is brought forward. The early initiation and shift of strain localisation bring considerable uncertainty of the disaster prevention for CO<sub>2</sub> sequestration underground. The damage of the microstructure by CO<sub>2</sub> also intensified the fracturing degree under both compression and tensile loading. The strain localisation propagation together with the stress threshold for unstable crack development are also accelerated with CO<sub>2</sub>, which should be considered in the reservoir rock to avoid unpredictable catastrophic failures.

In addition to the mineral distribution, the mineral composition which affects more in the dynamic deformation pattern is altered. The X-Ray Diffraction Analysis (XRD) on the dry Hawkesbury sandstone (Rathnaweera, Ranjith et al. 2015) before and after the CO<sub>2</sub> saturation shows that CO<sub>2</sub> dissolves 5-10% of quartz, with multiple, a small amount of brittle minerals such as mica, gypsum and halite taking its place. As a result, a higher percentage of brittle mineral caused by CO<sub>2</sub> saturated in dry sandstone increases Young's modulus and decrease the peak axial strain and Poisson's ratio. When sandstone is in a water saturated condition, the presence of CO<sub>2</sub> considerably decreases the percentage of quartz and calcite forming the clay mineral such as Kaolinite instead which leads to an opposite trend in Young's modulus and Poisson's ratio compared to dry sandstone. In terms of the saline environment, the CO<sub>2</sub> does not affect the dynamic Young's modulus and Poisson's ratio notably, even though the clay mineral is increased. It is quite different from the static results (Rathnaweera, Ranjith et al. 2015). It is expected to be the high rate sensitivity of NaCl crystallisation in the pore space

which make up the decrease in Young's modulus and Poisson's ratio by CO<sub>2</sub> at high strain rates.

### **(2) Free water effect**

Apart from the chemical and physical reaction between fluid and minerals, from the mechanics perspective, free water in the pores triggers the strain rate effect on the dynamic behavior of rock (Forquin et.al., 2010). Since the loading time is within hundreds of microseconds, the incompressible water in the pores is unable to move through the grain network which produce excess pore water pressure. It can be seen from Fig. 22(a) ~ (c) where D2 and DC2 gradually increase the initial Young's modulus, but W4, WC3, N2 and NC2 increase Young's modulus sharply. It can also explain the rate dependency of Young's modulus is in water or brine based sandstone rather than the dry sandstone. Besides, the water has viscosity, which can exert stress that resists the in plane shear of pore surface, known as Newton's inner friction effect (Zhou, Xin et al. 2016). This viscosity of water also works in the tensile opening between two pore surfaces, namely, Stefan effect and it is only valid when strain rate is high (Rossi 1991). Other effect such as Meniscus effect which is valid when water is not fast enough to reach the crack tip to generate the water wedge effect. Instead, a meniscus will be formed around the crack tip and resist the crack propagation (Kaszuba, Janecky et al. 2003). However, those enhancing effect is still not able to make up the attenuation effect in skeleton by chemical and physical reactions in this study. But unlike free water effects, skeleton damage is not rate dependent, it can be expected that when the strain rate is high enough, the water/brine/CO<sub>2</sub> saturated sandstone could have a larger strength than non-water-saturated sandstone. In other words, a relatively extreme loading may not cause the large damage but a strain rate below the critical value will do.

### **(3) Perspective**

Above patterns and rules should be dealt with caution when the grain size of sandstone varies. Since the different grain size would change the distribution and composition of the microstructures entirely, which further alters the mineral reaction with CO<sub>2</sub>, NaCl and water. Generally, according to the XRD analysis, the main difference (at least 10% difference) in the mineral composition in fine-grained (FG), medium-grained (MG) and coarse-grained (CG) sandstone is clay mineral (such as Kaolinite) and quartz. CG sandstone has the largest

percentage of quartz and least clay mineral, and FG sandstone has the least quartz but most clay mineral. Based on the findings in this study, CO<sub>2</sub> combined with water or brine mainly transform brittle minerals into clay minerals, under that circumstance, CG sandstone will have the most attenuation in mechanical properties. When CO<sub>2</sub> directly operates on the sandstone, the clay mineral remains steady but the percentage brittle minerals increases. As a result, the CG sandstone will exhibit a more brittle characteristic. The brine recrystallization tends to take place in the pores, therefore, its enhancement effect will be more notable in CG sandstone. However, when the strain rate is concerned, the result would be more complex since different grain-sized sandstone have different strain rate sensitivities. For example, an unusual behaviour was observed for coarse grained sandstone which has the maximum strength at the slowest strain rate, reversing the general decreasing trend of strength with decreasing strain rate (Wasantha, Ranjith et al. 2015). Moreover, little research investigated the grain-size effect in high strain-rate conditions. To comprehensively understand the fluid effect on the sedimentary rock at high-strain rates, study of grain size effect in the future is inevitable.

## 5.7 SUMMARY

- MG sandstone has the largest the rate sensitivity in strength which means after a critical strain rate ( $100 \text{ s}^{-1}$  in this study) MG sandstone is stronger than FG sandstone. In terms of Young's modulus, CG sandstone has the largest rate sensitivity which enhanced more than 3 times compared to static condition. Poisson's ratio in all grain-sized sandstones decreased to more than half at high strain rates. The stress threshold for crack initiation and unstable development behaved differently in different grain-sized sandstone. For FG sandstone, the crack initiated as soon as the loading applied. The fracturing distribution and evolution is identified in three modes.
- As a widely used method to determine the dynamic behavior of brittle material, SHPB is hard to achieve a same strain-rate comparison between different types of materials. Out-of-plane displacement, caused by the shear failure at the loading edge, is too small to affect the accuracy of using 2D-DIC. However, this small shear failure at edge makes the experiment result unable to represent the tensile strength. The propagation velocity of the strain localisation (as well as crack) is dependent on the

wave impedance of the rock. The strength of the rock can be estimated from the mineral composition and distribution in terms of clay, grain size and grain distribution.

- The compressive and tensile strength firstly increase and then decrease at a critical temperature between 400 °C and 800 °C. The stress thresholds normalized to the peak stress corresponding to cracks development were investigated and found that higher temperature induced larger normalized threshold. The strain field of the pre- and post-peak stage is analyzed, high-temperature will reduce the localization in vertical strain field but increase that in horizontal one to cause more significant fragmentation.
- The presence of CO<sub>2</sub> increases the dynamic Young's modulus but decrease Poisson's ratio for dry sandstone. This trend is opposite for the sandstone saturated in water. The compressive strength in dry sandstone is less attenuated (around 10%) than that in water-saturated sandstone (around 20%) by the injection of CO<sub>2</sub>. The presence of CO<sub>2</sub> has considerable effect on the above dynamic behaviours of sandstone saturated in brine. The enhancement effect of strain rate on the compressive strength still exists for all types of treatments, but the presence of CO<sub>2</sub> reduces the dynamic increase factor.
- No apparent strain rate effect on stress thresholds of crack initiation and unstable crack development in all treated sandstones. The presence of CO<sub>2</sub> brings forward the stress threshold of crack initiation and unstable crack development of dry or water-saturated sandstone, especially the water saturation with CO<sub>2</sub> in which the damage threshold was below 50%. CO<sub>2</sub> has less effect on the stress threshold of crack initiation of sandstone in brine but salinity does. For dry, water or brine saturated sandstone, the presence of CO<sub>2</sub> alters the crack initiation position and accelerates the propagation speed. CO<sub>2</sub> intensified the strain localisation degree in both dynamic compression and tension condition.

## REFERENCES

Aliha M, Ayatollahi M (2014) Rock fracture toughness study using cracked chevron notched Brazilian disc specimen under pure modes I and II loading—A statistical approach Theoretical and Applied Fracture Mechanics 69:17-25

Åkesson, U., et al. (2001). "Relationship between texture and mechanical properties of granites, central Sweden, by use of image-analysing techniques." *Bulletin of Engineering Geology and the Environment* 60(4): 277-284.

- Ayatollahi M, Aliha M (2007) Fracture toughness study for a brittle rock subjected to mixed mode I/II loading *International Journal of Rock Mechanics and Mining Sciences* 44:617-624
- Benson, S. M. (2015). "CO<sub>2</sub>Storage Preface." *Carbon Dioxide Capture for Storage in Deep Geologic Formations-Results from the CO<sub>2</sub> Capture Project: Vol 2-Geologic Storage of Carbon Dioxide with Monitoring and Verification*: 663.
- Brace, W. F. (1961). Dependence of fracture strength of rocks on grain size. The 4th US Symposium on Rock Mechanics (USRMS), American Rock Mechanics Association.
- Broch E The influence of water on some rock properties. In: *Proceedings of the Third Congress of the International Society for Rock Mechanics, Themes*, 1974. pp 1-2
- Brown DW A hot dry rock geothermal energy concept utilizing supercritical CO<sub>2</sub> instead of water. In: *Proceedings of the twenty-fifth workshop on geothermal reservoir engineering*, Stanford University, 2000. pp 233-238
- Colback, P. (1966). An analysis of brittle fracture initiation and propagation in the Brazilian test. 1st ISRM Congress, International Society for Rock Mechanics and Rock Engineering.
- Colback P, Wiid B (1965) The influence of moisture content on the compressive strength of rocks *Geophysics*
- Cui X, Bustin RM, Dipple G (2004) Selective transport of CO<sub>2</sub>, CH<sub>4</sub>, and N<sub>2</sub> in coals: insights from modeling of experimental gas adsorption data *Fuel* 83:293-303
- Ding Q-L, Ju F, Mao X-B, Ma D, Yu B-Y, Song S-B (2016) Experimental investigation of the mechanical behavior in unloading conditions of sandstone after high-temperature treatment *Rock Mechanics and Rock Engineering* 49:2641-2653
- Erarslan, N., et al. (2012). "Experimental and numerical studies on determination of indirect tensile strength of rocks." *Rock Mechanics and Rock Engineering* 45(5): 739-751.
- Fan L, Wu Z, Wan Z, Gao J (2017) Experimental investigation of thermal effects on dynamic behavior of granite *Applied Thermal Engineering* 125:94-103
- Forquin, P., Safa, K., & Gary, G. (2010). Influence of free water on the quasi-static and dynamic strength of concrete in confined compression tests. *Cement and concrete research*, 40(2), 321-333.
- French, W., et al. (2001). "Petrographic evaluation of aggregate parameters." *Proc. 8th Euroseminar on Microscopy Applied to Building Materials*: 4-7.
- Hamouda A, Tabrizy VA (2013) The effect of light gas on miscible CO<sub>2</sub> flooding to enhance oil recovery from sandstone and chalk reservoirs *Journal of Petroleum Science and Engineering* 108:259-266
- Hareland, G., et al. (1993). Normalized rock failure envelope as a function of rock grain size. *International Journal of Rock Mechanics and Mining Sciences & Geomechanics Abstracts*, Elsevier.
- Hawkins A, McConnell B (1992) Sensitivity of sandstone strength and deformability to changes in moisture content *Quarterly Journal of Engineering Geology and Hydrogeology* 25:115-130
- Huang S, Xia K (2015) Effect of heat-treatment on the dynamic compressive strength of Longyou sandstone *Engineering Geology* 191:1-7

- Huang S, Xia K, Yan F, Feng X (2010) An experimental study of the rate dependence of tensile strength softening of Longyou sandstone Rock mechanics and rock engineering 43:677-683
- Hugman III, R. and M. Friedman (1979). "Effects of texture and composition on mechanical behavior of experimentally deformed carbonate rocks." AAPG bulletin 63(9): 1478-1489.
- Kaszuba JP, Janecky DR, Snow MG (2003) Carbon dioxide reaction processes in a model brine aquifer at 200 C and 200 bars: implications for geologic sequestration of carbon Applied Geochemistry 18:1065-1080
- Kim EH, de Oliveira DBM The effects of water saturation on dynamic mechanical properties in red and buff sandstones having different porosities studied with Split Hopkinson Pressure Bar (SHPB). In: Applied Mechanics and Materials, 2015. Trans Tech Publ, pp 784-789
- Li, H., et al. (2017). "Experimental investigation on Brazilian tensile strength of organic-rich gas shale." SPE Journal 22(01): 148-161.
- Li D, Wong LNY, Liu G, Zhang X (2012) Influence of water content and anisotropy on the strength and deformability of low porosity meta-sedimentary rocks under triaxial compression Engineering Geology 126:46-66
- Liu S, Xu J (2014) Mechanical properties of Qinling biotite granite after high temperature treatment International Journal of Rock Mechanics and Mining Sciences 71:188-193
- Liu S, Xu J (2015) Effect of strain rate on the dynamic compressive mechanical behaviors of rock material subjected to high temperatures Mechanics of Materials 82:28-38
- Liu, S., et al. (2016). "Research on fracture toughness of flattened Brazilian disc specimen after high temperature." High Temperature Materials and Processes 35(1): 81-87.
- Lomov I, Hiltl M, Vorobiev OY, Glenn L (2001) Dynamic behavior of berea sandstone for dry and water-saturated conditions International journal of impact engineering 26:465-474
- Lundqvist, S. and M. Göransson (2001). "Evaluation and interpretation of microscopic parameters vs. mechanical properties of Precambrian rocks from the Stockholm region, Sweden." Proceedings of the eighth Euroseminar on microscopy applied to building materials, Athens, Department de Geologie, Athens: 13-20.
- Mendes, F. M., et al. (1966). The use of modal analysis in the mechanical characterization of rock masses. 1st ISRM Congress, International Society for Rock Mechanics.
- Middleton RS et al. (2015) Shale gas and non-aqueous fracturing fluids: Opportunities and challenges for supercritical CO<sub>2</sub> Applied Energy 147:500-509
- Perera M, Rathnaweera T, Ranjith P, Wanniarachchi W, Nasvi M, Abdulagatov I, Haque A (2016) Laboratory measurement of deformation-induced hydro-mechanical properties of reservoir rock in deep saline aquifers: An experimental study of Hawkesbury formation Marine and Petroleum Geology 77:640-652
- Přikryl, R. (2001). "Some microstructural aspects of strength variation in rocks." International Journal of Rock Mechanics and Mining Sciences 38(5): 671-682.

- Räisänen, M. (2004). "Relationships between texture and mechanical properties of hybrid rocks from the Jaala–Iitti complex, southeastern Finland." *Engineering Geology* 74(3): 197-211.
- Rathnaweera T, Ranjith P, Perera M (2014) Salinity-dependent strength and stress–strain characteristics of reservoir rocks in deep saline aquifers: an experimental study *Fuel* 122:1-11
- Rathnaweera T et al. (2015a) CO<sub>2</sub>-induced mechanical behaviour of Hawkesbury sandstone in the Gosford basin: An experimental study *Materials Science and Engineering: A* 641:123-137
- Rathnaweera T, Ranjith P, Perera M, Lashin A, Al Arifi N (2015b) Non-linear stress–strain behaviour of reservoir rock under brine saturation: an experimental study *Measurement* 71:56-72
- Rathnaweera T et al. (2017) An experimental investigation of coupled chemico-mineralogical and mechanical changes in varyingly-cemented sandstones upon CO<sub>2</sub> injection in deep saline aquifer environments *Energy* 133:404-414
- Rossi P (1991) A physical phenomenon which can explain the mechanical behaviour of concrete under high strain rates *Materials and Structures* 24:422-424
- Shukla R, Ranjith P, Choi S, Haque A, Yellishetty M, Hong L (2013) Mechanical behaviour of reservoir rock under brine saturation *Rock mechanics and rock engineering* 46:83-93
- Suggested methods for determining tensile strength of rock materials (1978) *International Journal of Rock Mechanics and Mining Sciences & Geomechanics Abstracts* 15:99-103  
doi:[https://doi.org/10.1016/0148-9062\(78\)90003-7](https://doi.org/10.1016/0148-9062(78)90003-7)
- Sutton M, Yan J, Tiwari V, Schreier H, Orteu J (2008) The effect of out-of-plane motion on 2D and 3D digital image correlation measurements *Optics and Lasers in Engineering* 46:746-757  
doi:10.1016/j.optlaseng.2008.05.005
- Sutton MA, Orteu JJ, Schreier H (2009) Image correlation for shape, motion and deformation measurements: basic concepts, theory and applications. Springer Science & Business Media, USA
- Tester JW et al. (2006) The future of geothermal energy: Impact of enhanced geothermal systems (EGS) on the United States in the 21st century Massachusetts Institute of Technology 209
- Tavallali, A. and A. Vervoort (2010). "Effect of layer orientation on the failure of layered sandstone under Brazilian test conditions." *International Journal of Rock Mechanics and Mining Sciences* 47(2): 313-322.
- Wang, Q., et al. (2004). "The flattened Brazilian disc specimen used for testing elastic modulus, tensile strength and fracture toughness of brittle rocks: analytical and numerical results." *International Journal of Rock Mechanics and Mining Sciences* 41(2): 245-253.
- Wang, S. Y., Sloan, S. W., Sheng, D. C., Yang, S. Q., & Tang, C. A. (2014). Numerical study of failure behaviour of pre-cracked rock specimens under conventional triaxial compression. *International Journal of Solids and Structures*, 51(5), 1132-1148.
- Wang, S. Y., Sloan, S. W., Fityus, S. G., Griffiths, D. V., & Tang, C. A. (2013). Numerical modeling of pore pressure influence on fracture evolution in brittle heterogeneous rocks. *Rock mechanics and rock engineering*, 46(5), 1165-1182.



Ward, C. R. (1972). "Sedimentation in the Narrabeen Group, Southern Sydney Basin, New South Wales." *Journal of the Geological Society of Australia* 19(3): 393-409.

Wasantha, P., et al. (2015). "Strain rate effect on the mechanical behaviour of sandstones with different grain sizes." *Rock Mechanics and Rock Engineering* 48(5): 1883-1895.

Willard, R. and J. McWilliams (1969). Microstructural techniques in the study of physical properties of rock. *International Journal of Rock Mechanics and Mining Sciences & Geomechanics Abstracts*, Elsevier.

Wong, L. N. Y., et al. (2014). "Fracturing and failure behavior of Carrara marble in quasistatic and dynamic Brazilian disc tests." *Rock Mechanics and Rock Engineering* 47(4): 1117-1133.

Wong, R. H., et al. (1996). Microcracking and grain size effect in Yuen Long marbles. *International Journal of Rock Mechanics and Mining Sciences & Geomechanics Abstracts*, Elsevier.

Xing H, Zhang Q, Braithwaite CH, Pan B, Zhao J (2017) High-speed photography and digital optical measurement techniques for geomaterials: fundamentals and applications *Rock Mechanics and Rock Engineering* 50:1611-1659

Xing H, Zhang Q, Ruan D, Dehkhoda S, Lu G, Zhao J (2018a) Full-field measurement and fracture characterisations of rocks under dynamic loads using high-speed three-dimensional digital image correlation *International Journal of Impact Engineering* 113:61-72

Xing H, Zhang Q, Zhao J (2018b) Stress Thresholds of Crack Development and Poisson's Ratio of Rock Material at High Strain Rate *Rock Mechanics and Rock Engineering* 51:945-951

Yin T, Li X, Cao W, Xia K (2015) Effects of thermal treatment on tensile strength of Laurentian granite using Brazilian test *Rock Mechanics and Rock Engineering* 48:2213-2223

Yin T, Li X, Xia K, Huang S (2012) Effect of thermal treatment on the dynamic fracture toughness of Laurentian granite *Rock mechanics and rock engineering* 45:1087-1094

Yu, M., et al. (2017). "The Coupled Effect of Loading Rate and Grain Size on Tensile Strength of Sandstones under Dynamic Disturbance." *Shock and Vibration* 2017.

Yu L, Zhang T, Su H, Jing H, Liu R, Zhang Q (2017) Influence of heat treatment on dynamic and physical properties of anthracite coal *Géotechnique Letters* 7:253-259

Yusof, N. and H. Zabidi (2016). "Correlation of mineralogical and textural characteristics with engineering properties of granitic rock from Hulu Langat, Selangor." *Procedia Chemistry* 19: 975-980.

Zhang Q, Zhao J (2013) Determination of mechanical properties and full-field strain measurements of rock material under dynamic loads *International Journal of Rock Mechanics and Mining Sciences* 60:423-439

Zhang, Q. and J. Zhao (2014). "Quasi-static and dynamic fracture behaviour of rock materials: phenomena and mechanisms." *International Journal of Fracture* 189(1): 1-32.

Zhang, Q. B. and J. Zhao (2013). "Effect of loading rate on fracture toughness and failure micromechanisms in marble." *Engineering Fracture Mechanics* 102: 288-309.

Zhang QB, Zhao J (2014) A review of dynamic experimental techniques and mechanical behaviour of rock materials *Rock mechanics and rock engineering* 47:1411-1478

Zhang Z, Yu J, Kou S, Lindqvist P-A (2001) Effects of high temperatures on dynamic rock fracture *International Journal of Rock Mechanics and Mining Sciences* 38:211-225

Zhao Y, Liu S, Jiang Y, Wang K, Huang Y (2016) Dynamic tensile strength of coal under dry and saturated conditions *Rock Mechanics and Rock Engineering* 49:1709-1720

Zhou, T. and J. Zhu (2017). An experimental investigation of tensile fracturing behavior of natural and artificial rocks in static and dynamic brazilian disc tests. *ISRM European Rock Mechanics Symposium-EUROCK 2017*, International Society for Rock Mechanics and Rock Engineering.

Zhou, Z., et al. (2014). "Dynamic Brazilian tests of granite under coupled static and dynamic loads." *Rock Mechanics and Rock Engineering* 47(2): 495-50

Zhou Z-l, Xin C, Yuan Z, Lu C, Xiong C, Li X-b (2016a) Strength characteristics of dry and saturated rock at different strain rates *Transactions of Nonferrous Metals Society of China* 26:1919-1925

Zhou Z, Cai X, Cao W, Li X, Xiong C (2016b) Influence of water content on mechanical properties of rock in both saturation and drying processes *Rock Mechanics and Rock Engineering* 49:3009-3025

Zhou Z, Cai X, Ma D, Du X, Chen L, Wang H, Zang H (2019) Water saturation effects on dynamic fracture behavior of sandstone *International Journal of Rock Mechanics and Mining Sciences* 114:46-61

## CHAPTER 6 DYNAMIC BEHAVIOUR OF ROCK SLAB UNDER INTERMEDIATE-VELOCITY PROJECTILE IMPACT

Within the non-deformable projectile impact regime, the perforation on thin slab can be further divided into high-velocity (normally above 500 m/s) and intermediate-velocity (under 500 m/s) perforation. Two types of perforation have significant different damage models, however, the intermediate-velocity perforation is seldom studied. In this study, 24 shots were conducted on sandstone thin slabs with three nose-shape projectiles at velocities ranging from 120 m/s to 403 m/s. Three ultra-high-speed cameras were employed to capture the perforation process at frame rates up to 380,000 frames per second (fps). The volume and velocity of ejected fragments were obtained by high-speed 3D digital image correlation (DIC). A perforation model of thin slab at intermediate impact velocity is established. Equations of perforation limit, ballistic limit and residual velocity are proposed, respectively. The perforation mechanism and the critical velocity distinguishing intermediate and high-velocity impact are identified.

### Nomenclature

$C, \rho_s, E$	P-wave velocity, density, Young's modulus of sandstone
$\sigma_t, \sigma_{ucs}, \tau_s$	Tensile, compressive and shear strength of sandstone
$H_c, H_t, H_p, H_{rc}, H_s$	Height of front cratering, tunnel, plugging, rear crater, scabbing
$H_{per}, V_{BL}$	Perforation limit and ballistic limit
$D_t, D_s$	Equivalent diameter of perforated hole and scabbing
$k$	Crater depth coefficient
$\theta_p$	Shear plugging angle
$H$	Thickness of slab
$l_0, l_s, l$	Nose length, body length and whole length of projectile
$d, M$	Mass and diameter of projectile
$a_{mean}, \mu$	Mean deceleration, mean resistance coefficient
$B$	Coefficient of dynamical resistance

## CHAPTER 6 DYNAMIC BEHAVIOUR OF ROCK SLAB UNDER INTERMEDIATE-VELOCITY PROJECTILE IMPACT

$N_1, N_2$	Projectile nose shape factors
$S$	Empirical constant
$F_p, F_s, A_s$	Projectile resistance, shear force and area on the shear surface
$V_0, V_p, V_r$	Initial velocity, shear plugging velocity, residual velocity of projectile
$V_{pf}, \Omega_p$	Ejecting velocity, volume of the rear plug target
$\eta$	Correlation coefficient,
$D_e, \theta_e, \Omega_e$	Diameter, angle and equivalent volume of the ejected fragment

### 6.1 INTRODUCTION

Projectile impact (or ballistic impact) in concrete and geological material has been investigated extensively in protective structural engineering. Overall, three approaches are necessary to investigate the projectile impact problem, which are numerical, empirical and semi-analytical methods. Numerical simulation has the advantages in investigating the real-time response of multi-scale and complex structure under projectile impact with full-field solutions such as stress and strain fields. However, the progress of numerical simulation greatly depends on the development of theoretical models. A detailed summary of the numerical methods of projectile impact on concrete and geological material can be referred to (Fang and Wu 2017). Empirical method aims to build up the relationship between impact parameters and terminal ballistic parameters by statistical analysis of the test results. It is the most reliable and straightforward approach but exclusive to particular material and even unit dependent. Semi-analytical methods are physically substantiated with good applicability. The prime issue in semi-analytical method is improving the resistance formulae and constitutive model to better describe the interaction between projectile and target. A comprehensive review of semi-analytical approaches is referred to (Ben-Dor, Dubinsky et al. 2014). To establish and improve a semi-analytical model, projectile impact experiment provides the only evidence to develop and verify the proposed models. Great efforts have been made in the experimental study of projectile impact on geomaterial. Goldsmith and Wu (Goldsmith and Wu 1981) applied a long metal bar with pointed end impacting the rock target to monitor the relationship between the force and penetration depth history by one-dimensional wave theory. Forrestal et.al. (Forrestal, Frew et al. 2003) applied an on-board

accelerometer to obtain the deceleration-time history of a projectile penetrating into a semi-infinite concrete target. The result showed that the resistance increased almost linearly during the cratering stage and remained constant since tunnelling stage began until stopped. But the projectile has to be large enough to carry the recorder of the accelerometer. Strain gauges were employed on the rear face by Lee et.al. (Lee, Kim et al. 2018) to measure the strain of the concrete target during projectile impact, which was found associated with crack initiation and development. However, the crack should be determined by the maximum principle strain rather than the strain in the direction of the strain gauge. Acoustic emission measurement was applied in the evaluation of damage degree and efficiency during the impact loading (Wang, Sloan et al. 2011). An analytical model to predict rock grain size effect on the damage pattern by penetration was investigated by scanning electron microscopy (SEM) by (Kumano and Goldsmith 1982). The application of high-speed photography (Xing, Zhang et al. 2017) significantly promotes the estimation of the damage response in projectile impact tests, for example, the penetration test conducted on sand (Cole 2010, Borg, Morrissey et al. 2013) and transparent soil (Chen, Omidvar et al. 2014, Guzman, Iskander et al. 2015). The applications of high-speed photography were more used to track the projectile trajectory (Borvik, Gjørsvik et al. 2007, Seah, Børsvik et al. 2011) and fragments movement (Hogan, Spray et al. 2013, Hogan, Spray et al. 2013, Hogan, Spray et al. 2014) in rock and concrete material. In terms of the digital optical measurement, digital speckle radiography (DSR) (Collins, Addiss et al. 2011) and particle image velocimetry (PIV) (Heineck, Schultz et al. 2002) were applied to obtain the quantitative response of sand and soil. Infrared radiation thermography (IRT) was instrumented by Shi et.al. (Shi, Wu et al. 2007) to study the deformation features by the radiant characteristics of a marble plate during the impact. However, both the accuracy and frame rate of IRT measurements were low. Overall, the measurement applied during projectile impact is important and remains development.

For a target with finite thickness, perforation (the projectile passes through the target) happens as the increase of the projectile velocity. Most of the existing experimental studies for projectile perforations were carried out on thick concrete slabs ( $H / d > 5$ ) (Hanchak, Forrestal et al. 1992, Cargile, Giltrud et al. 1993, Unosson 2000, Li, Lv et al. 2013, Wu, Fang et al. 2015). Few experiments conducted on thin geometrical slabs ( $H / d \leq 5$ ) are reported. Although (Chen, Li et al. 2008) and (Wu, Fang et al. 2012) developed projectile perforation

models for thin concrete slabs, those models have not been verified since the related test data, such as residual projectile velocity, is rarely available. The empirical parameters derived from concrete are not able to be directly applied by rock material. Additionally, the previous proposed perforation models corresponded to high-velocity impact from 500 to 1000 m/s. Two-stage (Yankelevsky 1997) and three-stage (Wu, Fang et al. 2012) models proposed for high-velocity impact can not describe the perforation patterns by the impact at an intermediate velocity. Therefore, there requires the experiment data and analytical models for the projectile perforation on thin rock slabs at intermediate velocities.

In this paper, perforation experiments were conducted on the sandstone thin slab by projectiles with three types of noses at velocities from 120 to 403 m/s. High-speed photography and combined 3D-DIC technique were applied to detect the real-time displacement of projectile and target. The equations to predict the perforation limit, ballistic limit and residual velocity were proposed and the empirical constants were calibrated. The velocity distinguishing the high- and intermediate-velocity perforation was identified.

## **6.2 EXPERIMENTAL SET-UP**

### **6.2.1 Material specification**

The target rock slabs were made from Hawkesbury sandstone whose grain composition and distribution are shown in Fig. 6.1(a). The mechanical properties for the sandstone are as following, density  $\rho_s = 2.21 \text{ g/cm}^3$ , P-wave velocity  $C = 1957 \text{ m/s}$ , elastic modulus  $E = 8.39 \text{ GPa}$ , tensile strength  $\sigma_t = 3.8 \text{ MPa}$  and UCS  $\sigma_{ucs} = 41 \text{ MPa}$ . The rock slab was manufactured in  $200 \times 200 \times 30 \text{ mm}^3$ . The rear face was coated with white paint and manually speckled by a marker pen for DIC tracking, as shown in Fig. 6.1(b). The front surface was coated by white paint for a better contrast to identify the crater boundary.

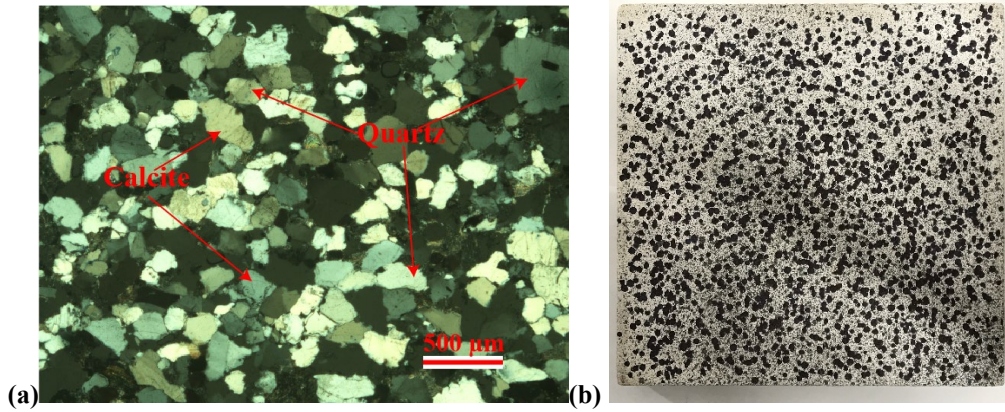


Fig. 6.1(a) Microscopic image of the thin section of sandstone (b) Speckled sandstone slab

### 6.2.2 Loading equipment and projectile

The setup of the impacting apparatus is shown in Fig. 6.2. The loading apparatus consists of a nitrogen gas tank, a pressure regulator, a barrier, I beam support, a sample holder and a PMMA safety cover. The nitrogen gas tank inflates nitrogen gas to the gas gun at a pressure controlled by the regulator, the gas pressure launches and accelerates the projectile along the barrel. The barrel has an inner diameter of 0.5 inches (12.7 mm). The target slab is fully fixed to the sample holder with four clamps on each edge, the distance between target and gas gun muzzle is 30 cm which is short enough to ensure the projectile trajectory aligns the center of the slab.

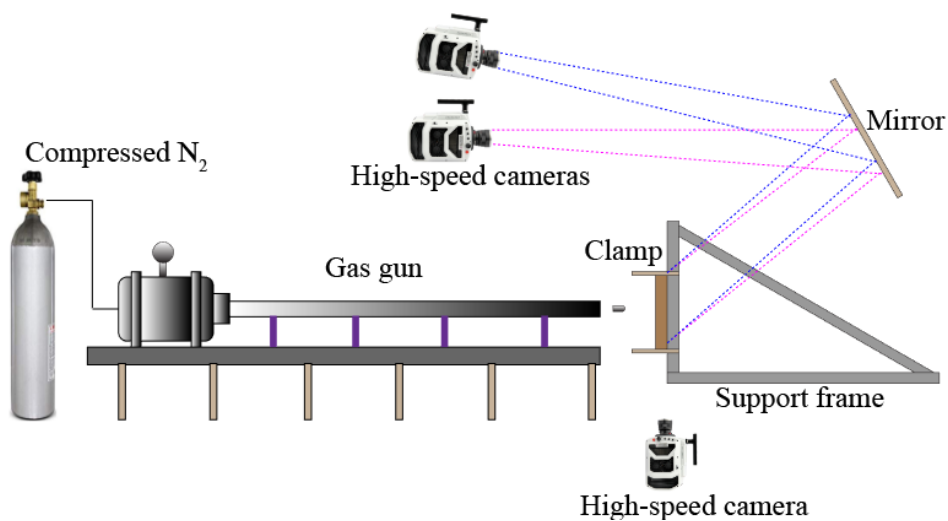


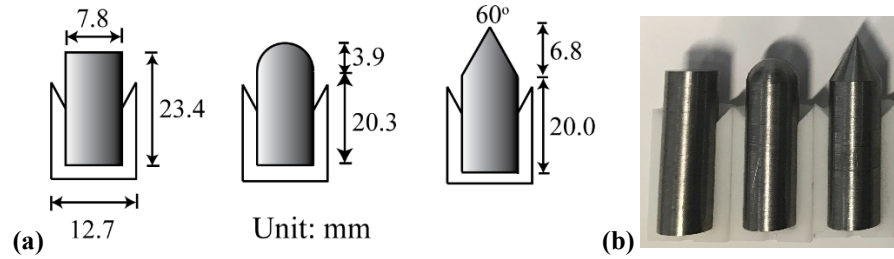
Fig. 6.2 Schematic of the experiment setup

The specification and geometry of the projectiles are shown in Table 6.1 and Fig. 6.3. The ratio of target thickness to projectile diameter is 3.8 which is less than 5 and is considered as

the thin slab penetration. The length of the target is 25 times larger than the projectile diameter which eliminates the boundary effect. Different lengths of projectile are determined to ensure the same weight of 10.1 g. To seal the gas between projectile and gas gun reservoir, sabots were used to hold the projectile properly and match with the gas gun barrel dimension. Sabot can position the projectile in order to minimize the pitching of the trajectory during launch. To eliminate sabots impacting the target, a two-piece split sabot was 3D printed with the material of ABS-like resin according to the design by (Kokaa and Mathewb 2017). Upon exiting the barrel, a radial force as well as a drag pressure is generated on the bevel surface causing the sabot to rotate and separate away from the projectile.

**Table 6.1** Specifications of the projectiles

Material	Hardness	Density (kg/m <sup>3</sup> )	Weight	Diameter	Nose shape
Mild steel	71 HRB	9000	10.1 g	7.82 mm	HS, flat and conical



**Fig. 6.3(a)** Sketch of flat, hemispherical and conical projectiles; and **(b)** a photograph of the projectiles and split sabots

### 6.2.3 High-speed imaging and 3D-DIC measurement

Three ultra-high-speed cameras are applied in the test, two of which (Phantom V2511) focus at the rear face of the target through the reflection in the mirror at 384×288 pixels, 150,000 fps and 6 μs exposure time. The third high-speed camera (Phantom V2512) is placed from the side of the specimen to capture the trajectory of the projectile flying in and out of the specimen at 256 × 128 pixels, 380,000 fps. A photo of the setup is shown in Fig. 6.4.





**Fig. 6.4** Setup of three high-speed cameras in projectile impact

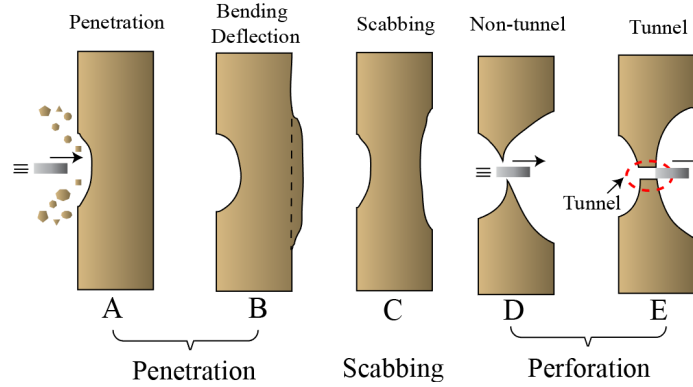
DIC was applied to reconstruct the deformation and velocity of rear surface. The zone of interest (ZOI) in the rear view of target is  $232 \times 135$  pixels corresponding to an area of  $239.4 \times 130.8 \text{ mm}^2$ , which means a pixel represents 0.97 mm. The accuracy of DIC in this study is controlled as 5% pixel which is 0.048 mm.

## **6.3 RESULTS**

### **6.3.1 Damage mode and parameters**

According to the post-failure phenomenon on the front and rear face of the slab, the impact damage on geological slabs are categorized into three modes which are penetration, scabbing, and perforation, as illustrated in Fig. 6.5 (Zhang, Shim et al. 2005). Perforation can be further classified into two types, non-tunnelling (D in Fig. 6.5) and tunnelling (E in Fig. 6.5) perforation.

## CHAPTER 6 DYNAMIC BEHAVIOUR OF ROCK SLAB UNDER INTERMEDIATE-VELOCITY PROJECTILE IMPACT



**Fig. 6.5** Failure modes: A. Penetration, B. Bending deflection C. Scabbing; D Non-tunnelling perforation; E Tunnelling perforation;

To further understand the damage of thin slab caused by the projectile impact, quantitative assessment of damage pattern is essential. Based on the damage pattern of perforation at high velocity (normally above 500 m/s), as illustrated in Fig. 6.6(a), the mainly concerned terminal ballistic parameters include depth of penetration (DOP) and height of rear crater  $H_{rc}$  induced by shear plugging. However, two zones (side view of slab in Table 6.3) appeared within the rear crater under the intermediate velocity impact, which are shear plugging and scabbing zone. Accordingly, the terminal damage parameters evaluated in this study includes DOP (sum of height of crater  $H_c$  and tunnel  $H_t$ ), shear plugging angle  $\theta_p$ , height of scabbing  $H_s$  as well as diameter of perforated hole and scabbing, as described in Fig. 6.6(b). Above terminal damage parameters in each shot are listed in Table 6.2.

The impact conditions and corresponding damage modes for all shots in this study are listed in Table 6.2. Photographs of some typical damaged rock slabs and projectiles are listed in Table 6.3. It was believed that the tunnel can only exist in the thick-slab perforation. However, tunnelling perforation was observed, for example, HS-1. Tunnelling perforation was also observed in conical projectile perforation but no one was observed in flat-head projectile impact even at the velocity of 397 m/s. Thus, nose shape and velocity of projectile play key roles in the tunnelling formation during the perforation.




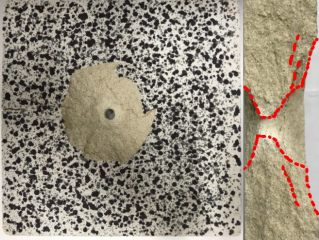




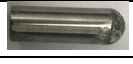
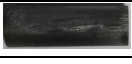

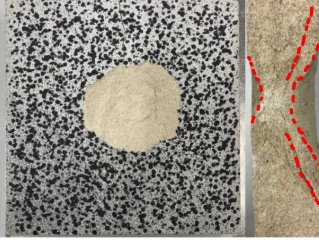






**Table 6.2** Ballistic damage mode and parameters for each test, unit (mm)

ID	$V_0$ (m/s)	Mode	Crater		Tunnel		DOP		Plugging		Scabbing	
			$H_c$	$D_t$	$H_t$		$H_c + H_t$		$H_p$	$\theta_p$	$H_s$	$D_s$
HS-1	364	E	7.5	10	5.0		12.5		0.5	50 °	17.0	78
HS-2	331	D	9.5	12	0		9.5		2.0	49 °	18.5	82
HS-3	294	D	6.0	9	0		6.0		5.0	43 °	19.0	83

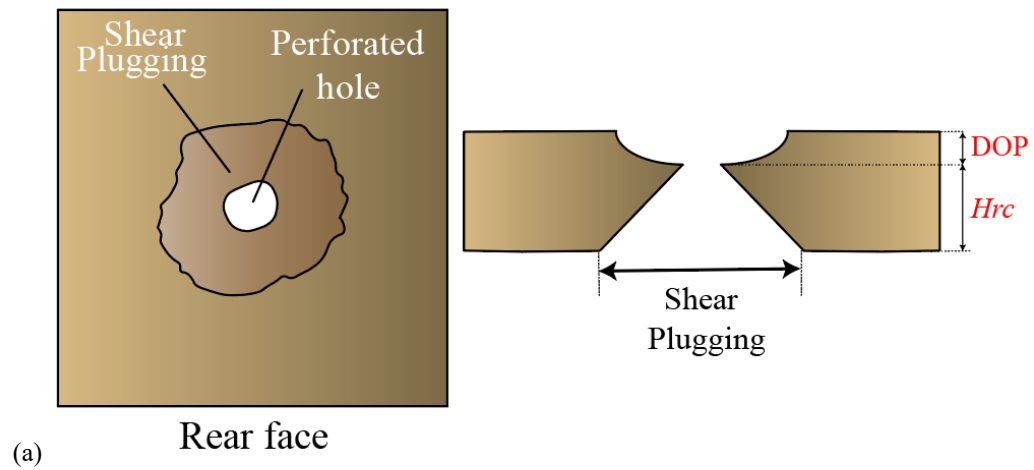
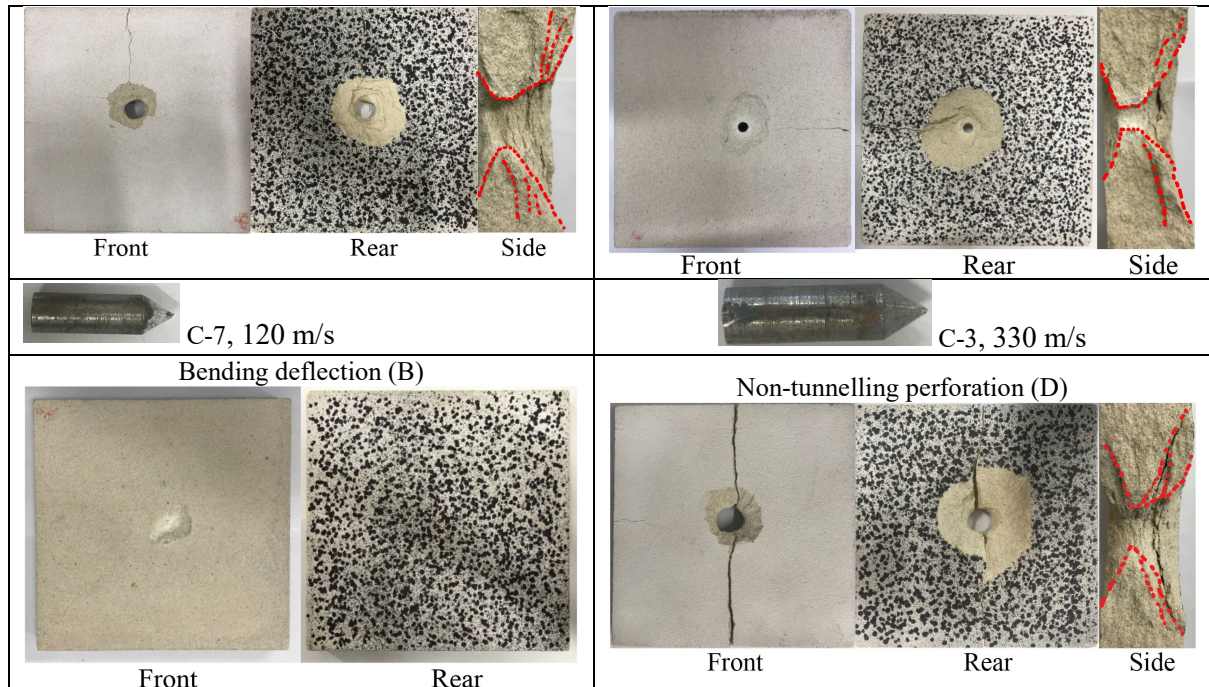
**CHAPTER 6 DYNAMIC BEHAVIOUR OF ROCK SLAB UNDER INTERMEDIATE-VELOCITY PROJECTILE IMPACT**

HS-4	288	D	8.0	11	0	8.0	2.0	42 °	20.0	76
HS-5	268	D	8.0	12	0	8.0	2.5	37 °	19.5	80
HS-6	230	D	9.0	12	0	9.0	2.0	21 °	19.0	69
HS-7	197	D	7.0	9	0	7.0	3.5	14 °	19.5	71
HS-8	160	C	8.0	N/A		8.0	N/A		19.5	64
F-1	397	D	12.5	16	0	12.5	0.5	45 °	17.0	64
F-2	338	D	7.5	18	0	7.5	3.5	43 °	19.0	88
F-3	330	D	9.5	14	0	9.5	2.0	40 °	18.5	72
F-4	298	D	8.5	16	0	8.5	2.5	35 °	19.0	81
F-5	296	D	8.0	15	0	8.0	3.5	32 °	18.5	85
F-6	287	D	10.0	17	0	10.0	1.0	31 °	19.0	74
F-7	270	D	7.5	13	0	7.5	3.0	29 °	19.5	74
F-8	245	D	3.5	8	0	3.5	7.5	26 °	19.0	79
F-9	178	D	3.5	9	0	3.5	7.5	21 °	19.0	74
C-1	403	E	6.0	9	5.5	11.5	2.5	44 °	16.0	71
C-2	397	E	4.5	9	7	11.5	2.5	43 °	16.0	65
C-3	330	D	9.5	16	0	9.5	4.0	32 °	16.5	83
C-4	288	D	9.5	14	0	9.5	4.0	30 °	16.5	84
C-5	230	D	10.0	13	0	10.0	3.5	28 °	16.5	91
C-6	177	D	9.0	9	0	8.5	5.0	25 °	16.0	82
C-7	120	B	9.0	N/A		9.0	N/A			

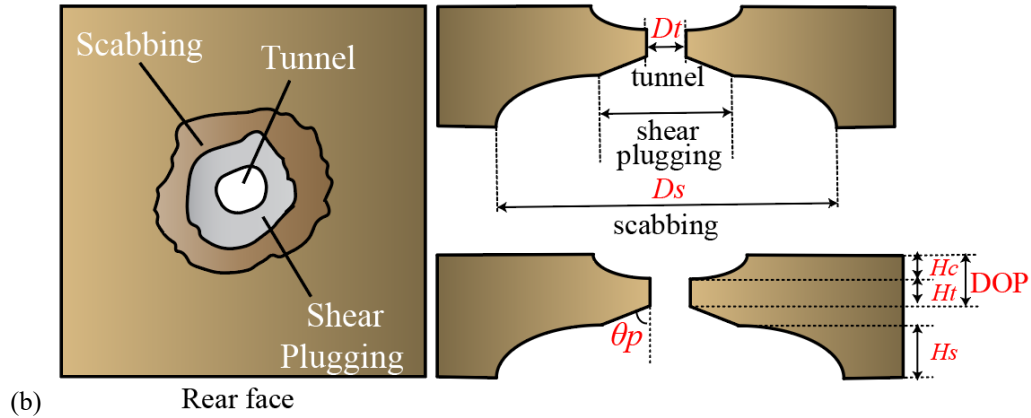
**Table 6.3** Typical damaged slabs and projectile after impact tests

 HS-1, 364 m/s			 HS-5, 268 m/s		
<b>Tunnelling Perforation (E)</b>   			<b>Non-tunnelling perforation (D)</b>   		
 HS-8, 160 m/s			 F-6, 287 m/s		
<b>Scabbing (C)</b>   			<b>Non-tunnelling perforation (D)</b>   		
 F-1, 397 m/s			 C-1, 403 m/s		
Non-tunnelling perforation (D)			Tunnelling perforation (E)		

# CHAPTER 6 DYNAMIC BEHAVIOUR OF ROCK SLAB UNDER INTERMEDIATE-VELOCITY PROJECTILE IMPACT



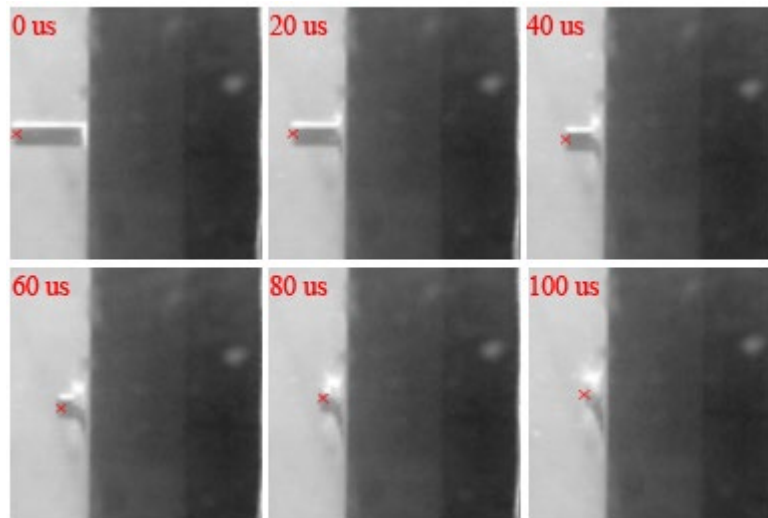




**Fig. 6.6** Damage zones and concerned parameters in (a) high-velocity perforation (b) intermediate-velocity perforation

### 6.3.2 Projectile kinematic measurement

The depth of penetration, DOP, is directly dependent on the resistance of the slab on the projectile. According to Newton's second law, for non-abrasive projectile, the resistance is a function of deceleration which can be revealed by the velocity change rate,  $dV/dt$ . By tracking the end of the projectile in the high-speed photography, the velocity history of projectile is determined until projectile almost entirely entering the slab. A typical sequence of high-speed photography of flat projectile F-1 penetrating into the slab is shown in Fig. 6.7.



**Fig. 6.7** Process of Test F1: projectile penetrating into the slab. The projectile end (cross) is used to track velocity

In some tests, the velocity was not obtained because the projectile was partly blocked by the debris or separated sabot. Base on the final DOP in Table 6.2, a summary of measured

## CHAPTER 6 DYNAMIC BEHAVIOUR OF ROCK SLAB UNDER INTERMEDIATE-VELOCITY PROJECTILE IMPACT

velocity at the beginning and end of the penetration as well as the duration are listed in Table 6.4.

**Table 6.4** Velocity and duration during penetration

ID	Mode	$V_0$ (m/s)	$V_c$ (m/s)	Penetrating time ( $\mu$ s)	Calculated deceleration ( $10^6$ m/s <sup>2</sup> )
HS-1	E	364	280	40	2.11
HS-2	D	331	264	33	2.03
HS-4	D	288	230	29	2.00
HS-5	D	264	198	33	2.00
HS-7	D	197	115	42	1.95
F-1	D	397	291	40	2.65
F-3	D	330	238	36	2.56
F-4	D	298	238	24	2.50
F-6	D	287	197	37	2.43
F-7	D	270	199	30	2.37
C-1	E	403	331	33	2.18
C-3	D	330	266	30	2.13
C-4	D	288	202	42	2.05
C-5	D	230	115	56	2.05

### 6.4 PERFORATION MODEL

#### 6.4.1 Perforation limit and ballistic limit

Perforation limit (minimum thickness of the slab required to prevent the perforation) and ballistic velocity limit (minimum velocity of the projectile required to perforate the slab) are two of the most concerned parameters in the perforation study. The perforation limit is the sum up of DOP and height of rear crater  $H_{rc}$  when the critical perforation occurs. Hence, the perforation limit  $H_{per}$  is obtained as

$$H_{per} = DOP + H_{rc}, \quad (6.1)$$

where the height of rear crater  $H_{rc}$  is associated with the impact velocity as follow,

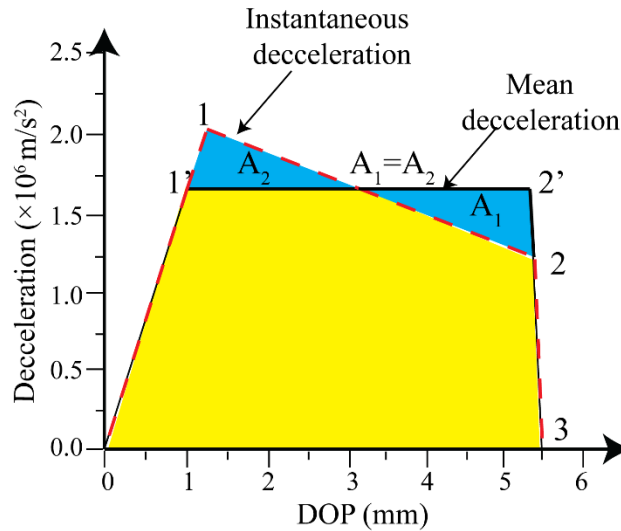
$$H_{rc} = H_p \text{ (high-velocity impact)}$$

$$H_{rc} = H_p + H_s \text{ (intermediate-velocity impact)} \quad (6.2)$$

DOP is the combination of the height of cratering and tunnelling. The cratering height  $H_c$  in deep penetration is independent on velocity determined as  $kd$ , where  $k$  is the crater depth coefficient determined as (Chen and Li 2002, Li and Chen 2003, Li, Weng et al. 2004),

$$k = 0.707 + l_0/d, \quad (6.3)$$

where  $l_0$  is the nose length of projectile. According to Eq. 6.2,  $k$  is 1.207, 0.707 and 1.872 for HS, flat and conical projectile corresponding to a front crater depth of 9.4 mm, 5.5 mm and 14.6 mm for HS, flat and conical projectile, respectively. However, the depth of the front crater  $H_c$  obtained in this study is velocity-dependent whose average is 7.9 mm, 7.7 mm, 8.1 mm for HS, flat and conical projectile, respectively. The crater depth coefficient was also observed decreasing with the reduction of the slab thickness (Wu, Fang et al. 2015). Notably, when the slab thickness is thin, the crater depth is in the same order as the slab thickness as well as projectile diameter making Eq. 6.3 invalid. Therefore, a mean resistance method was applied to represent the deceleration during both cratering and tunneling stage. The mean resistance approach was proposed by (Fang and Wu 2017) based on dynamic cavity expansion approximation according to the deceleration-time histories in penetration test (Wu, Fang et al. 2015). The deceleration increased almost linearly during the cratering stage and declined in the tunnelling stage until penetration finishing, as shown as the red dash line in Fig. 6.8. To avoid the complex instantaneous deceleration, the mean resistance is proposed as a constant (black solid line) to ensure the actual and mean deceleration are equal.



**Fig. 6.8** Illustration of mean resistance (Fang and Wu 2017)

The mean deceleration is proposed as following,

$$a_{mean} = \frac{\pi d^2}{4M} [1 + \mu \delta(V_0)] N_1 S \sigma_{ucs} \quad (6.4)$$

$$\delta(V_0) = \frac{I_0}{N} = \frac{B N_2 \rho_s V_0^2}{N_1 S \sigma_{ucs}} \quad (6.5)$$

## CHAPTER 6 DYNAMIC BEHAVIOUR OF ROCK SLAB UNDER INTERMEDIATE-VELOCITY PROJECTILE IMPACT

$I_0$  and  $N$  are two dimensionless parameters proposed by (Chen and Li 2002)

$$I_0 = \frac{MV_0^2}{N_1 S \sigma_{ucs} d^3}, N = \frac{M}{BN_2 \rho_s d^3} \quad (6.6)$$

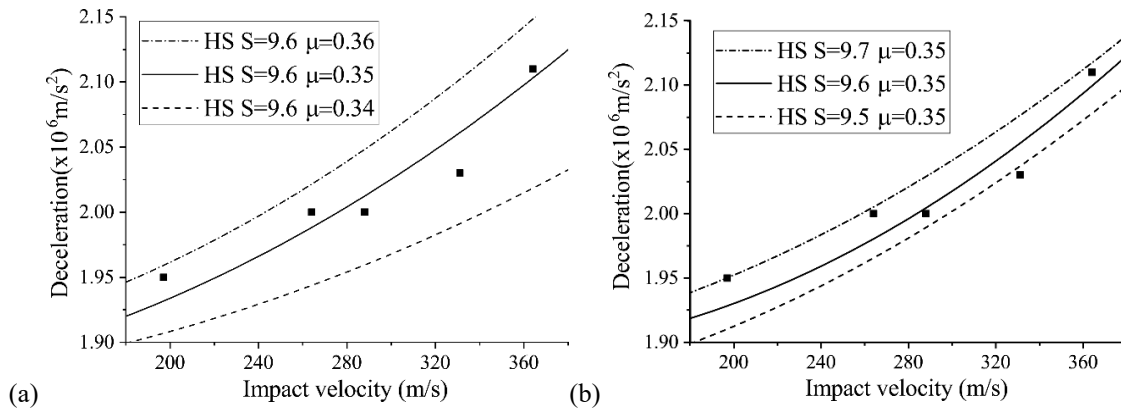
Therefore,

$$DOP = (V_0^2 - V_p^2)/2a_{mean} \quad (6.7)$$

By solving Eq. 6.4-7,

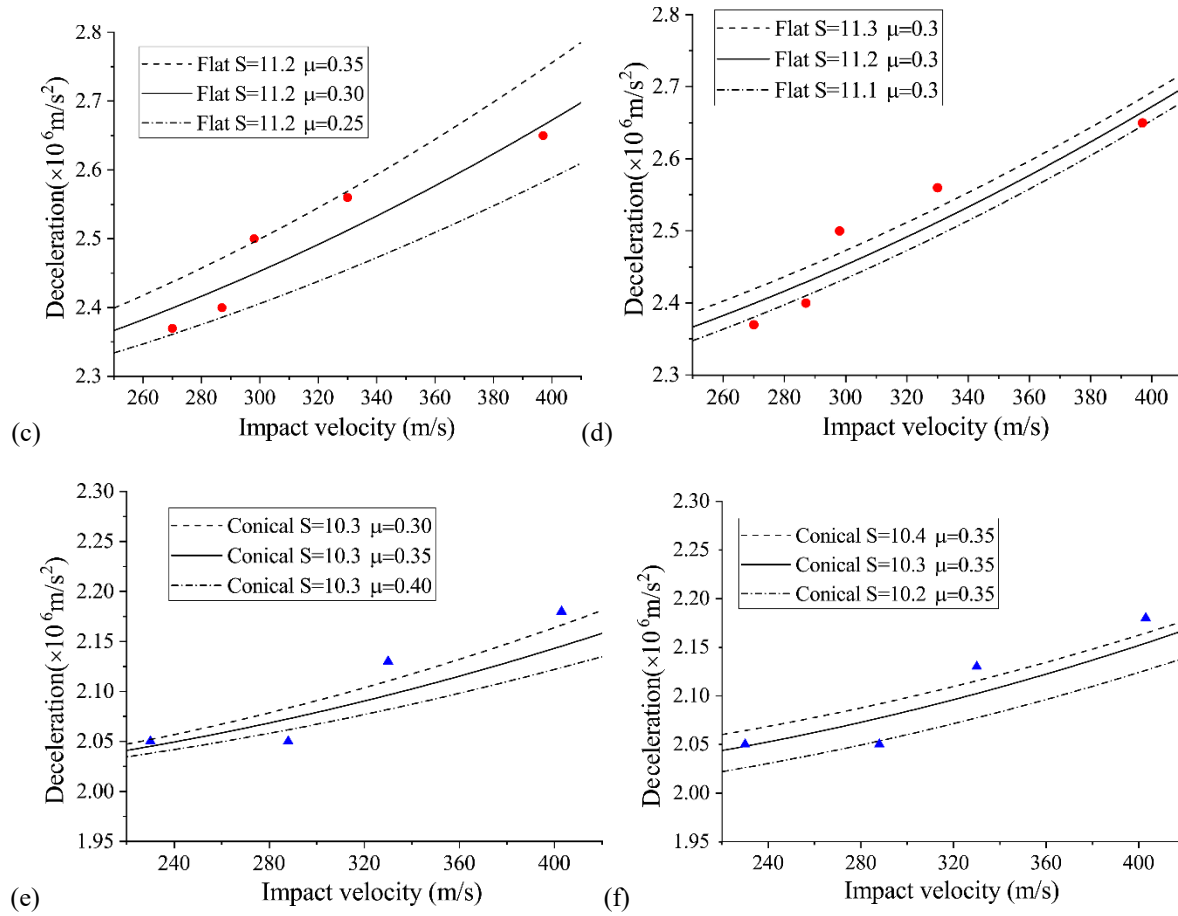
$$DOP = \frac{2M(V_0^2 - V_p^2)}{\pi d^2 [1 + \mu \delta(V_0)] N_1 S \sigma_{ucs}} \quad (6.8)$$

where  $V_0$  is the impact velocity,  $V_p$  is the projectile velocity when plugging starts,  $\sigma_s$  is the quasi-static target material strength;  $B$  is the coefficient of dynamical resistance derived from dynamic cavity expansion analysis which is suggested as 1;  $N_1$ ,  $N_2$  are projectile nose shape factors suggested as both 1 for flat projectile, 1 and 0.25 for conical projectile and 1 and 0.5 for HS projectile (Chen and Li 2002);  $S$  is empirical constant which is determined from recorded impact velocity and penetration depth for each test.  $S$  is mainly controlled by target uniaxial strength and partly affected by projectile diameter and nose shape. In the previous study,  $S$  is normally taken as 10.6 for concrete target.  $\mu$  is the mean resistance coefficient which was calibrated as 0.4 based on the results in a deep penetration test where projectile stops at the end. The projectile velocity remains a certain value at the end of the penetration in perforation test (transition from penetration to shear plugging). Therefore, both empirical constant  $S$  and mean resistance coefficients  $\mu$  require calibration. Two constants in Eq. 6.4 were calibrated with the actual mean deceleration (Table 6.4) determined by high-speed imaging as shown in Fig. 6.9.





## CHAPTER 6 DYNAMIC BEHAVIOUR OF ROCK SLAB UNDER INTERMEDIATE-VELOCITY PROJECTILE IMPACT



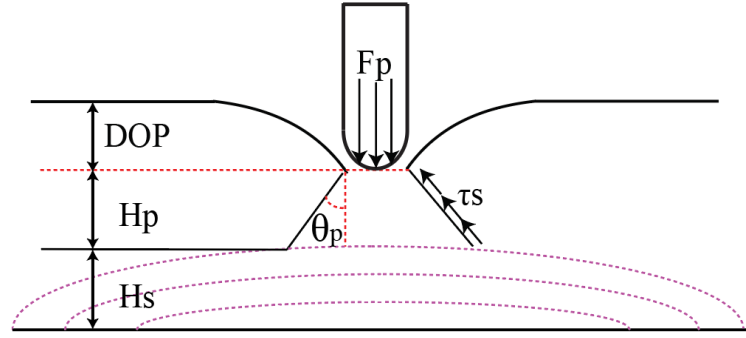
**Fig. 6.9** Calibration of  $S$  and  $\mu$  in Eq. 4 for projectiles of three types of noses

The calibrated empirical constant  $S$  and mean deceleration coefficient  $\mu$  are listed in Table 6.5.

**Table 6.5** Calibrated empirical constant  $S$  and mean deceleration coefficient  $\mu$

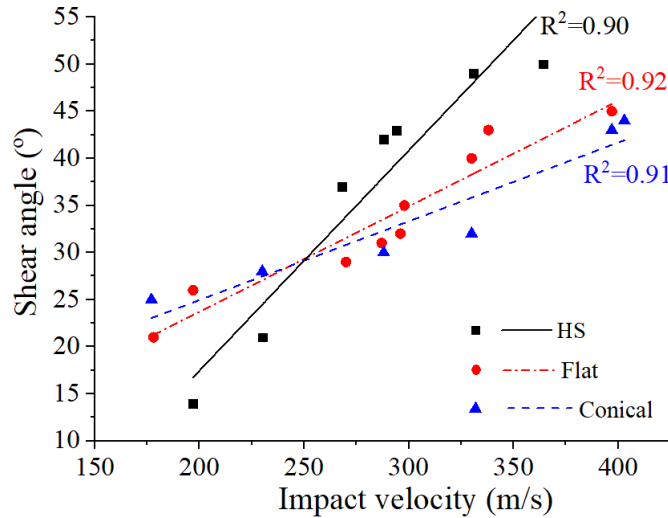
Nose shape	$S$	$\mu$
Hemispherical	9.6	0.35
Flat	11.2	0.30
Conical	10.3	0.35

The shear plugging zone is considered a cone shaped with two important parameters i.e. shear angle  $\theta_p$  and height  $H_p$ , as demonstrated in Fig. 6.10.



**Fig. 6.10** Cone plugging zone formation

Dancygier (Dancygier 1998) regarded the shear angle  $\theta_p$  as a constant of  $66^\circ$  for normal strength concrete (NSC) which is independent of impact velocity. However, different impact velocities will result in different strain-rate loading between projectile and target during the penetration. The rate-dependent inter-friction angle was discussed in dynamic uniaxial (Xing, et al. 2018) and triaxial compression test (Si, X. et.al., 2019), which was also found in this study as illustrated in Fig. 6.11 based on the results in Table 6.2.



**Fig. 6.11** Angle of the plugging zone versus velocity for all projectiles

By linear fitting the test results, we estimate the shear angle as follows,

$$\begin{cases} \theta_p = 0.23V_0 - 29 & \text{(HS)} \\ \theta_p = 0.11V_0 + 1 & \text{(Flat)} \\ \theta_p = 0.08V_0 + 8 & \text{(Conical)} \end{cases} \quad (6.9)$$

The shear angle exhibits dependency on the nose shape and impact velocity where the angle increases with the rise of the impact velocity. The rate-dependent shear plugging angle  $\theta_p$  in

the form of  $\tan\theta_p$  varies from 0.9 to 2.6 which significantly affects the estimation of height of shear plugging.

Shear plugging occurs as soon as the instantaneous axial resistant force on the projectile nose equals to the maximum shear strength on the plugging surface, as shown in Fig. 6.10.

The resistance  $F_p$  on the interface between projectile and cone surface at velocity  $V_p$  is determined as (Forrestal et al 1994, Forrestal et al 1996),

$$F_p = \frac{\pi d^2}{4} [1 + \delta(V_p)] N_1 S \sigma_{ucs} \quad (6.10)$$

The total shear force  $F_s$  provided by the shear surface of the sandstone cone is determined by

$$F_s = \tau_s A_s \cos\theta_p \quad (6.11)$$

The dynamic shear strength  $\tau_s$  is related to the dynamic uniaxial compression strength (Li and Tong, 2003) as

$$\tau_s = \frac{1}{\sqrt{3}} \sigma_{ucs} \quad (6.12)$$

$A_s$  is the shear area of the cone plug surface given as

$$A_s = \frac{1}{\cos\theta_p} (dH_p\pi + H_p^2\pi\tan\theta_p) \quad (6.13)$$

Therefore shear plugging occurs when

$$F_p = F_s \quad (6.14)$$

By solving Eq. 6.10-14, the plugging height  $H_p$  can be determined as

$$H_p = d \left( \sqrt{1 + \tan\theta_p [1 + \delta(V_p)] N_1 S \sigma_{ucs} / \tau_s} - 1 \right) / 2 \tan\theta_p \quad (6.15)$$

Scabbing is a wave-induced dynamic fracture phenomenon (Rossmanith and Uenishi 2006), the height of scabbing  $H_s$  is related to the wave length which is further dependent on the projectile length. According to 24 scabbing depths collected in this study, as shown in Fig. 12, we propose the dimensionless height of scabbing as

$$\frac{H_s}{l_s} = 0.8 \quad (6.16)$$

$l_s$  is the effective body length of the projectile where  $l_s = l$  for HS and flat projectile,  $l_s = l - l_0$  for conical projectile.

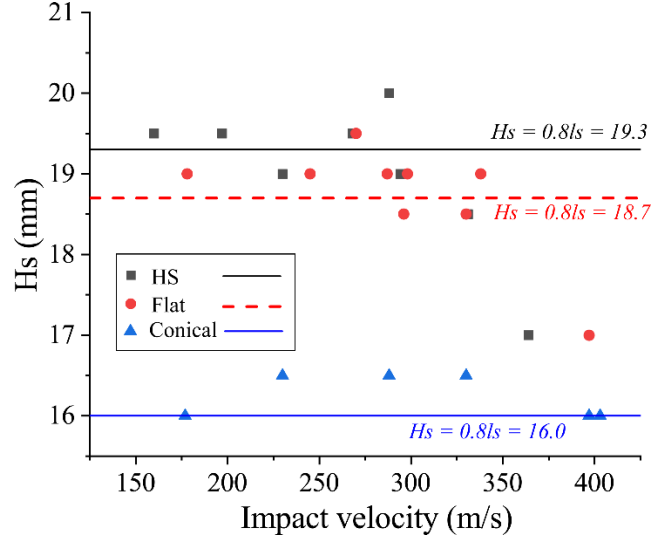


Fig. 6.12 Height of scabbing in all impacts

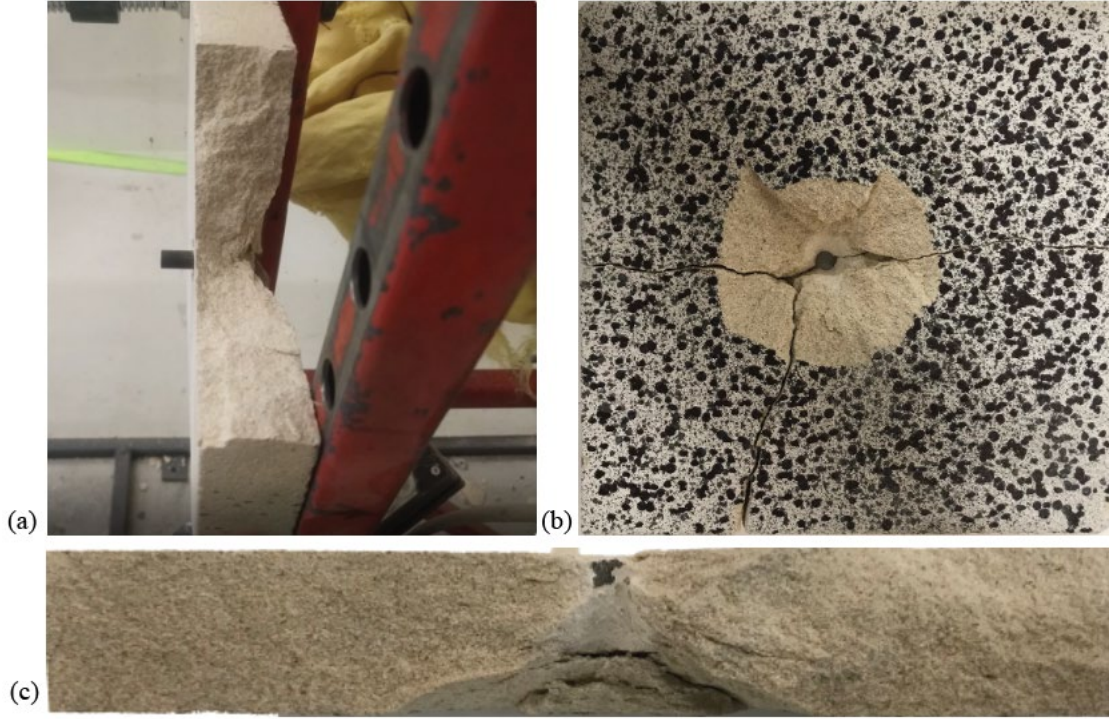
By substituting Eq. 6.8, 15 and 16 into Eq. 6.1, perforation limit is determined as

$$H_{per} = \frac{2M(V_0^2 - V_p^2)}{\pi d^2 [1 + \mu \delta(V_0)] N_1 S \sigma_{ucs}} + d \left( \sqrt{1 + \tan \theta_p [1 + \delta(V_p)] N_1 S \sigma_{ucs} / \tau_s} - 1 \right) / 2 \tan \theta_p + 0.8 l_s \quad (6.17)$$

It could be seen from Eq. 6.17,  $H_{per}$  is the function of  $V_p$ . Taking the derivative of  $V_p$ , the first derivation of Eq. 6.17 is negative which means Eq. 6.17 reaches the maximum when  $V_p$  is close to zero, Therefore, when  $V_p = 0$ ,

$$H_{per} = 2MV_0^2 / \pi d^2 [1 + \mu \delta(V_0)] N_1 S \sigma_{ucs} + d \left( \sqrt{1 + \tan \theta_p N_1 S \sigma_{ucs} / \tau_s} - 1 \right) / 2 \tan \theta_p + 0.8 l_s \quad (6.18)$$

For a hemispherical projectile at  $V_0 = 364$  m/s, the perforated limit is 60.4 mm which is 12% larger than 53.7 mm obtained by Eq. 6.18 with uncalibrated empirical parameters ( $S = 10.6$ ,  $\mu = 0.4$ ) and fixed shear angle ( $\theta_p = 66^\circ$ ). The ballistic limit  $V_{BL}$  can be deduced reversely from the  $H_{per}$  equation. To perforate the 30 mm sandstone slab, the ballistic limit  $V_{BL}$  is calculated as 175 m/s, 165 m/s and 172 m/s for flat, HS and conical projectile, respectively. This is validated by F-9 test (178 m/s) where a critical perforation (residual velocity was 0 m/s) happened, as shown in Fig. 6.13.



**Fig. 6.13** A critical perforation in F9, flat projectile at 178 m/s.

#### 6.4.2 Residual velocity

The residual velocity of the projectile  $V_r$  is deduced from the conservation of kinetic energy as follow,

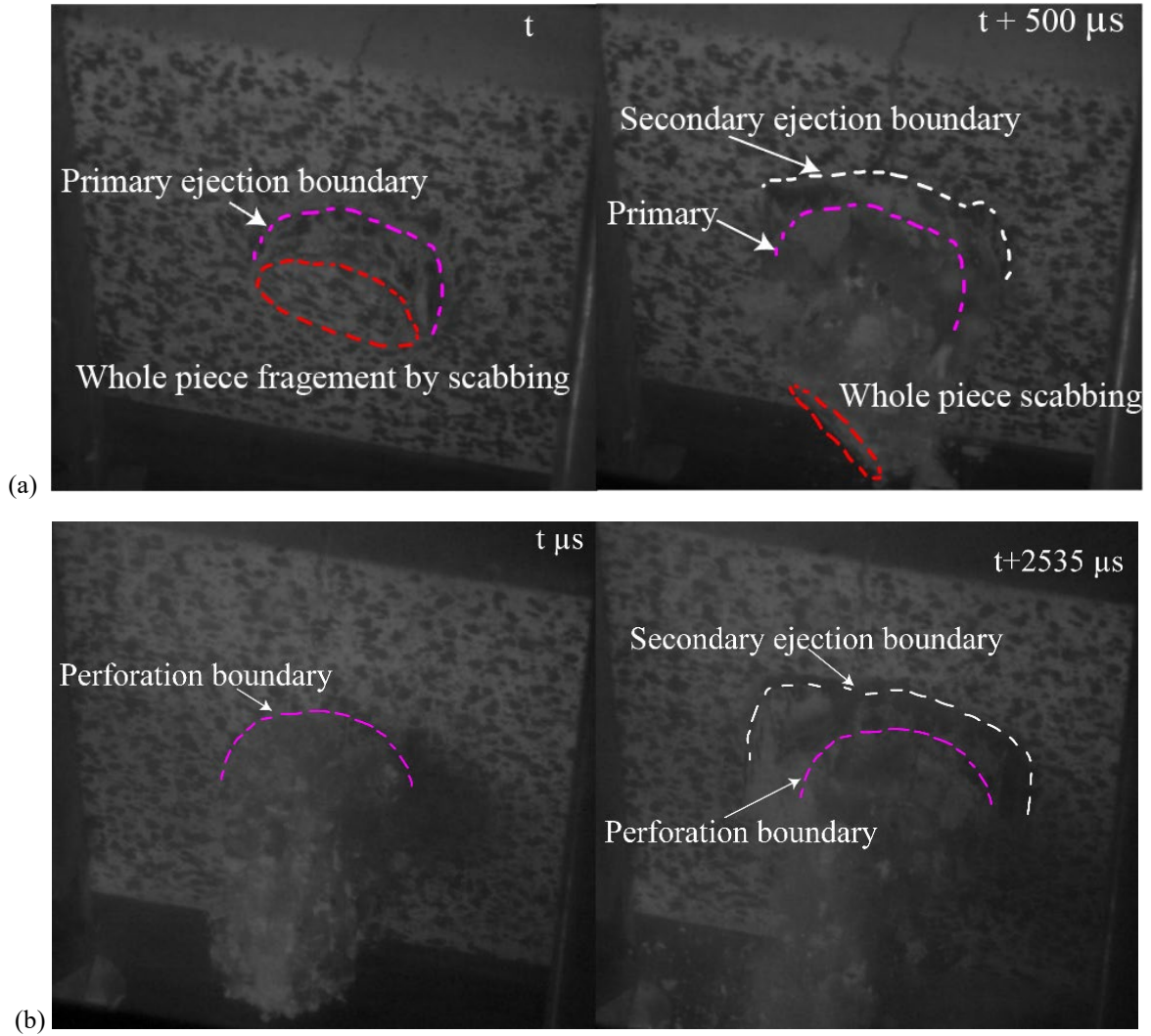
$$MV_0^2 = MV_{BL}^2 + MV_r^2 + \rho\Omega V_{pf}^2 \quad (6.19)$$

where  $V_{pf} = \eta V_r$  represents the ejecting velocity of the rear plug target,  $\eta$  is the correlation coefficient,  $\Omega$  is the volume of the ejected fragment.

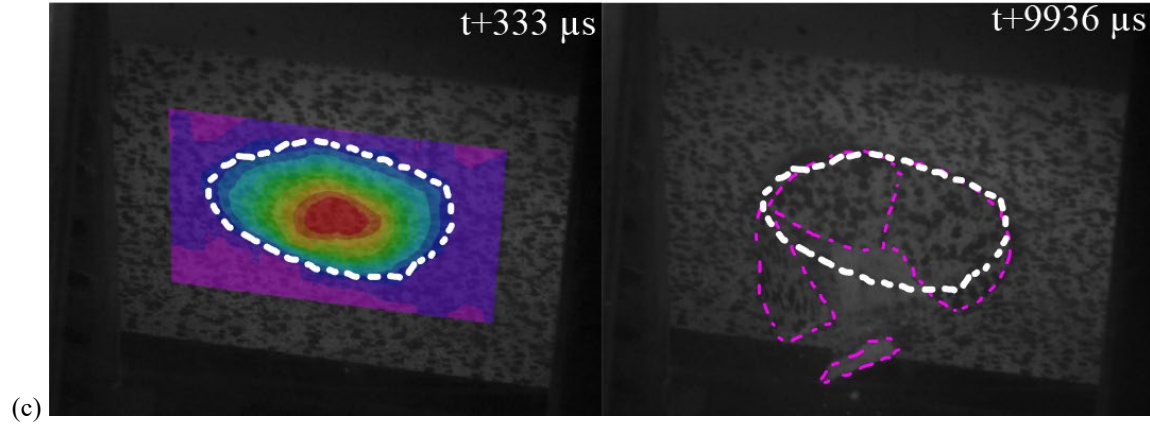
Three typical ejection patterns were found by high-speed photography as shown in Fig. 6.14. A relatively intact fragment caused by scabbing was pushed by the projectile behind for non-tunnelling perforation HS-5, as shown in Fig. 6.14(a). It proves that the scabbing has already finalised before perforation taking place. Afterwards, the ejected fragments spalled the neighbouring scabbing fragments forming the secondary ejection boundary, as indicated by the white dash line. When the impact velocity was high, for example tunnelling perforation HS-1 as shown in Fig. 6.14(b), the ejection was led by the projectile in front followed by debris in a cone shape. Around 2 ms later, the scabbing fragments were spalled by the flying debris forming the ultimate rear crater. The process of scabbing only (Mode C) is shown in

CHAPTER 6 DYNAMIC BEHAVIOUR OF ROCK SLAB UNDER INTERMEDIATE-VELOCITY PROJECTILE IMPACT

Fig. 6.14(c) where the boundary is indicated by the out-of-plane displacement field in 3D-DIC at  $333\ \mu\text{s}$  since penetration took place. Around 9 ms later, the scabbing fragment ejected at velocity around 5 m/s.

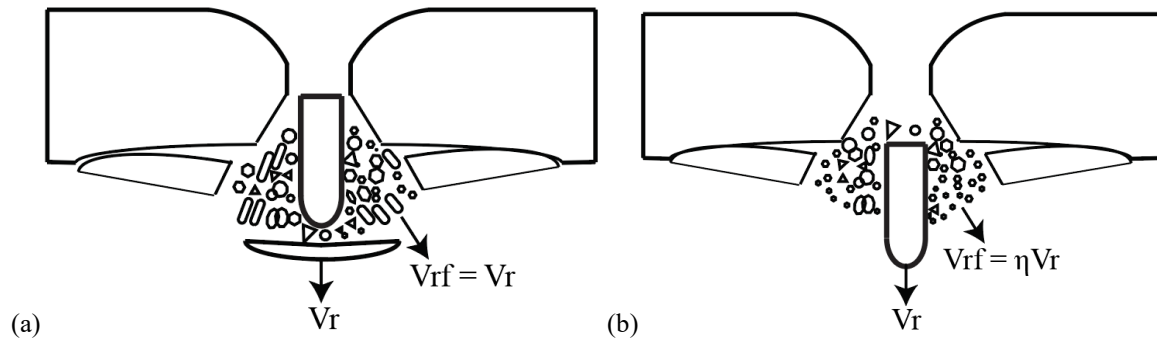






**Fig. 6.14** Three typical ejection modes: (a) HS-5; (b) HS-1; (c) F-7, left: out-of-plane displacement boundary by 3D-DIC, right: scabbing fragmentation;

Because two types of ejection modes exist in the perforation, the ejecting velocity of the rear plug target should be discussed in two cases. If the projectile velocity is lower, during the shear plugging the momentum of projectile gradually transfer to the fragments ahead until reaching the same velocity and ejecting out of the rear face, i.e.  $\eta = 1$ , as indicated as Mode X in Fig. 6.15(a). Whereas if the projectile is fast enough, it has a faster exiting velocity than the fragments corresponding to  $\eta < 1$ , as illustrated as ejection Mode Y in Fig. 6.15(b).



**Fig. 6.15** Fragments ejection velocity (a) Mode X: same with projectile (b) Mode Y: correlated to projectile

Because the velocity of scabbing fragment is around 5 m/s which is less than 10% of shear plugging ejection velocity. Meanwhile, scabbing volume has a same order with that of shear plugging, resulting in the kinetic energy of scabbing is less than 1% that of shear plugging which is not considered in Eq. 6.19.

The ejected shear-plugging fragment is theoretically assumed as, whose volume had the expression of

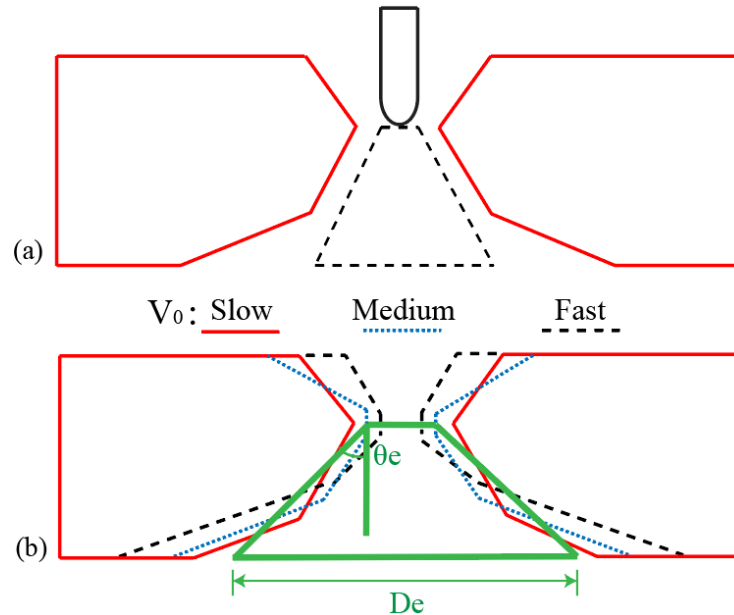
$$\Omega_t = \frac{\pi}{3} H_{cr} (4 \tan^2 \theta_p H_{cr}^2 + 6 d \tan \theta_p H_{cr} + 3 d^2) \quad (6.20)$$

However, it was found that the volume determined by Eq. 6.20 greatly underestimated the actual fragment volume extruded from the distal face, as shown as dash line in Fig. 6.16(a). The actual top area is the diameter of the perforated hole  $D_t$  which is larger than projectile diameter  $d$ . The actual bottom diameter  $D_e$  of ejected fragments is also larger than that determined by Eq. 6.20, as demonstrated in Fig. 6.17. According to Table 6.2,  $\theta_p$ ,  $H_{cr}$  and  $D_t$  varied as the velocity  $V_0$  increases, but the ejected volume was near equivalent to a frustum of a cone as illustrated in Fig. 6.16(b). The diameter of ejection  $D_e$  determined by out-of-plane displacement in 3D-DIC (Fig. 6.17) was found as

$$D_e = D_t + 2 H_{cr} \tan \theta_e \quad (6.21)$$

where  $\theta_e$  is determined as  $54^\circ$ ,  $52^\circ$  and  $51^\circ$  for HS, flat and conical projectiles. The diameter  $D_t$  is  $1.5d$  for HS, conical projectile and  $2d$  for flat projectile. Hence, the equivalent volume of ejected fragments is described as follows,

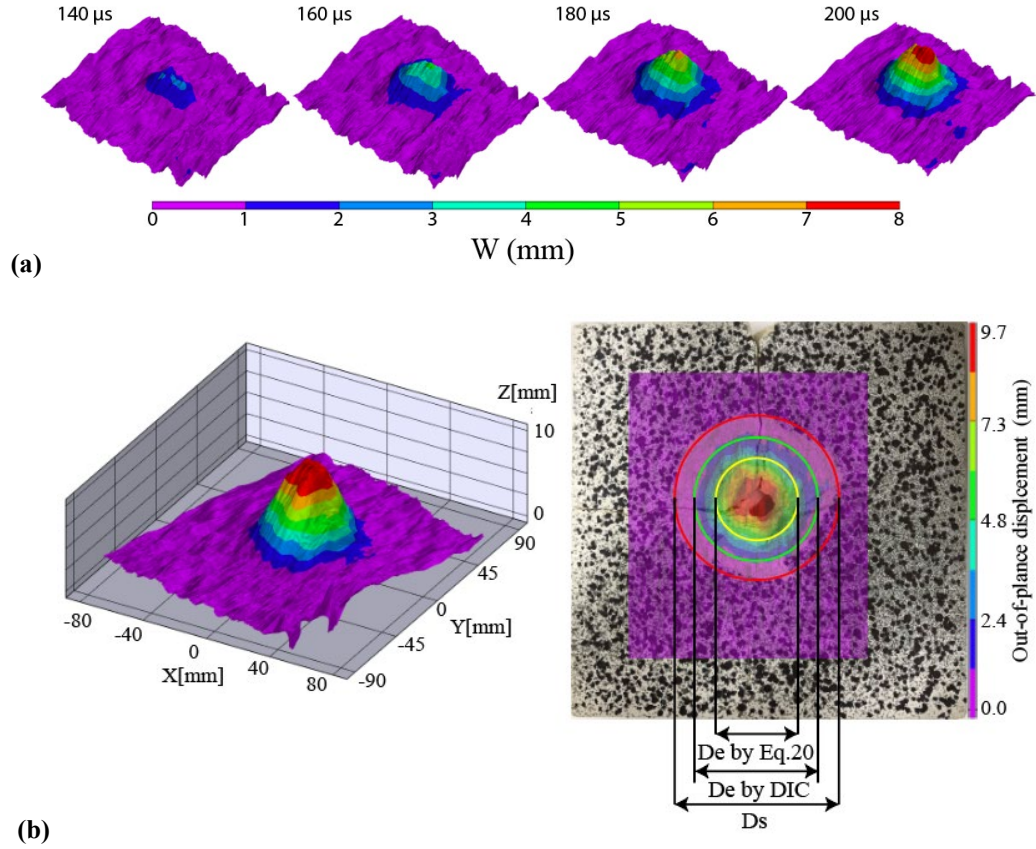
$$\Omega_e = \frac{\pi}{3} H_{cr} (D_e^2 + D_e D_t + D_t^2) \quad (6.22)$$



**Fig. 6.16** Schematic of (a) actual rear crater compared to ejection volume (dash line) by Eq. 20 (b) Equivalent ejection volume (coarse solid line) representing ejection volume under different impact velocities.

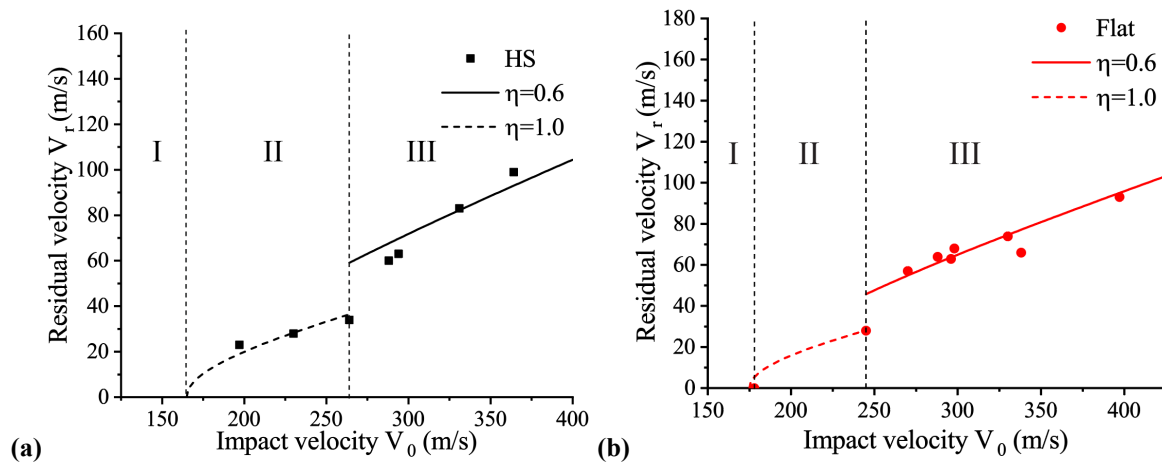


## CHAPTER 6 DYNAMIC BEHAVIOUR OF ROCK SLAB UNDER INTERMEDIATE-VELOCITY PROJECTILE IMPACT

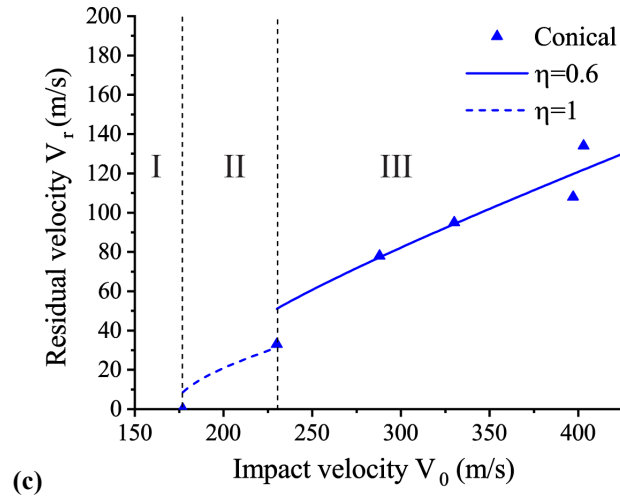


**Fig. 6.17**(a) Out-of-plane displacement field in F-1 by 3D-DIC, (b) Ejection fragment diameter determined by Eq.20 and high-speed 3D-DIC

Substituting ballistic limit  $V_{BL}$  and fragment volume (Eq. 6.21 and 6.22) into Eq. 19, the predicted residual velocity shows a good agreement with test data (Table 6.6) when the correlation coefficient  $\eta$  is found as 0.6 for Mode B ejection, as shown in Fig. 6.18.



# CHAPTER 6 DYNAMIC BEHAVIOUR OF ROCK SLAB UNDER INTERMEDIATE-VELOCITY PROJECTILE IMPACT



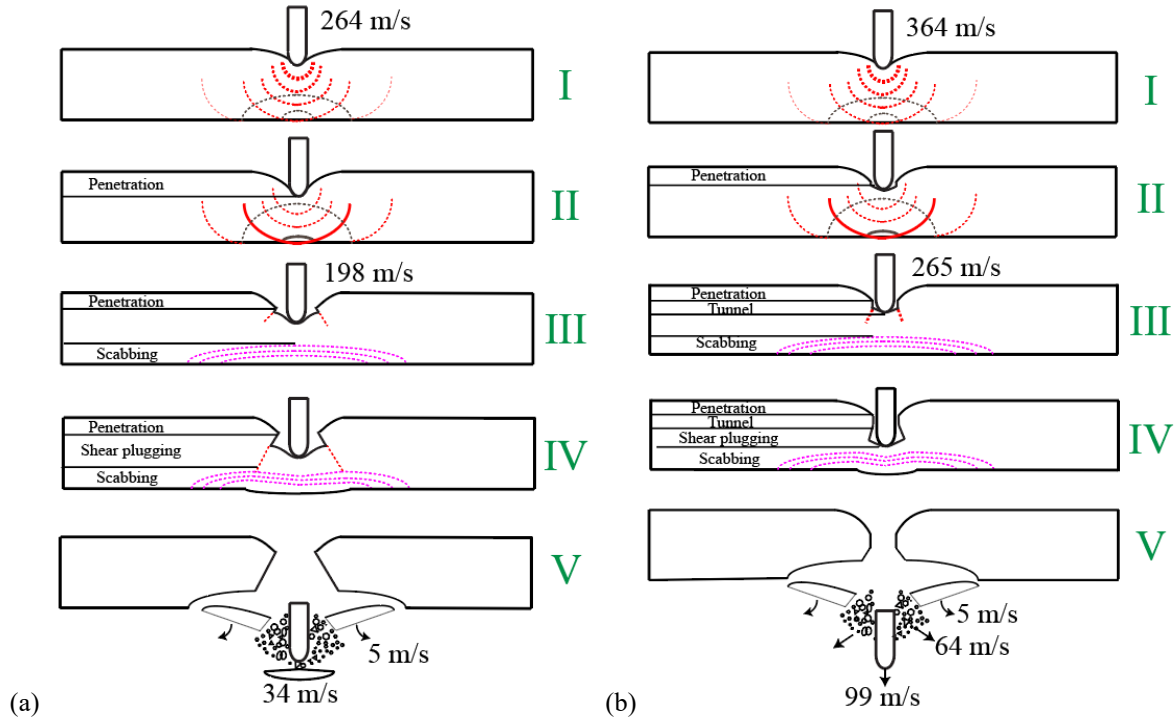
**Fig. 6.18** Predictions of residual velocity versus initial velocity and test data of (a) HS (b) flat (c) conical projectiles (I: unperforated, II: Mode X ejection, III: Mode Y ejection)

**Table 6.6** Initial velocity and residual velocity of projectile

ID	Mode	$V_0$ (m/s)	$V_r$ (m/s)
HS-1	E	364	99
HS-2	D	331	83
HS-3	D	294	63
HS-4	D	288	60
HS-5	D	264	34
HS-6	D	230	28
HS-7	D	197	23
HS-8	C	160	0
F-1	D	397	93
F-2	D	338	66
F-3	D	330	74
F-4	D	298	68
F-5	D	296	63
F-6	D	287	64
F-7	D	270	57
F-8	D	245	28
F-9	D	178	0
C-1	E	403	134
C-2	E	397	108
C-3	D	330	95
C-4	D	288	78
C-5	D	230	33
C-6	D	177	0
C-7	B	120	0

## 6.5 DISCUSSION

Based on the parameters in Table 6.2 and proposed perforation model, the perforation stages by intermediate velocity impact are identified, for example, the perforation process of HS-5 and HS-1 shown in Fig. 6.19.



**Fig. 6.19** Key stages in the perforation of (a) HS-5 and (b) HS-1 (I, Penetrating; II, Peak compressive wave reaches bottom, scabbing starts, (tunnel starts for HS-1); III, Shear plugging starts; IV, Extrusion from rear face; V, Projectile and debris eject out).

Stage I is the beginning of penetrating process where the projectile penetrates the surface of the target. Meanwhile, a compressive wave initiates from elastic zone ahead of projectile and propagates towards the distal face of the target. The wave is assumed to be spherically symmetric propagating at p-wave velocity of sandstone. The wave length is double of the projectile effective body length  $l_s$ , the peak amplitude is at the middle of the waveform. As a result, the compressive wave reaches the distal face of the slab at  $T_A = H/C$  = approximately  $15.3 \mu s$  when the tensile stress wave generates from the distal face of slab. Because the amplitude of the front wave is lower than the one, the superposed wave is still compressive wave but reduces in magnitude in the axial direction. As compressive wave continues propagating, the peak of compressive wave reaches the bottom at  $T_B = (H + l_s)/C$  which was  $25 \mu s$ ,  $25 \mu s$  and  $27 \mu s$  for HS, flat and conical projectile, respectively. From this

instance the reflected tensile wave is stronger than the following compressive wave, the superposition of wave becomes tensile wave, as indicated as Stage II in Fig. 6.19. Because the tensile strength of rock is much lower than the compressive strength, scabbing starts as soon as the tensile wave forms at the distal face. Multiple scabbing layers form due to the upcoming compressive waves reflect on the newly generated free surface. Meanwhile, penetration goes deeper, projectile with a higher impact velocity transits to tunnelling stage as HS-1. The scabbing is approximately finalized at  $T_C \approx (H + 1.8l_s)/C$ , as indicated Stage III in Fig. 6.17. The velocity of the scabbing fragments is around 5 m/s which moved 0.5 mm in 100  $\mu$ s, during which the projectile completes the perforation. Therefore, the scabbing process is almost static compared to the projectile movement. Because the scabbing reduces the remaining thickness resulting in the decline of shear resistance. For a slab with a thickness of  $H$  that is thinner than  $H_{per}$ , if the remaining thickness after scabbing is sufficient to provide shear strength against the projectile resistance,  $V_p$  is determined by Eq. 6.15, accordingly  $DOP$  is determined by Eq. 6.7. While the shear strength based on the remaining thickness after scabbing is weaker than the projectile resistance, shear plugging happens as soon as the scabbing finalises, at a projectile velocity of  $V_p$  determined as following,

$$V_p = t_p a_{mean} = \frac{t_p \pi d^2}{4M} [1 + \mu \delta(V_0)] N_1 S \sigma_{ucs} \quad (6.23)$$

Thus,

$$DOP = V_0 t_p - 0.5 t_p^2 \quad (6.24)$$

$$H_p = H - 0.8 l_s - DOP \quad (6.25)$$

Finally, as indicated as Stage IV and V in Fig. 6.19, the projectile and fragments exit from the rear face with a residual velocity.

The mechanism distinguishing the intermediate- and high-velocity impact is the priority between scabbing and shear plugging. A high-velocity perforation process is illustrated in Fig. 6.20. A higher velocity not only leads to a deeper DOP in a shorter time but also generates a larger resistance on the interface between projectile and target. Higher resistance and thinner remaining thickness of slab activate the shear plugging taking place before scabbing initiating, as demonstrated Stage III in Fig. 6.20. In other words, the duration of

penetration  $t_p$  should be less than the time for peak compressive wave reaching the bottom, as described in Eq. 6.26,

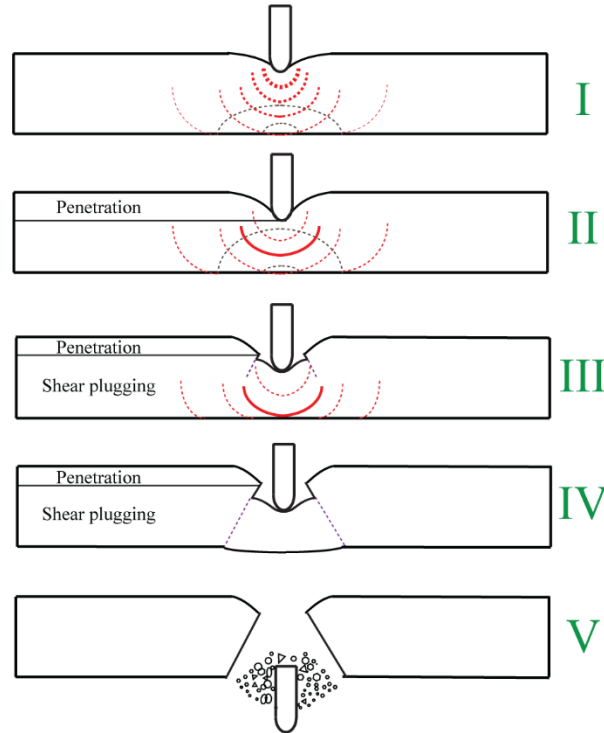
$$t_p < (H + l_s)/C \quad (6.26)$$

$$t_p = \frac{2DOP}{V_0 + V_p} \quad (6.27)$$

The height of shear plugging in high-velocity perforation on thin slab was proposed as

$$H_p = H_{rc} = 0.5H \quad (6.28)$$

by Fang and Wu (Fang and Wu 2017) based on the fitting of existing perforation results in (Chen, Li et al. 2008) and (Wu, Fang et al. 2015).  $V_p$  can be derived by substituting Eq. 6.28 into Eq. 6.15, which further determines  $V_0$  (threshold of high-velocity perforation) in Eq. 6.27. For the 30mm sandstone slab in this study, the lower limit of impact velocity to generate high-velocity impact is 600, 590 and 580 m/s for flat, HS and conical projectiles, respectively. Compared to the perforation limit around 170 m/s, the intermediate-velocity impact consumed 92% less energy to perforate a slab.



**Fig. 6.20** Illustration of perforation on thin slab at a high velocity (over 500 m/s)

## CHAPTER 6 DYNAMIC BEHAVIOUR OF ROCK SLAB UNDER INTERMEDIATE-VELOCITY PROJECTILE IMPACT

Even though the impact with an initial velocity  $V_0$  less than 1 km/s is normally considered as the non-deformable perforation regime, intermediate and high-velocity impacts of thin sandstone slabs display two entirely different perforation models. It is essential to examine the critical velocity and choose the right model to predict the ballistic damage.

There are also some limitations in this work. For example, the confinement within the shear zone is considered as zero based on the model proposed in (Li and Tong, 2003). However, in more recent works it was reported that the impact resistance of a targets made of concrete or rock-like materials was rather driven by a combination of the confined compression strength plus the dynamic tensile strength rather than the uniaxial (unconfined) compression strength (Forquin et al, 2008; 2015; Warren and Forquin, 2016). In addition, the strain rate effect on the shear strength is only revealed from shear angle, the magnitude of shear strength is not modified with strain rate. Therefore, more investigations are expected to evaluate the confinement and strain rate within the shear plugging zone. In terms of the residual velocity which is calculated from theory of energy balance. In this study, the energy used for pore collapse, fracture formation and ejecta rotation are not evaluated independently. Those energies are quantitatively included when calculating the residual kinetic energy of ejected fragments by using the equivalent ejection volume. By fitting the residual velocity curve, the energy balance is satisfied. However, predicting the residual velocity with empirical formulae can not reveal the physical meaning. The investigation of each independent energy dissipation is important to look into the failure mechanism in each stage. The basic physics in each stage, for example the transition from cratering to tunnelling, is still based on assumptions. Through the microscopic measurement, such as scanning electron microscopic, the mechanism (melt, tensile, shear or mixed) is able to be revealed by the topography of the change on grain surface. When it comes to the measurement in this study, the change of projectile velocity during perforation indicates the deceleration. However, the tracking of projectile is only valid during the cratering stage until the projectile being blocked by the target. With the help of a transparent material or a special beacon on projectile that could be sensed by a receiver regardless of target transparency, the whole projectile trajectory and velocity profile can be determined. The perforation performance and mechanism of different types of rock thin slab with different hardness remain unknown.

## 6.6 SUMMARY

Intermediate-velocity perforation tests were conducted on thin rock slab with HS, flat and conical projectiles. The deceleration of projectile was captured by high-speed cameras. The real-time and full-field deformation of target were extracted by 3D-DIC. The perforation model was carried out including perforation limit, ballistic limit and residual velocity. The perforation stages between intermediate- and high-velocity perforation were also discussed in detail. The main conclusions of this paper are as follows:

- High-performance high-speed photography, as a non-destructive measurement, was proven convenient and successful in detecting the deceleration of projectile during perforation. Based on the measured deceleration, the empirical constants in semi-analytical models are calibrated corresponding to the actual projectile and target material. A variation could be over 10% in predicting the DOP with calibrated and uncalibrated parameters in the equation.
- The perforation limit and ballistic limit equations for intermediate-velocity impact were established. The DOP was predicted by the mean resistance approach based on dynamic cavity expansion approximation. The prediction of shear plugging height was given where the dynamic shear plugging angle is dependent on nose-shape and impact velocity. The dimensionless height of scabbing was determined as  $0.8l_s$ .
- According to two different ejection modes, the model to predict the residual velocity after intermediate-velocity perforation was carried out. Using the equivalent volume detected by high-speed 3D-DIC, the correlation coefficient was determined as 0.6.
- A time-scale perforation process in intermediate-velocity projectile impact was reconstructed with the key moments identified. According to the priority between shear plugging and scabbing, the critical velocity between intermediate- and high-velocity impact was discussed. The scabbing damage is the most significant difference in damage pattern between intermediate- and high-velocity perforation. The scabbing effect greatly reduces the remaining thickness making the shear failure more prone to happen. It saves up to 92% kinetic energy to perforate a slab compared with the critical high-velocity perforation mode.

## REFERENCES

- Ben-Dor, G., A. Dubinsky and T. Elperin (2014). "Engineering models of high-speed penetration into geological shields." *Central European Journal of Engineering* 4(1): 1-19.
- Borg, J., M. Morrissey, C. Perich, T. Vogler and L. Chhabildas (2013). "In situ velocity and stress characterization of a projectile penetrating a sand target: experimental measurements and continuum simulations." *International Journal of Impact Engineering* 51: 23-35.
- Borvik, T., O. E. Gjorv and M. Langseth (2007). "Ballistic perforation resistance of high-strength concrete slabs." *Concrete international* 29(06): 45-50.
- Cargile, J., M. Giltrud and V. Luk (1993). *Perforation of thin unreinforced concrete slabs*, Sandia National Labs., Albuquerque, NM (United States).
- Chen, X. and Q. Li (2002). "Deep penetration of a non-deformable projectile with different geometrical characteristics." *International Journal of Impact Engineering* 27(6): 619-637.
- Chen, X., X. Li, F. Huang, H. Wu and Y. Chen (2008). "Normal perforation of reinforced concrete target by rigid projectile." *International Journal of Impact Engineering* 35(10): 1119-1129.
- Chen, Z., M. Omidvar, M. Iskander and S. Bless (2014). "Modelling of projectile penetration using transparent soils." *International Journal of Physical Modelling in Geotechnics* 14(3): 68-79.
- Cole, R. P. (2010). "Ballistic penetration of a sandbagged redoubt using silica sand and pulverized rubber of various grain sizes."
- Collins, A., J. Addiss, S. Walley, K. Promratana, F. Bobaru, W. Proud and D. Williamson (2011). "The effect of rod nose shape on the internal flow fields during the ballistic penetration of sand." *International Journal of Impact Engineering* 38(12): 951-963.
- Dancygier, A. N. (1998). "Rear face damage of normal and high-strength concrete elements caused by hard projectile impact." *Structural Journal* 95(3): 291-304.
- Erzar, B., & Forquin, P. (2010). An experimental method to determine the tensile strength of concrete at high rates of strain. *Experimental Mechanics*, 50(7), 941-955.
- Fang, Q. and H. Wu (2017). *Concrete structures under projectile impact*. Concrete Structures Under Projectile Impact, Springer: 497-558.
- Forquin, P., Arias, A., & Zaera, R. (2008). Role of porosity in controlling the mechanical and impact behaviours of cement-based materials. *International Journal of Impact Engineering*, 35(3), 133-146.
- Forquin P., Sallier L., Pontiroli C. (2015) A numerical study on the influence of free water content on the ballistic performances of plain concrete targets. *Mechanics of Materials*. 89, 176-189.
- Warren T., Forquin P. (2016) Penetration of common ordinary strength water saturated concrete targets by rigid ogive-nosed steel projectiles. *Int. J. Impact Eng.*, 90, 37-45.
- Forrestal MJ, Altman BS, Cargile JD, Hanchak SJ (1994) An empirical equation for penetration depth of ogive-nose projectiles into concrete targets. *Int J Impact Eng* 15:395-405.



## CHAPTER 6 DYNAMIC BEHAVIOUR OF ROCK SLAB UNDER INTERMEDIATE-VELOCITY PROJECTILE IMPACT

Forrestal MJ, Frew DJ, Hanchak SJ, Brar NS (1996) Penetration of grout and concrete targets with ogive –nose steel projectiles. *Int J Impact Eng* 18:465–476.

Forrestal, M., D. Frew, J. Hickerson and T. Rohwer (2003). "Penetration of concrete targets with deceleration-time measurements." *International Journal of Impact Engineering* 28(5): 479-497.

Guzman, I. L., M. Iskander and S. Bless (2015). "Observations of projectile penetration into a transparent soil." *Mechanics Research Communications* 70: 4-11.

Hanchak, S., M. Forrestal, E. Young and J. Ehrgott (1992). "Perforation of concrete slabs with 48 MPa (7 ksi) and 140 MPa (20 ksi) unconfined compressive strengths." *International Journal of Impact Engineering* 12(1): 1-7.

Heineck, J., P. Schultz and J. Anderson (2002). "Application of three-component PIV to the measurement of hypervelocity impact ejecta." *Journal of visualization* 5(3): 233-241.

Hogan, J. D., J. G. Spray, R. J. Rogers, G. Vincent and M. Schneider (2013). "Dynamic fragmentation of natural ceramic tiles: ejecta measurements and kinetic consequences." *International Journal of Impact Engineering* 58: 1-16.

Hogan, J. D., J. G. Spray, R. J. Rogers, G. Vincent and M. Schneider (2013). "Dynamic fragmentation of planetary materials: ejecta length quantification and semi-analytical modelling." *International Journal of Impact Engineering* 62: 219-228.

Hogan, J. D., J. G. Spray, R. J. Rogers, G. Vincent and M. Schneider (2014). "Impact failure of planetary materials." *Experimental Mechanics* 54(4): 665-675.

Jinzhu, L., L. Zhongjie, Z. Hongsong and H. Fenglei (2013). "Perforation experiments of concrete targets with residual velocity measurements." *International Journal of Impact Engineering* 57: 1-6.

Kokaa, T. R. and A. T. Mathewb (2017). "Design of Sabot & Catcher System of Single Stage Gas Gun for Bird and Hailstone Impact test."

Lee, S., G. Kim, H. Kim, M. Son, G. Choe and J. Nam (2018). "Strain Behavior of Concrete Panels Subjected to Different Nose Shapes of Projectile Impact." *Materials* 11(3): 409.

Li, Q. and X. Chen (2003). "Dimensionless formulae for penetration depth of concrete target impacted by a non-deformable projectile." *International journal of impact engineering* 28(1): 93-116.

Li, Q. and D. Tong (2003). Perforation thickness and ballistic limit of concrete target subjected to rigid projectile impact. *Journal of Engineering Mechanics*, 129(9), 1083-1091.

Li, Q., H. Weng and X. Chen (2004). "A modified model for the penetration into moderately thick plates by a rigid, sharp-nosed projectile." *International journal of impact engineering* 30(2): 193-204.

Rossmannith, H. and K. Uenishi (2006). "The mechanics of spall fracture in rock and concrete." *Fragblast* 10(3-4): 111-162.

Seah, C. C., T. Børvik, S. Remseth and T.-C. Pan (2011). "Penetration and perforation of rock targets by hard projectiles." *Advances in Rock Dynamics and Applications*. CRC Press, Boca Raton, FL.

## CHAPTER 6 DYNAMIC BEHAVIOUR OF ROCK SLAB UNDER INTERMEDIATE-VELOCITY PROJECTILE IMPACT

- Shi, W., Y. Wu and L. Wu (2007). "Quantitative analysis of the projectile impact on rock using infrared thermography." *International Journal of Impact Engineering* 34(5): 990-1002.
- Si, X., Gong, F., Li, X., Wang, S., & Luo, S. (2019). Dynamic Mohr–Coulomb and Hoek–Brown strength criteria of sandstone at high strain rates. *International Journal of Rock Mechanics and Mining Sciences*, 115, 48-59.
- Unosson, M. (2000). "Numerical simulations of penetration and perforation of high-performance concrete with 75mm steel project." Defence Research Establishment (FOA).
- Wang, S. Y., Sloan, S. W., Liu, H. Y., & Tang, C. A. (2011). Numerical simulation of the rock fragmentation process induced by two drill bits subjected to static and dynamic (impact) loading. *Rock mechanics and rock engineering*, 44(3), 317-332.
- Wu, H., Q. Fang, Y. Peng, Z. Gong and X. Kong (2015). "Hard projectile perforation on the monolithic and segmented RC panels with a rear steel liner." *International Journal of Impact Engineering* 76: 232-250.
- Wu, H., Q. Fang, Y.-D. Zhang and Z.-M. Gong (2012). "Semi-theoretical analyses of the concrete plate perforated by a rigid projectile." *Acta Mechanica Sinica* 28(6): 1630-1643.
- Xing, H., Q. Zhang, C. H. Braithwaite, B. Pan and J. Zhao (2017). "High-speed photography and digital optical measurement techniques for geomaterials: fundamentals and applications." *Rock Mechanics and Rock Engineering* 50(6): 1611-1659.
- Yankelevsky, D. Z. (1997). "Local response of concrete slabs to low velocity missile impact." *International journal of impact engineering* 19(4): 331-343.
- Zhang, M., V. Shim, G. Lu and C. Chew (2005). "Resistance of high-strength concrete to projectile impact." *International Journal of Impact Engineering* 31(7): 825-841.

## CHAPTER 7 CONCLUSIONS AND FUTURE WORKS

In this thesis, high-speed and full-field measurement are performed to investigate dynamic behaviour of rock materials. A brief overview of the findings of the main research topics, the advances in the state of the art, and recommendations for future work is given below.

### 7.1 CONCLUSIONS

#### (1) Dynamic properties and fracture by full-field measurement

High-speed 3D-DIC method was successfully implemented on the rock dynamics study and proven to be a powerful tool to investigate the dynamic deformation of rock in terms of velocity, strain and strain rate. The strain histories obtained by DIC shows differences with those obtained by traditional strain gauge method. 2D- DIC shows a relatively large error in 3D rock dynamic deformation compared to 3D-DIC. The existence of the axial and radial inertial effect on the specimen are revealed. The dynamic Poisson's ratio is rate-dependent and changing during the loading and negative at the beginning. The stress thresholds of cracks development are characterized and no elastic stage was found in dynamic compression. The evolution and distribution of crack are identified.

#### (2) Intrinsic and external effects on dynamic behaviour of rock

MG sandstone has the largest the rate sensitivity in strength, CG sandstone has the largest the rate sensitivity in Young's modulus. The stress threshold for crack initiation and unstable development behaved differently in different grain-sized sandstone. As a widely used method to determine the dynamic behavior of brittle material, SHPB is however hard to achieve a same strain rate comparison between different types of materials. The propagation velocity of the strain localisation (as well as crack) is dependent on the wave impedance of the rock. The strength of the rock can be estimated from the mineral composition and distribution in terms of clay, grain size and grain distribution.

The compressive and tensile strength firstly increase and then decrease defined by a critical temperature between 400 °C and 800 °C. The stress thresholds normalized to the peak stress corresponding to cracks development were investigated and found that higher temperature resulted in larger normalized threshold. The temperature will reduce the localization in

vertical strain field but increase that in horizontal direction causing more significant fragmentation.

The presence of CO<sub>2</sub> increases the dynamic Young's modulus and decrease Poisson's ratio for dry sandstone. This trend is opposite for the sandstone saturated in water. The compressive strength in dry sandstone is less attenuated than that in water-saturated sandstone by the injection of CO<sub>2</sub>. The presence of CO<sub>2</sub> has considerable effect on the above dynamic behaviours of sandstone saturated in brine. The enhancement effect of strain rate on the compressive strength still exists for all types of treatments, but the presence of CO<sub>2</sub> reduces the dynamic increase factor. The presence of CO<sub>2</sub> brings forward the stress threshold of crack initiation and unstable crack development of dry or water-saturated sandstone. CO<sub>2</sub> has less effect on the stress threshold of crack initiation of sandstone in brine but salinity does. For dry, water or brine saturated sandstone, the presence of CO<sub>2</sub> alters the crack initiation position and accelerates the propagation speed. CO<sub>2</sub> intensified the strain localisation degree in both dynamic compression and tension condition.

### **(3) Dynamic behaviour of rock slab under intermediate-velocity projectile impact**

Based on the measured deceleration, the empirical constants in semi-analytical models are calibrated corresponding to the actual projectile and target material. The constants in the equation have to be calibrated rather than choosing the empirical one to minimize the error. The perforation limit and ballistic limit equations for intermediate-velocity impact were established. The DOP was predicted by the mean resistance approach based on dynamic cavity expansion approximation. The prediction of shear plugging height was given where the dynamic shear plugging angle is dependent on nose-shape and impact velocity. The dimensionless height of scabbing was found related to the effective body length of projectile. The model to predict the residual velocity after intermediate-velocity perforation was carried out. A time-scale perforation process in intermediate-velocity projectile impact was reconstructed with the key moments identified. The critical velocity between intermediate- and high-velocity impact was discussed.

## 7.2 LIMITATION AND FUTURE WORK

### (1) Dynamic properties and fracture by full-field measurement

In this chapter, the deformation such as displacement, strain and strain rate were directly measured which is an advance over the traditional indirect measurement by strain signals. However, the stress measured in SHPB test was still obtained by strain signal calculation which means the determination of Young's modulus was based on half direct measurement and half indirect measurement. Photoelasticity is one of the most useful method to have a stress field of the material. It is expected in the future to combine the stress field obtained by photoelasticity and strain field by DIC to determine full-field mechanical properties not only Young's modulus but also constitutive model that involves both stress and strain information. The constitutive model is one of the most important components in numerical simulation of rock engineering problems. Related to those models are constitutive constants to describe the properties of specific materials. To satisfy the complex behaviour of rock under various loading condition, the unknown constants tend to be of a large quantity. When rate dependency has to be taken into consideration in dynamic cases, the undetermined parameters would be much more than the static case, for example, over twenty in HJC model. Characterizing the unknown constants is always challenging and important to the applicability and accuracy of a constitutive model. Traditional direct determination of constitutive parameters requires a large number of different tests and specimens. Inverse method is an essential solution to identify or validate unknown constitutive parameters, through repeated comparison between experimental and numerical key variables (strain, stress history or stress-strain curve) with algorithms such as least-square or other mathematical programming techniques of error minimization. The coupling DIC-DEM inverse method is a good method to interpret the constitutive constants by minimising the difference in strain field obtained between DIC and DEM method. This has been used in alloy material with quasi-static test. This technology has not been employed in the dynamic tests let alone rock dynamics. It is believed to be a useful method promoting the development in numerical simulation of rock dynamics.

The real-time and full-field fracture pattern of specimen surface were analysed, the timing for internal fracture initiation and development was identified. However, how the internal fracturing starts and propagates remain unknown. To fully identify the dynamic fracture

process of rock, it is necessary to understand the evolution, distribution, energy and mechanism of the fracture development inside the specimen. A comprehensive understanding of the surface deformation, internal fracturing and fragments could provide an whole picture of rock dynamic failure process. To achieve the internal deformation measurement, options are X-Ray, digital volume correlation (DVC) and acoustic emission (AE). Among them, AE, due to its high sampling rate, promises to have the most potential for internal examination and detection of failures in dynamic testing of rocks. There have been several studies (Liu, Li et al. 2015, Woo and Kim 2016) using AE sensor to detect the AE events and energy in SHPB tests. However, in those tests only one channel was adopted for parameter-based analysis which could not determine the spatial and temporal development of fracture. Therefore, in the future, multi-channel, i.e. waveform-based, AE test is expected to analyse the internal crack evolution, distribution, energy and mechanism in rock subjected to the dynamic loading. In addition to the study of the fracturing behavior for intact specimen, the dynamic fragmentation of a single particle also deserves a lot of attention. It provides a basis for better understand of the fragmentation process. Drop shatter test is a mature testing method to investigate the sphere fragmentation under various loading conditions. With the high-speed photography and 3D-DIC, the deformation of a single particle and energy utilization by comminution can be well identified.

## **(2) Intrinsic and external effects on dynamic behaviour**

Even though we found that DIF is weakened by the presence of CO<sub>2</sub> in dry, water or brine saturated sandstone. However, if we want to investigate how the weakening effect of CO<sub>2</sub> changing with the strain rates variation, the difficulty arises that the actual strain rate for the specimen treated or untreated by CO<sub>2</sub> is different. For example, WC3 and NC3 have quite similar strain rates (148 and 151 s<sup>-1</sup>, respectively), but it is still hard to decouple the strain rate effect. Because according to the principle of the SHPB, the stress  $\sigma(t)$ , strain  $\varepsilon(t)$  and strain rate  $\dot{\varepsilon}(t)$  on the specimen can be, respectively, determined by the two-wave method as below,

$$\sigma(t) = \frac{A}{A_s} E \varepsilon_t(t), \dot{\varepsilon}(t) = -2 \frac{C_0}{L} \dot{\varepsilon}_r(t), \varepsilon(t) = -2 \frac{C_0}{L} \int_0^t \dot{\varepsilon}_r(t) dt$$

Therefore, the strain rate is controlled by the reflective wave, which further depends on the wave impedance ratio between the bar and the sample. When the sandstone is treated, under the same loading configuration, the strain rate will definitely differ from each other. This is also an inevitable shortcoming for SHPB when the investigation is expected to perform on different types of material with same strain rate. It is not like the servo-hydraulic UCS machine in which the strain rate can be controlled according to the feedback from the specimen displacement to achieve the same strain rate. One way to overcome this difficulty is to do a large number of tests and reducing the gap of loading pressure for each impact. This is time and money-consuming. Another method is to detecting the wave impedance and calculating how much the impact pressures are required to achieve the same strain rate.

There are some techniques being adapted to the current loading equipment to simulate an in-situ environment, for example, a furnace, a loading cell or a water tank to achieve a constant thermal, pre-stress or hydraulic condition, respectively. For CO<sub>2</sub> saturation, the reaction requires high pressure chamber and months to achieve the balance, which makes it difficult to modify the SHPB bar or carry out a real-time in-situ environment-like condition for samples during the loading. In the future, a universal external treatment cell is expected to be invented with which the treated specimen can be easily loaded or unloaded to the SHPB without any disturbance of the treatment on rock.

### **(3) Dynamic behaviour of rock slab under intermediate-velocity projectile impact**

The confinement within the shear zone in this thesis was considered as zero. However, in more recent works it was reported that the impact resistance of a targets made of concrete or rock-like materials was rather driven by a combination of the confined compression strength plus the dynamic tensile strength rather than the uniaxial (unconfined) compression strength. In addition, the strain rate effect on the shear strength is only revealed from shear angle, the magnitude of shear strength is not modified with strain rate. Therefore, more investigations are expected to evaluate the confinement and strain rate within the shear plugging zone. In terms of the residual velocity which is calculated from theory of energy balance. In this study, the energy used for pore collapse, fracture formation and ejecta rotation are not evaluated independently. Those energies are quantitatively included when calculating the residual kinetic energy of ejected fragments by using the equivalent ejection volume. By fitting the

residual velocity curve, the energy balance is satisfied. However, predicting the residual velocity with empirical formulae can not reveal the physical meaning. The investigation of each independent energy dissipation is important to look into the failure mechanism in each stage. The basic physics in each stage, for example the transition from cratering to tunnelling, is still based on assumptions. Through the microscopic measurement, such as scanning electron microscopic, the mechanism (melt, tensile, shear or mixed) is able to be revealed by the topography of the change on grain surface. When it comes to the measurement in this study, the change of projectile velocity during perforation indicates the deceleration. However, the tracking of projectile is only valid during the cratering stage until the projectile being blocked by the target. With the help of a transparent material or a special beacon on projectile that could be sensed by a receiver regardless of target transparency, the whole projectile trajectory and velocity profile can be determined.



## Curriculum vitae

### Haozhe Xing

Department of Civil Engineering

Monash University, Clayton VIC 3800

**Date of Birth:** 04/11/1989

**Nationality:** China

**Email:** Haozhe.xing@monash.edu; Haozhexing@hotmail.com



### Education

- |                        |                                                                                                                                                                                                                                                                                       |
|------------------------|---------------------------------------------------------------------------------------------------------------------------------------------------------------------------------------------------------------------------------------------------------------------------------------|
| <b>12.2015—Present</b> | <b>Doctor of Philosophy in Civil Engineering</b><br><b>Monash University, Australia</b><br>Supervisors: Prof. Jian Zhao, Dr. Qianbing Zhang,<br>Dr. Sevda Dehkhoda                                                                                                                    |
| <b>09.2012—09.2015</b> | <b>Successive postgraduate and doctoral program candidate</b><br><b>in Disaster Prevention and Reduction Engineering</b><br><b>State Key Laboratory (SKL) of Disaster Prevention &amp;</b><br><b>Mitigation of Explosion &amp; Impact, China.</b><br>Supervisors: Prof. Mingyang Wang |
| <b>08.2008—07.2012</b> | <b>Bachelor of Engineering (Honour)</b><br>Civil Engineering,<br>Zhejiang University, Hangzhou, China                                                                                                                                                                                 |

### Research Experiences

- |                |                                                                                                                                                                                                                                  |
|----------------|----------------------------------------------------------------------------------------------------------------------------------------------------------------------------------------------------------------------------------|
| <b>04.2019</b> | <b>Co-proposer (editor), Australian Synchrotron (No.14423)</b><br><br>Program on the Imaging and Medical Beamline (In-kind ANSTO<br>Grant Value: \$ AUD 65,568.00)<br><br>• Grain size effect on the dynamic fracturing of rocks |
|----------------|----------------------------------------------------------------------------------------------------------------------------------------------------------------------------------------------------------------------------------|

### Patents:

- Fan, P.X, Wang, M.Y., Jiang, K.F. and **Xing, H.Z.**. An equivalent material for brittle rock and its preparation method. Filed 2014.

- Fan, P.X, Wang, M.Y. and **Xing, H.Z.**. A method of adjusting the bulk density of the equivalent material by barite sand. Filed 2014.

## **Teaching Experiences**

- Teaching assistant, Undergraduate Course CIV 3247, Geomechanics 2, Fall 2018.
- Co-supervisor, Final year project, “Effect of loading rate on brittle particle breakage” by Mr. Weiyu Li 2017-2018.

## **Honours and Awards**

- 2019 Postgraduate Publication Award, Monash University
- Best Publication Award in 2018 Monash University Civil Engineering Postgraduate conference
- Highly commended for student paper award in 11th International Conference on Structural Integrity and Failure
- CSIRO top-up postgraduate scholarship
- 2012, Second Prize of the Ninth Huawei Cup National Graduate Mathematical Modeling Competition, State Key Laboratory;
- 2012, Outstanding Graduates of 2012, Zhejiang University;
- 2010-2011, Huahui Lingyan Scholarship, Zhejiang University
- 2009-2010, Nandu Scholarship, Zhejiang University
- 2009-2011 Excellent Student Award, Zhejiang University;
- 2009-2011 Third-Class Scholarship for Outstanding Students, Zhejiang University;
- 2009-2011 Third-Class Scholarship for Outstanding Merits, Zhejiang University;

## **Research Interests**

- Dynamic behaviour of rock
- Fracture mechanics
- High-speed photography
- Digital image correlation

## **Reviewer for Technical Journals**

Rock Mechanics and Rock Engineering, Tunnelling and Underground Space Technology, Optics Express, Measurement, Tectonophysics, Journal of Testing and Evaluation

## **Organizing Conference**

- Organizing committee member of International Conference on Design and Analysis of Protective Structures (DAPS) 2017.
- Conference Secretariat: 2nd International Conference on Rock Dynamics and Applications (RocDyn-2), 18 – 19 May 2016, Suzhou, China.

## **Publications and Metrics**

(Citations: 42, from Google Scholar, on 18 March 2019)

### **Journal Articles**

1. **Xing, H. Z.**, Zhang, Q. B., Braithwaite, C. H., Pan, B., & Zhao, J. (2017). High-speed photography and digital optical measurement techniques for geomaterials: fundamentals and applications. *Rock Mechanics and Rock Engineering*, 50(6), 1611-1659.
2. **Xing, H. Z.**, Zhang, Q. B., Ruan, D., Dehkhoda, S., Lu, G. X., & Zhao, J. (2018). Full-field measurement and fracture characterisations of rocks under dynamic loads using high-speed three-dimensional digital image correlation. *International Journal of Impact Engineering*, 113, 61-72.
3. **Xing, H. Z.**, Zhang, Q. B., & Zhao, J. (2018). Stress Thresholds of Crack Development and Poisson's Ratio of Rock Material at High Strain Rate. *Rock Mechanics and Rock Engineering*, 51(3), 945-951.
4. **Xing, H. Z.**, Wu, G. L. N., Dehkhoda, S., Ranjith, G. & Zhang, Q. B. (2019). Fracture and mechanical characteristics of CO<sub>2</sub>-saturated sandstone at extreme loading conditions. *International Journal of Rock Mechanics and Mining Sciences*. Vol.50, pp.1611-1659.
5. Fan, P.X., **Xing, H.Z.**, Ma, L.J., Jiang, K.F. & Wang, M.Y. (2014). Density adjustment of resin-based equivalent material for rock. *International Journal of Physical Modelling in Geotechnics*.
6. **Xing, H.Z.**, Fan, P.X., Jiang K.F. & Li, A. (2013). Reviews on the Failure Mechanism and Stress Condition of Rock Core Discing. *Electronic Journal of Geotechnical Engineering*, 18/S, 4201-4215.

### **Conference Papers**

1. **Xing, H. Z.**, Wu, G. L. N., Dehkhoda, S., Zhang, Q. B., & Zhao, J. (2018). A preliminary study of using high-speed Digital Image Correlation (DIC) to characterize the penetration on geomaterial. In *Rock Dynamics and Applications 3* (pp. 175-178). CRC Press.
2. **Xing, H. Z.**, Wu, G. L. N., Zhang, Q.B., Dehkhoda, S., & Zhao, J. (2018). Characterization of thermal/strain rate effect on the rock fracture using high-speed 3D-DIC. 10th Asian Rock Mechanics Symposium.
3. **Xing, H. Z.**, Dehkhoda, S., Zhang, Q. B., & Zhao, J. (2018). The dynamic fracturing patterns of multiple types of rock with Brazilian tests investigated by high-speed 3D-DIC. 11<sup>th</sup> International Conference on Structural Integrity and Failure.
4. Wu, G. L. N, **Xing, H. Z.**, Zhang, Q.B. and Dehkhoda, S. (2019). Dynamic shear fracture and SEM study of granite and marble. 53rd US Rock Mechanics / Geomechanics Symposium.